Simulation of High Frequency Seismic Waves generated by Rockfalls on Real Topography

Julian Kuehnert

UNIVERSITÉ DE PARIS

université PARIS DIDEROT PARIS 7

École Doctorale STEP'UP – ED 560

Institut de Physique du Globe de Paris – Équipe de Sismologie

Simulation of High Frequency Seismic Waves generated by Rockfalls on Real Topography

par

Julian Kühnert

Thèse de doctorat de Sciences de la Terre et de l'Environnement

dirigée par **Anne Mangeney**

et par **Yann Capdeville**

présentée et soutenue publiquement le

27 november 2019

devant un jury composé de

Domniki Asimaki	Professeure (Caltech, CA)	Rapportrice
Heiner Igel	Professeur (LMU München, Munich, Allemagne)	Rapporteur
Denis Jongmans	Professeur (ISTerre, Grenoble, France)	Examinateur
Maurizio Ripepe	Professeur (Univ. degli Studi di Firenze, Florence, Italie)	Examinateur
Jean-Paul Montagner	Professeur (Université Diderot, Paris, France)	Président

UNIVERSITÉ DE PARIS

université PARIS DIDEROT PARIS 7

École Doctorale STEP'UP – ED 560

Institut de Physique du Globe de Paris – Équipe de Sismologie

Simulation of High Frequency Seismic Waves generated by Rockfalls on Real Topography

par

Julian Kuehnert

Thèse de doctorat de Sciences de la Terre et de l'Environnement

dirigée par **Anne Mangeney**

et par **Yann Capdeville**

présentée et soutenue publiquement le

27 novembre 2019

devant un jury composé de

Domniki Asimaki	Professeure (Caltech, CA)	Rapportrice
Heiner Igel	Professeur (LMU München, Munich, Allemagne)	Rapporteur
Denis Jongmans	Professeur (ISTerre, Grenoble, France)	Examinateur
Maurizio Ripepe	Professeur (Univ. degli Studi di Firenze, Florence, Italie)	Examinateur
Jean-Paul Montagner	Professeur (Université Diderot, Paris, France)	Président

Institut de Physique du Globe de Paris – Équipe de Sismologie – 1 rue Jussieu, 75238 Paris cedex 05, France

Abstract

Rockfall hazard has to be evaluated and monitored in order to prevent loss of life and infrastructure. In this regard it is important to create event catalogs and understand rockfall dynamics. Seismic waves can help for this purpose as they carry valuable information of the event. They are generated when rockfalls impact the ground and can be used to detect, classify and locate events. Beyond that, rockfall properties such as their volume and their dynamic behavior can be inferred. Yet, high frequency seismic signals (> 1 Hz) are poorly understood. This is because they are associated to complex seismic sources which are spatially distributed and can rapidly vary over time. On top of this, high frequency seismic waves are prone to be scattered and diffracted due to interactions with soil heterogeneities or surface topography. This thesis takes an important step forward to enhance understanding of high frequency rockfall seismic signals by simulating seismic wave propagation on domains with realistic velocity profiles and 3D surface topographies using the Spectral Element Method (SEM).

The influence of the topography on the seismic wave field is investigated. It is found that topography induced amplification is substantially different between deep sources and sources located at the surface. This is because surface waves generated by shallow sources are exposed to constant scattering and diffraction when traveling along the surface.

The energy decay along the surface is investigated for different velocity models and equations are derived to back-calculate the total seismic energy radiated by the source. This is of interest as the rockfall seismic energy is related to the rockfall volume. In order to account for topography effects, a correction factor is proposed which can be introduced in the energy calculation.

Observed seismic signals generated by rockfall at Dolomieu crater on Piton de la Fournaise volcano, La Réunion, are analyzed. Synthetic seismograms are used to identify and interpret observed signals generated by single impacts. The influence of topography on the waveforms is demonstrated and the sensitivity on source location as well as source direction is evaluated. Signal characteristics such as amplitudes and frequency content are explained based on Hertz contact theory.

Additionally, inter-station spectral ratios computed from rockfall seismic signals are shown to be characteristic of the source position. Comparison with simulated spectral ratios suggest that they are dominated by the propagation along the topography rather than the mechanism of the source. Based on these findings, a method is proposed for the localization of rockfalls using simulated inter-station energy ratios. The method is applied to localize rockfalls at Dolomieu crater. The implementation of the method involves a sliding time window which allows a straightforward application on continuous seismic signals. The potential of the method to monitor rockfall activity in real-time is emphasized.

Keywords: **rockfalls · rockfall seismic signal · surface waves · seismic wave simulation · spectral elements · site effects · topography · source localization**

Résumé

Les risques d'éboulements doivent être évalués et surveillés afin de prévenir les pertes de vies humaines et dommages aux infrastructures. A cet égard, il est important de créer des catalogues d'événements et de comprendre la dynamique des éboulements. Les ondes sismiques peuvent être utiles à cette fin, car elles transmettent des informations précieuses sur l'événement. Elles sont générées lorsque des éboulements touchent le sol et peuvent être utilisées pour détecter, classer et localiser des événements. Plus encore, on peut déduire des propriétés des éboulements telles que leur volumes et leur comportement dynamique. Cependant, les signaux sismiques hautes fréquences (> 1 Hz) sont mal compris. En effet, ils sont associés à des sources sismiques complexes qui sont réparties dans l'espace et peuvent varier rapidement dans le temps. De plus, les ondes sismiques hautes fréquences sont susceptibles d'être diffusées et diffractées en raison des interactions avec les hétérogénéités du sol ou la topographie de surface.

Cette thèse franchit une étape importante dans la compréhension des signaux sismiques hautes fréquences des éboulements en simulant la propagation des ondes sismiques en utilisant la méthode des éléments spectraux (SEM) avec des profils de vitesse réalistes et des topographies de surface 3D.

L'influence de la topographie sur le champ des ondes sismiques est étudiée. On constate que l'amplification induite par la topographie est sensiblement différente entre les sources situées en profondeurs et celles situées en surface. En effet, les ondes de surface générées par des sources peu profondes sont exposées à une diffusion et à une diffraction constantes lorsqu'elles se déplacent le long de la surface.

La désintégration de l'énergie le long de la surface est étudiée pour différents modèles de vitesse et des équations sont dérivées pour calculer rétroactivement l'énergie sismique totale rayonnée par la source. Ceci est intéressant du fait du lien entre l'énergie sismique et le volume d'éboulement. Afin de tenir compte des effets topographiques, il est proposé un facteur de correction qui peut être introduit dans le calcul de l'énergie.

Les signaux sismiques générés par les éboulements du cratère Dolomieu du Piton de la Fournaise, à La Réunion, sont analysés. Les sismogrammes synthétiques sont utilisés pour identifier et interpréter les signaux observés qui sont générés par des impacts uniques. L'influence de la topographie sur les formes d'onde est démontrée et la sensibilité avec l'emplacement et la direction de la source est évaluée. Les caractéristiques du signal telles que les amplitudes et le contenu fréquentiel sont expliquées sur la base de la théorie du contact de Hertz.

De plus, les rapports spectraux entre stations, calculés à partir des signaux sismiques d'éboulement, sont considérés comme caractéristiques de la position de la source. La comparaison avec les rapports spectraux simulés suggère qu'ils sont dominés par la propagation le long de la topographie plutôt que par le mécanisme de la source. Sur la base de ces résultats, une méthode est proposée pour la localisation des éboulements à l'aide de rapports énergétiques simulés entre stations. La méthode est appliquée pour localiser les éboulements dans le cratère de Dolomieu. La mise en œuvre de la méthode implique une fenêtre temporelle glissante qui permet une application simple sur des signaux sismiques continus. L'accent est mis sur la capacité de la méthode à surveiller l'activité des éboulements en temps réel.

Mots clefs: **éboulements · signaux sismiques · ondes de surface · simulation d'ondes sismiques · éléments spectraux · effets de site · topographie · localisation de source**

Merci!

Pretty exactly 3 years ago I arrived at IPGP on the famous 3rd floor [1] to settle in office 321. While the years passed by, some old faces left, some new faces arrived, and for some faces it is hard to imagine an IPGP without them. Here I want to acknowledge all people that helped me during these 3 years and made this period such a memorable, insightful, rich, and fun experience.

First of all I want to thank **Anne** for giving me the opportunity to carry out this PhD project. From the beginning on I was really excited about the subject and the full range of topics which came with it. Your ambition never seems to fade and you keep pushing forward. Nevertheless you gave me the freedom and time I needed. I also appreciate that you talked to me in French from day one. Thank you for this patience!
Next I want to thank **Yann** who was always there for me. Communication couldn't have been faster if you would have been in the office next door. You became so familiar to me that I am surprised when we meet in person, realizing that we have rarely crossed each other. During one of my two visits in Nantes you taught me a wisdom for life when you left for surfing one afternoon, saying: If I would wait until I have time, I would never go. Thanks for this!
I want to thank **Emmanuel** and **Jean-Pierre** who accompanied me during my whole PhD, being members of my *Comité de suivi de thèse*. Besides helping me in questions on dispersive attenuation and scattering, Emmanuel always made me feel confident in what I was doing and encouraged me to keep on going. Thanks to Jean-Pierre for being Jean-Pierre with whom nothing can not be discussed.
Thanks to Fabian who boosted my understanding on site effects. Jean-Philippe who picked dispersion curves for me. Eleonore for reviewing drafts and for discussions on surface waves and their polarizations. Pascal for his experienced view on any sort of things related to the seismic wave propagation. Jean-Paul for being Jean-Paul (maybe one day we can publish together this article on anisotropy from my MSc thesis). Luis Rivera and Heiner Igel, who both had an open ear and valuable insights (and for coming up with this amazing concept of the Skience school!). Claudio for some detailed discussions, especially in the Fourier domain.
Speaking of Fourier domain, I also remember some discussions with Matthias. Besides all other support, I have to acknowledge him strongly for these amazing 2D colormaps which he made publicly accessible on GitHub (see Chapter 5). Thanks to Gael who helped me compiling SEM codes on Malbec and Ludovic who supported me with PML problems and

1. Yes, at IPGP the floor number is more significant than the study group.

offered me to correct my manuscript. Speaking of Malbec, thanks to Genevieve of course - has there ever been a PhD student in the history of IPGP who never passed by her office at one point? Thanks to Michel for all the amazing technical support and even being available on weekends, and thanks to Sylvie for all the efforts.
Thinking back (faces that have left) thanks to Virginie who introduced me to the world of rockfall seismic signals and videos as well as to El Hadji who supported my first steps in SHALTOP. Florent, providing an excellent kick-off into the PhD-student life as president of the HEKLA. Martha for her good vibes. Gino & Dilruba for being great neighbors in the 20ème. Here also thanks to Christian & Marion as well as to my flatmates Adèle and Carolina who all contributed to this period in Paris.
Thanks to Shipra, my comrade-in-arms regarding SEM and Bollywood dancer and all my fellow 3rd-year students Marina, Julien, Hugo, Mathurin, Miao, Sergey, Dongyang, Thijs, Hanjin... We all went through the same emotional roller coaster during these last months and it was great driving not alone. Plus, I so much enjoyed the *Shut up & write*-Sunday sessions *à la maison*. Thanks to Matthew and Marc, in particular for discussions on the Hertz impact force and SHALTOP. Thanks to my office mates Pauline, Hugo and Tristan (not to forget the faces that have left Agnès and Alessandro), who provided enough occasions for relaxing laugh. Also remembering the Pétanque rivalries with Alister, Hugo and Julien in the *Arènes de Lutèce* - this fight is not over! And to all the other fellow PhD students who I could not list here, please feel addressed!
Finally, thanks to my family. You supported me in every aspect during my whole studies up until the PhD. I know you are always there for me and you even came visit me wherever I am. And to Gabriela, you let me see the world through different eyes.

Contents

List of Figures

List of Tables

Introduction

'Things are getting unstable'

The full title of a newspaper article published last week (October 2, 2019) in *The Guardian* reads: ***'Things are getting unstable': global heating and the rise of rockfalls in Swiss Alps*** (Hruby, 2019). It is not the first time that rising temperatures are linked to increased rockfall activity in high-mountain environments. Retreating glaciers, thawing permafrost and the subsequent infiltration of water into the rock are suspected to destabilize slopes, eventually leading to failure (Huggel et al., 2012; Bader et al., 2017). Yet, not only high-mountain environments are prone to be affected by climate change induced mass wasting processes. For example, global warming related cumulation and intensification of heavy rainfalls is expected to increase landslide hazard and risk (Gariano and Guzzetti, 2016; Handwerger et al., 2019). [2] In this context, it seems more acute than ever to understand slope stability and landslide dynamics in order to mitigate risk for example with the help of early warning systems of structural protections.
Nevertheless, thawing ice and heavy rainfalls are by no means the only causes for mass wasting processes. Earthquakes can trigger numerous landslides of big volumes. Recent examples are the 2018 Hokkaido earthquake which reportedly triggered more than 6,000 landslides and the 2018 Sulawesi earthquake for which the induced landslides caused the most fatalities (Petley, 2019). Furthermore, mass wasting processes frequently occur in volcanic environments. This originates from unconsolidated and thus unstable structures as well as seismic activity linked to eruptions or volcano-tectonic events.
The consequences of landslides can be severe. According to *The International Disaster Database* EM-DAT more than 17,000 fatalities have been reported since the year 2000 related to landslides. An additional number of 400,000 people lost their homes. On top of that, events may impact infrastructure such as buildings, roads, railways, and power lines. Risks can be exacerbated when human activity such as deforestation and mining is poorly regulated.

In order to assess landslide risk, it is critical to create event catalogs and understand the dynamic behavior of landslides. This can be a challenging task regarding the spatial and temporal unpredictability of landslides. Fortunately, vibrations in form of seismic waves are generated through the forces exerted by the landslide on the ground. These seismic waves carry valuable information on the events which we can try to extract from recorded seismograms.

2. *Landslide* is used as an umbrella term for different kinds of gravity driven mass wasting processes such as rockfalls, dry granular flows and wet granular flows. We will go more into detail in Chapter 2.

This way, it has been shown that landslide seismic signals can help to detect, locate and classify events. Furthermore, landslide properties such as their volume were determined and their dynamic flow history could be constrained. In addition, growing networks of seismic stations allow to monitor continuously large areas of interest in real time.

When relating seismic signals to landslide behavior, it is crucial to understand the mechanisms of the seismic source. In other words, the forces generated by the landslide on the ground have to be studied in order to be able to interpret the generated seismic waves. This has been successfully addressed for low frequency seismic sources, meaning sources which vary slowly over long periods of time. Their temporal evolution could be associated to the macroscopic acceleration and deceleration of landslides.
In contrast, high frequency landslide seismic sources are poorly understood. They are related to single particles impacting the ground. In general, this can result in a spatially distributed force field of high temporal variability. Consequently, the recorded seismic signal is a superposition of incoherent seismic waves generated at different positions.
To make things even more complex, high frequency seismic waves are prone to be strongly distorted on their path from the source to the receiver. This originates from interactions with soil heterogeneities and surface topography. As a result, the recorded seismic signal can not directly be related to the seismic source even if the source consists of a simple single impact. Instead, the wave propagation has to be carefully considered before interpretation.

Objectives

The objectives of the present work can be summarized in three bullet points:

- **Enhance understanding of high frequency landslide seismic sources**
  Landslide basal forces are numerically simulated on real topographies using a continuum model in order to evaluate their temporal evolution and their frequency content. Forces generated by single boulder impacts are predicted using Hertz contact theory.
- **Quantify the influence of topography on surface wave propagation**
  The seismic wave propagation is simulated on real topographies using the Spectral Element Method (SEM). The landslide generated seismic waves are modeled by point forces located at the surface. The influence of topography is evaluated based on waveforms, amplitudes and the spectral content of the synthetic seismograms.
- **Analyze rockfall seismic signals recorded at Piton de la Fournaise volcano**
  The high frequency seismic signal (>1 Hz) generated by rockfalls at Dolomieu crater on Piton de la Fournaise volcano (La Réunion) is modeled. Spectral amplitude ratios as well as energy ratios between station pairs are analyzed. Furthermore, the signal characteristics of single boulder impacts are interpreted.

Organization

Chapter 1 introduces the study site, namely Dolomieu crater on Piton de la Fournaise volcano, La Réunion. It presents the geological setting as well as the instrumentation deployed by the *Observatoire Volcanologique du Piton de la Fournaise* (OVPF). Subsequently, the shallow subsurface structure is characterized which is fundamental for the numerical simulations of the seismic wave propagation. More precisely, the seismic velocity-depth profile is determined and spectral site amplification factors are estimated in order to account for lateral soil heterogeneities. The estimated site effects are compared simulations on a model with topography to evaluate the influence of topography. Finally, intrinsic attenuation and scattering of the seismic signals at Dolomieu crater are discussed.
Chapter 2 is all about landslides. The utility of seismology to classify and characterize events is emphasized and previous research related to landslide seismic signals is reviewed. This is followed by a discussion on landslides models. Granular flow on the topography of Dolomieu crater is simulated using a thin-layer model. The simulated basal forces and their spectral content are analyzed. Thereafter, Hertz contact theory is introduced. This is a fundamental theory which describes the contact between two colliding bodies. It will be used later to interpret the seismic signal generated by boulder impacts. Finally, rockfalls at Dolomieu crater are presented and their temporal evolution is analyzed by means of camera images and recorded seismic signals.
Chapter 3 focuses on the propagation of seismic waves. The Spectral Element Method (SEM) is introduced and technical aspects regarding the implementation of topography as well as the velocity model are presented. A convergence test is conducted and the wave propagation is compared between models with different seismic velocity profiles. A second part of the chapter analyzes the seismic energy decay of the seismic waves along the surface as a function of source-receiver offset. Equations are derived for the computation of source generated energy from the seismic recording of a single receiver at the surface of the domain. Assumptions as well as complications for a heterogeneous velocity model are discussed and estimation errors are quantified.
Chapter 4 dives into the seismic wave propagation at Dolomieu crater. The effect of topography is analyzed depending on different velocity models. A synthetic crater model helps to evaluate the respective influence of crater depth and crater curvature. Subsequently, real seismic signals generated by rockfalls at Dolomieu crater are explored. Observations and simulations are compared by means of spectral ratios between station pairs. Thereafter, the signal characteristics of single boulder impacts are analyzed making use of Hertz contact theory. In a second part, the estimation of the source energy is discussed in case of topography. A topography correction factor is proposed and preliminary results are shown.
Chapter 5 makes use of the findings from the previous chapter and proposes a method to localize rockfalls based on energy ratios between stations. Here, the effect of topography is deliberately exploited in order to enhance resolution of the localization. Limitations of the method as well as future developments are discussed.

Chapter 1

Study site: Piton de la Fournaise

Situated in the Indian Ocean, around 700 km east of Madagascar and 175 km southwest of Mauritius, Réunion is - besides Martinique and Guadeloupe - an island of the French overseas territory with active volcano. Piton de la Fournaise is one of the most active volcanoes worldwide. It is monitored by the local *Observatoire Volcanologique du Piton de la Fournaise* (OVPF) which is administrated by the *Institut de Physique du Globe de Paris* (IPGP). The permanent monitoring of volcanic activity in real time with diverse and dense instrumentation offers excellent research conditions.
Volcanic environments are prone to mass wasting processes such as landslides and rockfalls. In the case of Piton de la Fournaise, its caldera collapse in 2007 left 340 m deep Dolomieu crater with highly unstable crater walls. Since then, rockfalls frequently occur inside Dolomieu crater. The high quantity of events within this very confined space provides a perfect opportunity for the study of rockfalls.

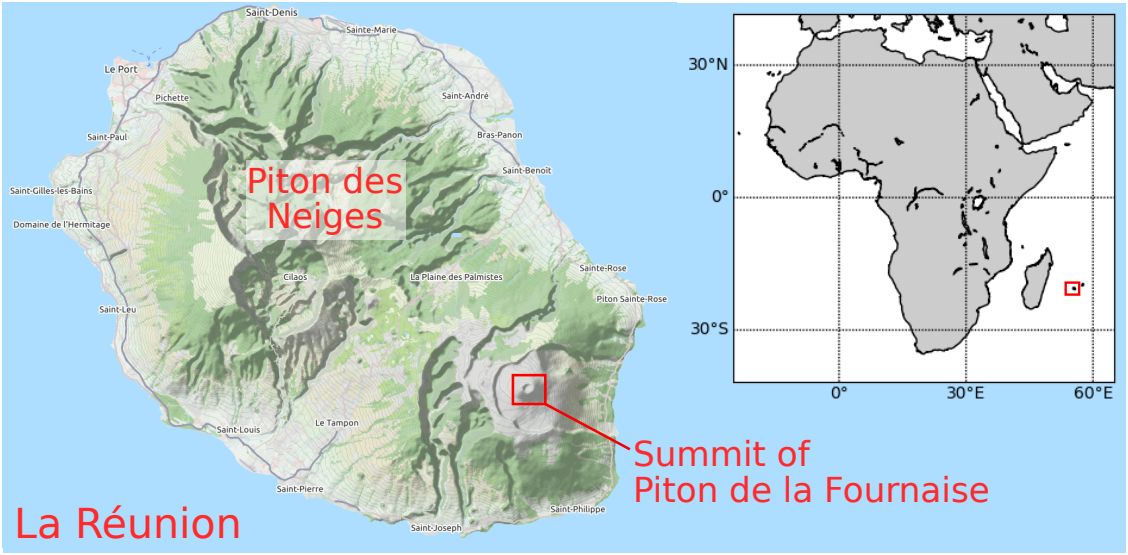

Figure 1.1 – Map of La Réunion. La Réunion is located in the Indian Ocean east of Madagascar (see red rectangle in inset). The present day island is built up by two volcanoes: dormant Piton des Neiges in the northwest and active Piton de la Fournaise in the southeast. The summit of Piton de la Fournaise is characterized by Dolomieu crater as shown in Figure 1.2.

In the following we will summarize the volcanic setting of Piton de la Fournaise and present the available instrumentation which will be used in this study. Thereafter, we will discuss subsurface properties which are significant for seismic wave propagation.

1.1 Volcanic setting

The island of Réunion is characterized by two volcanoes, namely Piton des Neiges in the northeast, dormant since around 12 ka (Deniel et al., 1992), and Piton de la Fournaise in the southeast, active till present day since about 500 ka (Merle et al., 2010). With around one eruption every 10 months, Piton de la Fournaise is one of the most active volcanoes worldwide (Roult et al., 2012). It belongs to the class of basaltic shield volcanoes, which are predominantly formed by occasional effusive eruptions (Peltier et al., 2012). As the lava is rather fluid, it can spread over wide areas which is why shield volcanoes are characterized by gentle side slopes. In contrast, eruptions of stratovolcanoes are mainly of explosive nature and involve faster cooling lava which result in steeper profiles.
Besides lava flows and pyroclastic deposits, which are so-called exogenous processes, volcanoes can grow due to expansion of internal magma chambers, so-called endogenous processes as for example intrusions. In parallel, destructive events such as crater collapses and landslides form the counterpart of growing processes. One of such destructive events occurred on Piton de la Fournaise in April 2007 with its caldera collapse, leaving behind the present day characteristic shape of Dolomieu crater. In the following section we will briefly discuss its formation as well as its structure, which is of importance to understand occurrences of mass wasting processes within the crater.

1.1.1 Dolomieu crater

Present day Dolomieu crater was formed in April 2007 during one of the most intense eruptions of Piton de la Fournaise in recent history (e.g. Staudacher et al., 2009). Its extension originates from a first collapse in 1931, after which it had been progressively filled up with lava (Michon et al., 2013). The 2007 eruption lasted in total around 1 month and just a few days after its beginning, in the night of April 5, the rock column beneath Dolomieu crater collapsed (Michon et al., 2007, 2009; Peltier et al., 2012). Within 24 h, the center of the caldera dropped by more than 300 m. Figure 1.2 illustrates the topographic structure of Dolomieu crater. Michon et al. (2009) identified a cyclic behavior during the collapse, characterized by small-scale deflation and inflation of the summit area accompanied with an increase and decrease of seismicity. They drew parallels to caldera collapses on other basaltic volcanoes and related the cyclic behavior to pressure release caused by drainage of the underlying magma chamber and simultaneous pressure increase caused by the downward movement of the collapsing column.
The caldera collapse plays a defining role for the resulting crater structure which in turn determines regions of instability and hence rockfall occurrences. There are significant structural differences between northern and southern part of Dolomieu crater. While the collapse revealed subvertical scarps along the northern side, terraces at the level of the former crater floor were left on the southern side, which subsided subsequently into the

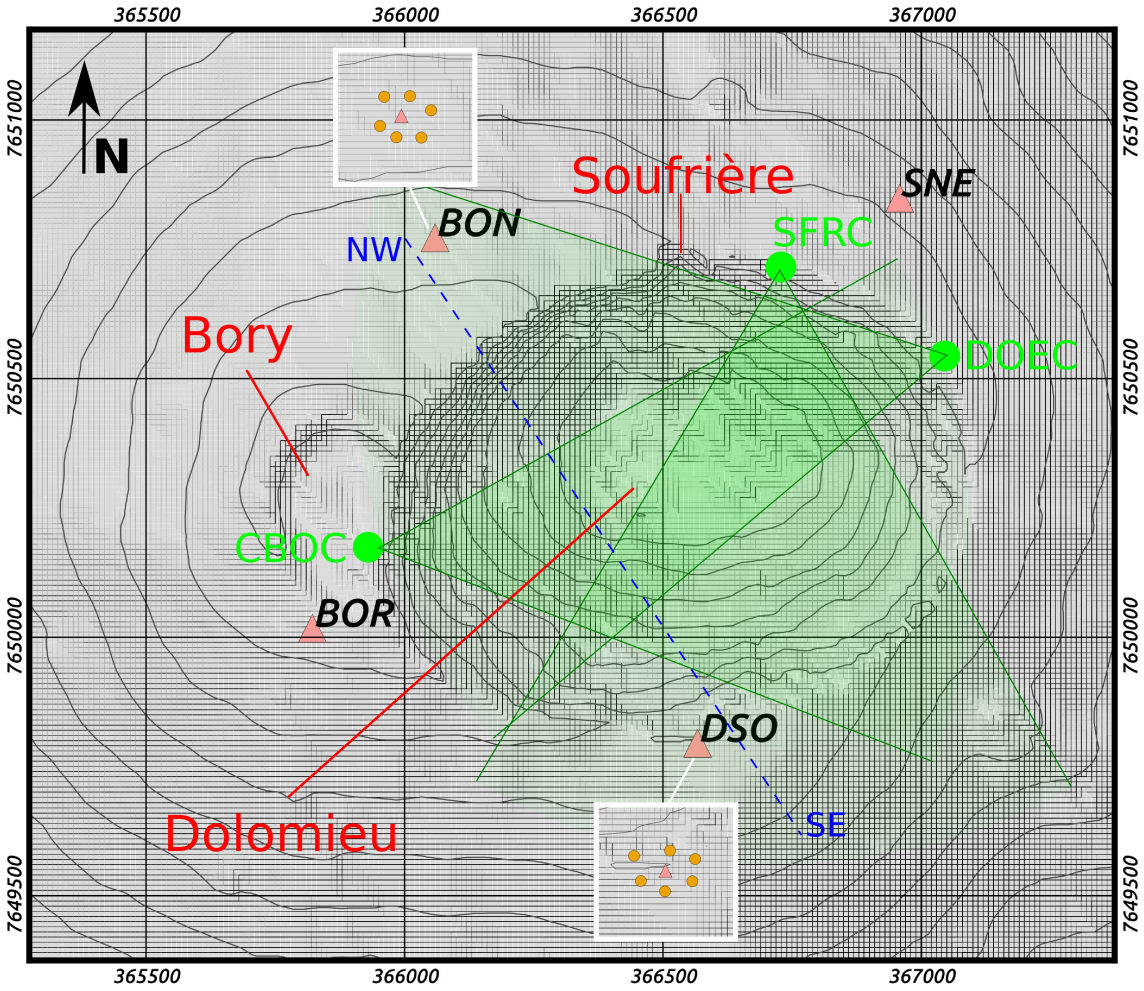

Figure 1.2 – Dolomieu crater and instrumentation. Topographic representation of Piton de la Fournaise summit (see Figure 1.1 for location). The summit is characterized by Dolomieu crater with smaller Bory crater at its east and Soufrière crater at its north. Contour lines show elevation differences of 40 m. Position of seismic stations BON, BOR, DSO and SNE are marked by red triangles. The small insets show antennas of 6 stations (orange dots) around BON and DSO. Positions of cameras CBOC, DOEC and SFRC are marked by green dots. Green cones indicate the camera's range of vision. Blue dashed line corresponds to the structural cross-section shown in Figure 1.3.

newly formed crater (Michon et al., 2009). Derrien et al. (2019) recently published a detailed interpretation on the current crater structure and the involved faulting mechanisms, shown in Figure 1.3. Objective of their investigation was to assess the risk of caldera rim instabilities to prevent accidents for tourists, scientific teams and other visitors. The structural difference between north and south can be seen on the crater cross-section in Figure 1.3. As mentioned before, while the northern crater wall is characterized by a steep scarp with talus from rockfall deposits at its bottom end, the south consists of step-like terraces on which scree is deposited almost up to the crater edge. This has consequences for both the occurrence and type of mass wasting processes which are generally speaking of rockfall type (referred to as *rock topple* by Derrien et al. (2019)) in the north and of dry granular flow type (referred to as *debris avalanche* by Derrien et al. (2019)) in the south (for landslide classification used in the present work see Figure 2.1 in section 2.1). We will review rockfall activity at Dolomieu crater and discuss individual events in section 2.3 of

Chapter 2.

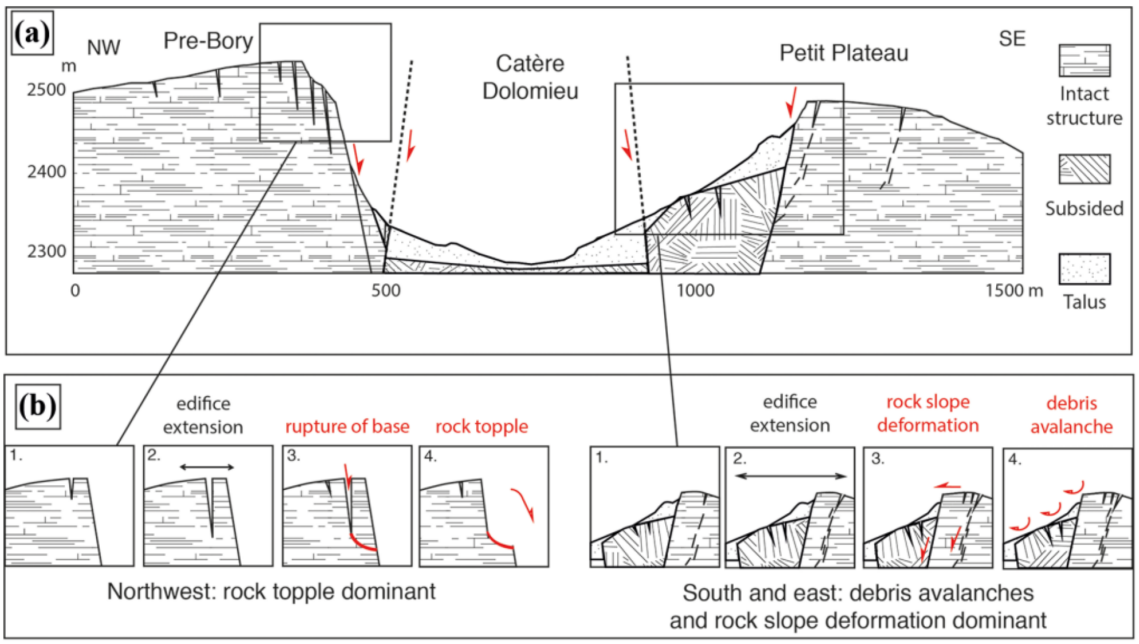

Figure 1.3 – Structural cross-section through Dolomieu crater. (a) NW-SE cross-section showing an interpretation of faults and geological structure of the subsurface. Its location is indicated by the blue dashed line in Figure 1.2. **(b)** Mechanisms of crater wall instabilities in relation with volcano deformation cycles of inflation and deflation. Different mechanism dominate processes on the northern and the southern crater side. Figure extracted from Derrien et al. (2019).

1.2 Instrumentation

Piton de la Fournaise volcano is monitored by the *Observatoire Volcanologique du Piton de la Fournaise* (OVPF). The installed instrumentations can be grouped into 5 networks: cameras, meteorological stations, seismic stations, stations for deformation measurements (including inclinometers, extensometers and GPS stations), and geochemical sensors. The present study uses data from the cameras and from the seismic network, which will be introduced in the following.

1.2.1 Cameras

Three cameras are positioned at the edge of the crater rim, monitoring its inside. Figure 1.2 indicates their location as well as their range of vision. The cameras record continuously 2 frames per second. Based on a semi-automatic detection of rockfall seismic signals, only images within time windows corresponding to events are transferred to the OVPF. Camera snapshot examples during a large rockfall on the northwestern crater wall on October 2, 2016, are illustrated in Figure 1.4.

Figure 1.4 – View from the cameras installed on Dolomieu crater rim. Snapshots from the three cameras on October 2, 2016, at 7:43:43 (UTC) during a large rockfall located at the northwestern crater wall. The rockfall is partly visible on CBOC and fully visible on DOEC. Thanks to the high stand of the sun the crater is almost completely illuminated without major shadow zones. Neither clouds, fog nor rain hinders the view.

1.2.2 Seismic stations

For the present study the four closest seismic stations surrounding Dolomieu crater are used, namely BON, BOR, DSO, and SNE (see Figure 1.2 for location). The response band for BON and SNE is broadband (i.e. corner frequency $\geq 10\,\mathrm{s}$), while BOR and DSO are short-period (i.e. corner frequency $< 10\,\mathrm{s}$). All stations are sampled at 100 Hz and have three components except for DSO, which has only vertical orientation. Table 1.1 summarizes the station attributes together with their coordinates.

Table 1.1 – Coordinates and type of seismic stations. UTM coordinates, elevation above sea level and type of the four seismic stations surrounding Dolomieu crater. Their locations are mapped in Figure 1.2. Note that '1C' and '3C' denote vertical sensors and 3-component sensors, respectively.

	Easting (m)	Northing (m)	Elevation (m)	Orientation, Band
BON	366058.98	7650772.23	2549.0	3C, High Broad Band
BOR	365821.67	7650017.06	2540.0	3C, Extremely Short Period
DSO	366566.99	7649794.54	2517.0	1C, Extremely Short Period
SNE	366958.00	7650848.96	2505.0	3C, High Broad Band

Seismic signals and their spectra recorded at all four stations are shown in Figure 1.5. The signal corresponds to the large rockfall on October 2, 2016, which was already pictured in Figure 1.4 in the previous section. From the spectra we can deduce a main frequency content of the rockfall signal between 2 and 10 Hz. The signal below 1 Hz is contaminated by a high noise level, which originates most probably from the ocean at the nearby coast. This makes it difficult to identify low frequency seismic waves generated by rockfalls of this size (signals generated by mass wasting events of bigger volumes contain significant amplitudes below 1 Hz, see e.g. Zhao et al. (2015)).

In addition to the permanent seismic stations of OVPF, two antennas of 6 stations each were installed in 2014 in the framework of the ERC SLIDEQUAKES project. They are located around station BON and station DSO as can be seen in Figure 1.2. All stations are short-period with 3-components. The recordings correspond from top to bottom to station BON, BOR, DSO, and SNE. They will be used hereafter to deduce a 1D velocity profile.

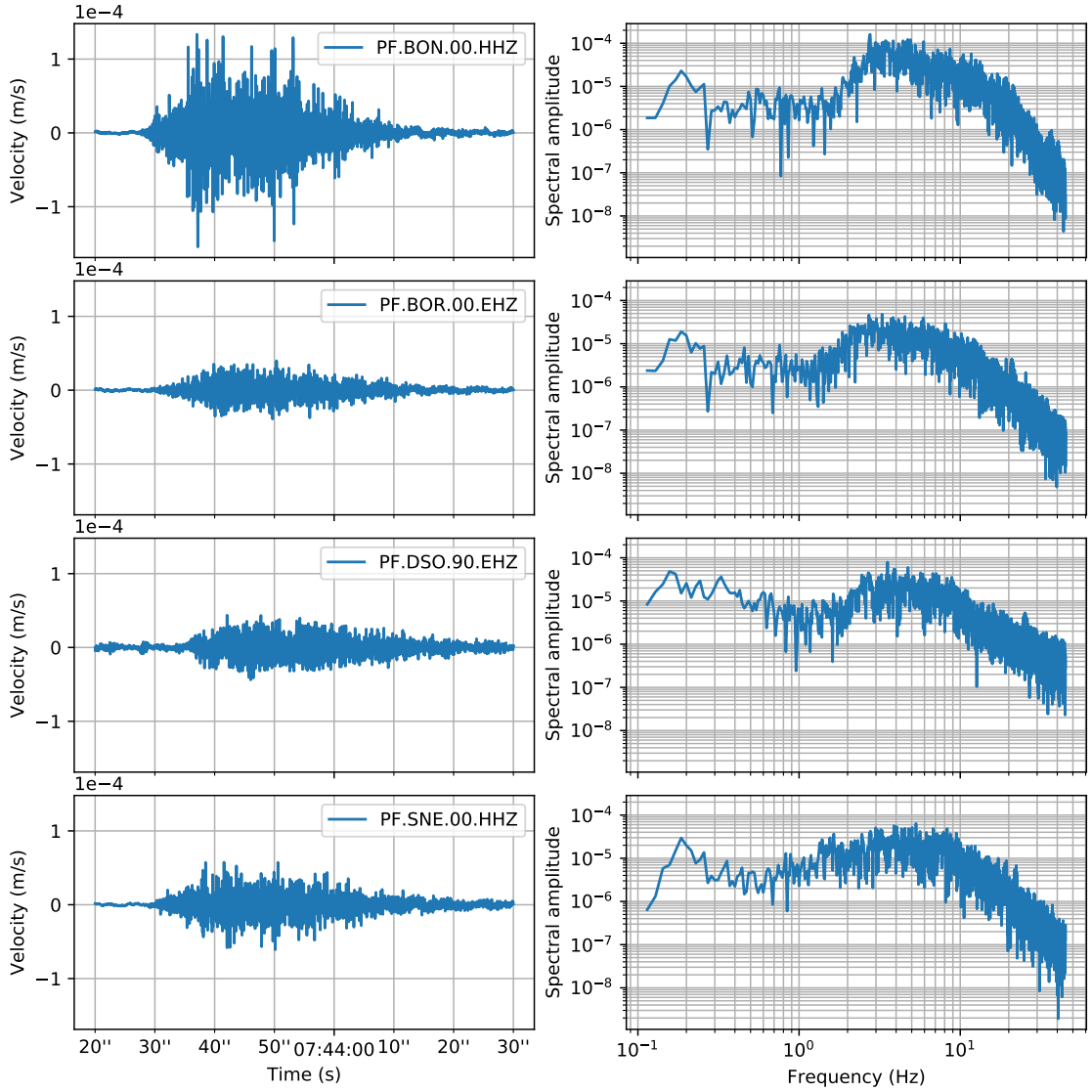

Figure 1.5 – Seismic recordings at the 4 stations surrounding Dolomieu crater. Seismic signals (*left column*) and their spectra (*right column*) corresponding to a rockfall on October 2, 2016 (see Figure 1.2 for location and Fig. 1.4 for visual observation). Main frequency content of the rockfall signal is between 2 and 10 Hz. Noise from ocean-coast interactions are contaminating the signals below 1 Hz.

1.3 Subsurface characterization for seismic wave propagation

The internal structure of volcanoes is essentially dependent on the cycles of growth and destruction. Building history can be inferred by interpretation of subsurface structure. A detailed study of the internal structure and the building history of Piton de la Fournaise was carried out by Peltier et al. (2012) who made use of new outcrops revealed by the 2007 caldera collapse of Piton de la Fournaise.

For the present study on seismic signals from rockfalls at Dolomieu crater, we are interested in the subsurface properties which govern the seismic wave propagation. In the following we will try to find an effective description of the medium which allows us to build models for numerical simulations. This includes a discussion on the seismic velocity model, on site effects due to local geological structures at the seismic stations as well as on properties of

seismic scattering and intrinsic attenuation.

1.3.1 Seismic velocity model

The seismic velocity structure of Piton de la Fournaise has been investigated by several authors (e.g. Nercessian et al., 1996; Brenguier et al., 2007; Prôno et al., 2009). Mordret et al. (2015) invert a high-resolution 3D anisotropic S-wave velocity model after cross-correlating 4 years of seismic noise data from 2009 to 2013. Frequencies up to 2.5 Hz are used in the inversion. Depth and lateral resolutions are limited to 400 m and 2000 m, respectively. The obtained model contains minimum S-wave velocities of around 850 $km.s^{-1}$ at shallow depth (see Figure 1.6 for a distribution of 1D velocity profiles extracted from the model at positions around Dolomieu crater). This is in accordance with studies based on seismic noise recordings from the temporary experiment *VolcArray* in 2014, which involved three seismic arrays installed on the edifice of Piton de la Fournaise (Brenguier et al., 2016). Using a plane wave beamforming method, Brenguier et al. (2016) report surface wave velocities of 1.0 $km.s^{-1}$ and 0.75 $km.s^{-1}$ for frequency bands of 1-3 Hz and 3-6 Hz, respectively. Nakata et al. (2016) find similar values applying a double beamforming technique on the same array data.
However, for the following study on rockfall seismic signals, we need a velocity model which is valid up to 20 Hz. Recently, Lesage et al. (2018) compared shallow velocity structures of 11 different volcanoes. The comparison reveal similar structures in the first 500 m of andesitic and basaltic volcanoes: a strong velocity gradient close to the surface which is progressively decreasing with depth. Given the smooth gradient variation, they suggest an analytic function which can be used as a generic model for the shallow velocity structure on these volcano types:

$$c_i(z) = c_{i0}[(z + a_i)^{\alpha_i} - a_i^{\alpha_i} + 1], \tag{1.1}$$

where c is the wave speed, $i = P, S$ stands for P-wave and S-wave, respectively, and z is the depth below surface. Fitting the observed average velocity curves, they determine the following parameters:

$$\begin{cases} c_{P0} = 540\,\mathrm{m.s^{-1}},\ \alpha_P = 0.315,\ a_P = 10, & \text{for P-wave,} \\ c_{S0} = 320\,\mathrm{m.s^{-1}},\ \alpha_S = 0.300,\ a_S = 15, & \text{for S-wave.} \end{cases} \tag{1.2}$$

The left graph in Figure 1.6 shows the proposed generic P-wave and S-wave velocity variations with depth. They are compared to S-wave velocities in the vicinity of Dolomieu crater from the model of Mordret et al. (2015). A large discrepancy in the first 100 m can be observed which originates from the missing high frequency content above > 2.5 Hz in the model of Mordret et al. (2015). Further below, the Lesage model describes the velocity profiles reasonably well.
In order to validate the velocity model of Lesage et al. (2018) above 2.5 Hz for our study site, we conduct dispersion curve analyses from noise measurements at two circular antennas positioned around station BON and DSO (see Figure 1.2). For the analysis we perform spacial autocorrelation (SPAC, based on Aki, 1957) using the MSPAC (*Modified Spatial Autocorrelation*) toolbox (Köhler et al., 2007; Wathelet et al., 2008) as implemented in the Geopsy software (www.geopsy.org). SPAC is a popular method to obtain velocity profiles

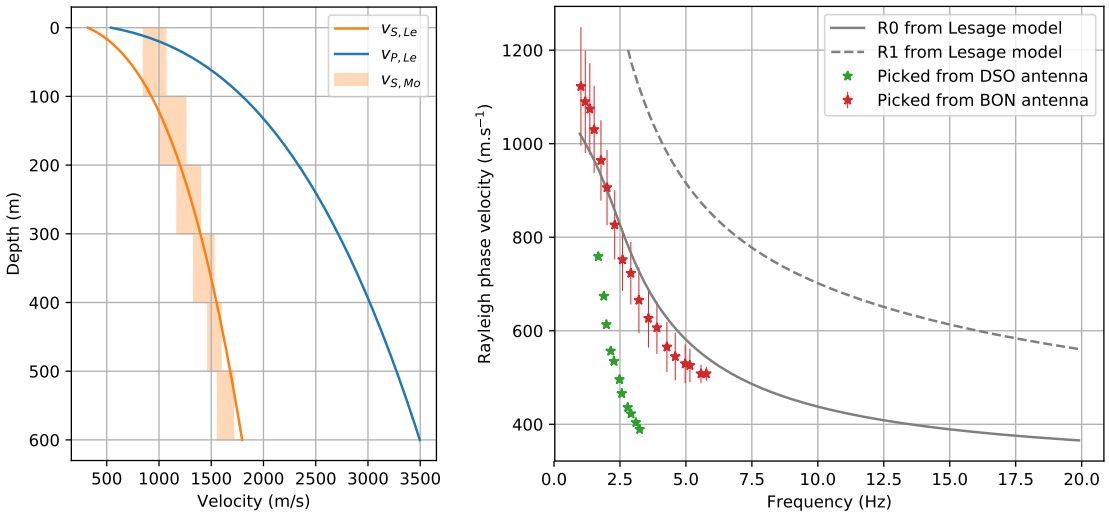

Figure 1.6 – Shallow velocity profile of Piton de la Fournaise. *Left:* Velocity-depths profiles $v_{S,Le}$ and $v_{P,Le}$ from the model proposed by Lesage et al. (2018) for S-wave and P-wave, respectively. The S-wave velocity is compared with values $v_{S,Mo}$ (orange shaded zone) from the model inverted by Mordret et al. (2015). $v_{S,Mo}$ represents a distribution of extracted profiles in the vicinity of Dolomieu crater.*Right:* Theoretical Rayleigh dispersion curves of the model by Lesage et al. (2018) for fundamental mode R0 and first higher mode R1. Picks from the antennas around BON and DSO are marked by red and green stars, respectively. A good agreement is found between the picks from BON and the fundamental mode. Errors on BON values are estimated directly from the uncertainties during the picking process.

on volcanoes (e.g. Ferrazzini et al., 1991; Métaxian et al., 1997; Chouet et al., 1998; Saccorotti et al., 2003; Mora et al., 2006; Perrier et al., 2012).

The picked inversion curves are compared on the right graph in Figure 1.6 with theoretical Rayleigh dispersion curves obtained from the Lesage velocity model. The theoretical dispersion curves were calculated with modal summation using *Computer Programs in Seismology* (Herrmann, 2013). We compare dispersion curves instead of velocity-depth profiles to avoid the predefinition of velocity layers which is necessary to invert the picked velocities.

Measurements from the antenna around BON (red stars in Figure 1.6) shows a good agreement with the fundamental mode Rayleigh dispersion curve and hence confirms the validity of the Lesage model in the frequency range of 1-6 Hz. Unfortunately, no coherent dispersion curves are found above 6 Hz. For higher frequencies, smaller antenna apertures would be needed (smallest stations distance of available antennas is 30 m). Data from DSO antenna did hardly show any coherent dispersion curve patterns. A small window picked around 2.5 Hz shows very low velocities (green stars in Figure 1.6). The lack of consistent dispersion curves might be explained by the proximity of the antenna to the southern crater wall, leading to a scattered wave field. Consequently, we decide to omit the measurements from the DSO antenna for the velocity analysis.

Given the lack of velocity estimations above 6 Hz, we assume that the velocity model of Lesage et al. (2018) is able to describe adequately the shallow velocity structure of Piton de la Fournaise. The fact that the model is based on data from similar volcanoes confirms the validity of the assumption. Comparison of synthetic seismograms with observed seismic signals from rockfall impacts in Chapter 4 will reveal that the Lesage model adequately

reproduces arrival times and complexity of waveforms.
For the simulation of seismic wave propagation on Piton de la Fournaise, we will implement the velocity model of Lesage et al. (2018) so that it follows the topography elevation. In other words, looking at equation 1.1, we impose $z = 0\,\mathrm{m}$ at any position on the surface of the domain. This is reasonable as a main cause for velocity variation is the compaction of material with depth due to the increasing overburden pressure (Lesage et al., 2018). The resulting model is presented in Figure 4.3 on page 95 (Chapter 4).

1.3.2 Geological site effects

Geological structures and soil properties (e.g. soft surface layers) can locally modify seismic amplitudes (e.g. Borcherdt, 1970; Mora et al., 2006; Gélis and Bonilla, 2014; Chávez-García et al., 2018). To evaluate the importance of these effects on the seismic stations surrounding Dolomieu crater, we estimate amplification factors by means of data from volcano-tectonic (VT) events. However, not only local subsurface properties but also variation of the surface topography can modify seismic amplitudes and thus bias the estimation of geological site effects (Davis and West, 1973). As we would like to examine geological site effects isolated from topographic effects, we will subsequently evaluate the potential influence of topography by numerically modeling its response on a domain with Dolomieu crater topography and Lesage velocity profile.

Site effect estimation from volcano-tectonic (VT) events

Local site effects can be identified by stripping off the source signature and propagation path influences from the measured seismic signal. Mathematically, this is easily realized by a deconvolution in time domain or a division in frequency domain. The difficult part is the knowledge on source and path terms. A classical approach is the site-to-reference spectral ratio method (SRM), originally proposed by Borcherdt (1970). Assuming the same seismic source and similar propagation paths, SRM evaluates local site effects relative to a reference station which is supposed to be unaffected by these site effects. In practice however, the concept of an ideal reference site is hard to fulfill, even if the station is installed on bedrock. Estimated site effects can be easily biased if the reference station itself is exposed to site amplification. For this reason, the choice for the station of reference have to be evaluated carefully.
For the present study we want to evaluate geological site effects on the 4 stations surrounding Dolomieu crater, namely BON, BOR, DSO and SNE. The station on the stiffest site (i.e. with the highest seismic velocity) is normally chosen as reference. However, as could be seen in the previous section, we are missing information on local velocity profiles for all stations. As station DSO only contains one component, it is excluded as potential candidate for the reference station. Its proximity to the crater and the impossibility to pick a nice dispersion curve from the surrounding antenna (see previous section) neither advocate for this choice. To investigate the potential of the three remaining stations, we calculate the spectral ratio between horizontal and vertical (H/V) ground motion using noise records. Peaks in this ratio are indicators for site amplification. This is due to the

fact that site amplification is normally characteristic to a certain wavelength. Due to the velocity difference of S- and P-wave, spectral amplification peaks shift accordingly on the corresponding components.
Figure 1.7 shows the calculated H/V ratios using 35 noise records of around 30 s each. Spectral ratios of all recordings combined for each station by calculating their logarithmic mean. In order to avoid spurious fluctuations of the ratios, the smoothing function proposed by Konno and Ohmachi (1998) with bandwidth $b = 40$ is applied on the FFTs. This smoothing method is appropriate as it ensures symmetrical windows of constant width across a logarithmic frequency range.

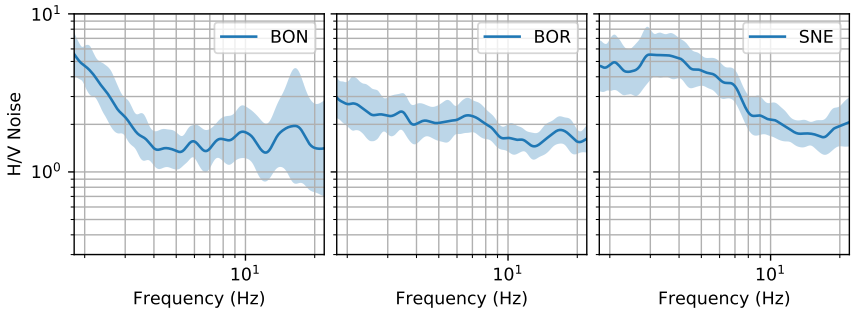

Figure 1.7 – Noise H/V. Spectral ratios calculated from 35 noise recordings of around 30 s each for station BON, BOR and SNE. Blue shaded zone marks the standard deviation from the distribution of ratios.

Analyzing the spectral ratios, station BON shows the lowest values above 4 Hz while having increasing values towards lower frequencies. The spectral ratio of station BOR is generally low, gradually decreasing with increasing frequencies. Station SNE shows the highest values with a minimum at around 15 Hz. From this analysis we conclude that station BON and BOR are least affected by site amplification and hence appropriate reference stations. However, before taking a final decision we will evaluate the recorded spectra of seismic events.
For the estimation of site effects we chose to analyze signals from volcano-tectonic (VT) events. VTs are suitable because sources are centered beneath the crater and the generated seismic waves are less biased by topography than waves traveling along the surface from shallow sources such as rockfalls (in the next section we will assess the influence of topography on the site effect estimation).
VTs are selected from a catalog compiled by Duputel et al. (2019) who use template matching and relocation techniques to detect and locate events on Piton de la Fournaise between June 2014 and July 2018. As station DSO tends to saturate in case of very strong ground motion, medium sized VTs are chosen. Later it is ensured that the considered frequency content has a signal to noise ratio above 3. The final selection contains 36 events which is assumed to be sufficient to ensure a normal distribution. The corresponding source positions are illustrated in Figure 1.8.
The selected VTs are located around 2 km below the crater. At this depth, the inter-station spacing is not negligible. Thus, in order to account for weakening of the signal due to geometrical spreading, the measured amplitudes are corrected by source-receiver distance r. Figure 1.9 shows recorded spectra of three randomly chosen events. Globally it can be observed that station BON and BOR have the smallest amplitudes on all components. This suggests that they are not affected by local site amplification and can be chosen as reference stations.

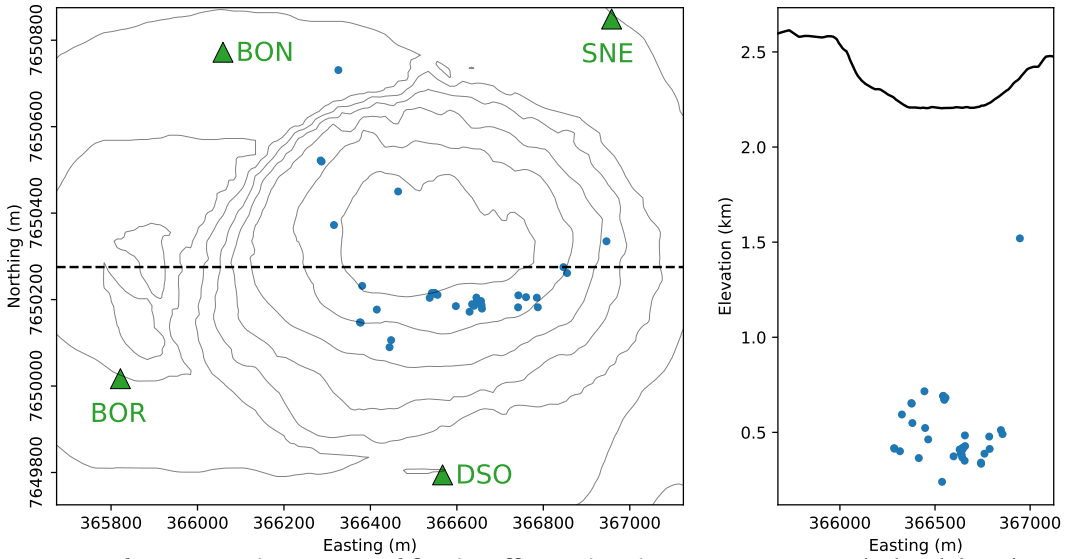

Figure 1.8 – Volcano-tectonic events used for site effect estimation. VT positions marked with bue dots. *Left:* Positions projected on a horizontal plane to show their lateral coordinates. Contour lines denote elevation differences of 40 m. *Right:* Depth of events, projected on a plane with east coordinate. Black line shows cross-sectional profile of Dolomieu crater, corresponding to the dashed line on the left. The aspect ratio is set to respect equal scales.

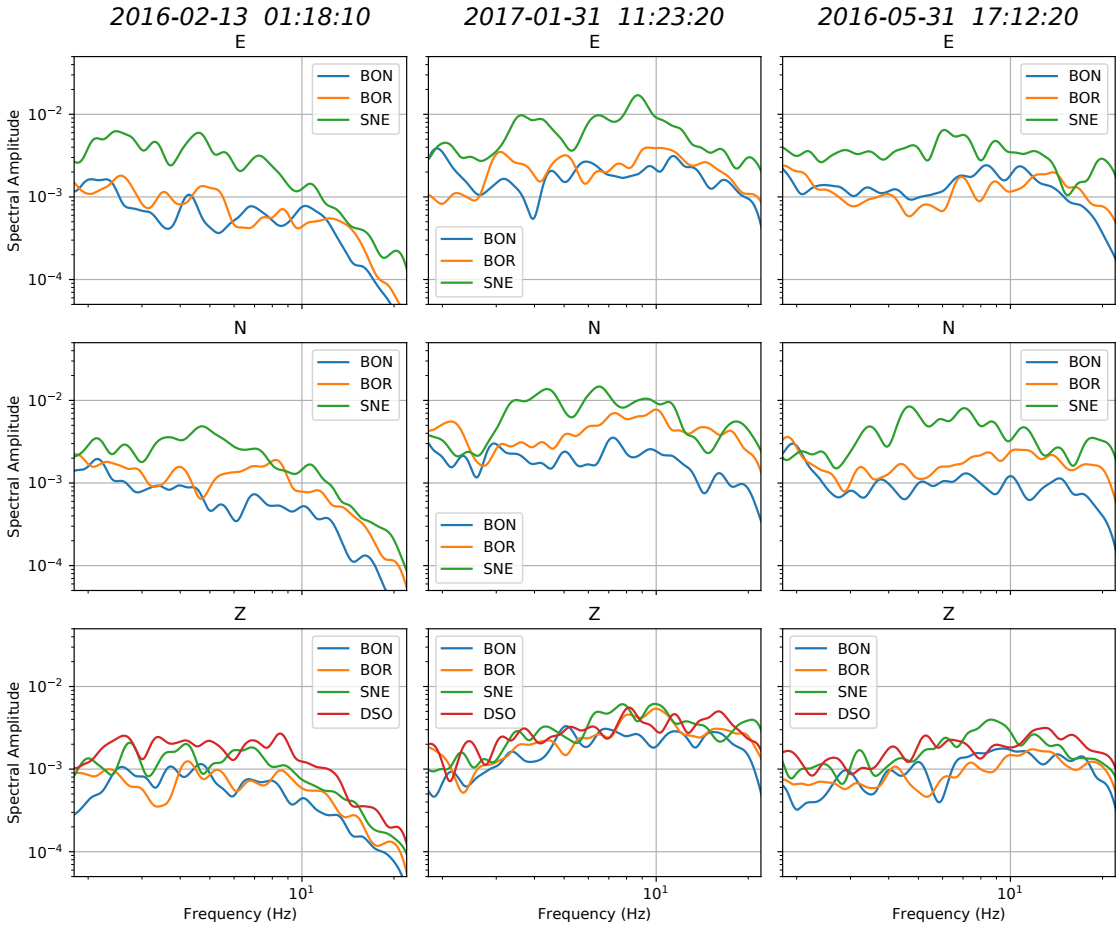

Figure 1.9 – Recorded amplitude spectra from volcano-tectonic (VT) events. Recorded spectra at each station for each component (row-wise) and for three exemplary VTs (column-wise). The shown spectra are corrected for the source-receiver distance calculated from locations shown in Figure 1.8 and smoothed using the Konno-Ohmachi function. Note that DSO has only one component.

We decide to take the mean of the two stations as reference for the site effect estimation. Then, if $\hat{v}_{ijk}(f)$ is the Fourier transform of ground velocity $v_{ijk}(t)$ measured at station i on component j for VT event k, the spectral amplification $A_{ijk}(f)$ is calculated as follows:

$$A_{ijk}(f) = \frac{\hat{v}_{ijk}(f)}{0.5[\hat{v}_{\mathrm{BON}jk}(f) + \hat{v}_{\mathrm{BOR}jk}(f)]}. \tag{1.3}$$

Spectral amplifications of all VT events k are combined for each station by calculating their logarithmic mean. The obtained amplification function at each station is shown in Figure 1.10 for the vertical component and in Figures 1.11 and 1.12 for the horizontal components in north and east direction, respectively. Note that station DSO is single component which is why horizontal site amplification cannot be determined.

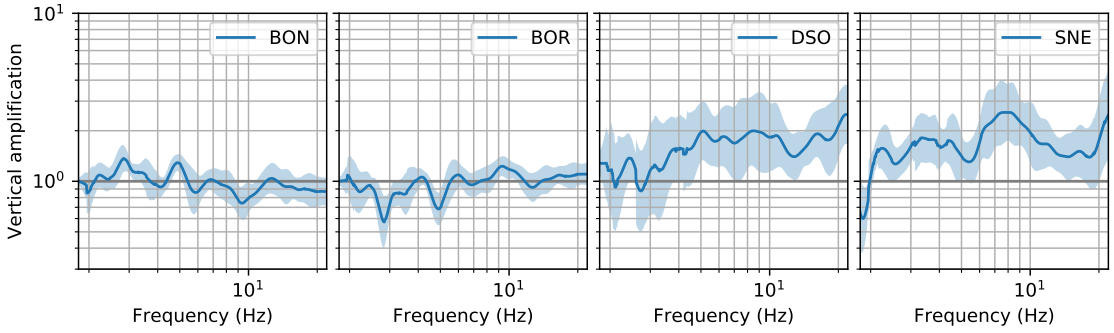

Figure 1.10 – Site effects on vertical component. Vertical amplification factor as a function of frequency for each station. Computed from VT with the mean of BON and BOR as reference. Blue shaded zone denotes estimation error which corresponds to the standard deviation of the amplification distribution of all events.

As expected, station BON and BOR show flat ratios fluctuating around unity. Only for the horizontal component in north direction BOR seems to be amplified relative to BON. We will check hereafter if this could be originating from the nearby topography of Dolomieu crater or smaller Bory crater. Both stations DSO and SNE exhibit moderate amplification on the vertical component of factors in between 2 and 3 (Figure 1.10). A spectral peak is visible at SNE around 8 Hz. On the horizontal components, station SNE is stronger amplified. Amplification reaches factors up to 5 for both north- and east-component (Figure 1.11 and 1.12). Maximum amplification is located at around 4 Hz. It might be related to the peak at around 8 Hz on the verical component, shifting down in frequency due to the lower S-wave velocity if we assume predominantly shear waves on the horizontal components.

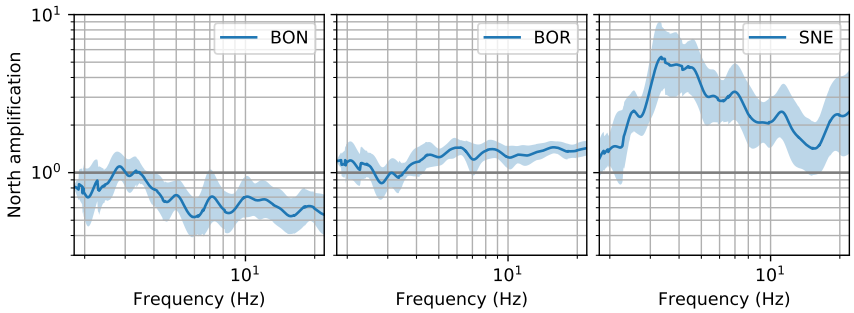

Figure 1.11 – Site effect on horizontal component (north). As in figure 1.10 for frequency variant amplification on north component.

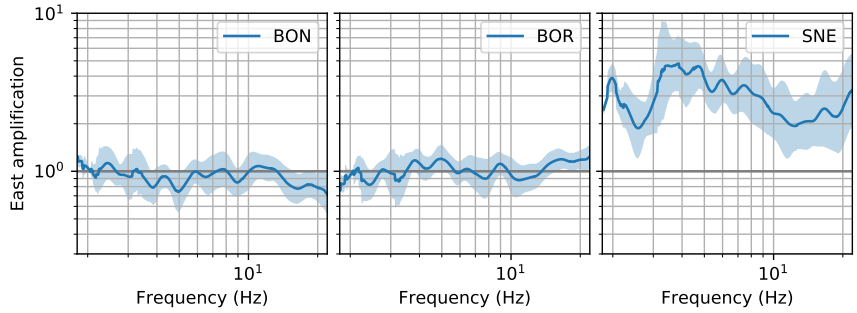

Figure 1.12 – Site effect on horizontal component (east). As in figure 1.10 for frequency variant amplification on east component.

Topographic influence on geological site effect estimation

As mentioned earlier, topography variations can have strong effects on ground motion. In order to verify that the site amplification factors estimated in the previous section are mainly caused by local geological features, we will investigate the possible topographic with the help of numerical simulations. Note that for shallow sources, such as the later studied landslide seismic sources, seismic waves propagate mainly along the surface. Consequently, influence of topography is expected to be essentially different than for deep sources. This will be investigated in detail in Chapter 4.

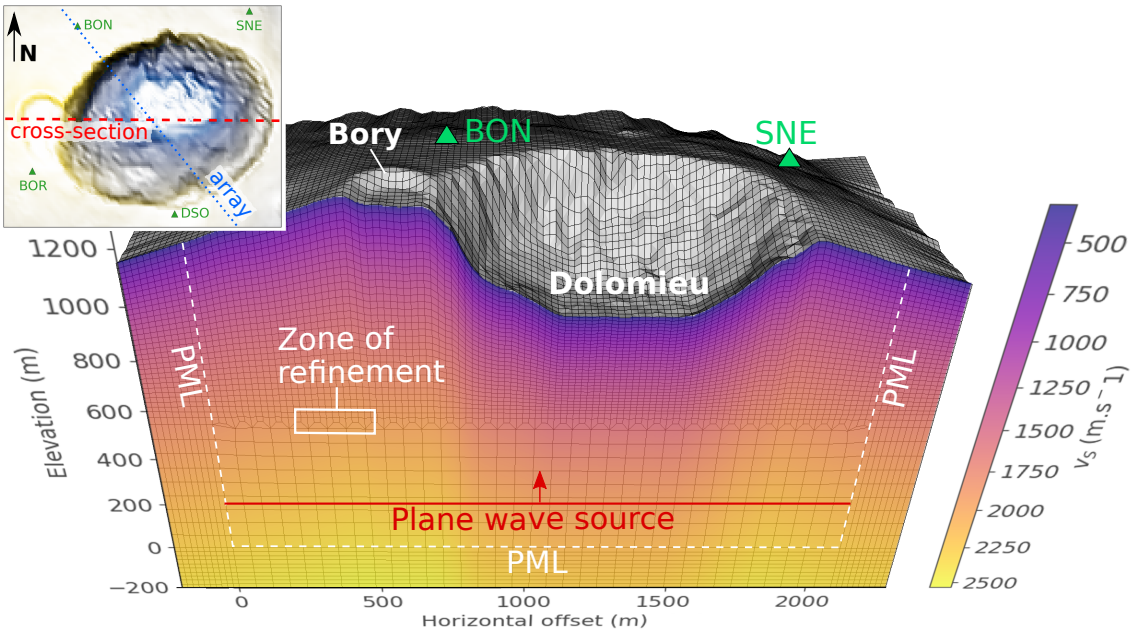

Figure 1.13 – Numerical model with plane wave of vertical incidenc. Cross-section through Dolomieu crater (see inset for orientation). The mesh is built up of elements with side lengths of 60 m (bottom part) and 20 m (top part). A zone of refinement connects the different element sizes. Above, the elements are vertically deformed in order to accommodate the surface topography. The plane wave source is located at 200 m elevation. The color map corresponds to the Lesage velocity model (see section 1.3.1). Absorbing boundaries (PMLs) of 200 m thickness are attached to the sides and the bottom of the domain.

For a quantitative analysis of topographic effects on seismic waves from deep sources, we simulate seismic wave propagation using the Spectral Element Method (SEM). The reader is referred to section 3.2 in Chapter 3 for all details on the method as well as the architecture of the computational domain including the 3D surface topography. The here used domain is based on a cube of dimensions $x = 1800\,\mathrm{m}$, $y = 1800\,\mathrm{m}$ and $z = 1200\,\mathrm{m}$.

Figure 1.13 illustrates the numerical model on which the surface topography of Piton de la Fournaise is imposed.
The simulation is carried out using a 7 Hz Ricker-type plane wave of vertical incidence. A plane wave approach has two benefits. Firstly, we do not have to carry out several simulations in order to average over sources of varying lateral positions (as it is done in the site effect estimation from the observed VTs). Secondly, it can be used as far-field approximation for sources situated at great depth directly underneath the crater which is why we don't have to consider different source-receiver distances for each station. Due to the finite computational domain, plane wave approaches are often used in numerical studies (e.g. for site effect estimations in the 2D simulations of De Martin et al. (2013)).
The plane wave source is implemented by a horizontal grid of point sources with 30 m lateral spacing at around 800 m below surface. Two velocity models are considered. A homogeneous model with $v_S = 1000\,\mathrm{m.s^{-1}}$ and $v_P = 2000\,\mathrm{m.s^{-1}}$ for S-wave and P-wave, respectively, and the velocity model proposed by Lesage et al. (2018). The latter is implemented in a way to follow the elevation of topography. This is visualized in Figure 1.13. Intrinsic attenuation is taken into account with quality factor $Q_S = 50$ and $Q_P = 80$ for S-wave and P-wave, respectively.
Figure 1.14 shows the synthetic seismograms recorded at the surface along an array across Dolomieu crater (see the inset in Figure 1.13 for the location of the array).

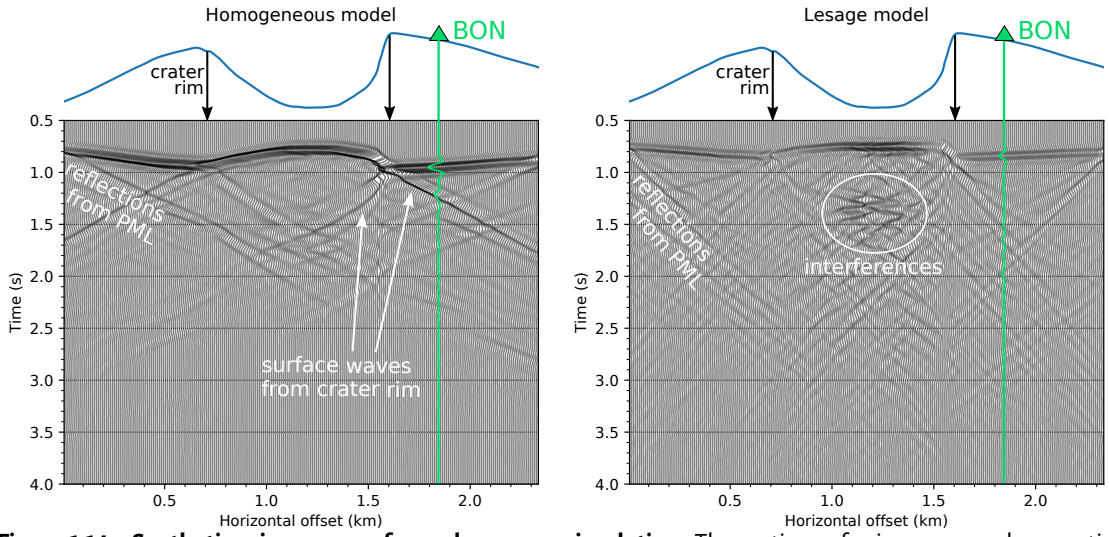

Figure 1.14 – Synthetic seismograms from plane wave simulation. The sections of seismograms show vertical ground velocity from simulations on the homogeneous velocity model *left* and on the Lesage velocity model *right*. Stations are located along the topographic profile indicated by the blue line on top, which corresponds to an array across Dolomieu crater (see Figure 1.13).

The sections of seismograms show how the plane wave is propagating upwards and arrives first at the bottom of the crater and at the deeper flanks on the outside of the domain. Unfortunately, despite experimenting with the properties of the PMLs (*Perfectly Matched Layers*, see section 3.2.1 for more details on these energy absorbing boundaries), we could not avoid reflections from the boundaries when the plane wave is hitting the surface. These reflected waves can be detected in the shown section as they are generated at zero and maximum offset and travel into the center of the domain. A crude way forward to avoid these reflections is to increase the computational domain. However, this is computationally very

expensive. For now, we will interpret the results bearing in mind these reflections. In fact, it is not counterintuitive that also in the real case, for a VT source below the summit of Piton the la Fournaise, waves would arrive from the sides as they are traveling upwards and guided along the surface towards the peak.

Analyzing the synthetic seismograms, the crater rim, which is located at offsets around 0.7 km and 1.5 km, causes the most distinctive wave-field. Subsequent to the arrival of the plane wave at the crater rim, waves are traveling along the surface into opposite directions, i.e. towards the bottom of the crater and away form the crater. In particular in the case of the Lesage model, the waves traveling towards the bottom of the crater are interfering at the center where we can see strong amplitudes (at a time around 1.5 s). Bearing the 3D crater symmetry in mind, the recorded amplitudes can result from waves traveling towards the center from all directions. This effect is not as pronounced for the homogeneous model. This might be caused by the fact that more wave energy is guided along the surface in the case of the Lesage model due to the strong velocity gradient.

In the following we will compute spectral ratios from the synthetic seismograms and compare them to the previously estimated site effects. If the amplification functions show similar features, we can conclude that the these might be caused by the topography as the numerical models do not consider local geological structures.

Site-to-reference spectral ratio

In order to compare observed and synthetic spectral ratios, we apply the same spectral analysis on the simulated seismograms, taking the mean of station BON and BOR as reference. Figure 1.15 compares the vertical spectral amplification functions estimated from VTs (as shown above) with spectral ratios from simulations on the homogeneous velocity model and on the Lesage velocity model. In general, we cannot identify correlations between observations and simulations. The only accordance observable is a peak at around 8 Hz at station SNE which is reproduced on the Lesage model. However, the synthetic spectral ratio at station SNE is strongly fluctuating which make final conclusions difficult. These strong fluctuations might be related to the reflections from the PML as stations SNE is located closer to the domain boundary than the other stations.

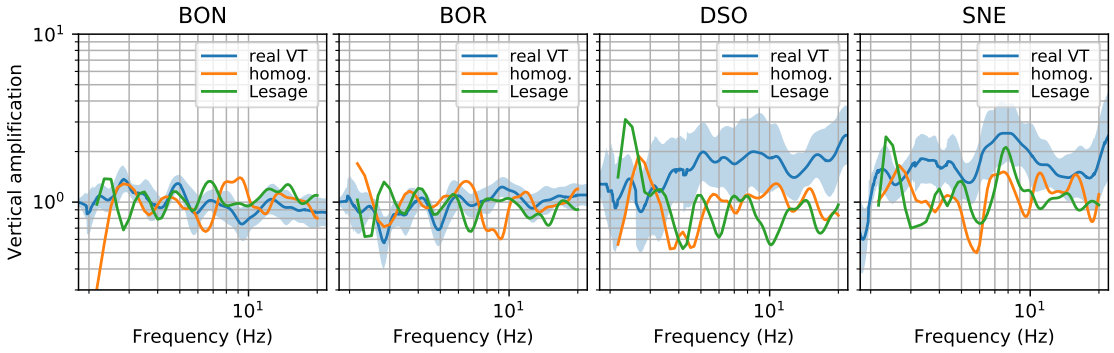

Figure 1.15 – Simulated topographic effect and observed site effects on vertical component. Vertical amplification factor as a function of frequency for each station computed from observed VT events (*real VT*, same as in Figure 1.10), and from simulations of a vertically polarized plane wave on the homogeneous velocity model (*homog.*) and on the Lesage velocity model (*Lesage*).

The observed amplification factors on the horizontal components are compared with simulations on the Lesage model. Figures 1.16 and 1.17 shows the spectral ratios for north- and east-competent, respectively. As for the vertical component, no correlation can be

observed. Again, stronger value fluctuations are present at station SNE which might be related to the proximity to the domain boundary.

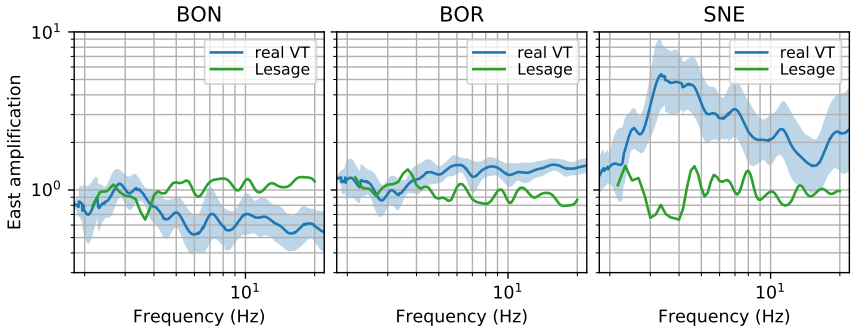

Figure 1.16 – Site effect on horizontal component (north). As in figure 1.15 for frequency variant amplification on north component.

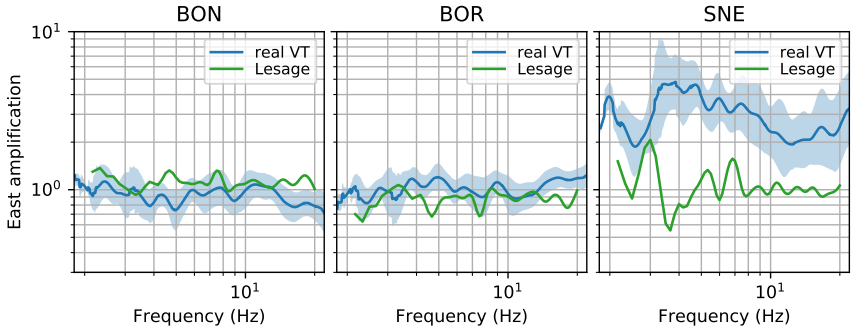

Figure 1.17 – Site effect on horizontal component (east). As in figure 1.15 for frequency variant amplification on east component.

As no clear correlation are identified between simulated and observed spectral ratios, we assume that influences from topography on the estimated geological site effects can be neglected in the frequency band of interest. Considering that the crater dimensions are much bigger than the seismic wavelengths, this result might have been expected. More concretely, the diameter of the crater measures around 1000 m (see profile in Figure 1.14) while seismic wavelengths range between 25 m and 250 m for the shown frequency band from 2 Hz to 20 Hz (assuming an effective S-wave speed of around 500 $\mathrm{m.s^{-1}}$ close to the surface, see Figure 1.13). This means that the orders differ by a factor of 10. Nonetheless, the synthetic seismograms shown in Figure 1.14 demonstrate that the wave field is influenced by the crater topography. In particular, surface waves are generated and guided along the topography. This can cause interferences as observed in the center of the crater. The spatial distribution of topographic amplification from a deep source is further investigated in appendix 1.4.1. Similar amplification maps will be studied in Chapter 4 for sources located at the surface in the context of rockfall generated wave fields. We will see, that amplification patterns caused by surface sources differ substantially from amplification patterns caused by deep sources. This is because topography influences surface waves on their whole trajectory. For this reason, the influence of topography on surface waves has to be considered as a propagation effect rather than a local site effect at the station.

1.3.3 Intrinsic attenuation

The amplitudes of seismic waves are attenuated with traveled distance due to processes referred to as internal friction. These attenuating medium properties can be characterized by so-called quality factors Q_P and Q_S for P-wave and S-wave, respectively. The higher

the quality factor of a medium, the less attenuated are seismic waves. The theoretical formulation of intrinsic attenuation will be introduced in chapter 3.
In order to describe the medium of Piton de la Fournaise we define $Q_P = 80$ and $Q_S = 50$. These values correspond to estimates from former studies at Piton de la Fournaise (Battaglia and Aki, 2003; Hibert et al., 2011) and are close to values used for similar volcanoes (e.g. De Gori et al., 2005; O'Brien and Bean, 2009).

1.3.4 Scattering

Heterogeneities in the subsurface cause scattering of the wave field. Scattering can lead to prolonged ground motion, recorded as the so-called coda after a seismic event. The duration of coda-waves can well exceed the duration of the source mechanism. For the present study we are interested if scattering plays a major role in the observed rockfall seismic signals. In the following we evaluate the scattering potential of the medium at Piton de la Fournaise using a test on energy equipartition. It has been shown that stabilization of the time varying ratio between vertical and horizontal (V/H) kinetic energy indicates a multiple scattering regime (Margerin et al., 2009; Souriau et al., 2011).
We apply the test on seismic signals of a VT as well as a rockfall event. In detail, after preprocessing the seismic signals they are filtered in a frequency band of interest. The squared ground velocities are subsequently smoothed with a sliding window of length l_0. Finally, ratio V/H is calculated as $(v_z^2)^{0.5}/(v_x^2 + v_y^2)^{0.5}$. Figure 1.18 shows filtered and smoothed squared ground velocities together with the corresponding V/H ratios at stations BON, BOR and SNE for two different events.

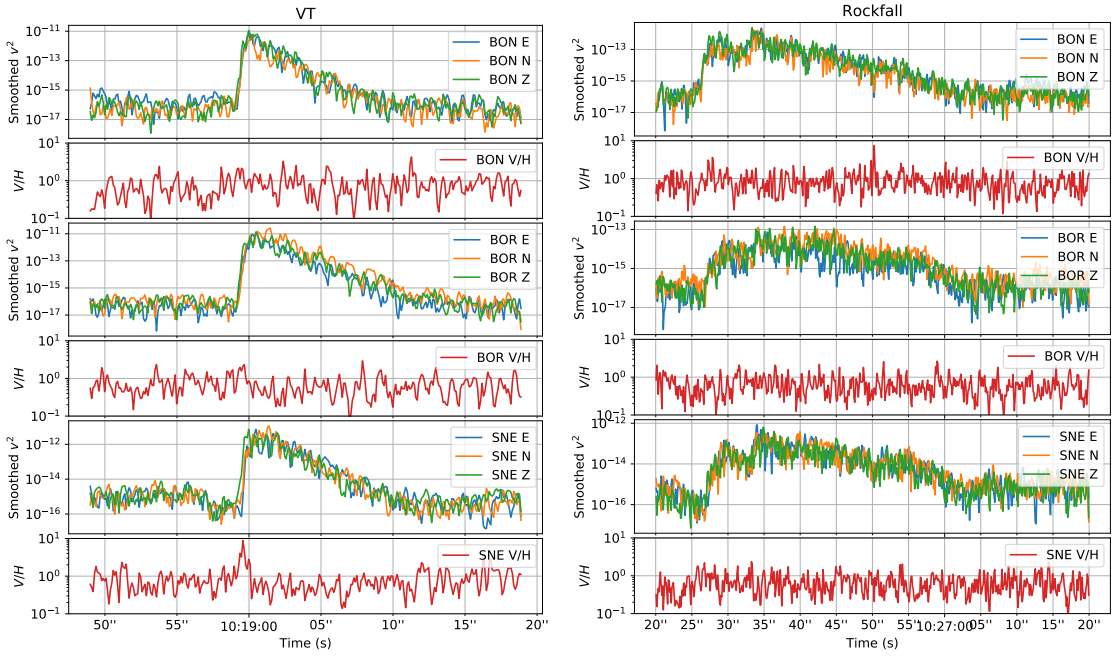

Figure 1.18 – Evaluation of scattering from energy equipartition. Test on energy equipartition for a VT event on January 31, 2017 (*left*) and a rockfall event on January 22, 2017 (*right*). For each station, squared ground velocities filtered between 12.5 Hz and 17.5 Hz and smoothed with a sliding window of length $l_0 = 0.1$ are shown for each component. The corresponding V/H ratio is plotted below.

No stabilization for the V/H ratios is observed. The test was carried out with the same

result in different frequency bands and using different sliding window lengths. This means either that heterogeneities in the ground do not cause significant scattering or that if the coda exists, it is below the noise level and not measurable. Note that energy equipartition is not observed for the the seismic noise due to the continuous activity of noise sources.
From the above analysis it is impossible to issue a clear statement on the scattering regime. However, we will see in Chapter 2 that the duration of the recorded rockfall seismic signals is dominated by the propagation phase of the events. This indicates that scattering is indeed negligible.

1.4 Appendices

1.4.1 Spatial distribution of topographic amplification for wave fields of vertical incidence

In order to assess the spatial variability of topographic amplification, simulations on a model with topography are related to a flat reference model regarding the total kinetic energy. Subsequently we will compare the amplification maps to the curvature of the topography. The frequency scaled curvature (FSC) was proposed by Maufroy et al. (2015) to be a proxy for topographic amplification.

Energy amplification maps

To calculate maps of topographic amplification calculate the energy ratio between simulations from a model with topography and a flat reference model. For this, the ground velocity is recorded on a grid of stations on the whole domain surface. Then, the squared ground velocities of all three components are summed and integrated over the whole duration of seismic motion. This value is used as a measure for seismic energy. Subsequently, the energy ratio $E_{\text{topo}}/E_{\text{flat}}$ between model with topography and flat reference model is calculated at each grid point in order to obtain a map of amplification.
The energy ratio is shown for the homogeneous model and the Lesage model in Figure 1.19 in case of a plane wave with vertical polarization. The ratios are computed from the unfiltered synthetic seismograms. With the Ricker source of 7 Hz dominant frequency, the amplification patterns hence correspond to wavelengths of around 70 m (assuming an effective S-wave speed of around 500 m.s^{-1} close to the surface, see Figure 1.13).

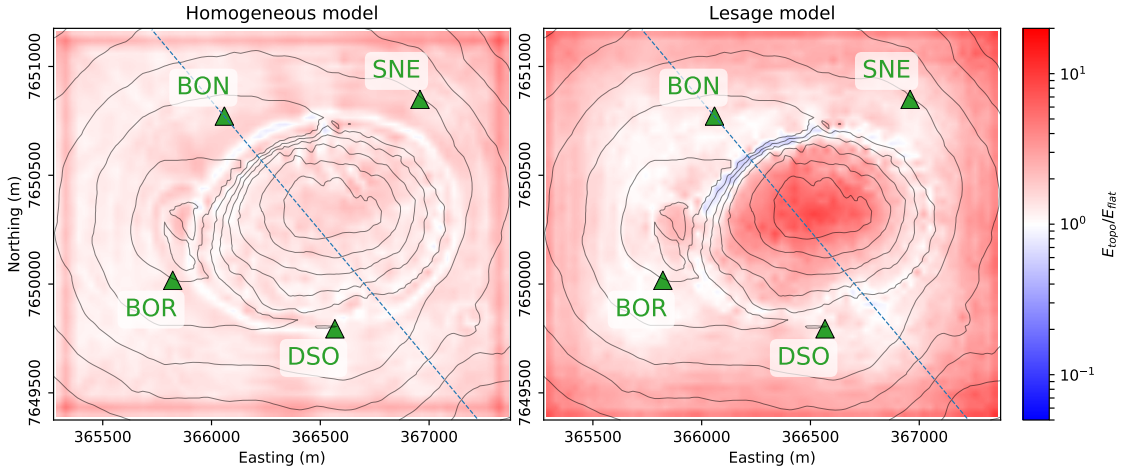

Figure 1.19 – Topographic amplification for a vertically polarized plane wave of vertical incidence. Energy ratio $E_{\text{topo}}/E_{\text{flat}}$ between model with topography and flat reference model for homogeneous velocity (*left*) and Lesage velocity profile (*right*). Blue dashed line marks location of cross-section shown in Figure 1.14 and contour lines count for 60 m elevation difference.

We remark a general amplification due to topography which increases close to the borders of the domain. This general amplification can be attributed to the artifact reflections from the PMLs (see Figure 1.14; note that these reflections are not present in the flat case). However, as discussed in section 1.3.2, waves might also arrive from the sides in the real

case as they are traveling upwards and guided along the surface towards the peak. Simulations on a significantly bigger domain could help to evaluate this hypothesis.
Ignoring the general amplification, the amplification map of the homogeneous model (left hand side of Figure 1.19) does not show any prominent features except for a circle of less amplification (of white color) around the crater rim. This feature is possibly caused by destructive interference of reflected plane wave and rim-generated surface wave. In contrast, the Lesage model shows amplification at the center of the crater. This results from the previously discussed waves reflected at the crater rim and traveling towards the bottom of the crater (see Figure 1.14). Apart from that, the only remarkable feature on the Lesage model is a deamplified zone at the steep northwestern crater wall. This means that less energy is present at this steep slope in comparison to the flat surface.
Figure 1.20 shows amplification patterns on the model Lesage model from horizontally polarized plane wave in east-direction (*left*) and in north-direction (*right*).

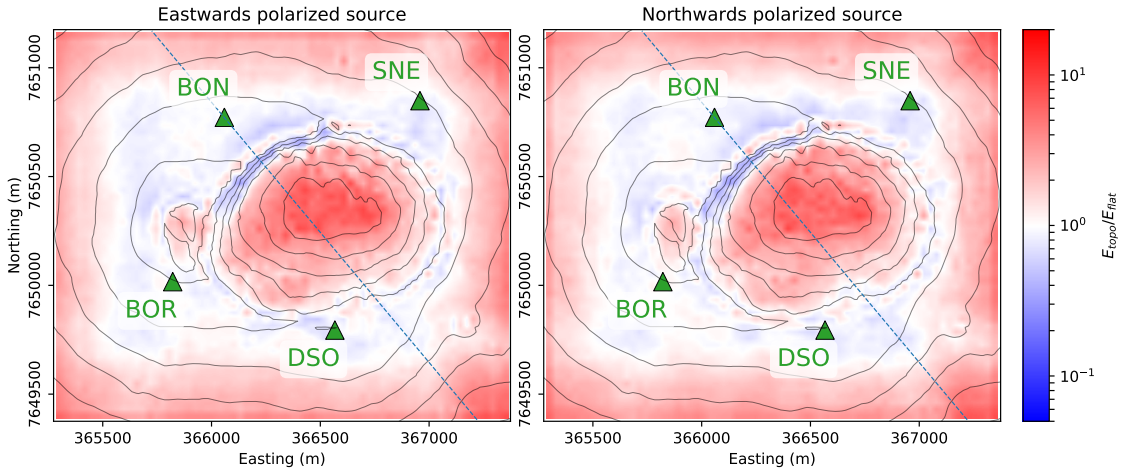

Figure 1.20 – Topographic amplification for a horizontally polarized plane waves of vertical incidence. Energy ratio $E_{\text{topo}}/E_{\text{flat}}$ on the Lesage model for plane wave horizontally polarized in east direction (*left*) and in north direction (*right*). Blue dashed line marks location of cross-section shown in Figure 1.14 and contour lines count for 60 m elevation difference.

Again we can observe a general amplification which increases towards the boundaries possibly due to the reflections from the PMML. Besides that, strong amplification is present at the crater center, similar to the vertically polarized source. The same explanation of reflected seismic waves traveling towards the crater bottom holds as previously. Besides a tendency for deamplification at the crater walls we can remark slight amplification directly at the crater rim. The mechanism which explains this phenomenon is that energy from waves traveling upwards end up being trapped at the crater rim.

Frequency scaled curvature

The concept of frequency scaled curvature (FSC) was proposed by Maufroy et al. (2015) as a proxy for topographic amplification. By comparison with ground motions from 200 3D earthquake simulations, they found correlation between topographic amplification and topography curvature smoothed over a characteristic length equal to half the wavelength of the amplified S-wave. Accordingly, convex shapes such as the top of hills and ridges are

linked to seismic amplification, whereas concave shapes such as valleys are deamplified. This confirms many observations regarding earthquake ground shaking which have been reported in a multitude of research articles (e.g. Davis and West, 1973; Hartzell et al., 1994; Hough et al., 2010). Note that this amplification is related to topography and does not consider amplification due to the subsurface structure as for example the often observed amplification in valleys due to basin fillings. For calculating a FSC map, the topography curvature, which is the second spatial derivative of the elevation, is smoothed by performing a double convolution with a $n \times n$ unit matrix. The characteristic length of the smoothing matrix is defined as $L_S = 2n\Delta x$, where Δx is the space increment of the DEM.
In order to compare the FSC maps to the simulated amplification maps above, comparable wavelengths have to be chosen. The simulation were carried out with a dominant frequency of 7 Hz, leading to a dominant wavelength of around 70 m (assuming an effective S-wave speed of around 500 m.s^{-1} close to the surface, see Figure 1.13). According to Maufroy et al. (2015), correlations of topographic amplification are found between curvature smoothed over smoothing lengths of double the wavelength. For this reason we define the smoothing length $L_s = 140$ m. For comparison, a smoothing length of $L_s = 80$ m is applied, corresponding to a wavelength of 40 m or a frequency of 12.5 Hz. The resulting FSC maps of Dolomieu crater are shown in Figure 1.21.

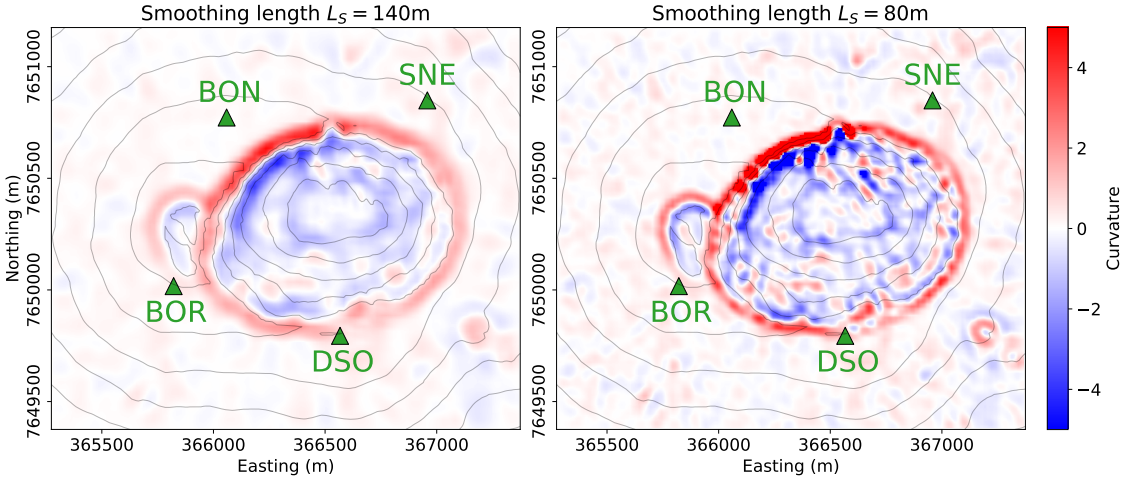

Figure 1.21 – Frequency scaled curvature (FSC) of Dolomieu crater. FSC calculated using different smoothing lengths: $L_s = 140$ m on the left and $L_s = 70$ m on the right. According to Maufroy et al. (2015), this is a proxy for amplified wavelengths of 70 m and 40 m, respectively. Amplification is expected for convex curvature (positive values), whereas concave curvatures (negative values) results in deamplification of the seismic signal.

Immediately observable is the strong positive curvature (red colored) of the crater rim which persists for both smoothing lengths. According to Maufroy et al. (2015), amplification is expected at these positions due to the convex curvature of the topography. In contrast, the concave shape of the crater inside results in deamplification (blue colored). Going from long smoothing length (low frequency) to short smoothing length (high frequency), the FSC map becomes more scattered due to small-scale variations of the topography. High frequency seismic waves (corresponding to around 12.5 Hz) are expected to interact with these small-scale variations. Regarding the seismic stations, no amplification is expected as they are positioned on comparably flat topographic relief. Only station DSO is located very close to the crater rim and thus might be affected by amplification. Again

we point out that these amplification patterns hold for the wave field of deep sources. Surface waves generated by shallow sources can experience a substantially different topographic amplification as will be shown in Chapter 4.
Comparing with simulated amplification patterns above, we can find similar amplification patterns at the sides of the crater. This is true in particular for a horizontally polarized source (see Figure 1.20), for which the crater walls are deamplified whereas amplification exists directly at the top of the crater rim. However, the amplification at the crater rim persists only partly and is not as wide as the red ring shown by the FSC maps. Furthermore, the FSC maps do not predict at all the strong amplification observed in the center of the crater, which is caused by the interferences observed in Figure 1.14. In order to be able to compare amplification patterns for different wavelengths, the simulated amplification patterns have to be calculated from band-filtered synthetic seismograms. This was omitted for the here presented simulations from deep sources but will be done in Chapter 4 for the analysis of amplification patterns from surface sources.

Chapter 2

Landslides and generated seismic waves

Landslides are gravitational mass wasting processes which represent a major natural hazard on society and play an important role in erosion processes, predominantly occurring in mountainous, volcanic and coastal environment. In order to mitigate risk, it is critical to understand and predict the behavior of landslides. Yet, the term landslide itself is not constrained on a single physical process. In the words of Jones (1992):

> *It is essential to recognise at the outset that the term landslide is the most over-used and loosely defined term employed in slope studies. It is merely a convenient short-hand or umbrella term employed to cover a very wide range of gravity-dominated processes that transport relatively dry earth materials ... downslope to lower ground, with displacement achieved by one or more of three main mechanisms: falling, flowing ... and sliding ... .*

For this reason, many approaches exist in order to classify and describe landslide processes. One recently developed possibility is to use recorded signals of landslide generated seismic waves. Growing networks of continuously measuring seismic stations enable high detection rates and monitoring of instable sites.
However, we have to be aware of the two-fold nature of the problem: the landslide propagation and the seismic wave propagation. These two physical processes are interconnected by the landslide seismic source, which is constituted by the landslide basal forces. The study of landslide seismic sources can be approached from two sides: in a forwards manner, by modeling landslide dynamics or in a backwards manner, by analyzing and inverting landslide seismic signals. Ultimately, these two approaches are combined. As we will see in the following, this has been successfully carried out in a low frequency approximation, modeling the seismic signal from a modeled landslide seismic source.
In this chapter, we will first focus on the landslide seismic signal, revealing its utility for both classification and determination of landslide properties and dynamics. Thereafter, we will cover the modeling of landslide basal forces, presenting different numerical models as well as Hertz contact theory which describes the stress-strain relationship between two colliding bodies. Finally, rockfall activity at Dolomieu crater is reviewed and example events are analyzed by correlating camera images and recorded seismic signals.

2.1 From seismic signal to landslide source

Seismology has been proven to be of high utility to study and monitor physical processes at the Earth's surface such as storms (e.g. Ebeling and Stein, 2011), rivers(e.g. Gimbert et al., 2014), glaciers (e.g. Tsai et al., 2008; Podolskiy and Walter, 2016; Sergeant et al., 2016), snow avalanches (e.g. Suriñach et al., 2005), and landslides (e.g. Hibert et al., 2011; Allstadt, 2013; Bottelin et al., 2014). These studies are commonly referred to as environmental seismology (Larose et al., 2015).
In the present work we are interested in landslide related seismic signals. In the following we review how these signals can be used to classify events. Thereafter we will go more into detail on the link between physical landslide processes and the seismic signal in the low frequency and high frequency regime. Finally we will discuss how laboratory experiments of granular flows and grain impacts are used to better understand landslide radiated seismic waves.

2.1.1 Landslide seismic source classification

Landslides classification is often based on the initiating rupture process, the type of movement, the displacement speed, the involved type of material, the water content, or the volume. An extensive review on landslide classification was compiled by Hungr et al. (2001). Here we focus on landslide classification in relation with generated seismic waves. This is a powerful tool as it directly relates the seismic signal with physical processes.
Leprettre et al. (1998) showed, for the case of snow avalanches, that events can be detected and classified by extracting characteristic features from the associated seismic signal. The same approach has been applied to landslides (e.g. Dammeier et al., 2011; Hibert et al., 2014b; Manconi et al., 2016; Maggi et al., 2017; Provost et al., 2017; Hibert et al., 2017c). Based on this principle, Provost et al. (2018) recently proposed a typology of landslide seismic sources based on common features in the recorded signals. They considered landslide seismic sources as illustrated in Figure 2.1.
Analyzing signal features such as duration, number of peaks and frequency content, they define three main classes of landslide events: *slopequakes*, *rockfalls*, and *granular flows*.

- *Slopequakes* comprise all seismic signals produced by subsurface processes such as fracturing, shearing or fluid migration (see Fig. 2.1 (d)-(g)). They can be identified by relatively short signal durations ($< 10\,\mathrm{s}$). We will not go into further detail as slopequakes are not in the scope of the present work.
- *Rockfalls* refer to seismic signals generated by the downward movement of single blocks, impacting the ground after free fall or during processes such as bouncing and rolling (see Fig. 2.1 (c)). Depending on the detachment phase, they are often referred to as rock topples (Varnes, 1978). Rockfall seismic signals are characterized by well separated peaks which correspond to successive impacts. Their duration ranges from 5 s up to tens of seconds, depending on the trajectory and the cliff height. Frequency content can be very high ($> 100\,\mathrm{Hz}$) while most energy is measured between 20 and

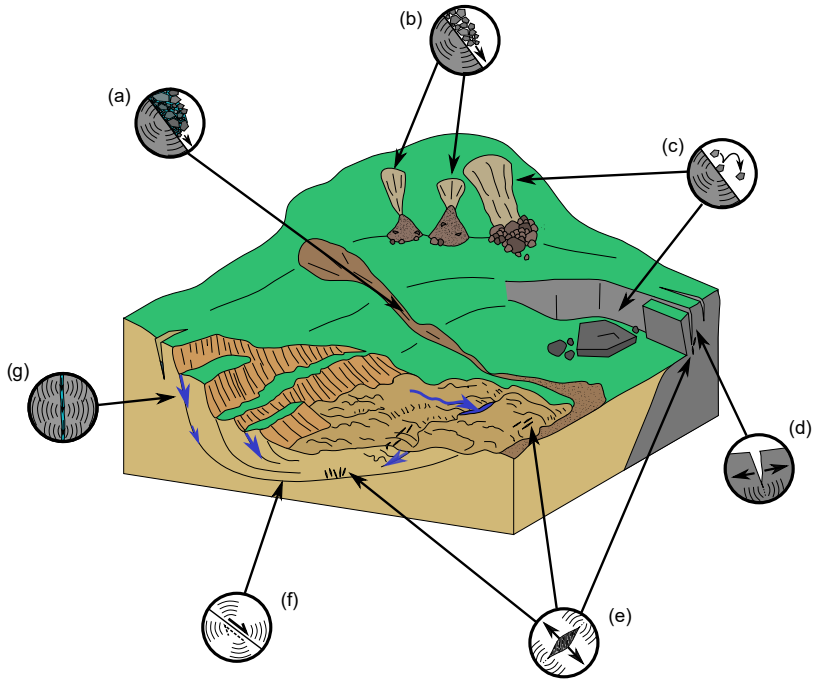

Figure 2.1 – Landslide seismic source processes. Landslide seismic sources generated by **(a)** wet granular flow, **(b)** dry granular flow, **(c)** rockfall, **(d)** tensile fracture opening, **(e)** tensile cracks opening, **(f)** shearing, and **(g)** fracture fluid migration. Figure extracted from Provost et al. (2018).

40 Hz (note here that the measured frequency content also depends on the source-receiver distance, with increased attenuation of higher frequencies).

- *Granular flows* denote seismic signals produced during the downslope movement of either dry or wet granular material (see Fig. 2.1 (a)-(b)). Compared to rockfalls, granular flows can involve a wide distribution of different grain sizes. The seismic signals are often described as cigar-shaped, characterized by a smooth envelope with emergent onset. Signals of dry granular flows last up to 500 s with frequency content between 1 and 35 Hz, while signals of wet granular flow can continue for several thousands of seconds to several hours with slightly higher frequency contents.

Following this classification, rockfalls can be distinguished from granular flows by the observation of well separated successive peaks with high frequency content. However, this observation can blur in case of simultaneous or progressive impacts of multiple blocks. Also, what starts as a rockfall can rapidly turn into a granular flow when blocks break apart during detachment or during impact (e.g. Hibert et al., 2011), or when additional material is entrained along the trajectory as for example erosion of underlying debris (e.g. Dammeier et al., 2011). Vice versa, large spikes in signals of granular flows may be observed corresponding to strong impacts of large boulders (in analogy discussed for debris flows by Burtin et al., 2016).

Regarding landslide events at Dolomieu crater, we will see that the generated seismic signals contain both rockfall and granular flow characteristics. This is due to the fact that events often involves both impacts of single blocks and the spreading of granular mass. We will generally refer to them as rockfalls.

It is worthwhile mentioning, that machine-learning techniques are increasingly used to automatically detect and classify landslide seismic signals. As for example based on Random Forest algorithms, Provost et al. (2017) classifies seismicity of slow-moving Super-Sauce landslide in the French Alps and Hibert et al. (2017c) identifies rockfalls and volcano-tectonic earthquakes at Piton de la Fournaise.

2.1.2 Landslide properties and dynamics

Thanks to the classification above, signal characteristics can be associated to specific landslide types. However, the seismic signals can be exploited even more. It has been shown that landslide properties as well as their temporal evolution can be inferred.
In the following we will review previous studies which derive landslide properties and dynamics from seismic signals. Firstly, we will present studies which follow a low frequency approximation. This simplifies landslide dynamics to the smooth global behavior of an effective granular medium and makes it possible to invert the force-time function from seismic signals. Secondly, studies which are not based on the low frequency approximation are discussed. This means that no information from the signal is lost and makes it for example possible to estimate the total energy generated by landslides. However, the high frequency content of the signal increases complexity and restricts techniques like the force inversion.

Low frequency

When considering the low frequency seismic signal recorded at a distant receiver, the landslide can be approximated as a point source with fixed position over time. This is because the landslide dimension and its trajectory are negligible small compared to seismic wavelength and source-receiver distance. This principle is illustrated on the left hand side of Figure 2.2. To get a rough idea, let's consider a landslide trajectory of 1 km. Then, to justify the low-frequency approach, the studied wavelengths should be at least 10 km. This results in signal periods of above 10 s (< 0.1 Hz) for a minimum wave speed of 1 km.s^{-1}. This is in accordance with the studies reviewed below, which typically consider signals periods above 10 s. The source-receiver distance should be of several wavelengths, i.e. around at least 40 km, in order to be outside the range of the near-field. On a side note, large landslides can be recorded at a few hundreds of kilometer distance from the source (e.g. Brodsky et al., 2003).
Following this low frequency approximation, the landslide seismic source simplifies to a single force varying over time. Authors have been using different approaches in order to relate observed seismic signals to this force-time function. On the one hand, an appropriate shape of the force-time function can be assumed and successively adjusted in timing and amplitude by fitting synthetic and observed seismograms (Kanamori and Given, 1982; Eissler and Kanamori, 1987; Dahlen, 1993; La Rocca et al., 2004). On the other hand, in a more elegant way, the force-time function is derived directly from the recorded seismic signals. This can be done by deconvolution or waveform inversion (Kanamori et al., 1984; Kawakatsu, 1989; Lin et al., 2010; Moretti et al., 2012; Ekström and Stark, 2013; Yamada et al., 2013; Allstadt, 2013; Hibert et al., 2014a; Zhao et al., 2015; Yamada et al., 2016). In this process, numerical models of landslide dynamics can help to constrain force parameters and to better interpret inversion results and their ambiguity.
The nature of the source-time function was first studied first by Kanamori and Given (1982). Analyzing Rayleigh and Love wave phase radiation patterns associated with a landslide during Mount St. Helens volcano eruption in 1980, they concluded that a bell-shaped horizontal force mechanism could best reproduce observed seismograms. Shortly

later, Kanamori et al. (1984) estimated the force-time function by direct deconvolution of the observed seismogram with a synthetic impulse response. This revealed a source-time function of sinusoidal shape. Eissler and Kanamori (1987) interpreted that the additional negative portion of the force history originates from the deceleration phase of the sliding mass. This hypothesis was confirmed by Kawakatsu (1989) who performed a force inversion of the observed seismograms based on a simple description of a block sliding down a slope. Refining the description of the landslide dynamics, Brodsky et al. (2003) modeled the force evolution using a rigid block sliding down a ramp of decreasing slope. By this, they could constrain the coefficient of basal friction. Since then, the advancement of numerical models have helped to describe both horizontal and vertical forces in more detail. They take into account complex flow behaviors which may result from interactions with the underlying topography or erosion along the path (e.g. Favreau et al., 2010; Moretti et al., 2012, 2015). A simple simulation of a granular mass sliding down a slope is presented in appendix 2.4.1. Acceleration and deceleration phase of the flowing mass can clearly be derived from the spatially distributed basal forces.
The inferred force-history can eventually help to constrain landslide properties and dynamics, such as for example the involved volume (e.g. La Rocca et al., 2004), the runout distance (e.g. Brodsky et al., 2003; Moretti et al., 2015) or the flow velocity (e.g. Hibert et al., 2014a). However, in a certain way the low frequency approximation is restricted on big landslides which involve large volumes of material. This is because only big landslides generate low frequency seismic waves of magnitudes which are detectable at large distances. Still, to get a better general understanding of landslide activity, it is of importance to analyze a broad range of events from small to big volumes. In the next section we will review studies which do not rely on the low frequency approximation.

High frequency

For high frequency landslide seismic signals, typically above 1 Hz, the seismic source can no longer be described by a single-point force. With the seismic station located closer to the event, the spatial distribution of a moving force field cannot be neglected. In addition, high frequency seismic waves are more exposed to diffraction and scattering at heterogeneities in the ground and at the surface topography. The increased complexity of the problem is illustrated in Figure 2.2.
Despite the increased complexity, high frequency signals potentially contain landslide informations of higher temporal and spatial resolution. Analyzing rockfall signals, Deparis et al. (2008) identified the time of rock detachment followed by rock impact after a short free fall. This temporal reconstruction has been applied to both granular flows (e.g. Hibert et al., 2014a) and rockfalls (e.g. Bottelin et al., 2014; Zimmer and Sitar, 2015; Gualtieri and Ekström, 2017). Studying the physical processes during rockfall impacts, Farin et al. (2015) used Hertz contact theory (see section 2.2.2) in order to predict impact forces and seismic signal characteristics in terms of amplitude and frequency content. Before applying the theory on real-size rockfall experiments carried out by Dewez et al. (2010), they successfully predict seismic signals generated during laboratory experiments.
Indeed, laboratory experiments can help to understand the dynamics of granular flows (e.g. Delannay et al., 2017) and rockfalls impacts (e.g. Labiouse and Heidenreich, 2009) as well

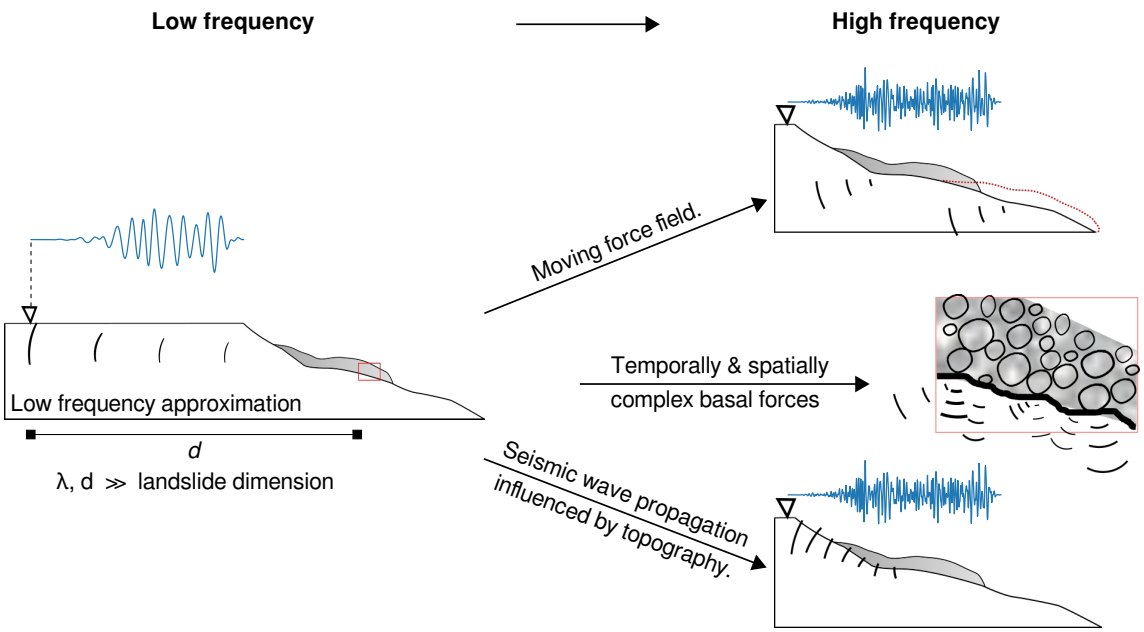

Figure 2.2 – From low to high frequency landslide seismic signal. *Left:* Low frequency approximation. Landslide dimension and its trajectory are negligible small compared to seismic wavelength λ and source-receiver distance d. The seismic signal at the station (triangle) is recorded at low frequencies. *Right:* Physical processes of the landslide and the seismic wave propagation which have to be taken into account when the seismometer (triangle) is located closer to the landslide and records higher frequencies.

as the generated seismic signals (McLaskey and Glaser, 2010; Farin et al., 2015; Bachelet et al., 2018). Complementary to this are real-scale experiments as for example carried out by Hibert et al. (2017a), releasing single blocks within a gully in the French Alps. Using the generated seismic signals, they were able to retrieve mass and velocity of each block before impact. This was realized by finding laws between potential energy loss, kinetic energy and seismic energy.

Scaling laws present a statistical approach to relate seismic signals to landslide properties. This way, many authors investigated the relation between loss in potential energy and generated seismic energy (Berrocal et al., 1978; Weichert et al., 1994; Vilajosana et al., 2008; Deparis et al., 2008; Hibert et al., 2011; Dammeier et al., 2011; Hibert et al., 2014b; Levy et al., 2015). Using numerical landslide models, Hibert et al. (2011) shows the proportionality between potential energy loss and generated seismic energy and propose an empirical relationship to estimate landslide volume. Fundamental to this is the estimation of generated seismic energy which involves assumptions on the propagation and distribution of the generated energy in the underlying subsurface. In other words, it has to be estimated how much of the totally generated energy is recorded at the station. This task is not trivial, even for a synthetic subsurface model of known parameters as we will see in section 3.3 on page 71, where we derive an equation for the energy calculation.

Finally, landslide seismic signals can be used to not only locate events but also follow the position of a moving source over time. This can be realized by using for example polarization methods (Vilajosana et al., 2008) or beam-forming methods (Lacroix and Helmstetter, 2011; Bottelin et al., 2014). We will come back to localization methods in Chapter 5 on 141.

In this section we could see the potential of seismic waves to infer information of landslide properties and dynamics. To fully exploit this potential, it is crucial to understanding the mechanisms of the seismic source which is constituted by the basal forces imposed from the landslide on the ground. Modeling landslide dynamics can help to enhance understanding. In the following, we will present different models which are adequate to describe certain types of landslides.

2.2 Modeling landslide seismic sources

Landslide numerical modeling is an important tool to better understand and constrain landslide dynamics and the forces generated on the ground. As we discussed before, the basal forces are the interconnection between landslide physics and radiated seismic waves and thus key to understand recorded seismic signals. Different approaches are used to model different landslide classes. Generally speaking, we can distinguish between continuum models and discrete models:

- **Continuum models** take a macroscopic approach and model the landslide as a continuous mass. Often based on Navier-Stokes equations, they are used to simulate the fluid like behavior of granular flows. The basal forces are essentially related to acceleration and deceleration of the mass due to variations of the topography. One of the main issues for landslide continuum models is the estimation of the effective friction coefficient between the flowing mass and the underlaying ground. Observations have shown long runout distances for large landslides, suggesting high mobility due to apparent low friction which is also referred to as friction weakening (Lucas et al., 2014; Levy et al., 2015; Delannay et al., 2017). Obviously, continuum models can not resolve the dynamics of individual particles. Consequently, generated seismic waves are limited to rather low frequencies corresponding to the macroscopic landslide dynamics. High frequencies, generated by grain-grain interaction or boulder impacts, cannot be considered.
- **Discrete models** take a microscopic approach, describing the dynamics of individual grains or boulders and the involved interactions. Dependent on the complexity of the model, they take into account free fall, bouncing, sliding, and rolling of single particles (e.g. Dorren et al., 2004). For models describing granular flows of many particles, assumptions have to be made on the distribution of grain sizes and grain shapes. Very commonly, individual particles are modeled as perfect spheres. Generally, these models are computationally more expensive than continuum models and may not be adequate to simulate the dynamics of real-scale granular flows.

In reality, landslides can possess wide distributions of particle sizes and shapes and can change dynamical regimes during their movement (e.g. from a falling rock block to a flowing granular mass). The different scales and dynamics make it difficult to have a model which can universally be applied. For this reason it is important to determine the objective of study (e.g. simulation of runout distance, basal forces, shape and height of deposit, ...) prior to choosing a model.
In the following we will introduce a continuum model which is based on the thin-layer

approximation and can be used to simulate granular flows on 3D topographies. We will use this model to show that the frequency content of generated forces can increase with the roughness of the topography. However, even if the runout distance can well be estimated on the rough topography, the continuum model can not be used to reproduce the necessary high frequency forces ($> 1\,\mathrm{Hz}$) for the observed rockfall seismic signal at Dolomieu crater. For higher frequencies, the impacts of single particles has to be considered. For this reason, we will introduce the Hertz contact theory (Hertz, 1882). This theory is commonly used to model the stress-strain relationship between two colliding particles. It is applied for both modeling grain-grain interactions and boulder impacts on the ground. This model will serve later for the estimation of maximum impact forces of rockfalls. The predicted forces will then be used to calibrate seismic waves simulations in order to allow comparison with real signals.

2.2.1 SHALTOP granular flow simulations

SHALTOP is a numerical model for the simulation of incompressible flow on 3D topography (Bouchut et al., 2003; Bouchut and Westdickenberg, 2004; Mangeney et al., 2007). It is based on a thin-layer (or shallow-water) assumption which implies that the thickness of the flow is small compared to its horizontal extent, a concept which was first applied to granular flows by Savage and Hutter (1989). To reduce the computational time, the flow speed is averaged over the thickness of the flow which leads to the hydrostatic approximation. Eventually, SHALTOP solves for the time varying flow thickness $h(x, y, t)$ normal to the topography and depth-averaged flow velocity $u(x, y, t)$. Topography elevation is described by $z = b(x, y)$ while (x, y, z) are the Cartesian coordinates. The basal friction is described according to Coulomb's law of friction with either constant or velocity- and thickness-dependent friction coefficient. Friction coefficient μ can be related to friction angle φ using $\mu = \tan\varphi$. Friction angle φ is empirically estimated and represents the mean effective friction of the depth-averaged model. It is related to the mean energy dissipation during the flow (Roche et al., 2011). SHALTOP has been applied successfully to reproduce real-scale granular flows (e.g. Kuo et al., 2009; Favreau et al., 2010; Hibert et al., 2011; Moretti et al., 2012; Levy et al., 2015; Zhao et al., 2015; Moretti et al., 2015; Yamada et al., 2016). The model is used here to investigate the spatially distributed force field generated by granular flows on the ground. In appendix 2.4.1 we simulate the forces generated by a column collapse on a flat surface and by a mass sliding down a slope. It can be observed how the forces are related to acceleration and declaration of the mass. In the following, we analyze the forces generated by a granular flow on a real topography. We expect that the topography variations can introduce abrupt accelerations and thus higher frequency contents of the forces.

Example at Dolomieu crater

A granular flow on the real Dolomieu crater topography is modeled and the influence of topography roughness and friction coefficient on the generated basal forces and their frequency content is analyzed. This is important in order to evaluate if this model can be

used to describe the force field which generates the observed rockfall seismic signals.
Topography is implemented using the DEM of Dolomieu crater with 2 m resolution (*rough* case) and its smoothed version which is low-pass filtered with a corner wavelength of 20 m (*smooth* case). Coulomb-type friction with constant friction coefficient is applied. Two different friction angles are tested, namely $\delta = 35\,^\circ$ and $\delta = 37\,^\circ$. These values correspond to empirical values determined in former studies of granular flows at Dolomieu crater (Hibert et al., 2011, 2014b).
Simulations are carried out in comparison to a granular flow on the southwestern crater wall on April 24, 2013. For initiating the numerical simulation, a mass volume of $52\,\mathrm{m}^3$ is released on top of the crater wall, corresponding to the position of detachment of the real event. The shape of the released mass is described by a half-sphere of 5 m radius.
Figure 2.3 shows three instants of the event, namely 1) shortly after releasing the mass in the simulation, 2) 5 s seconds afterwards, and 3) after 20 s when most movements cease in the simulation. Note that the initiation processes are essentially different between reality and simulation. First movements of the real granular flow can be detected on the video around 10 s before the start of the simulation. While the mass of the real granular flow increases gradually, the simulation releases the whole mass at once. Furthermore, several boulders continue to descend towards the crater bottom in the real case. This rockfall-type behavior could not be reproduced with the SHALTOP model. Despite all these discrepancies, we want to emphasize that the objective of this study is to determine the frequency content of simulated basal forces. The real event is not entirely reproduced, merely the extent of the spreading granular mass is compared for evaluation of the simulations.
Each instant in Figure 2.3 shows camera snapshots of the real event and simulations on rough and on smooth topography for friction angle $\delta = 37\,^\circ$. In the camera snapshots, the generated dust clouds approximately indicate the extent of the granular flow. This spreading extent is well reproduced by the simulation on the unfiltered topography. For the low-pass filtered topography, the mass is sliding faster and longer due to the smoothness of the bed, even for the here shown high friction angle of $37\,^\circ$. The simulated basal forces are spatially scattered on the rough topography, while showing a smooth character on the smooth topography.
The force-time functions measured at three fixed position in space are compared between all simulations in Figure 2.4. Position 1 is at the location of the released mass, positions 2 and 3 are placed downhill with spacings of around 40 m. For each position, forces F_x, F_y, and F_z in $x-$, $y-$, and $z-$direction are shown, respectively.
The black dashed lines indicate the first movement which is measured at each position. As the mass is released abruptly at position 1, the dashed line is positioned at time $t = 0\,\mathrm{s}$. Subsequently, the mass arrives successively at position 2 and 3. Generally it can be observed that the vertical force F_z is the biggest. This is because it is associated to the gravitational force which is imposed by the mass on the ground. At position 1, F_z is positive, meaning that it points upwards due to the removal of mass. For the two other positions, the vertical force points downwards as mass is added at these positions. At position 2 we can see that F_z is non-zero at the end of the simulation for the friction angles of $\delta = 37\,^\circ$. This means that part of the mass stopped at this position without moving on downslope. No force at all is measured at position 3 in case of the rough surface with friction angle $\delta = 37\,^\circ$. The rough surface together with the high friction angle decelerates

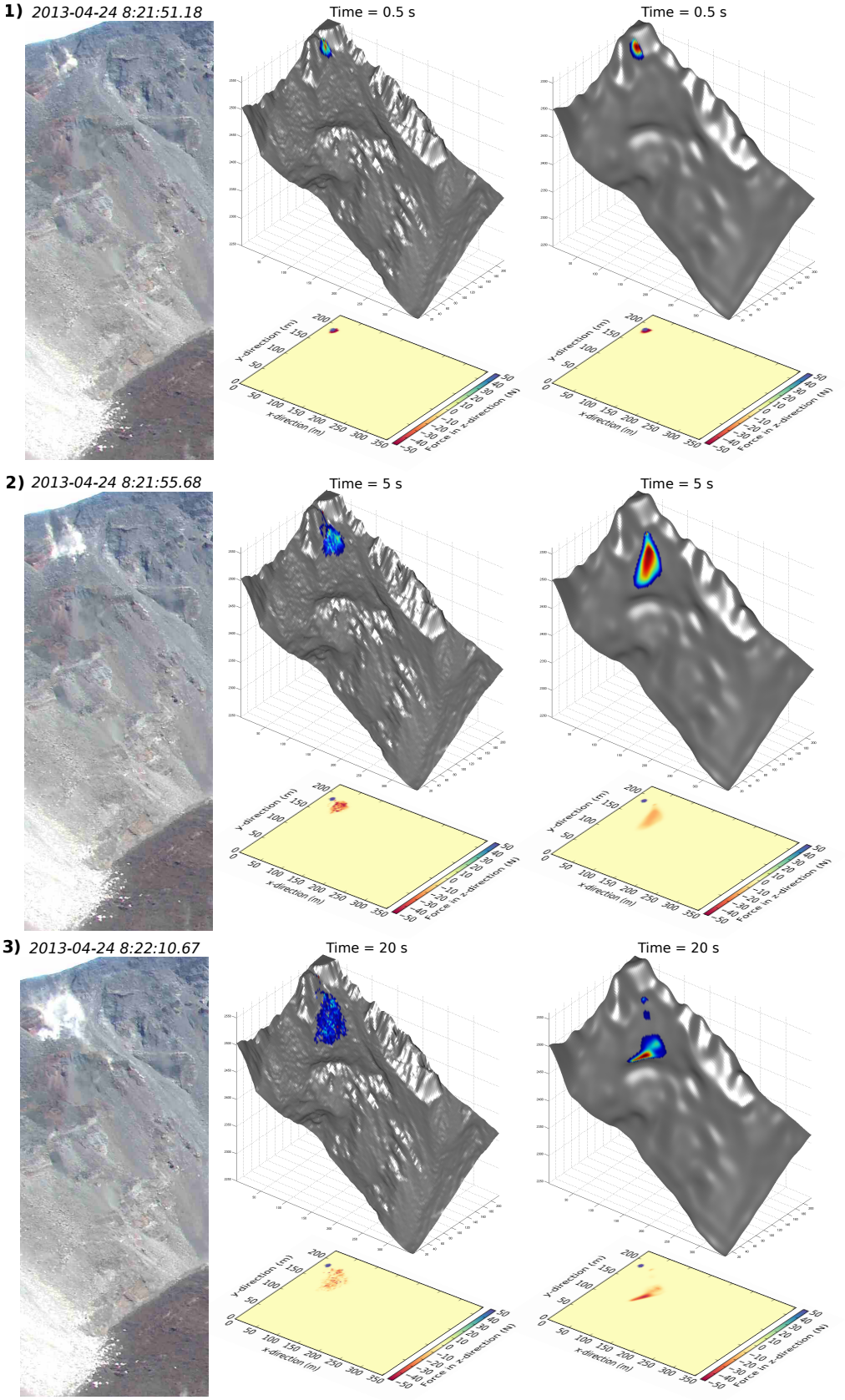

Figure 2.3 – Modeled landslide basal forces on topography. *Left column:* Camera snapshots of a rockfall on the southwestern side of Dolomieu crater on April 24, 2013. Dust clouds indicate the spreading spatial extent of the granular flow. *Middle and right columns:* SHALTOP simulations on rough and smooth topography with friction angle $\delta = 37\,^{\circ}$. The color scale indicates the relative thickness of the flow at each time instant. Underlying panels show generated basal forces in vertical direction. The moving force field is more scattered in case of the rough topography (middle column). The time-invariant blue spot (positive force) corresponds to static forces due to removal of the initial mass.

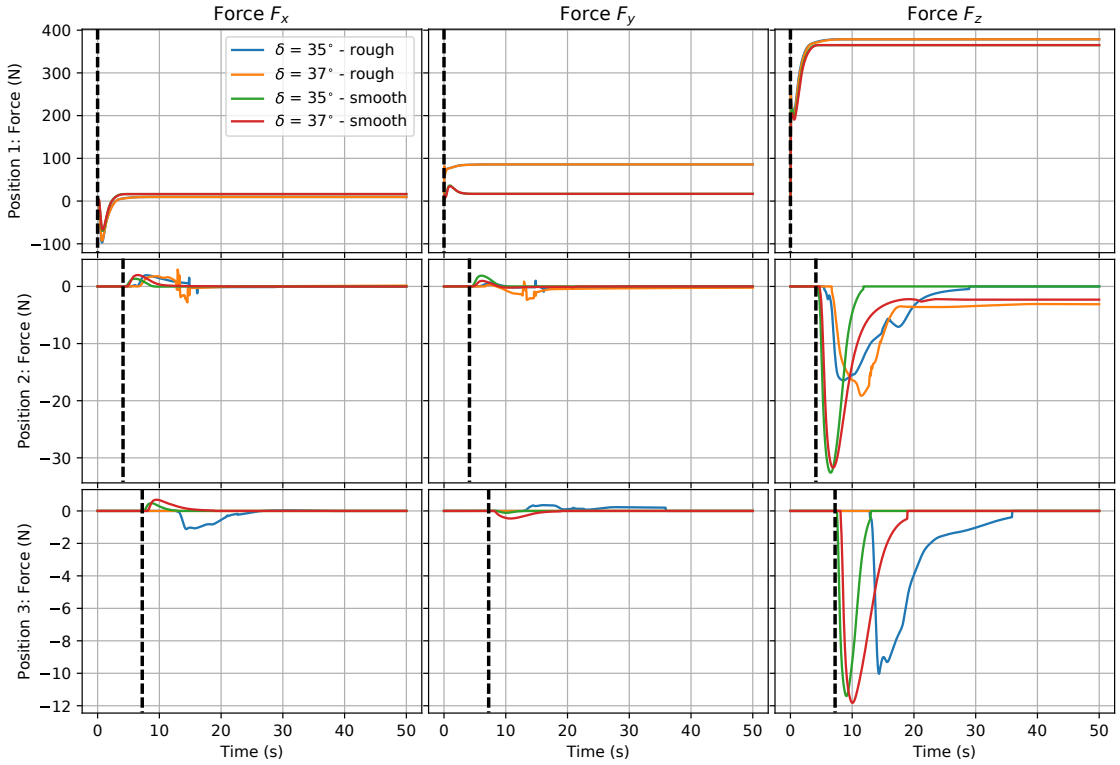

Figure 2.4 – Basal forces measured at three fixed positions. Forces F_x (*left*), F_y (*middle*), and F_z (*right*) at three different positions 1, 2, and 3. Simulated forces on rough (real DEM of 2 m resolution) and smooth (low-pass filtered with 20 m corner wavelength) topography with friction angle of $\delta = 35\,^\circ$ and $\delta = 37\,^\circ$. Black dashed line marks the time at which the first movement is measured.

the mass so that it does not arrive at position 3.

We will now analyze in more detail the generated forces at position 2. For this, the forces are plotted in Figure 2.5 without equal force axes. Besides the force amplitude, we can analyze the curves in terms of timing, polarization and smoothness:

- **Timing** shows when and how fast the flow is passing the measurement position. It can be observed that the mass passes the quickest in case of smooth topography and low friction angle. Increasing the friction angle results in a wider force-time function as the velocity of the flow becomes smaller. This is also true when going from smooth topography to rough topography. The decrease of flow velocity can also be identified by the later arrival. The remaining force on the z-component for big friction angles reveals that mass is resting till the end of the simulation at the position of measurement.
- **Polarization** has to be interpreted differently for horizontal forces and vertical forces. For horizontal forces it is related to tangential acceleration and deceleration of the flow along the slope in the axis direction, indicated by positive and negative values, respectively. The force in x-direction is mostly positive for all simulations, indicating a downslope acceleration as the x-directions is close to the direction of the steepest slope. Only the simulation on rough topography with high friction angle is showing an important negative portion, which means that mass is decelerating at the measurement position for later times. This can similarly be observed for the forces in y-direction. As mentioned before, the force in z-direction is mainly linked

to the process of adding or removing mass. At the measurement position we can see exclusively negative values (i.e. forces pointing downwards), meaning that mass is temporally added. The remaining negative force in case of the high friction angles reveals the mass is resting at the measurement position.

- **Smoothness** of the curves can tell us about the dynamics and the shape of the flowing mass. More abrupt changes of movement on the rough topography result in spikier horizontal forces. The vertical forces, as mentioned before, are mainly linked to the mass, and thus the thickness of the flow. For the smooth topography we can observe curves consisting of a single lobe. This means that the thickness of the passing mass is gradually increasing and decreasing. The vertical forces on the rough topography show more fluctuations, indicating fluctuations of the flow thickness.

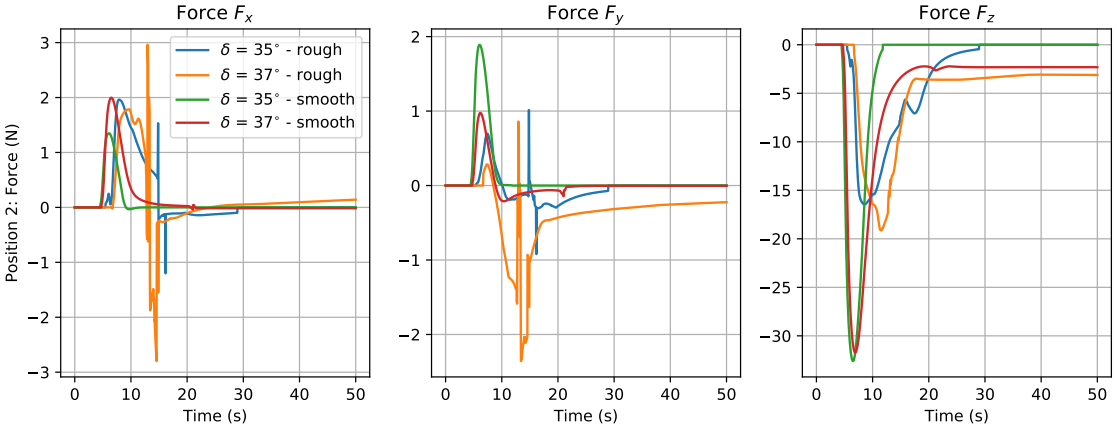

Figure 2.5 – Basal forces on varying topography roughness. Force-time functions at position 2 ($x = 60$ m, $y = 170$ m, see Figure 2.3) for each component. Forces are simulated on rough and smooth topography with friction angle of $\delta = 35\,°$ and $\delta = 37\,°$. Note the different scales of the force axes.

In summary, the time variations of forces are linked to flow velocity, flow thickness and acceleration-deceleration phases which all are influence by bed roughness and friction. In turn, the frequency content of generated seismic waves is determined by the time variation of the basal forces. For this reason we take a look at the frequency content of the whole force field.

First of all, we calculate the total force by integrating over the whole surface. The resulting total forces for all simulations are shown in Figure 2.6 together with their amplitude spectra.

Directly noticeable is the spiky character of the forces from the simulations on the rough topography, in particular in case of friction coefficient $\delta = 35\,°$. This are numerical artifacts which are related to strong velocity gradients caused by the rough surface. Also remarkable is that the vertical force is no longer bigger as the horizontal forces. This is due to the fact that the forces related to the gravitational mass canceled each other out. Apart from that it is interesting to see that the simulations on the smooth slope contain a second main lobe at around 12 s which is not visible for the simulations on the rough surface. It is plausible that this second lobe is related to the deceleration phase of the mass. Comparing with Figure 2.3 we can observe that the mass on the smooth surface is stopped by a little hill which probably cause the observed deceleration forces. In contrast, the mass on the rough surface is stopped more continuously due to the rough surface. It is also visible that the forces F_y are of opposite polarity compared to the forces F_x. This has to be explained

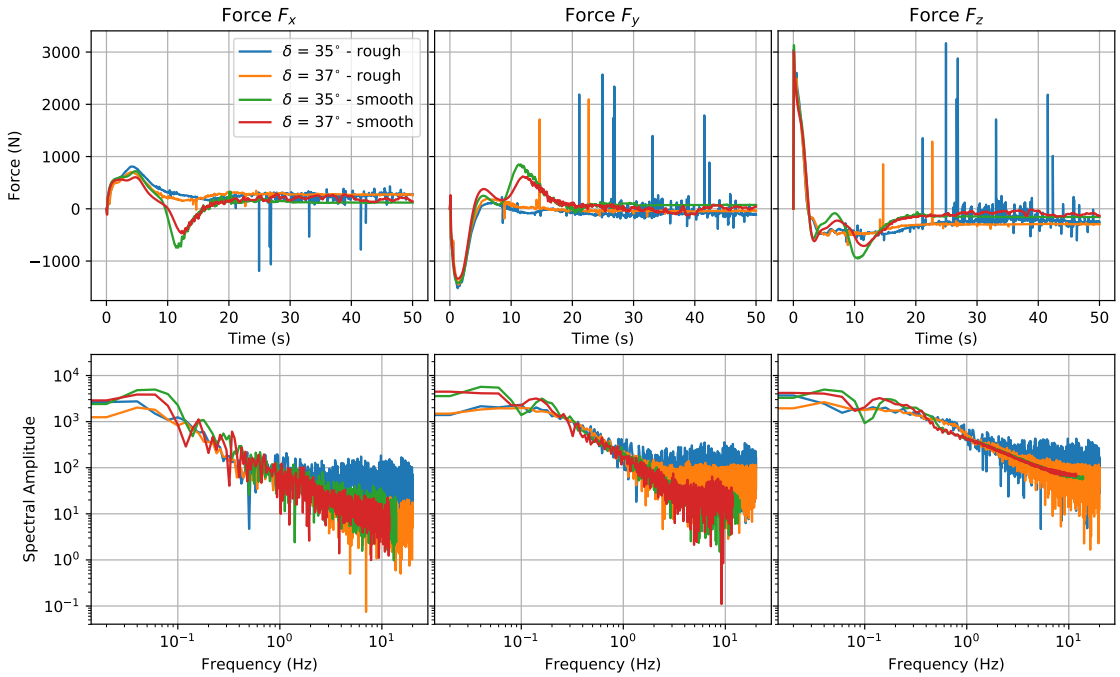

Figure 2.6 – Total force summed over the whole surface and corresponding frequency spectrum. *Top:* Total force calculated integrating all forces over the whole surface. This can be done when the associated seismic wavelengths are larger than the force field. *Bottom:* Frequency spectra of the total forces above.

by the fact that the slope of deepest descent points in negative y-direction.
The spectra show gradually decreasing amplitudes towards higher frequencies. Amplitude spectra on the smooth topographies are slightly higher at lower frequencies, probably resulting from longer flow durations. At higher frequencies the simulations on the rough bed contain higher values. However, numerical noise could effect these results. To verify their validity, the results have to be tested on convergence by decreasing the numerical time step.
Summing of the forces in the time domain is only valid in a low-frequency approximation. At higher frequencies the different source positions have to be considered since the corresponding wavelengths are not necessarily larger than the force field of the landslide. To avoid the superposition of forces in the time domain, we carry out another analysis for which we first calculate the amplitude spectra measured at each point of the domain and sum them up subsequently. The resulting spectra for each simulation are shown in Figure 2.7. Similar to the spectra in Figure 2.6, the spectral amplitudes are decreasing towards higher frequencies. However, by first calculating the FFTs at each position and subsequently summing, forces of opposite polarity do not cancel each other out. As a result, the values of the spectra are almost a magnitude higher. This is especially evident for the low frequency vertical force which is related to the adding and removing of mass.
Again, amplitude spectra on the smooth topographies are generally higher at lower frequencies. Interestingly, the smooth bed simulation with higher friction coefficient shows higher amplitudes on the y-component. This might be linked to more lateral spreading of the flow. Apart from that the rough topography can potentially increase high frequency content. Comparing for example the vertical force component, the rough bed simulation with low friction angle contains the highest amplitudes for frequencies above 1 Hz. As said

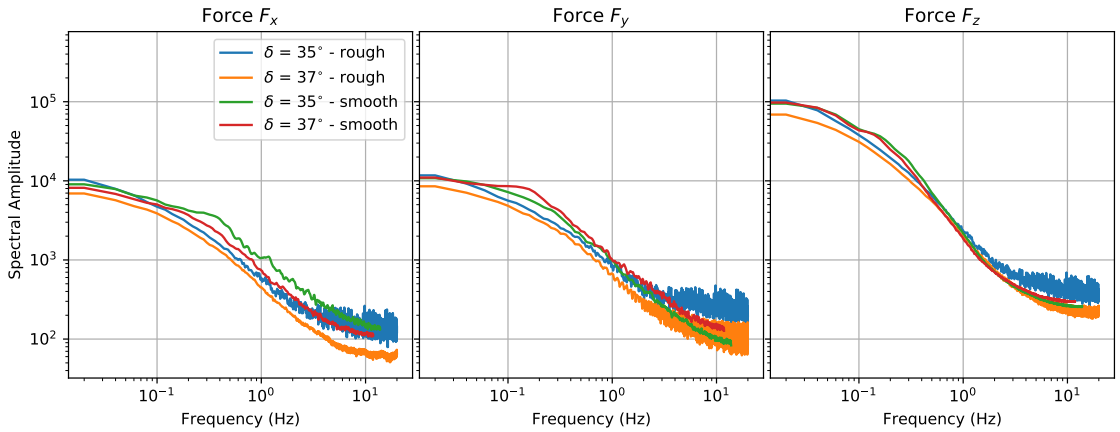

Figure 2.7 – Sum of all frequency spectra. In contrast to the spectra shown in Figure 2.6, the FFTs are first computed at each position and subsequently summed. By this, the superposition of forces in the time domain is avoided which can lead to the canceling of forces.

before, convergence tests with decreasing time step have to be carried out in order to see if the higher values are physical meaningful.
Nonetheless, even with increased force-time variations through stronger topography roughness or smaller friction angles, the SHALTOP model does not seem to be adequate for simulating high frequency basal forces. For this, it is inevitable to use models which allow the description of individual impacts. In the next section we will introduce the Hertz contact theory, which is a classical model to describe the collision between two bodies.

2.2.2 Hertz impact model

The Hertz contact theory (Hertz, 1882) is a fundamental and widely-used model for the stress-strain relation between two colliding bodies. Let's consider an elastic sphere impacting an elastic half space. Following Hertz theory, the impact force F_H normal to the plane, can be described by means of the indentation depth δ, which is a measure of interpenetration of sphere and plane, as follows:

$$F_H(t) = \frac{4}{3} E R^{1/2} \delta^{3/2}(t). \tag{2.1}$$

R is the sphere radius and E is the effective Young's modulus defined as follows:

$$\frac{1}{E} = \frac{1-\nu_s^2}{E_s} + \frac{1-\nu_p^2}{E_p}, \tag{2.2}$$

where ν_s, ν_p, E_s, and E_p are Poisson's ratio and Young's modulus of sphere and impacted plane, respectively. With the time varying impact force F_H of equation 2.1 by hand and ignoring the force of gravity, we can set up the sphere's equation of motion:

$$m \mathrm{d}_{tt}^2 \delta(t) = -\frac{4}{3} E R^{1/2} \delta^{3/2}, \tag{2.3}$$

where m is the mass of the sphere. From this differential equation, the maximum indentation depth $\delta_{\max}$ can be derived:

$$\delta_{\max} = \left(\frac{15 m v_n^2}{16 E R^{1/2}} \right)^{2/5}, \tag{2.4}$$

where v_n is the velocity normal to the plane. Substitution into equation 2.1 gives the maximum normal impact force F_0:

$$F_0 = \frac{4}{3} E R^{1/2} \delta_{\max}^{3/2} = \frac{4}{3} E R^{1/2} \left(\frac{15 m v_n^2}{16 E R^{1/2}} \right)^{3/5}. \tag{2.5}$$

Assuming a Coulomb type friction, tangential maximum force F_t can be derived from normal maximum force $F_n = F_0$ by means of friction coefficient μ:

$$F_t = \mu F_0. \tag{2.6}$$

As in the previous section, friction coefficient μ is related to friction angle φ via $\mu = \tan \varphi$. Important in regards to generated seismic waves is the impact characteristic frequency content, which is related to the behavior of the force over time. Johnson (1987) showed that the temporal evolution of indentation depth δ can be approximated by a sine-function:

$$\delta(t) \approx \delta_{\max} \sin(\pi t / T_c), \quad 0 \leq t \leq T_c. \tag{2.7}$$

The ground velocity at the impact location can thus be described by a cosine-function as

$$\dot{\delta}(t) \approx \frac{\pi \delta_{\max}}{T_c} \cos(\pi t / T_c), \quad 0 \leq t \leq T_c, \tag{2.8}$$

where $\dot{\delta}$ is the time derivative of δ. It is plotted in Figure 2.8 together with its frequency spectrum. Both are shown as functions of impact duration T_c.

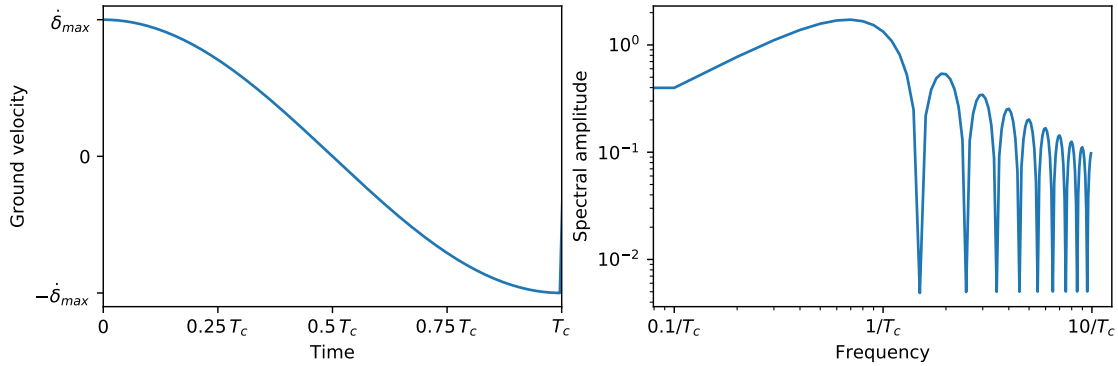

Figure 2.8 – Time derivative of Hertzian indentation depth. *Left:* Time derivative $\dot{\delta}$ of Hertzian indentation depth δ normalized by maximum indentation depth $\delta_{\max}$ in dependency of impact duration T_c, which represents the time during which the two bodies are in contact. *Right:* Frequency spectrum of the ground velocity. The inverse impact time $1/T_c$ is related to the corner frequency f_c after which the spectral amplitude decays exponentially. The maximum amplitude is located at frequency f=0.7/T_c.

It can be observed that the amplitude spectrum of the ground velocity decays exponentially above a corner frequency f_c which is related to the inverse of contact time T_c. The

maximum spectral amplitude is located at a frequency $f = 0.7/T_c$.
Combining equations 2.1 and 2.7, the time evolution of the Hertz impact force can be approximated as

$$F_H(t) \approx F_0 \sin(\pi t/T_c)^{3/2}, \quad 0 \leq t \leq T_c. \tag{2.9}$$

The time-dependent impact force is illustrated in Figure 2.9 together with its spectrum similar as in Figure 2.8.

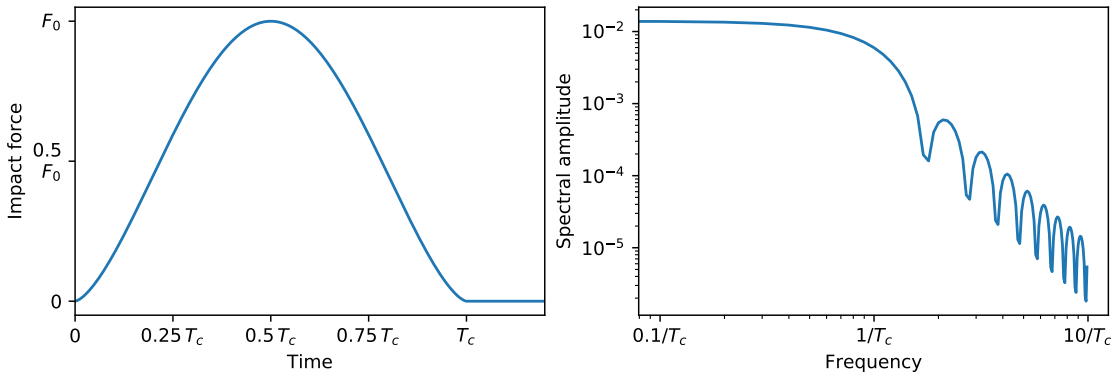

Figure 2.9 – Hertzian impact force and corresponding frequency spectrum. *Left:* Hertzian force-time function F_H normalized by maximum impact force F_0 in dependency of impact duration T_c, which represents the time during which the two bodies are in contact. *Right:* Frequency spectrum of the force-time function. The inverse impact time $1/T_c$ is related to the corner frequency f_c after which the spectral amplitude decays exponentially.

Also for the force spectrum an exponentially decay can be observed above a corner frequency f_c which is related to the inverse of contact time T_c. At higher frequencies, the spectrum consists of a series of low amplitude nodes. McLaskey and Glaser (2010) are able to well reproduce the spectrum and the node locations carrying out experiments of a ball colliding on a massive plate.
According to Johnson (1987), impact or contact duration T_c can be approximated by:

$$T_c \approx 2.94 \frac{\delta_{\max}}{v_n}, \tag{2.10}$$

with maximum indentation depth $\delta_{\max}$ and impact speed v_n normal to the impacted plane. This means, the higher the impact velocity v_n, the shorter the impact duration T_c and the higher the corner frequency f_c. In other words, we can expect higher frequency contents in rockfall signals for impact of boulders with higher velocity. All dependencies of impact force, impact duration and corner frequency are summarized in Table 2.1.

Table 2.1 – Dependency of impact force, duration and corner frequency on impact parameters. Behavior of impact force F_0, impact duration T_c and upper corner frequency f_c as function of sphere mass m, sphere radius R, effective Young's modulus E, impact speed v_n and inelasticity P. Dependencies are derived from equations 2.5 and 2.10 except for the dependency on inelasticity P which is deduced from Farin et al. (2015). ↗: increasing value; ↘: decreasing value.

	m ↗	R ↗	E ↗	v_n ↗	P ↗
F_0	↗	↗	↗	↗	↘
T_c	↗	↘	↘	↘	↗
f_c	↘	↗	↗	↗	↘

The Hertz contact theory is an elastic model and does not consider inelasticity such as plastic deformation. In reality, plastic deformation plays an important role during rockfall impacts, for example due to fracturing of the impacting rock. Plastic behavior during the collision occurs, when the pressure on the contact area exceed the yield strength of the material. There are several approaches to take plastic deformation into account. For example, Zhang et al. (2018a) derives a maximum impact force based on the concept of a sphere with an outer zone of elastic deformation and an inner zone of plastic deformation. Farin et al. (2015) describes introduces plastic deformation by dividing the temporal evolution of the Hertz impact in three phases. Starting with 1) a fully elastic phase for the time in which the exerted pressure is inferior to the shield strength, the second phase is described by 2) a fully plastic deformation which is related to an impact force smaller than in the elastic case, finally followed by 3) an elastic rebound for which the indentation depth has been corrected due to the plastic deformation. Numerically solving the established equation, they show that the impact force decreases with increasing plasticity, whereas the force-time function becomes wider. This means that the contact time T_c becomes longer. As a result, plastic deformation during a rockfall decreases high frequency content in the corresponding seismic signal.
The estimation of impact forces is an important task for the design of structural protections, in particular for infrastructure facilities in mountainous regions. A review of Volkwein et al. (2011) compiles relevant research on characterization of rockfall hazard and corresponding protection measures. Several countries use their own standard to estimate rockfall impact forces. A comparison can be found in Zhang et al. (2018a). Most models seem to be based on Hertz contact theory before being calibrated to empirical relations as for example parameters of the cushion layer (as e.g. in the Swiss guidline ASTRA, 2008).

2.3 Rockfalls at Dolomieu crater

As described in Chapter 1, rockfalls occur very frequently at Dolomieu crater on Piton de la Fournaise since its caldera collapse in 2007. The high event rate, due to unstable crater walls, together with the dense instrumentation of OVPF provide laboratory-like conditions for the study of rockfalls. In the following we will review previous studies on rockfall activity at Dolomieu crater. Afterwards we introduce a catalog of selected events before presenting and analyzing exemplary rockfalls by means of camera images and seismic recordings.

2.3.1 Previous studies

Combining methods based on photogrammetry and georeferencing, Derrien et al. (2019) estimate total mass-wasting volumes at Dolomieu crater of $4.2 \pm 0.1 \times 10^6\,\mathrm{m}^3$ and $1.8 \pm 0.1 \times 10^6\,\mathrm{m}^3$ in periods from April 2007 to April 2008 and from April 2008 to May 2015, respectively. Investigating fracture processes and slope deformation, they distinguish two main mechanisms of instability, namely rock topples on the northwestern crater walls and sliding slopes on the southeastern sides (see Figure 1.3). Hibert et al. (2017b) uses seismic methods to analyze the spatio-temporal evaluation of rockfalls at Dolomieu crater.

For the period between May 2007 and April 2011, they estimate a total rockfall volume of $3.23 \times 10^6\,\mathrm{m}^3$. Similar to Derrien et al. (2019), they find the largest volumes in the months after the caldera collapse. The seismic analysis enables them to count the number of rockfall events. This way, they detect more than 6000 events in the studied period. While the two month after the crater collapse are characterized by up to 80 rockfalls per day, the number is decreasing afterwards to a long-term rate of up to 5 rockfalls per day. The average rockfall volume is constantly decreasing from $650\,\mathrm{m}^3$ in 2007/2008 to $19\,\mathrm{m}^3$ in 2010/2011. Furthermore, triggering mechanisms are investigated. While occasional correlation with rainfall is found, there is a strong relation between volcanic seismicity and rockfall activity. Analyzing rockfall locations, they find intensification of rockfall activity towards the location of the next eruption. Durand et al. (2018) elaborates on the influence of external forcings on slope instabilities, concentrating on a period between 2014 to 2016 which is less biased by processes due to the post-collapse relaxation of Dolomieu crater. Using both photogrammetric and seismic data, they estimate a total rockfall volume of 80,000 to 100,000 m^3. They show that rain and volcanic activity can increase the number of rockfalls and, in particular, their volume. Similar to Hibert et al. (2017b), they find a tendency of rockfall activity to migrate towards locations of lava outbreaks. This is an important finding as it means that rockfall activity could be used to predict the location of proximate eruptions.

2.3.2 Rockfall examples: Video and seismic signal

In this section we will analyze three exemplary rockfalls at Dolomieu crater by means of camera images and corresponding seismic signals. We focus on small events of individual boulders for which we can identify separated impacts on the camera images. Figure 2.10 shows the different location of the three rockfalls.

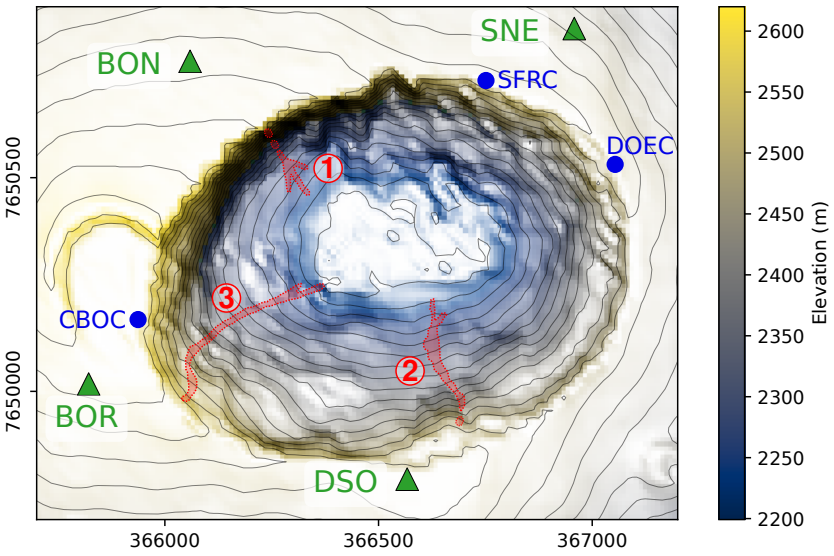

Figure 2.10 – Map of Dolomieu crater with rockfall trajectories. Topographic map of Dolomieu crater with surrounding seismic stations (triangles) and cameras (dots). Red shaded areas indicate estimated trajectory locations of three rockfalls discussed hereafter. The trajectories were inferred from videos. Contour lines mark elevation differences of 20 m.

When correlating camera images and seismic signals, we have to bear in mind the delay time caused by the travel path of seismic waves between position of impact and the position of measurement. In other words, we expect that the seismic signal of an impact

arrives after the impact time on the video. However, the visual detection of the rockfall trajectory relies mostly on dust clouds created during impacts as the boulders might be too small to be followed on the video. Hence, a small delay time might be existent between true impact and visual detection. Yet, this delay time is in the same order as the image sampling time, which is 0.5 s. Note that we will study the signal signature of impacts more precisely in Chapter 4 by comparing observed and simulated waveforms. As we will see, a precise definition of arrival times is impossible as the waveforms are very complex without clear onset due to the underlying velocity structure and the surface topography.
Besides camera snapshots, we show images of the reconstructed rockfall trajectory. These images were generated by Frédéric Lauret (OVPF), analyzing differences between two successive snapshots. Detected differences during the total rockfall duration are then superposed in order to obtain an image of the whole trajectory.
Following the classification of landslide seismic signals proposed by Provost et al. (2018) which was presented in section 2.1, the signals at Dolomieu crater are best attributed to the class of granular flow due to their rather smooth envelope and major frequency content between 1 and 35 Hz with maxima around 10 Hz. However, we will see that rockfall characteristic peaks caused by individual impacts become visible in high frequency bands. Furthermore, we will observe that the duration of seismic signal is similar to the duration of rockfall propagation. This corresponds to finding of Hibert et al. (2011) for rockfalls at Dolomieu crater and suggests that scattering effects of the medium on the seismic waves can be neglected when analyzing the seismic signals. Tests on the energy equipartition in section 1.3.4 neither indicated a multiple scattering regime of the medium surrounding Dolomieu crater.

1) Rockfall on January 22, 2017

The first example is a rockfall on the steep northwestern crater wall, occurring on January 22, 2017 (event **1** in Figure 2.10). Trajectory, snapshots and seismic signals in different frequency bands as well as the spectrogram are shown in Figure 2.11. Clouds close to the upper edge of the crater obstruct the visibility which is why only the lower part of the rockfall can be seen on the trajectory. Snapshot a) shows the first event which is detectable by eye on the video. From the seismic traces we can tell that sources were already active before that time. The clouds may hinder the ability to visually detect earlier events on the upper crater wall. Impact a) corresponds most probably to the subsequent peak in the seismic signal, best visible at 10-15 Hz. Snapshot b) shows the most pronounced impact of this rockfall. The corresponding boulder hits the crater wall after a free fall. The seismic signal shows a clear peak especially in the higher frequencies (most distinct at 25-30 Hz). At snapshot c) we can identify at least three boulders moving on different trajectories. The boulders might originate from fragmenting of the initial block, by subsequent detachments or by activation of underlying debris. The seismic signal contains several small peaks at higher frequencies and amplitudes with smooth envelopes at 1-5 Hz, corresponding to a generally active granular material. Snapshot d) shows the impact of a subsequent block at the bottom of the outcropped wall. The impact can be identified by a nicely visible peak at 20-25 Hz. Snapshot e) corresponds to the time at which the last movement is visually detectable on the video. The seismic signal only shows some minor amplitudes probably

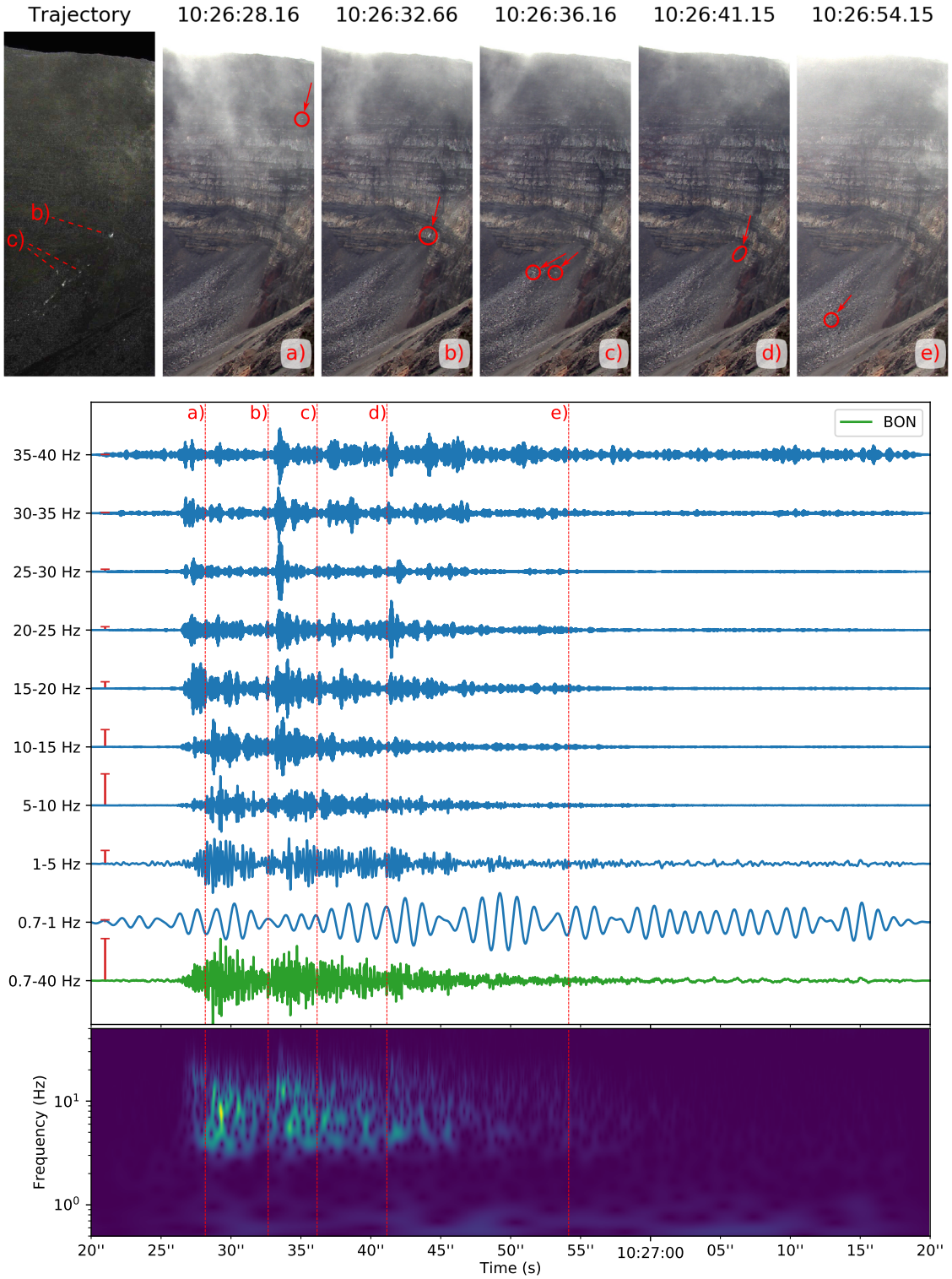

Figure 2.11 – Rockfall at northwestern wall of Dolomieu crater. For location see rockfall **1** in Figure 2.10. *Top:* Images taken from camera DOEC. Trajectory on the top left is reconstructed from differences between successive images during the whole rockfall duration. Circles mark event locations, while arrows indicate the direction of arrival. *Bottom:* Seismic signal at closest station BON in different frequency bands with spectrogram representation below (using Stockwell transform). Vertical lines from a) to e) correspond to times of camera snapshots above. Note that seismic traces are normalized individually by their maximum. Relative amplitudes can be deduced from the spectrogram.

caused by movements which are too small to detect on the video. This confirms that the duration of the seismic signal is controlled by the propagation phase of the rockfall.

2) Rockfall on February 28, 2016

The second example is a rockfall on the southern crater slope (event **2** in Figure 2.10). Images and seismic signals are shown in Figure 2.12. Rockfalls on the southern side generally have longer durations due to the smaller slope angle. The trajectory is greatly visible on the top left image for the whole event except for the detachment phase which is hidden in the shadow. The first movement is detected in snapshot a). From the seismic signals we can conclude that the detachment happened before, possibly associated with a small free fall causing a spiky signal. The rockfall subsequently tunnels through the small valley in between the rock formations. Snapshot b) corresponds to the time when the rockfall appears below the small valley. It then accelerates on the free plane of debris, resulting in the strongest impacts, detectable from the high amplitude peaks at time c). Several boulders can be detected at this point. The first block arrives at the bottom of the crater in snapshot d). The strong amplitudes at 5-15 Hz might be related to the stopping phase of this block superposed with signals generated by other blocks further above. Snapshot e) shows the last movement on the trajectory of the left branch. Scattered movements in the middle of the debris cone are visible afterwards, leading to small seismic amplitudes.

3) Rockfall on December 13, 2016

The last example is a rockfall on the southwestern crater slope (event **3** in Figure 2.10). Images and seismic signals are shown in Figure 2.13. The reconstructed trajectory shows nicely individual impacts. The location of detachment can be seen on snapshot a), which corresponds very well in time to the first amplitudes on the seismic traces. As for example 2), the rockfall trajectory is then hidden in a small valley, leading it towards the right in the image. Snapshot b) corresponds to the first appearance from behind the valley, approximately 20 s after the detachment. A strong peak is visible at 5-10 Hz at that time. Afterwards the rockfall accelerates and the seismic amplitudes become larger, reaching their maximum around time c). Snapshot d) confirms that the rockfall is composed from at least three boulders. The last movement is visible on snapshot e) when the third boulder is arriving at the crater bottom. Movements of smaller blocks which don't create a dust cloud might be going on afterwards. Interestingly, in comparison with the previous examples, the here discussed signal shows less high frequency content in the beginning of the event. Possible explanations might be linked to an absence of free fall after detachment and lower velocities. This leads to a decrease of the upper corner frequency f_c according to Hertz contact theory (see Table 4.2). Additionally, debris of former rockfalls below the position of detachment could act as cushion layer and prevent the generation of higher frequencies.

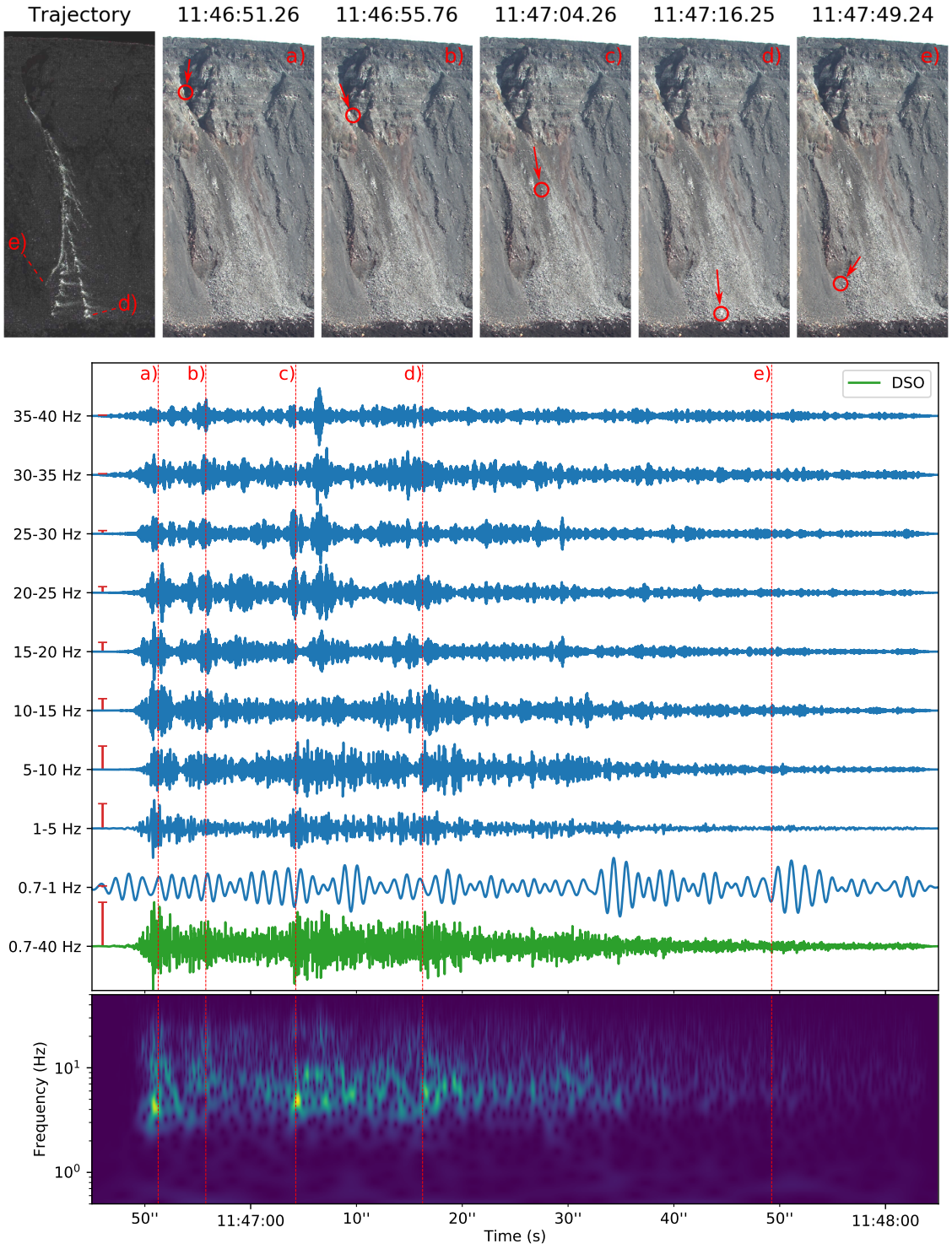

Figure 2.12 – Rockfall at southern wall of Dolomieu crater. For location see rockfall **2** in Figure 2.10. *Top:* Images taken from camera SFRC. Trajectory on the top left is reconstructed from differences between successive images during the whole rockfall duration. Circles mark event locations, while arrows indicate the direction of arrival. *Bottom:* Seismic signal at closest station DSO in different frequency bands with spectrogram representation below (using Stockwell transform). Vertical lines from a) to e) correspond to times of camera snapshots above. Note that seismic traces are normalized individually by their maximum. Relative amplitudes can be deduced from the spectrogram.

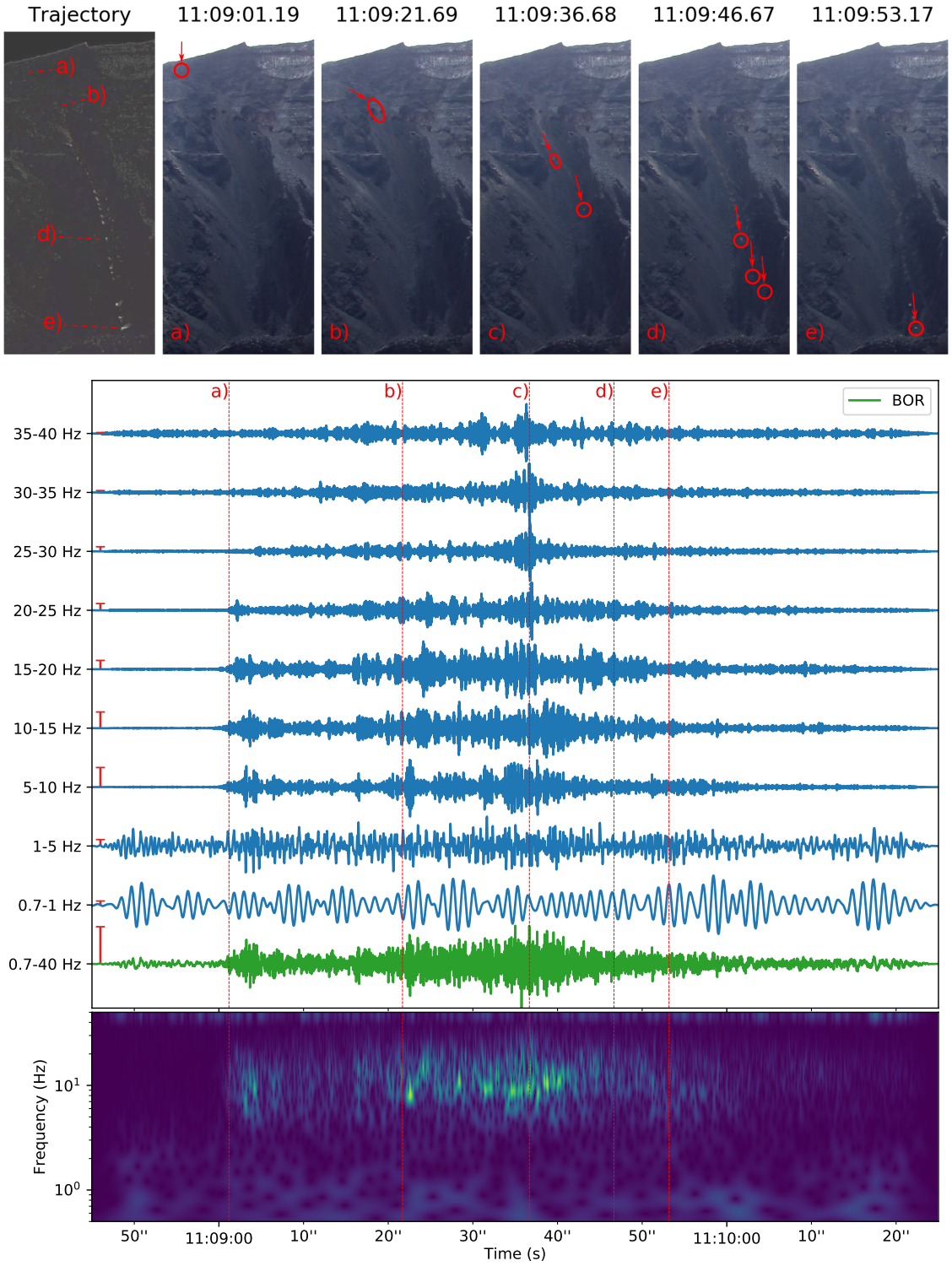

Figure 2.13 – Rockfall at southwestern wall of Dolomieu crater. For location see rockfall **3** in Figure 2.10. *Top:* Images taken from camera DOEC. Trajectory on the top left is reconstructed from differences between successive images during the whole rockfall duration. Circles mark event locations, while arrows indicate the direction of arrival. *Bottom:* Seismic signal at closest station BOR in different frequency bands with spectrogram representation below (using Stockwell transform). Vertical lines from a) to e) correspond to times of camera snapshots above. Note that seismic traces are normalized individually by their maximum. Relative amplitudes can be deduced from the spectrogram.

2.4 Appendices

2.4.1 SHALTOP simulations of granular mass

In order to relate seismic signals to landslide dynamics, it is crucial to understand the acting seismic source which is constituted by the forces imposed from the landslide on the ground. For this reason, simulations of granular mass on varying surface are conducted. Subsequently the resulting basal forces are analyzed. In the following we present SHALTOP simulations of a collapsing cylinder on a flat surface, as well as of a parabolic shaped mass released on a slope.

Column collapse on flat ground

The collapse of a column is a classical experiment to study the spreading of granular mass. Authors compare numerical models with laboratory experiments to understand the underlying physical processes (e.g. Mangeney-Castelnau et al., 2005). An example of a column collapse is illustrated in Figure 2.14.

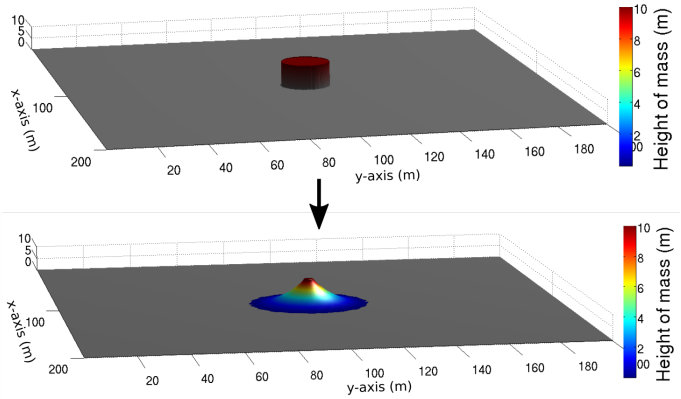

Figure 2.14 – Column collapse on flat surface.
Illustration of a granular mass of cylindrical shape collapsing on a flat surface. The collapse is shown for two times, corresponding to the initial geometry and to the time at which the collapse is reaching the central position.

In the here presented simulation we define a column of height 4 m and radius 5 m, the angle of internal friction is set to 10°. Cross-sections through the mass are shown in Figure 2.14 at different times. This allows to follow the evolution of the spreading mass regarding its shape. Additionally, the horizontal spreading velocity as a function of offset is shown.
We can observe how the collapse propagates from the edges of the column towards its center. The height of the center stays unchanged up to a time of around 1.8 s. After this time, the central height is decreasing until reaching a stable value of around 2 m after around 3.8 s. The horizontal velocity of the central position stays zero during the whole time as it only moves vertically. Highest horizontal velocity can be observed close to the forefront of the spreading mass.
The spreading history can similarly be derived from the spatial distribution of basal forces. A cross-section through the horizontal and vertical force field is shown in Figure 2.16 as a function of time. On top, the total force integrated over the whole surface is displayed.
The temporal evolution of the horizontal and vertical force field F_x and F_z show an initiation at zero time at the edges of the column (corresponding to $x = 90$ m and $x = 110$ m). As the collapse proceeds, the forces are propagating towards the center (located at $x = 100$ m)

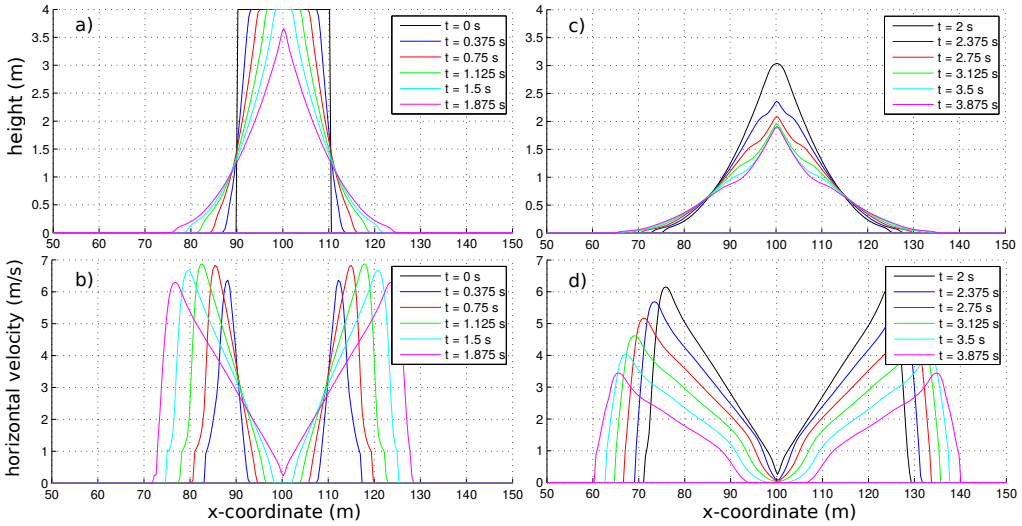

Figure 2.15 – Height profile and absolute horizontal velocity during a column collapse. Graphs on the top show the height profiles of the collapsing column at time steps of 0.375 s. Times until the central position starts to collapse (at around 1.8 s) are shown on the left hand side, times afterwards are shown on the right hand side. Beware of the unequal aspect ratio. The absolute horizontal velocity is shown below at the corresponding time steps.

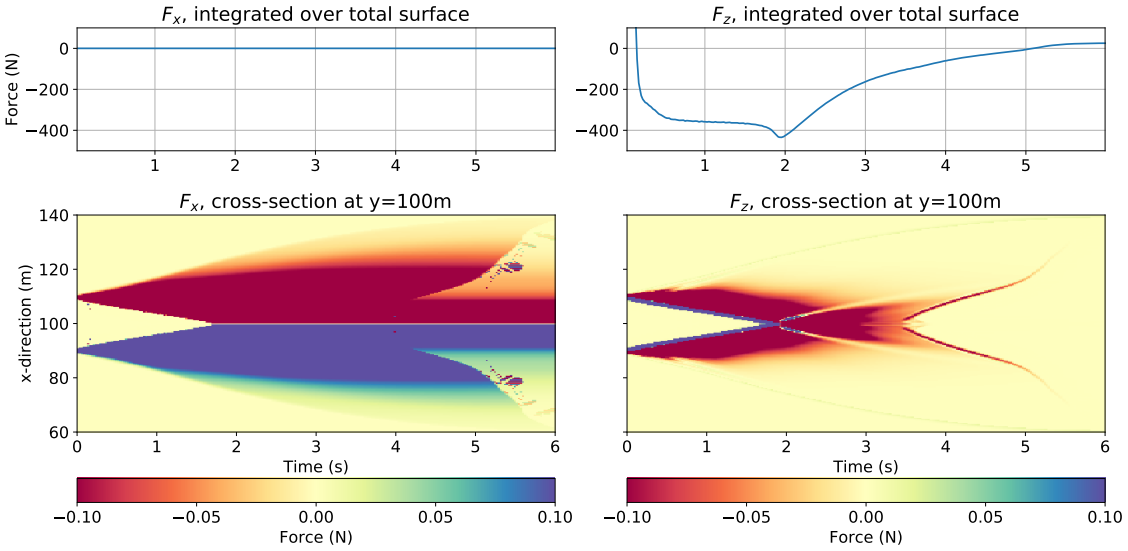

Figure 2.16 – Time evolution of forces generated by a column collapse. Total force integrated of the whole surface (*top*) and cross-section trough the spatially distributed force (*below*) for horizontal force F_x in x-direction (*left*) and vertical force F_z (*right*). Horizontal force in y-direction is not shown as it is equal to zero on the shown cross-section.

which is reached after around 1.8 s, just as observed above in the profiles and the velocities of the mass (see Figure 2.15). The horizontal forces (bottom left of Figure 2.16) show opposite polarity on either side of the center as they are related to the horizontal movement of the mass. At the precise position of the center (at $x = 100\,\mathrm{m}$), horizontal force F_x is always equal to zero. This corresponds to the observations of the horizontal velocity. The horizontal forces (right hand side of Figure 2.16), are predominantly negative due to the downwards movement of the mass. Only at the position where the column collapses we can

see a positive force, propagating towards the center. The upwards force can be explained by the removal of mass. At a time of around 1.8 s, when the center of the mass starts to collapse, we can observe a bright stripe (zero force) propagating outwards. Looking at the profiles after that time (right top of Figure 2.15), a wave can be detected traveling outwards. This wave of constant height can explain the stripe of zero force. In the end, starting at the center at around 3.5 s we can see a strong force propagating outwards. It is related to the stopping phase of the collapse, which starts at the center of the spreading mass. The high value might be caused numerically as high velocity gradients can be evoked during the stopping of the mass.
The total force integrated over the whole surface is zero in case of the horizontal force as the opposite polarized force vectors are canceling each other out. For the vertical force, we can remark a strong positive initial related to the sudden removal of mass at the sides of the column. As the collapse proceeds, the vertical mass movement results in a negative total force. As the collapse decelerates, the vertical force converges towards zero.
The global force-time functions are varying smoothly over time. This corresponds to the generation of low frequency seismic signals. Without any surface variations, the flow does not experience sudden (de-) accelerations which could cause higher frequencies. The only origin of higher frequencies are at the edges of the column, due to the sudden collapse.

2D parabola on exponentially shaped slope

To simulated the forces generated by the downslope movement of a landslide, a granular mass is released on top of a exponentially shaped slope. The geometry of the mass is defined to be parabolic with 20 m maximum height. The experiment is set up symmetrically along the y-axis with frictionless borders to avoid the lateral extension of the mass. This way, it can be compared to 2D analytical solutions which is omitted here. Figure 2.17 shows the mass before release and after sliding down the slope.

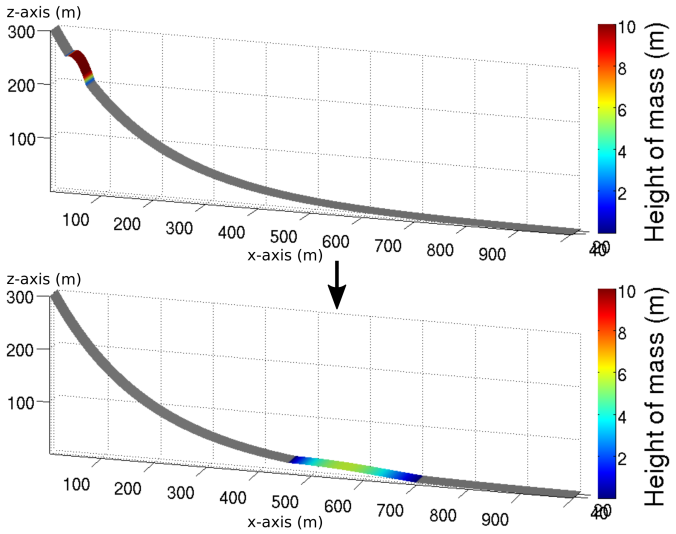

Figure 2.17 – Release of 2D parabola on exponentially shaped slope.
Granular mass of parabolic shape released on top of an exponentially shaped slope. The mass is shown at time $t = 0$ s before release, and at time $t = 30$ s after stopping.

The generated forces during the flow along the slope are illustrated in Figure 2.18. The horizontal force nicely shows the acceleration and deceleration of the sliding mass. Upon release, the mass accelerates and exerts a force on the ground in negative x-direction,

opposite to the direction of movement. At a position of around $x = 700\,\mathrm{m}$, the mass starts to decelerate. This corresponds to a time of around 12 s as can be seen in the evolution of the total force. The deceleration generates a force in positive x-direction, in direction of the movement, onto the ground. The mass stops it's movement at a time of around 26 m. The vertical force is positive in the beginning as mass is removed from its initial position. Afterwards, the force becomes positive pointing downwards. This is related to the vertical movement of the mass.

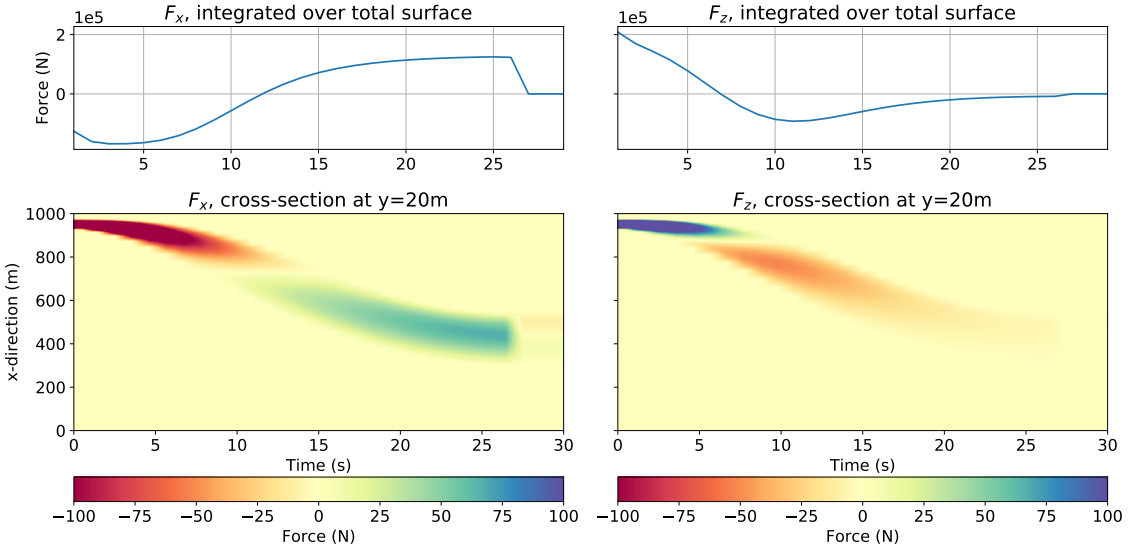

Figure 2.18 – Time evolution of forces generated by a granular mass sliding down a slope. Total force integrated of the whole surface (*top*) and cross-section trough the spatially distributed force (*below*) for horizontal force F_x in x-direction (*left*) and vertical force F_z (*right*). Horizontal force in y-direction is not shown as it is equal to zero on the shown cross-section.

As for the column collapse, a smooth global behavior of the forces can be observed. This corresponds to the generation of low frequency seismic waves. High frequencies are not generated as the slope is very smooth without small-scale topography variations and as the granular flow does not consider impacts of single boulders.

Chapter 3

Seismic wave propagation

The following chapter covers seismic wave propagation in a general way, i.e. unspecific to seismic waves generated by landslides. After introducing the fundamental wave equation, we will present the principals of the spectral element method (SEM) which will be used to numerically model seismic waves. We will discuss the benefits of this method and why it is suitable for the present thesis. Thereafter, some technical procedures will be detailed such as for example the implementation of topography onto the model domain.
The second part of this chapter deals with the seismic energy radiated by a surface load. The derivation of this theory will help afterwards to back-calculate the seismic energy generated by a landslide from a seismic signal recorded at a single seismometer.

3.1 Fundamentals

The propagation of seismic waves depends on the properties of the underlying medium. If stresses and strains obey a linear relationship, the medium is called *linear elastic*. The corresponding constitutive relation between stress tensor σ and strain tensor ε can be formulated as:

$$\sigma = C\varepsilon, \tag{3.1}$$

where C is often referred to as the stiffness tensor. In the most general case, the stiffness tensor contains 21 independent coefficients. However, due to symmetry axes in the medium, the number of independent coefficients reduces. A totally isotropic medium, i.e. a medium which is uniform in all directions, can be described by two independent variables, the bulk modulus and the shear modulus.
In this linearly elastic medium, the displacement $\mathbf{u}$ of each point can be described by the following equation of motion:

$$\rho\partial_{tt}^2\mathbf{u} = \nabla \cdot \sigma + \mathbf{f}, \tag{3.2}$$

where ρ is the material density and $\mathbf{f}$ is an external force.
Perfect elasticity is an idealized concept and does not exist in real materials. Instead, the

amplitudes of seismic waves attenuate with traveled distance due to a group of processes which we refer to as internal friction. The intrinsic attenuation of a given medium is quantified by dimensionless quality factors Q independently for P-wave and S-wave propagation. It can be defined as the relative energy loss per cycle (Aki and Richards, 2002):

$$\frac{1}{Q(\omega)} = -\frac{\Delta E/E}{2\pi}, \tag{3.3}$$

where E is the peak strain energy. Observations of Q show a roughly constant value over a wide frequency range (Komatitsch et al., 2005) which is why it is generally considered independent of frequency. However, this does not imply that the attenuation is not frequency dependent. Conversely, high frequency seismic waves experience stronger attenuation with distance as their cycle rate is higher. This can clearly be observed when describing wave amplitude A as a function of distance r, which decays exponentially from initial amplitude A_0 (Aki and Richards, 2002):

$$A(r) = A_0\, \mathrm{e}^{-\alpha r}, \text{ with } \alpha = \frac{f\pi}{Qc}, \tag{3.4}$$

where we defined the frequency dependent absorption coefficient $\alpha(f)$.

3.2 Numerical model based on the spectral element method (SEM)

The principle of the spectral element method (SEM) relies on subdivision of the model domain into smaller elements. By this, the complexity of a given problem is broken down into simpler subproblems. Regarding for instance seismic wave propagation in a heterogeneous medium, the subdivision of the domain can be of high utility: sharp material interfaces don't have to be resolved by fine discretization but can simply be placed at element boundaries. SEM is a a special case of the finite element method (FEM). The solution is approximated in each element using Lagrange polynomials whose interpolation nodes lie on the so-called *Gauss-Lobatto-Legendre* (GLL) points. This leads to *spectral* convergence of the method which is faster than for example using piecewise linear basis functions.

3.2.1 Developing the formalism of SEM

In the following the underlying formalism of SEM will be introduced briefly. For a more detailed review see for example Chaljub et al. (2007) or Chapter 7 in Igel (2017).
To introduce the spectral element method, we assume the 1D elastic wave equation which describes waves propagation in x-direction with transverse particle motion governed by shear modulus $\mu(x)$. The wave is initialized by an external force $f(x,t)$ perpendicular to the direction of propagation. On a domain D of length L with space variable $x \in D = [0, L]$, wave equation 3.2 then reduces to:

$$\rho\, \partial_{tt}^2\, u(x,t) = \partial_x \left[\mu(x)\, \partial_x\, u(x,t)\right] + f(x,t), \tag{3.5}$$

with stress-free boundary conditions:

$$\mu\,\partial_x u(x,t)\Big|_{x=0,L} = 0. \tag{3.6}$$

Rather than solving directly for the displacement field u, the spectral element method approximates the solution by summing over a finite number of basis functions $\varphi_i \to \varphi_i(x)$ which we will choose later. Summing over N_p basis functions, solution $\bar{u}$ is approximated by:

$$u(x,t) \approx \bar{u}(x,t) = \sum_{i=1}^{N_p} u_i(t)\varphi_i(x), \tag{3.7}$$

with time-dependent expansion coefficients u_i. Their name is motivated by the fact that these coefficients will correspond exactly to the value of displacement u at a given grid point x_j. This results from the choice of basis functions as we will see later.

The weak form of the problem

In order to find coefficients u_i, wave equation 3.5 is transformed into weak (or variational) form. This allows to explore the solution space with the help of time-independent test functions $v \to v(x)$ with square-integrable derivatives which represent all admissible displacements. Then, we define a function to find solution $\bar{u}$ such that for all admissible test functions $v(x)$:

$$\int_D v\,\rho\,\partial_{tt}^2\bar{u}\,\mathrm{d}x - \int_D v\,\partial_x(\mu\,\partial_x\bar{u})\,\mathrm{d}x = \int_D v\,f\,\mathrm{d}x, \tag{3.8}$$

where integration is carried over the whole physical domain D. Through integration by parts we can reduce the spatial derivative to first order. Using boundary conditions of equation 3.6 leads to

$$\int_D v\,\rho\,\partial_{tt}^2\bar{u}\,\mathrm{d}x + \int_D \mu\,\partial_x v\;\partial_x\bar{u}\,\mathrm{d}x = \int_D v\,f\,\mathrm{d}x. \tag{3.9}$$

Note here that free surface boundary conditions are implicitly fulfilled which is a big advantage of the method for example when it comes to geophysical applications in which the Earth's surface is involved. To illustrate this advantage we can draw a comparison with the finite difference method. To impose a stress free boundary in the latter method, grid points outside the model domain are required.
It is very convenient that the test functions are chosen to be identical to the basis functions used before in expansion 3.7. This is known as the Galerkin principle and is beneficial for both solving the system which is becoming symmetric and the precision of the numerical approximation. Thus, by replacing $v \to \varphi_j(x)$ and combining equations 3.7 and 3.9 we get following linear system of equations, valid for any φ_j:

$$\sum_{i=1}^{N_p}\Big[\partial_{tt}^2 u_i \underbrace{\int_D \rho\,\varphi_j\varphi_i\mathrm{d}x}_{M_{ji}}\Big] + \sum_{i=1}^{N_p}\Big[u_i \underbrace{\int_D \mu\,\partial_x\varphi_j\;\partial_x\varphi_i\,\mathrm{d}x}_{K_{ji}}\Big] = \int_D \varphi_j\,f\,\mathrm{d}x. \tag{3.10}$$

M_{ji} and K_{ji} are elements of the so called mass matrix $\mathbf{M}$ and stiffness matrix $\mathbf{K}$, respectively. Written in matrix-vector form:

$$\mathbf{M}\partial_{tt}^2\mathbf{u}(t) + \mathbf{K}\mathbf{u}(t) = \mathbf{f}(t), \tag{3.11}$$

After discretizing the time period of interest in time steps Δt, equation 3.11 can be solved for displacement $u(t+\Delta t)$ by using an adequate numerical integration scheme such as the Newmark method (Festa and Vilotte, 2005; Chaljub et al., 2007). Before that, mass matrix $\mathbf{M}$ has to be inverted. However, through the right choice of the numerical integration scheme in combination with the test function basis, the mass matrix will become diagonal and thus trivial to invert.

From global to local formalism

Up to this point the formalism follows a global approach. The domain is now subdivided into smaller elements which will increase the flexibility of the method. This is realized in straightforward manner by carrying out the integration over each subdomain D_e and subsequently summing over all n_e subdomains:

$$\sum_{i=1}^{N_p}\left[\partial_{tt}^2 u_i \sum_{e=1}^{n_e}\int_{D_e}\rho\,\varphi_j\varphi_i \mathrm{d}x\right] + \sum_{i=1}^{N_p}\left[u_i\sum_{e=1}^{n_e}\int_{D_e}\mu\,\partial_x\varphi_j\;\partial_x\varphi_i\,\mathrm{d}x\right] = \sum_{e=1}^{n_e}\int_{D_e}\varphi_j^e\,f\,\mathrm{d}x. \tag{3.12}$$

By defining local basis functions φ_i^e within each subdomain D_e, the sum over all subdomains drops and we can calculate solution u_i^e within each subdomain:

$$\sum_{i=1}^{N_p}\partial_{tt}^2 u_i^e\int_{D_e}\rho\,\varphi_j^e\varphi_i^e\mathrm{d}x + \sum_{i=1}^{N_p}u_i^e\int_{D_e}\mu\,\partial_x\varphi_j^e\;\partial_x\varphi_i^e\,\mathrm{d}x = \int_{D_e}\varphi_j^e\,f\,\mathrm{d}x. \tag{3.13}$$

It is convenient to transfer the global coordinates $x \in D$ of each subdomain D_e to local coordinates on a reference interval $\xi \in [-1,1]$. Considering an arbitrary function $f(x)$, the coordinate transformation from $x \to \xi$ is realized by a change of variables as follows:

$$\int_{D_e} f(x)\,\mathrm{d}x = \int_{-1}^{1} f(\xi)J(\xi)\,\mathrm{d}\xi, \quad \text{with Jacobian } J = \frac{\mathrm{d}x}{\mathrm{d}\xi}. \tag{3.14}$$

This mapping operation can become very complex depending on the shape of the elements. Nevertheless, it facilitates the operations under the integral which become independent of the global coordinates. Then for example, changing from from linear elements to higher order elements as presented in section 3.2.5 is just a matter of changing the Jacobian.

The choice of basis functions

We will now define the basis functions as well as the positions of the grid points on which the solution will be interpolated. The choice falls on Lagrange polynomials l_i defined on the so-called *Gauss-Lobatto-Legendre* (GLL) points x_j.
The Lagrange polynomials are constructed such that $l_i(x_j) = \delta_{ij}$ where δ_{ij} is the Kronecker

symbol. This can be observed in Figure 3.1 which shows the $N_p = N + 1$ Lagrange polynomials of order $N = 6$, defined on the $N + 1$ GLL points. It is also noteworthy that the GLL points are not equidistant but move closer to each other towards the boundaries. This configuration reduces spurious oscillations of the interpolation which are also known as Runge's phenomenon.

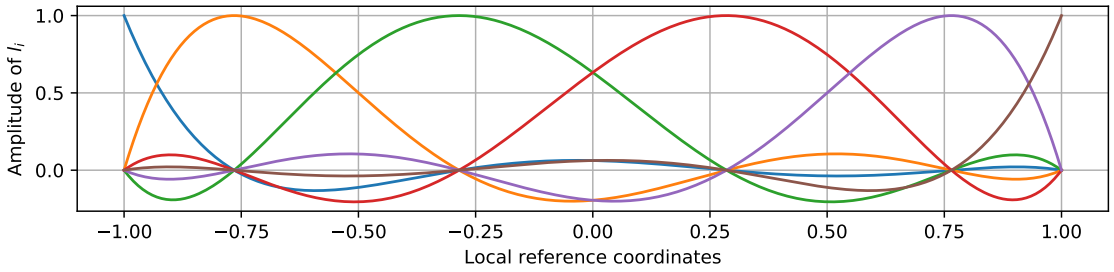

Figure 3.1 – Lagrange Polynomials. The $N + 1$ Lagrange polynomials l_i of order $N = 5$ defined on the $N + 1$ GLL points x_j. The GLL points are located at the zero crossings of the polynomials. Note that $l_i(x_j) = \delta_{ij}$ for $i, j = 1, \ldots, N + 1$.

Approximation of spatial integration

The task now is to find a way in order to carry out the integration over the subdomains numerically so that the introduced error is minimal. This is achieved by using the so-called *Gauss-Lobatto-Legendre* quadrature with Lagrange polynomials defined on GLL points as before. Using the GLL points in the quadrature leads to the so-called spectral convergence of the method with an error in the order $\mathcal{O}(2N - 1)$.
For an arbitrary function $f(x)$ integrated over interval $[-1, 1]$ the quadrature gives:

$$\int_{-1}^{1} f(x)\,\mathrm{d}x \approx \int_{-1}^{1} \sum_{i=1}^{N+1} f(x_i) l_i(x)\,\mathrm{d}x = \sum_{i=1}^{N+1} f(x_i) \underbrace{\int_{-1}^{1} l_i(x)\,\mathrm{d}x}_{w_i}, \tag{3.15}$$

where the integration weights w_i can be calculated analytically.
Approximating the integrals in equation 3.13 by the quadrature and introducing the Lagrange polynomials $\varphi_i = l_i$ leads to the final system of equations for each subdomain $e = 1, ..., n_e$:

$$\sum_{i=1}^{N+1} M_{ji}^e \partial_{tt}^2 u_i^e + \sum_{i=1}^{N+1} K_{ji}^e u_i^e = f_j^e, \tag{3.16}$$

with

$$\begin{aligned} M_{ji}^e &= w_j \rho \delta_{ji}, \\ K_{ji}^e &= \sum_{k=1}^{N+1} w_k \mu \partial_x l_j \partial_x l_i, \\ f_j^e &= w_j f. \end{aligned}$$

The equations for all elements can be assembled in a global system and solved with an appropriate time stepping scheme as mentioned before. The solution is continuous across element interfaces and the boundary of the computational domain is stress-free. In order to simulate an open domain we have to implement absorbing boundary conditions which we will introduce hereafter.

Absorbing boundaries (PML)

Apart from the free surface boundary, we want to simulate seismic wave propagation on a seemingly infinite model without artificially introduced boundary effects. However, the computational domain has to be truncated outside the area of interest. To do so we apply open boundaries by so-called *Perfectly Matched Layers* (PMLs). The design of these absorbing layers provide an exponential decay of the wave amplitude independent of the frequency within the PML without reflection of energy at its interface. A detailed description on the implementation in SEM can be found in Festa and Vilotte (2005).
The size of the PML has to be wide enough to accommodate big wavelength while its grid point distances have to be small enough to resolve small wavelength (see CFL criterion in section 3.2.3). This has to be carefully considered if for example the wavelength changes with depth due to the velocity model (note that in the here used SEM version, the width of the PML has to be constant with depth). To absorb all present wavelength, either a wide PML with increased polynomial degree is applied or several adjacent layers of PML are implemented.

3.2.2 Source input: body force and surface traction

The seismic source can be implemented in SEM as an external force $\mathbf{f}$ (see equation 3.2). In a 3D medium, a point force $f_i(\mathbf{x}, t)$ at location $\mathbf{x} = \xi$, pointing in direction of the x_n-axis, is described as (Aki and Richards, 2002):

$$f_i(\mathbf{x}, t) = A\psi(t)\delta(\mathbf{x} - \xi)\delta_{in}, \quad \text{for } i = 1, 2, 3, \tag{3.17}$$

where A is the amplitude of the force, $\psi(t)$ is an arbitrary force-time function, $\delta(\mathbf{x} - \xi)$ the 3D Dirac delta function and δ_{in} the Kronecker delta for directionality.
Other than that, seismic sources can also be implemented on the boundaries of the domain. This is convenient to describe surface sources as for example the force-field generated by a landslide during its flow along topography. For this, the stress-free boundary condition defined in 3.6 has to be modified. Introducing a non-zero boundary condition evokes an extra term during the integration by parts, going from equation 3.8 to equation 3.9. This way, time and space dependent surface tractions can be defined.
In the present study we primarily studied the wave propagation from point sources. The force-time function which was used to the describe these point sources is introduced in the following.

The Ricker wavelet

In order to simulate the seismic impulse response of a given body, known as Green's function, the force-time function ψ should be a Dirac delta function in time. In practice this is not possible as the numerical method cannot resolve the infinite frequency content. As an alternative, a so-called wavelet of finite frequency is used. In the present work we use the Ricker wavelet (also known as Mexican hat wavelet) which has zero mean and a Gaussian shaped frequency content. For a dominant frequency f_{dom}, force-time function ψ becomes (Wang, 2015):

$$\psi(t) = \left(1 - 2\left(\pi f_{\mathrm{dom}}(t-\tau)\right)^2\right) e^{-\left(\pi f_{\mathrm{dom}}(t-\tau)\right)^2}, \tag{3.18}$$

with time shift τ. Figure 3.2 illustrates the Ricker wavelet in both time and frequency domain.

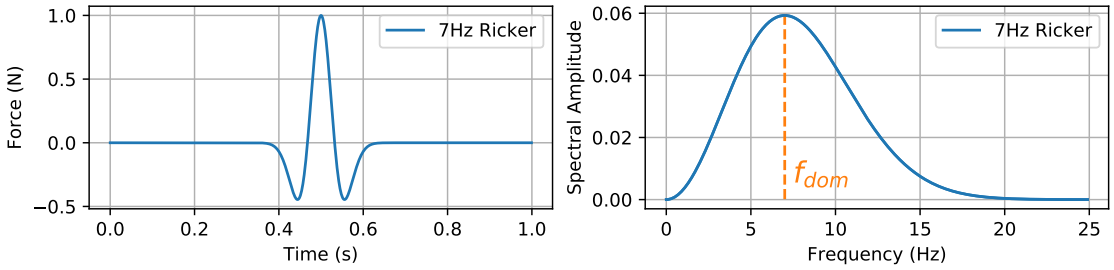

Figure 3.2 – Ricker wavelet. Ricker wavelet with dominant frequency $f_{\mathrm{dom}} = 7$ Hz and time shift $\tau = 0.5$ s in the time domain (*left*) and frequency domain (*right*).

Some wavelets are constructed in order to contain flat frequency plateaus. This can be convenient for spectral analyses but causes oscillations in the time domain. The Ricker wavelet on the contrary has a simple shape which makes interpretations in the time domain less complex.

3.2.3 Time step, spatial resolution and convergence

The time stepping used in the SEM formulation is carried out by an explicit Newmark scheme (Newmark, 1959; Hughes, 1987). This scheme is conditionally stable and time step Δt is subject to the *Courant-Friedrichs-Lewy* (CFL) criterion (Courant et al., 1928):

$$\Delta t \leq C \left(\frac{\Delta x}{c}\right)_{\mathrm{min}}, \tag{3.19}$$

where Δx is the distance in between adjacent GLL points, c is the seismic wave speed and C the Courant number which is < 0.5 for a stable scheme depending on the polynomial order and the mesh geometry (Chaljub et al., 2007).
The spatial resolution is likewise determined by both the element size and the polynomial degree. In practice, the element side length must not exceed the minimum seismic wavelength when using a polynomial degree of 5, corresponding to 6 GLL points per element.

This rule of thumb can be compromised by medium heterogeneities and surface topography.

Simulation of a wave field from a vertical point force

The wave field is simulated on a flat homogeneous domain in order to illustrate the convergence of the method. As a source, a Ricker wavelet of dominant frequency $f_{\mathrm{dom}} = 4\,\mathrm{Hz}$ is used. The upper limit of its frequency content can be estimated by $f_{\mathrm{max}} \approx 4\, f_{\mathrm{dom}} = 12\,\mathrm{Hz}$ (compare with Figure 3.2). The model domain is defined by S-wave and P-wave speeds of $v_S = 700\,\mathrm{m.s}^{-1}$ and $v_P = 1000\,\mathrm{m.s}^{-1}$, respectively. Thus, the minimum wave speed is $v_{\mathrm{min}} = v_S = 700\,\mathrm{m.s}^{-1}$. This leads to a minimum wavelength of $\lambda_{\mathrm{min}} = v_{\mathrm{min}}/f_{\mathrm{max}} \approx 60\,\mathrm{m}$. The polynomial order of the elements is 5 (6 GLL points). At this order, as mentioned above, the element size must not exceed the minimum wavelength. This means, that the side length of the elements should be smaller than 60 m.
Figure 3.3 shows snapshots at two different times of the simulated wave field generated by a vertical point force at the surface. Snapshots are shown for models with element size of 100 m, 80 m, and 40 m.

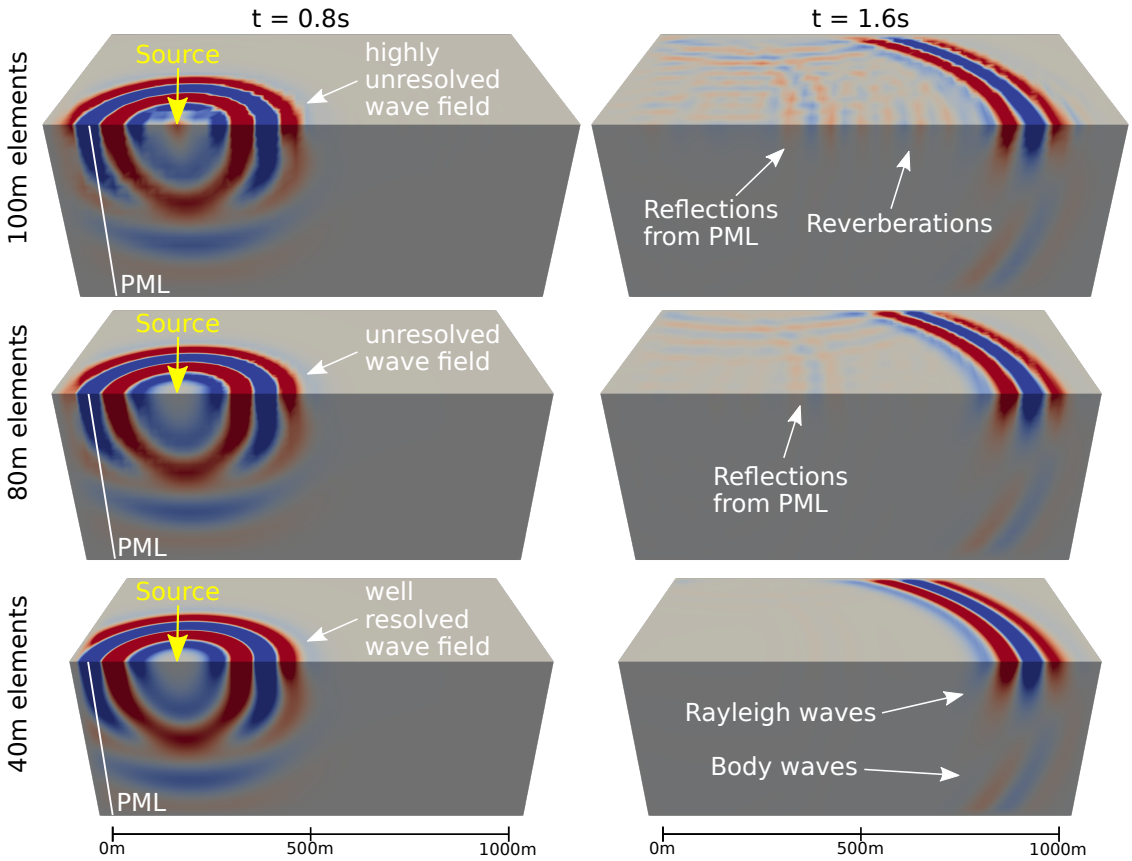

Figure 3.3 – Snapshots of wave field on models with different element sizes. Snapshots of the simulated wave field at time $t = 0.8\,\mathrm{s}$ (*left*) and $t = 1.6\,\mathrm{s}$ (*right*) on models with element size of 100 m (*top*), 80 m (*middle*), and 40 m (*bottom*). The snapshots show a cross-section through the domain which crosses the source location. PMLs of one element width are attached to the sides and bottom of the domain (indicated on the left by a white line). Wave speed of S-wave and P-wave are $v_S = 700\,\mathrm{m.s}^{-1}$ and $v_P = 1000\,\mathrm{m.s}^{-1}$, respectively. The wave field is generated by a vertical point force represented by a Ricker wavelet of 4 Hz dominant frequency. As Rayleigh wave speed is similar to v_S, the dominant wavelength of the visible Rayleigh waves is 175 m. Amplitudes correspond to vertical ground velocity.

We can observe that the resolution of the wave field gradually improves with decreasing element size. Furthermore, strong reverberations can be detected in the case of 100 m elements, following the leading wave front. Other than that, we can also see reflection from the boundary in the case of 100 m and 80 m elements. The width of the absorbing boundary layer is equal to one element. In case of the larger elements, the wave field is badly resolved in the PML layer and can therefore not be fully absorbed. This leads to the observed reflections.
To show the convergence with decreasing element size, the seismic signal is recorded at a horizontal position of 500 m (300 m away from the source). Synthetic seismograms and their frequency spectrum are shown in Figure 3.4 for all models.

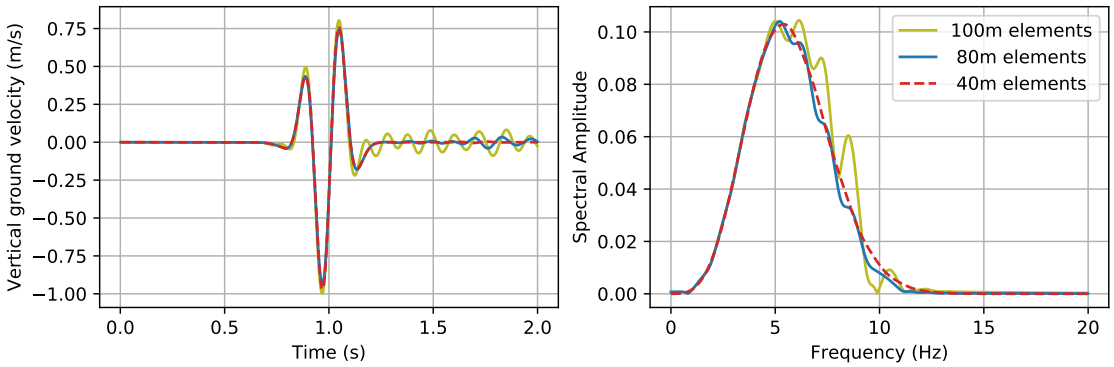

Figure 3.4 – Convergence of seismograms with decreasing element size. Seismograms (*left*) and corresponding frequency spectrum (*right*) recorded on models with different element sizes, corresponding to the models shown in Figure 3.3. Seismograms are recorded at the surface in a distance of 300 m from the source.

Looking at the seismograms in Figure 3.4, we can observe entailed reverberations in the case of 100 m elements. Reducing the element size to 80 m, the reverberations reduce and the signal fits better the signal from 40 m elements. However, a spurious signal can be observed towards the end of the recording. With the help of the snapshots above, we can relate this signal to the reflections from the boundaries. For the 40 m elements, no reverberations are left and we can assume that the solution has converged (here without proof by comparison with even smaller elements).
This can similarly be observed in the frequency domain. While the spectrum corresponding to the 100 m elements show large fluctuations, the spectrum from the 80 m elements converges towards the solution from the 40 m elements. Interesting to note is that the spectra up to this point in time are identical below 5 Hz, which corresponds to wavelengths larger than 140 m. This shows that all models are able to resolve these low frequencies.

3.2.4 Implementation of intrinsic attenuation

Intrinsic attenuation causes exponentially decaying wave amplitude as described in equation 3.4. In order to mimic numerically such an attenuating material, SEM introduces a series of standard linear solids (SLS), a principle which was proposed by Liu et al. (1976). Each of these solids is characterized by a single relaxation mechanism and through superposition a quality factor Q is obtained which is nearly constant over a certain frequency range. Figure 3.5 compares the resulting quality factor Q when using different numbers of

SLSs. In the simulations hereafter we will use 5 solids which we consider to be sufficient in order to obtain a nearly constant Q over the frequency range of interest ($\sim 1 - 20\,\mathrm{Hz}$).

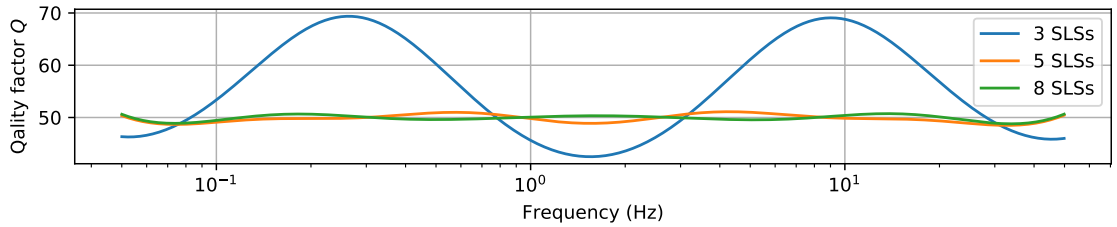

Figure 3.5 – Model for quality factor Q. An attenuating material of quality factor $Q = 50$ over a frequency range from 0.05 to 50 Hz was mimicked using 3, 5 and 8 standard linear solids (SLS), respectively. While 3 SLSs result in deviations up to 40%, 5 SLSs reach a nearly constant value. Improvements using 8 SLSs are negligible and thus not worthwhile the additional computational effort.

3.2.5 Implementation of topography

Surface topography is imposed onto the meshed domain by vertically adjusting the positions of grid points. In other words, the elements are stretched or compressed vertically around the mean value of elevation. Figure 3.6 illustrates this procedure. Grid points on the surface are shifted so that they represent the real elevation of the topography, while deformation below decreases successively towards a horizontal reference layer (here at the bottom of the domain).

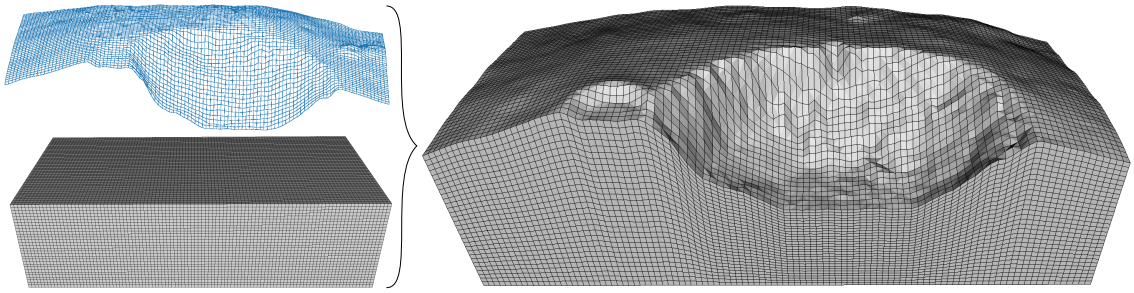

Figure 3.6 – Implementation of topography. *Top left:* Representation of digital elevation model (DEM) of 20 m resolution from a cross-section through Dolomieu crater (La Réunion). *Bottom left:* Rectangular mesh with cubic elements of 20 m side length. *Right:* Mesh with imposed topography through successive vertical deformation of cubic elements.

It is important to be aware that the deformation of elements modifies the distance of collocation points dependent on how many elements are used to accommodate the topography. This has to be considered carefully as it can affect the numerical scheme. On the one hand, the numerical time step decreases with the grid point distance (see equation 3.19) causing more expensive computations. On the other hand, increased distances can threaten the convergence of the method according to the polynomial degree and the simulated wavelength.
Figure 3.7 shows a first example of simulated wave propagation on a homogeneous model with topography. For this example, a part of Dolomieu crater topography was imposed on

the model. A vertical point force (4 Hz Ricker wavelet) acts at the bottom of the crater. Topography disturbs drastically the symmetric wave propagation observed on the model with flat surface (see Figure 3.3). For example, surface waves arriving at the rim of the crater are partly transmitted and reflected and continue traveling as surface waves in opposite directions. Also, body waves originating from the bottom of the crater travel directly to the the sides of the domain and can be detected at surface stations E to I.

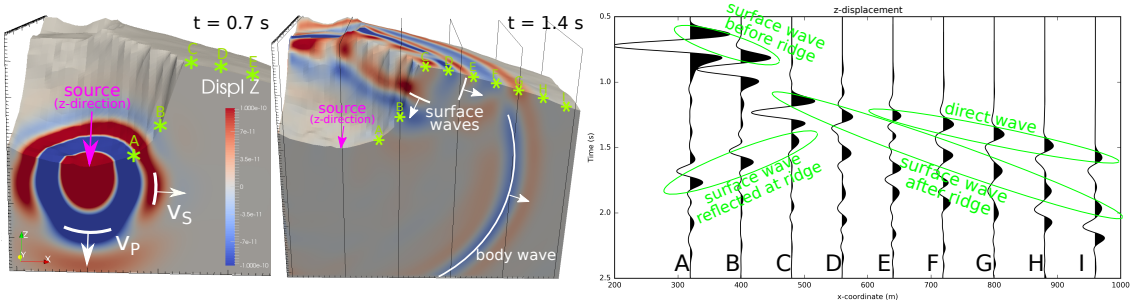

Figure 3.7 – Wave propagation on homogeneous model with topography. The vertical displacement field is shown in snapshots at time $t = 0.7$ s and $t = 1.4$ s (*left*). The seismic source is described by a 4 Hz Ricker wavelet which act as a point force on the bottom of the crater. The model is homogeneous with P-wave velocity $v_P = 1000\,\mathrm{m.s^{-1}}$, S-wave velocity $v_S = 700\,\mathrm{m.s^{-1}}$ and density $\rho = 2000\,\mathrm{kg.m^{-3}}$. *Right*: Synthetic seismograms recorded at stations marked by green stars in the snapshots on the left. Introduction of topography increases the complexity of the wave field (compare with wave field on flat domain shown in Figure 3.3).

The resolution of the model topography does not only depend on the available DEM of the study site but also on the element configuration in the meshed domain. In the next paragraph we will discuss the influence of topography resolution on synthetic seismograms by changing the element size in the mesh.
Generally, in order to not lose resolution, the element size should not be larger than the spatial discretization of the imposed DEM. However, using a mesh of small elements can lead to computationally expansive simulations. For this reason we will introduce thereafter two approaches which can increase topographic resolution while avoiding expensive mesh configurations. Concretely spoken, we will present higher order elements and the application of a buffer layer.

Topography resolution

As already indicated before, the topography resolution is both dependent on the available DEM file and the element size. Using linear elements, i.e. elements with flat faces, the maximum resolution is determined by the element side length (this will change when using higher order elements as discussed in the next paragraph). Figure 3.8 illustrates this issue by comparing meshes of different elements sizes.
As the seismic wave field interacts with the free surface, a poor representation of topography will obviously affect the simulated seismograms. In order to investigate this influence, we resume the previous simulation example on a homogeneous model with topography (see Figure 3.7). This time we build three models using element sizes of 40 m, 20 m and 10 m, respectively. The underlying topography resolution is 20 m. Top graph of Figure 3.9

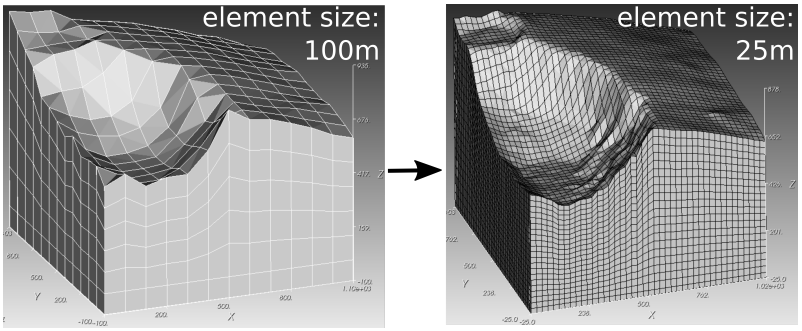

Figure 3.8 – Dependency of topography resolution on element size.
Decreasing the element size in the meshed domain from 100 m (*left*) to 25 m (*right*) results in a more detailed topography representation.

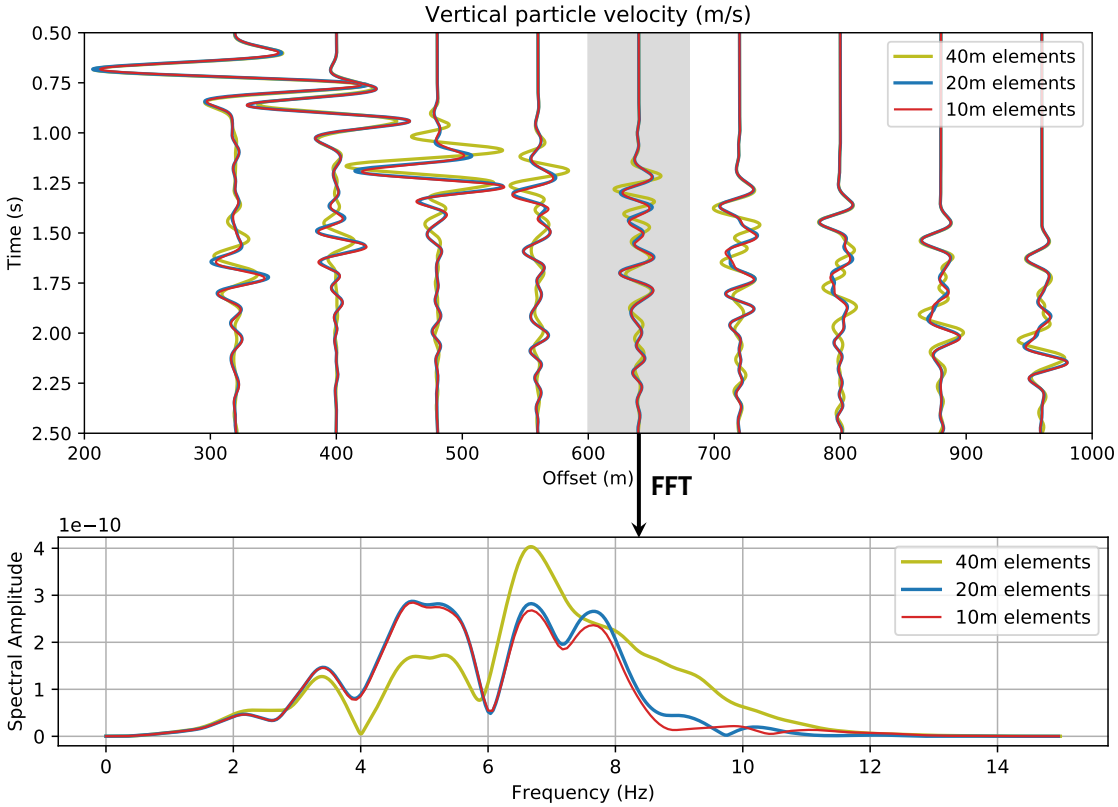

Figure 3.9 – Influence of topography resolution on synthetic seismograms. Comparison between models using element sizes of 40 m, 20 m and 10 m, respectively, which determines topography resolution (see Figure 3.8). *Top:* Seismograms recorded at station A to I marked with green stars in Figure 3.7. Differences between the 2 models with smaller elements are vanishing. *Bottom:* Spectra of seismograms from one station. Differences between the 2 models with smaller elements appear especially in the higher frequency range (above $\sim$ 7 Hz).

compares the simulated traces of each model. While models with 20 m and 10 m elements result in similar seismograms, recordings from model with 40 m elements are quite distinct. Yet, differences exist between the models with smaller elements. For a more detailed investigation, we compare spectral contents from one of the stations (bottom graph of Figure 3.9). Comparing the 2 models with small elements, we can in fact detect that the main differences arise from the higher frequency content, i.e. above $\sim$ 7 Hz. This corresponds to wavelengths below 100 m, given $v_S = 700\,\mathrm{m.s^{-1}}$ and assuming mainly S-waves and surface waves (see Figure 3.3). This means that changes of topography resolution up to 10 times smaller than the seismic wavelength can still affect the wave field. Similar observations were made by Ma et al. (2007).

Higher order elements

Up to now, the topography is imposed on the mesh by shifting the grid points at the corners of each element and determining the position of internal grid points accordingly by linear interpolation. This means that the surface of each element is flat and that sharp edges can be present at the interfaces of elements (see top of Figure 3.11). In other words, the derivative of the topography is discontinuous. This is not a problem for the numerical scheme but it introduces an error, in particular when the element size is bigger than the available resolution of the DEM.
A way to increase accuracy of the imposed topography without decreasing the element size is to use nonlinear elements. This is realized by going from linear interpolation in between the corners of the elements, to a higher degree of interpolation using additional control points. Figure 3.10 illustrates a 1^{st} order element with 8 control points and a 2^{nd} order element with 27 control points. In the latter configuration, a polynomial interpolation of 2^{nd} order can be used to map the solution from the local reference coordinates to the physical coordinates.

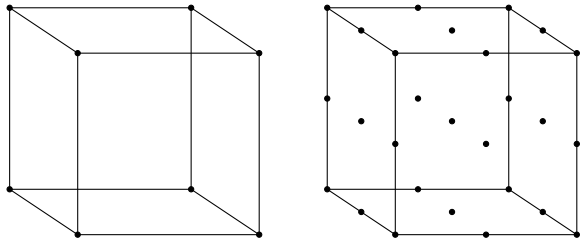

Figure 3.10 – From 8 to 27 control points per element.
Left: Element with 8 control points at each corner. *Right:* Element with 27 control points, which allow a curvilinear deformation of the element.

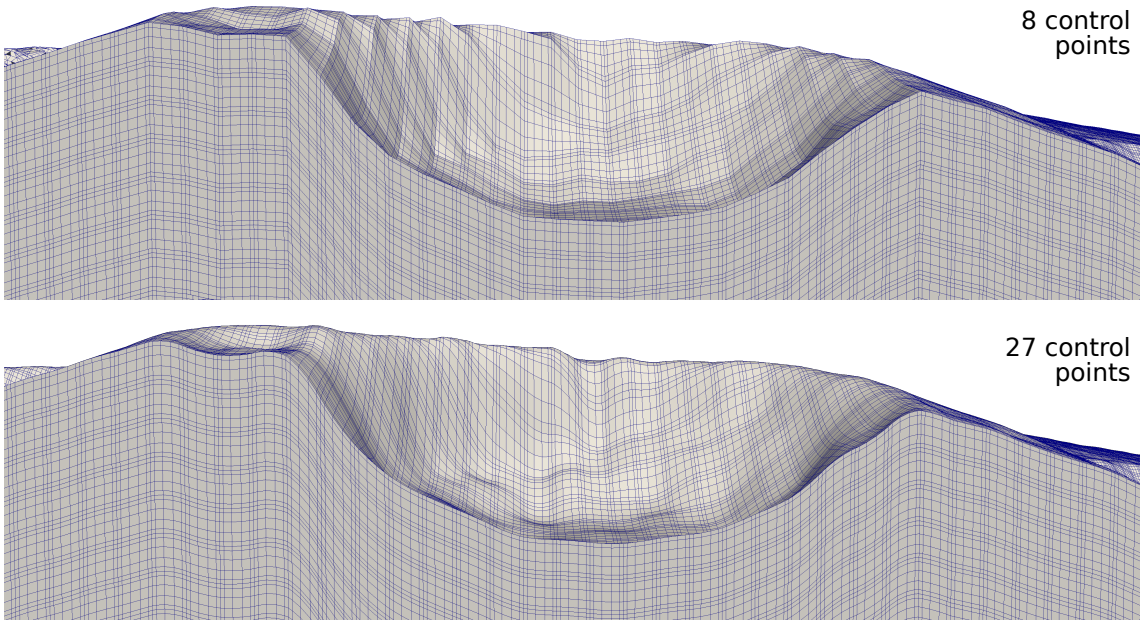

Figure 3.11 – Topography on meshes with elements of 1^{st} and 2^{nd} order. Cross-section of computational domains with imposed topography of Dolomieu crater. The blue lines run through the GLL points ($6 \times 6 \times 6$ GLL points per element). Element are of 30 m side length. Their boundaries can be identified by the densification of lines. *Top:* Mesh containing 1^{st} order elements with 8 control points. The surface of the elements is flat and sharp edges at the element boundaries are observable. *Bottom:* Mesh containing 2^{nd} order elements with 27 control points. Elements are curvilinear which results in a globally smooth topography.

In order to observe the difference between 1st and 2nd order elements, the topography of Dolomieu crater is imposed on a domain with cubic elements of 30 m side length. Figure 3.11 compares the two implementations. While the topography is assembled of flat faces with sharp edges when using linear elements, the utilization of curvilinear elements results in a globally smooth mesh.
Smoothly varying topographies can be implemented very efficiently using curvilinear elements. This is shown in Figure 3.12, where the seismic wave propagation is modeled on a domain with a Gaussian topography. Synthetic seismograms are shown in Figure 3.13. It can be observed, that signals are identical between meshes using 2nd order elements of 60 m side length and meshes using linear elements of 20 m side length. This has huge consequences on the computational effort. Decreasing the element size by a factor of 3 increases the number of elements by a factor of 27 and accordingly the computational cost.

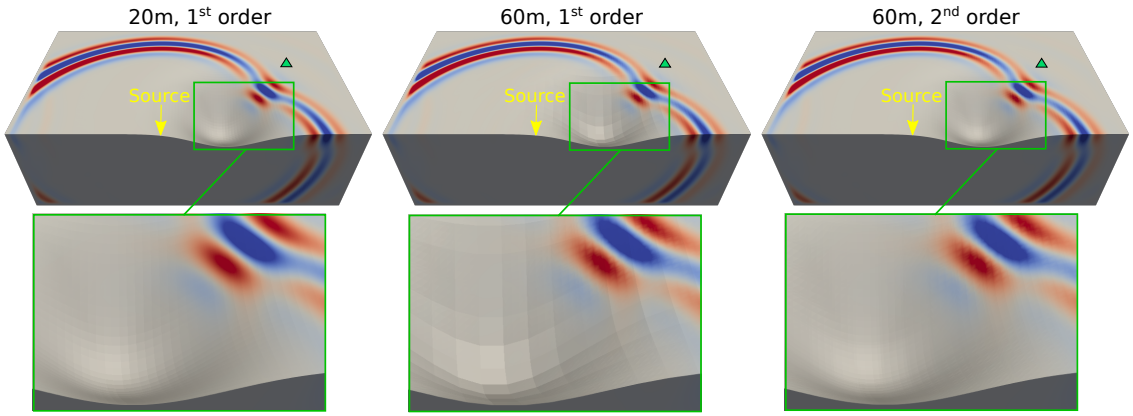

Figure 3.12 – Seismic wave propagation on Gaussian topography. Snapshot of the wave field taken at time $t = 1.6$ s for models with 20 m linear elements (*left*), 60 m linear elements (*middle*), and 60 m linear elements (*right*). Differences in the resulting topography can be seen in the zoomed insets: 20 m linear elements show a fine grid of flat faces which lead to a smooth topography. The flat faces become more obvious for 60 m linear elements. Finally, curvilinear elements are able to reproduce almost perfectly the smooth Gaussian shape. The green triangle marks the recording position of the seismograms in Figure 3.3.

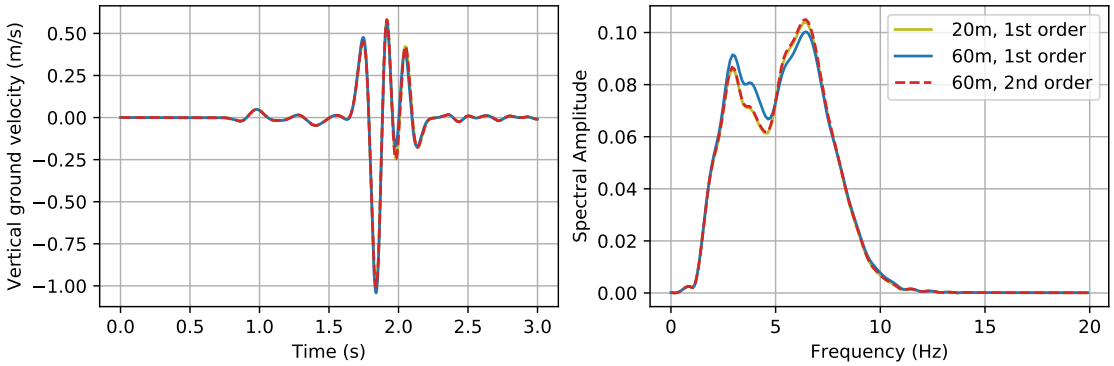

Figure 3.13 – Seismograms measured on linear and curvilinear elements. Seismograms (*left*) and corresponding frequency spectrum (*right*) recorded on models shown in Figure 3.12 at the position marked by a green trianble. Even though the signal look almost identical in the time domain, differences are noticeable in the frequency domain. The 60 m 2nd order elements are able to reproduce the solution from the 20 m linear elements.

However, the 2nd order elements, cannot represent topography variations of wavelength

smaller than twice the element size. To increase resolution, the element size has to be reduced.

Introduction of buffer layer

It comes without saying that SEM does not restrict the use of differently sized elements. This is very convenient to create efficient meshes. For example when simulating seismic waves, regions of higher seismic velocities and thus longer wavelengths can be meshed with larger elements. Also, complex structures can be meshed more precisely by decreasing the size of surrounding elements.
We use this feature to obtain a more detailed representation of the topography as already discussed before. However, to avoid expensive computations due to numerous small elements, we want to coarsen the mesh and use larger elements in the subsurface. For the transition between different element sizes, a refinement layer is used which breaks down the element size by a factor of 3. Its architecture is visualized in Figure 3.14.

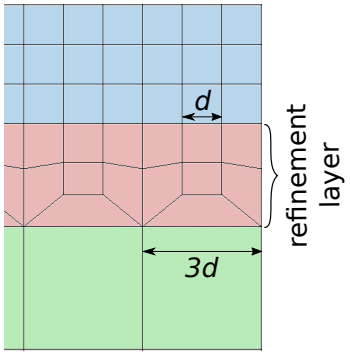

Figure 3.14 – Mesh refinement. Transition between elements of side length d (*blue*) and $3d$ (*green*) via the refinement layer (*red*). Note that this is a 2D view onto the plane in which the boundary of the big element is situated.

In practice, problems during the mapping in SEM can arise when the refinement layer is overly distorted due to strong topography variations. In this case we introduce a smooth horizon between surface topography and refinement layer. This horizon is a low-pass filtered version of the topography. Figure 3.15 illustrates the implementation of a buffer layer for the case of Dolomieu crater topography.

3.2.6 Implementation of velocity model

The construction of SEM allows variable medium properties within elements. Individual values of density ρ, S-wave velocity v_s and P-wave velocity v_p can be assigned to each GLL grid point (which in fact also means that the distance between GLL points determines the model resolution). The values in between grid points are interpolated with the Lagrange polynomials, just like the solution for displacement field u.
The software used here, SEM3D, is designed to define vertically layered material properties with boundaries at element interfaces. However, in order to be able to implement a vertically smooth varying velocity model, we modify the code to directly define material properties at the grid point level.
After doing so, the velocity model proposed by Lesage et al. (2018) for the shallow velocity structure of volcanoes can be implemented. This velocity model was introduced in section

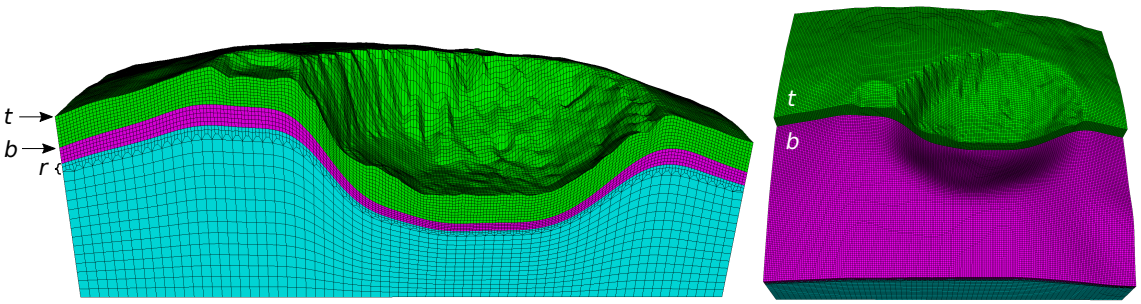

Figure 3.15 – Mesh with topography and buffer layer. Model with Dolomieu crater topography t of 10 m resolution. The mesh is built of linear elements with side length of 10 m above and 30 m below refinement layer r. A smooth buffer horizon b (low-pass filtered topography with wavelengths $\geq$ 200 m) is introduced between surface topography and refinement layer to accommodate high frequency topography variations. *Left:* Cross-section of the domain. The location of buffer horizon b can be identified by the green-magenta interface. Below this interface vertical mesh variations are smooth. Refinement layer r is situated below the magenta-cyan interface. *Right:* Top view on the 3D domain. The mesh above the buffer horizon was removed in the front part (up to the cross-section shown on the left). The difference between smoothly varying buffer horizon b and rough surface topography t is clearly visible.

1.3.1 on page 11.

Figure 3.16 compares the simulated wave propagation from a vertical point source on three different velocity profiles: a homogeneous model (*left*), a model with low velocity layer (*middle*) and a model with Lesage velocity profile (*right*).

Seismograms recorded at the surface of the homogeneous model show the propagation of surface waves with constant velocity. These are so-called Rayleigh waves which are characterized by particle motions in the vertical-radial plane. A small amount of body wave energy, arriving earlier than the Rayleigh waves, is visible at small offsets.

Introducing a shallow low velocity layer has various effects on the wave field. On the one hand side it leads to internal reflections of body waves within this layer. These so called multiples can be observed on the section of seismograms arriving successively with constant velocity. On the other hand side, the propagation speed of Rayleigh waves becomes dispersive, i.e. frequency dependent. This can be explained by their frequency dependent penetration depth. If the penetration depth is deeper than the shallow layer, the underlaying layer contributes to the propagation speed. Additionally, higher-order modes of Rayleigh waves can be generated. Higher-order modes exist in heterogeneous media as Rayleigh waves can travel with various speeds for a given frequency (changing their wavelength accordingly). In the present case, the fundamental mode is almost non-dispersive, as the penetration depth of the main frequency content does not reach the underlaying layer. This is why we can see a strong Rayleigh wave traveling with constant speed such as in the case of the homogeneous model. However, some contribution of dispersive 1-order modes results in Rayleigh wave oscillations with seemingly curved arrival times (this was analyzed with the help of the modal summation method within *Computer Programs in Seismology* (Herrmann, 2013)).

In case of the Lesage model, the velocity is smoothly increasing with depth. Without sharp layer interfaces, body waves can travel on a curved path through depth back to the surface instead of being reflected at layer boundaries. This causes diverging arrival times as marked by a white circle in the top right corner of Figure 3.16. Further, the Rayleigh

wave speed is continuously increasing with frequency which can nicely be observed at large offsets (marked by a white circle and denoted as *Fundamental Rayleigh*). Low frequency oscillations (wide wavelets) arrive earlier than high frequency oscillations (narrow wavelets). Beside the fundamental mode, the 1^{st}-order mode is visible traveling at higher speeds.

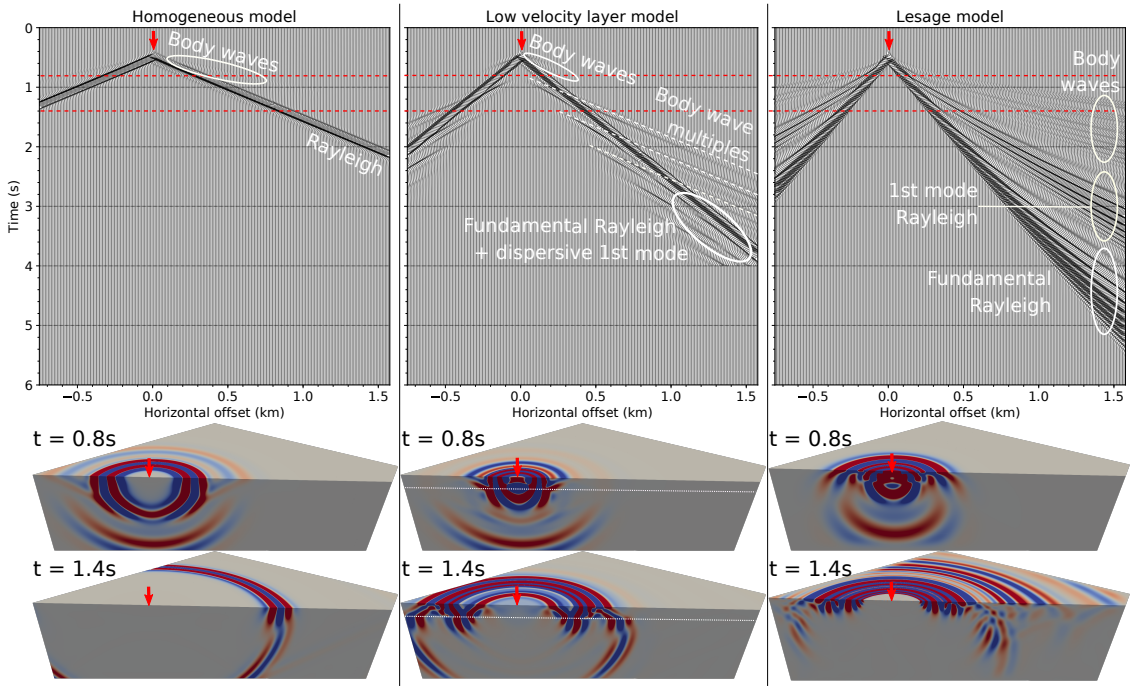

Figure 3.16 – Different velocity models on flat domain. Synthetic seismograms (*top*) and snapshots of the wave field at time $t = 0.8$ s and $t = 1.4$ s (*bottom*) for different velocity models: homogeneous model (*left column*), model with low velocity layer (*middle column*, the dotted white line on the snapshots indicate the layer depth) and model with Lesage velocity profile (*right column*). The sections of seismograms are recorded at the surface of the corresponding cross-section shown in the snapshots below. Amplitudes correspond to vertical ground velocity. Red arrows mark the source position, which is a 7 Hz Ricker vertical point force.

As can be seen from the illustrated snapshots of the wave field, the velocity model changes the partition between energy "lost" into the subsurface and energy traveling along the surface. This is of high importance for the following sections, in which we discuss how to back-calculate the generated energy of a source from the surface measurements of a distant seismometer.

3.3 Radiated seismic energy from a surface load

In the context of landslide generated seismic waves it is of interest to calculate the totally released seismic energy, for example in order to estimate the landslide volume. However, the only available input for this calculation is given by the seismic measurement of a single seismic station (or multiple stations if we are lucky) at the Earth's surface. This means that we have to find an estimate which tries to relate the energy measured at the surface to the energy present in the whole subsurface and integrate the total energy radiated in all directions around the source.

Typically, landslide seismic energy is estimated under the assumption of a single dominant

frequency (Vilajosana et al., 2008; Hibert et al., 2011, 2014b; Levy et al., 2015). Here we will derive an equation which takes the spectral wave properties into account. For this, we assume a vertical surface load whose position is known. Starting from a homogeneous model, for which an analytical solution is proposed, we will go to a heterogeneous model for which the energy decay will be investigated numerically.

3.3.1 Seismic energy decay as a function of traveled distance

Before establishing an equation to back-calculate the source generated energy from a single seismometer, let us observe the decay of seismic energy with distance r along the surface of a flat domain. Part of this decay is caused by intrinsic attenuation as described in equation 3.4. Intrinsic attenuation causes an exponential energy decay. Additionally, the seismic energy decays due to so-called geometrical spreading as it is distributed in space during propagation. In fact, body wave energy decays with $1/r^2$ as the wavefront is growing spherically, whereas surface wave energy decays on a cylindrical growing wavefront with $1/r$.
Here we compare the seismic energy decay on the three velocity models introduced in section 3.2.6, namely the model with homogeneous velocity, the model with shallow low velocity layer and the model with Lesage velocity profile. Figure 3.17 plots energy density multiplied by offset as a function of offset for radial and vertical component. Energy density e_{tot} is calculated by equation 3.21, which is introduced in the next section. Multiplication by offset r compensates for the geometrical spreading of surface waves. Thus, if only surface waves were measured, the energy density should decay exponentially which can easily be identified using a logarithmic scale.

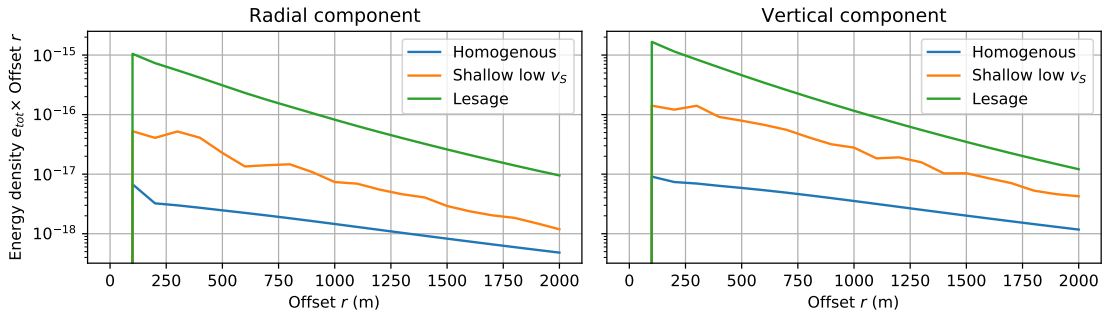

Figure 3.17 – Seismic energy decay as a function of traveled distance. Comparison of the seismic energy decay along the surface of domains with different velocity models: homogeneous model, model with shallow low S-wave velocity and model with Lesage velocity profile. Energy density e_{tot} is calculated for radial (*left*) and vertical (*right*) ground velocity. Multiplication by offset r compensates for geometrical spreading of surface waves. Linear decay on the logarithmic scale indicates that exclusively surface waves are measured.

In the case of a homogeneous model, the energy decays linearly on the semi-logarithmic scale. This suggests that mainly surface waves are measured. Only at very short offsets the assumption does not hold, possibly related to the presence of body waves. The decay of energy on the heterogeneous models is not perfectly linear. The model with shallow low velocity shows an oscillating decay which might be explained the interference of multiples (see Figure 3.16). The Lesage model shows a slightly curved decay. This is possibly related

to the dispersive surface wave velocities as well as the involvement of body waves measured at the surface (see Figure 3.16).
The observation that mainly surface waves are measured at the surface of a homogeneous model (in case of a vertical surface load), will be used in the following section to derive an analytical equation which allows to calculate the energy of the source. The involvement of body waves in case of a heterogeneous model will be investigated subsequently.

3.3.2 Estimation of source generated energy on homogeneous media

In this section we derive a formula to back-calculate the seismic energy radiated from a surface point source by means of a seismic surface measurement. First of all, we have to describe the total energy E_R radiated by a seismic source. For this, we measure the energy flux through a surface which encloses the source.
The energy density flux ϕ is defined as the energy E passing through a surface S within time t. Equivalent to this definition, the flux can be expressed as the energy density e propagating with velocity c as illustrated below:

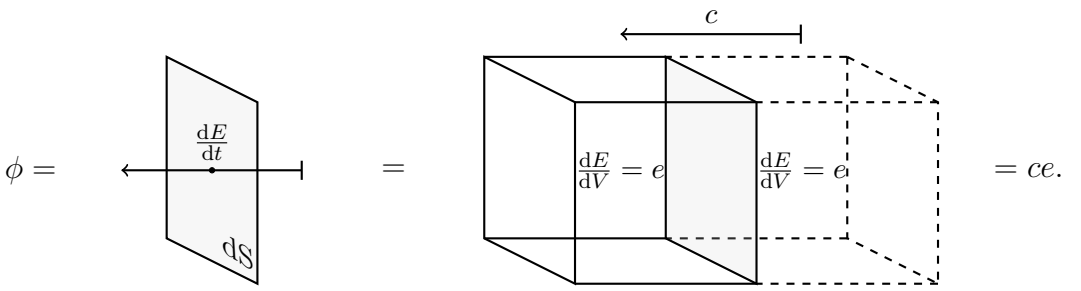

Regarding seismic waves, c refers to the wave propagation velocity whereas e is the total energy density $e = e_c + e_p$ composed of kinetic and potential energy density, respectively. The kinetic energy density can be measured by means of the ground velocity $\mathbf{v}$:

$$e_c(t) = \frac{1}{2}\rho \mathbf{v}^2(t), \tag{3.20}$$

with mass density ρ. In order to obtain the total energy density through time e_{tot}, we integrate from t_0 to t_1, the duration during which the seismic waves pass by the receiver. With $\int e_c \,\mathrm{d}t = \int e_p \,\mathrm{d}t$ and thus $e_{tot} = \int e \,\mathrm{d}t = 2 \int e_c \,\mathrm{d}t$ we have

$$e_{\mathrm{tot}} = \int_{t_0}^{t_1} \rho \mathbf{v}^2 \,\mathrm{d}t. \tag{3.21}$$

The totally integrated energy E_R radiated by a seismic source is equal to the energy density flux $\phi(\mathbf{r}, t)$ integrated over time and over a surface S_0 enclosing the source, thus:

$$E_R = \int_{t_0}^{t_1} \int_{S_0} c\rho \mathbf{v}^2 \,\mathrm{d}S \,\mathrm{d}t. \tag{3.22}$$

As we only have measurements from stations located at the Earth's surface we have to adjust the surface integral over S_0 accordingly. In order to consider energy radiated into

the subsurface, a factor will be introduced which considers the energy partition among different wave types.

Energy partition for surface loads

The energy partitions among different wave types were derived by Weaver (1985) for a semi-infinite solid based on a diffuse-field approach. The results were reinterpreted by Sánchez-Sesma et al. (2011) who explicitly pointed out their significance for surface point loads. In doing so, horizontal and vertical surface loads have to be distinguished. The relative energy partitions, which are directly derived from Weaver (1985), are illustrated in Figure 3.18 as functions of Poisson's ratio. It can be observed that for horizontal loads the majority of energy radiates as horizontal body shear waves whereas for vertical loads the majority of energy is released as Rayleigh waves.

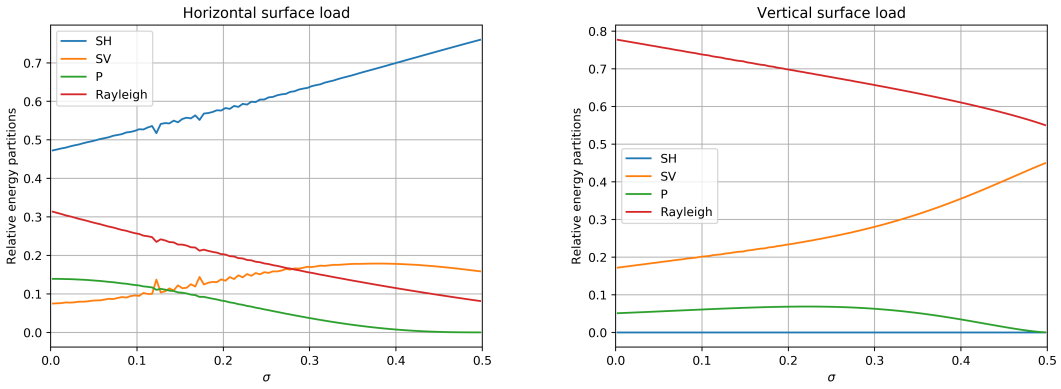

Figure 3.18 – Wave type energy partition. Relative energy partitions among horizontal and vertical S-waves (SH and SV, respectively), P-waves (P) and Rayleigh waves (R) for both horizontal (*left*) and vertical (*right*) surface loads as functions of Poisson's ratio σ.

Vertical load on semi-infinite solid

For a vertical surface load, as can be seen in Figure 3.18, Rayleigh waves constitute the major energy partition which we shall refer to as p_R. Further, as discussed in section 3.3.1, surface waves dominate the signal measured at a distant receiver since body waves decay faster and since energy does not propagate upwards in case of a surface load on a semi-infinite homogeneous medium. Assuming that exclusively surface waves are measured, the surface integral in equation 3.22 takes a cylindrical form and can be rewritten as

$$E_R = \frac{1}{p_R}\, c\rho \int_{t_0}^{t_1} \int_0^{2\pi} \int_0^{h} \mathbf{v}^2 \,\mathrm{d}z\, r \mathrm{d}\theta\, \mathrm{d}t, \tag{3.23}$$

with distance r between source and receiver and azimuth θ integrated over a full circle surrounding the source. Integration over depth z must be carried out along the dispersive penetration depth $h = h(f)$ varying with frequency f. In order to respect the frequency

dependency, equation 3.23 is transformed to frequency domain making use of Parseval's theorem:

$$E_R = \frac{1}{p_R} 2\pi r\, c\rho \int_{-\infty}^{\infty} h\hat{\mathbf{v}}^2 \, \mathrm{d}f = \frac{1}{p_R} 4\pi r\, c\rho \int_{0}^{\infty} h\hat{\mathbf{v}}^2 \, \mathrm{d}f, \tag{3.24}$$

where $\hat{\mathbf{v}} = \hat{\mathbf{v}}(f)$. Note that the discrete version of Parseval's theorem is derived in annex A.1

Due to intrinsic attenuation the signal amplitude A decays exponentially as described in equation 3.4. The energy decay is thus proportional to $\exp(-2\alpha r)$, where α is the frequency dependent attenuation coefficient. Correcting for this exponential decay we finally have:

$$E_R = \frac{1}{p_R} 4\pi r\, c\rho \int_{0}^{\infty} h\hat{\mathbf{v}}^2 \, \mathrm{e}^{2\alpha r} \, \mathrm{d}f, \tag{3.25}$$

Note that Rayleigh wave quality factor Q_R generally depends on both Q_P and Q_S, the quality factors of P-wave and S-wave. However, as Rayleigh wave velocity c_R is much more sensitive to S-wave velocity c_S, we can neglect the contribution of Q_P. This can be seen in appendix 3.4.1, in which we discuss the velocity dispersion of Rayleigh waves caused by attenuation. In the following we will present a way to efficiently integrate the dispersive Rayleigh penetration depth.

Rayleigh wave effective depth

In order to back-calculate the totally generated energy, the measured signal at a surface receiver has to be integrated in depth to account for the total Rayleigh wave energy. However, horizontal and vertical ground velocity amplitudes of Rayleigh waves are varying with depth. In the following, an effective penetration depth h is derived with which the surface measurement can elegantly be integrated.

In a semi-infinite homogeneous medium with depth $z \geq 0$, bounded by a free surface at $z = 0$, the horizontal and vertical ground velocities v_x and v_z of a Rayleigh wave traveling in x-direction can be described as (Maradudin, 1987):

$$v_x(x, z, t) = \omega \; AZ_x \; \sin(kx - \omega t), \tag{3.26}$$

$$v_z(x, z, t) = \omega \; AZ_z \; \cos(kx - \omega t), \tag{3.27}$$

with wavenumber k and angular frequency ω (note that in a homogeneous medium the dispersion relation $\omega = c_R k$ is linear, where c_R denotes the Rayleigh wave speed). A is constant, Z_x and Z_z are depth dependent horizontal and vertical amplitude functions:

$$Z_x(z) = \mathrm{e}^{-k\beta_P z} - \gamma \mathrm{e}^{-k\beta_S z}, \tag{3.28}$$

$$Z_z(z) = \beta_P \left(\mathrm{e}^{-k\beta_P z} - \frac{1}{\gamma} \mathrm{e}^{-k\beta_S z} \right), \tag{3.29}$$

with

$$\beta_P = \sqrt{1 - \frac{c_R^2}{c_P^2}}, \qquad \beta_S = \sqrt{1 - \frac{c_R^2}{c_S^2}}, \quad \text{and} \quad \gamma = 1 - \frac{c_R^2}{2c_S^2}, \tag{3.30}$$

where c_P and c_S are longitudinal and transversal wave speeds, respectively.
The depth distribution of the seismic energy is proportional to the squared ground velocity depth functions Z_x and Z_z, thus:

$$E_x(z) \propto Z_x^2(z) = \mathrm{e}^{-2k\beta_P z} + \gamma^2 \mathrm{e}^{-2k\beta_S z} - 2\gamma \mathrm{e}^{-k(\beta_P+\beta_S)z}, \tag{3.31}$$

$$E_z(z) \propto Z_z^2(z) = \beta_P^2 \left(\mathrm{e}^{-2k\beta_P z} + \frac{1}{\gamma^2}\mathrm{e}^{-2k\beta_S z} - \frac{2}{\gamma}\mathrm{e}^{-k(\beta_P+\beta_S)z} \right). \tag{3.32}$$

We are searching for an effective depth h so that the seismic energy measured at the surface multiplied by this effective depth corresponds to the depth integral of the true depth-amplitude curve, that is:

$$h_x E_x(0) = \int_0^\infty E_x(z)\mathrm{d}z, \tag{3.33}$$

$$h_z E_z(0) = \int_0^\infty E_z(z)\mathrm{d}z. \tag{3.34}$$

In order to illustrate the effective depth h, let's assume a medium with Poisson's ratio $\sigma = 0.33$ (corresponding to $c_P = 2000\,\mathrm{m.s^{-1}}$ and $c_S = 1000\,\mathrm{m.s^{-1}}$). For this case, the squared horizontal and vertical ground velocities are shown in Figure 3.19 as functions of depth, corresponding to equations 3.31 and 3.32, together with the effective depth h. Note that the depth axis is normalized by wavelength λ.

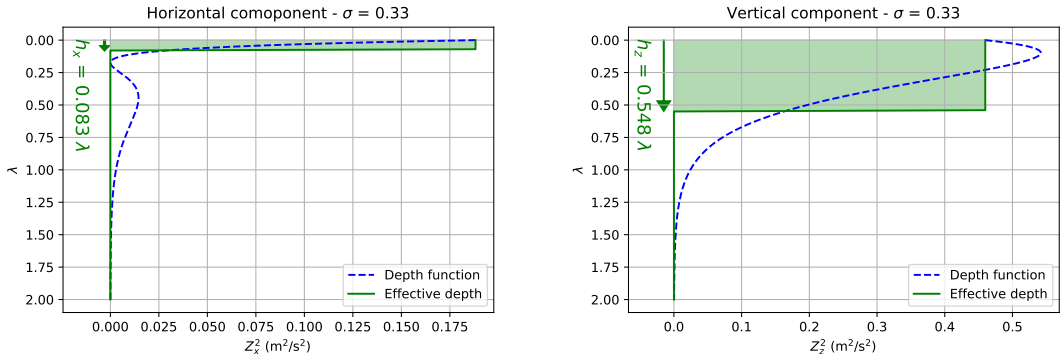

Figure 3.19 – Rayleigh wave depth function and effective depth. Squared horizontal (*left*) and vertical (*right*) amplitudes (blue dashed) together with effective depth h (solid green) as functions of depth in units of wavelength λ. The filled areas equal the integral of the corresponding depth function.

Substituting equations 3.31 and 3.32 into equations 3.33 and 3.34, respectively, we find the effective depth h as a function of the medium parameters:

$$h_x = \frac{1}{k} \frac{\frac{1}{2\beta_P} + \frac{\gamma^2}{2\beta_S} - \frac{2\gamma}{\beta_P+\beta_S}}{(1-\gamma)^2}, \tag{3.35}$$

$$h_z = \frac{1}{k} \frac{\frac{1}{2\beta_P} + \frac{1}{2\beta_S\gamma^2} - \frac{2}{(\beta_P+\beta_S)\gamma}}{\left(1-\frac{1}{\gamma}\right)^2}. \tag{3.36}$$

With this relation at hand, the effective depth for horizontal and vertical ground velocities can be plotted as functions of Poisson's ratio σ as shown in Figure 3.20. This is of great utility in order to easily integrate the seismic energy over depth from a surface measure-

ment.

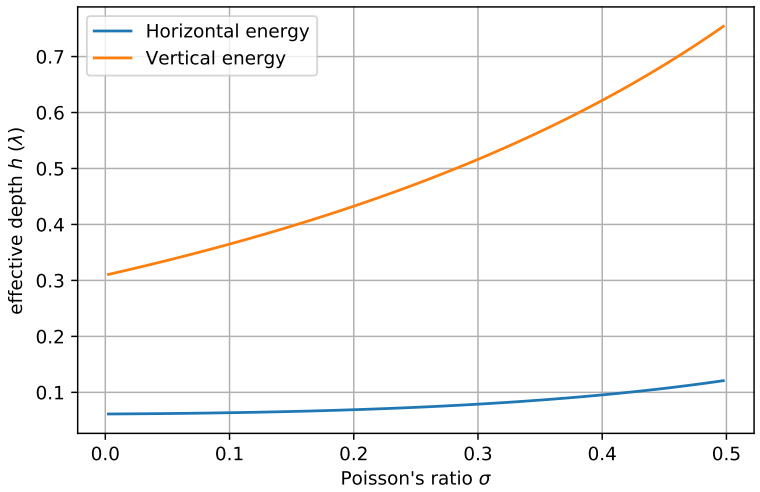

Figure 3.20 – Rayleigh wave effective depth as function of Poisson's ratio.
Effective depths h_x and h_z expressed in units of wavelength λ for horizontal and vertical energy (corresponding to squared ground velocity), respectively, as a function of Poisson's ratio σ.

Finally, equation 3.25 for estimating the generated energy can be completed by means of effective depth h:

$$E_R = \frac{1}{p_R} 4\pi r\, c\rho \int_0^\infty \left(h_x \hat{v}_x^2 + h_y \hat{v}_y^2 + h_z \hat{v}_z^2\right) \mathrm{e}^{2\alpha r}\, \mathrm{d}f, \tag{3.37}$$

while $h_x = h_y$.
We will now test the derived theory on synthetic examples of wave propagation on a flat domain.

Synthetic example for energy estimation

The previous sections presented the theory with which the source generated energy can be estimated from a distant receiver measurement in a semi-infinite solid. In the following, this theory will be validated numerically.
A homogeneous model is used with medium parameter $c_P = 2000\,\mathrm{m.s}^{-1}$,$c_S = 1000\,\mathrm{m.s}^{-1}$, and $\rho = 2000\,\mathrm{kg.m}^{-3}$. The source is a 7Hz Ricker wavelet pointing in vertical direction. Synthetic seismograms are calculated up to a maximal source-receiver distance of 2000 m on a model without and with intrinsic attenuation. Attenuation parameters in the latter are set to $Q_P = 80$ and $Q_S = 50$. This results in a Rayleigh quality factor of $Q_R = 51.4$, which was calculated numerically using *Computer Programs in Seismology* (Herrmann, 2013). The radiated energy is calculated using equation 3.37 without and with the exponential term for attenuation. Rayleigh effective depth is $h_x = 0.083\lambda$ and $h_z = 0.548\lambda$ (see Figure 3.19), while Rayleigh wave partition factor is $p_R = 0.6427$ (see Figure 3.18).
Figure 3.21 shows the estimated energy normalized by the true energy E_{Source} radiated from the source. Appendix 3.4.2 explains how we calculate the source energy E_{Source} generated by a point force.
Thanks to the derived spectral effective penetration depth and the Rayleigh partition factor, we are able to retrieve the original source energy. The estimation is flawed at short distances up to around 600 m offset. This is possibly due to interferences with body

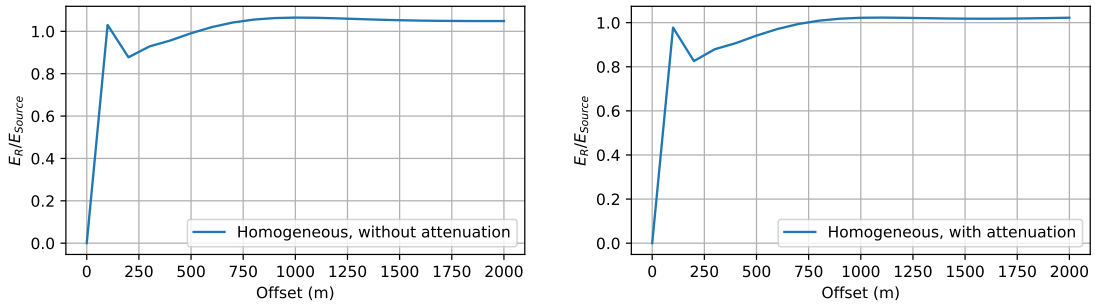

Figure 3.21 – Source generated energy estimated along offset. Energy estimation on a model without (*left*) and with (*right*) intrinsic attenuation. Up to an offset of around 600 m the estimation is flawed possibly due to the interferences with body waves. As the theory assumes measured surface waves, the energy estimation is flawed at short offsets.

waves which are not considered in the equation. Body waves have a dominant wavelength of almost 300 m ($2000\,\mathrm{m.s^{-1}} \div 7\,\mathrm{Hz}$), meaning that the influence persist up to distances of around 2 wavelengths from the source. A slight overestimation is observed at longer distances. This might originate from rounding errors and is not further investigated here. Assuming that the medium parameters are known, equation 3.37 can be used to efficiently calculate the source energy without knowledge on the source frequency. Keep in mind that the formula is only valid for vertical sources. Horizontal sources cause radiation patterns which are not radial symmetric. This, as well as the the strong presence of SH-waves (see Figure 3.18) are not considered in the derivation above.
In the next section we investigate the consequences when changing from a homogeneous to a heterogeneous medium.

3.3.3 Estimation of source generated energy on heterogeneous media

In the previous section we derived a formula to estimate the energy generated by a source on a homogeneous medium. For a heterogeneous medium, this formula becomes invalid, in particular due to the contribution of different wave types to the measurement such as higher modes and body waves. The implied complexities are studied hereafter on the example of the Lesage velocity model.
From the seismograms shown in Figure 3.16, we can see that in contrast to a homogeneous model, wave propagation on the Lesage model leads to the appearance of the 1$^{\mathrm{st}}$ mode Rayleigh waves as well as a higher proportion of body waves measured at the surface. A zoom of seismograms at source-receiver offsets between 500 m and 800 m is presented in Figure 3.22 which illustrates the contribution of the different Rayleigh wave modes.
The energy decay of the different wave field components is illustrated in Figure 3.23 as a function of offset r for radial and vertical components. The curves are multiplied by offset r to compensate for geometrical spreading of surface waves.
It is visible that at small offsets the energy of the entire signal is dominated by fundamental mode surface waves. While the contribution of fundamental Rayleigh waves decreases with offset, the 1$^{\mathrm{st}}$ mode Rayleigh waves seem to gain importance. The relative contributions are illustrated in Figure 3.24.
We can observe that the contributions are changing as a function of distance. While the

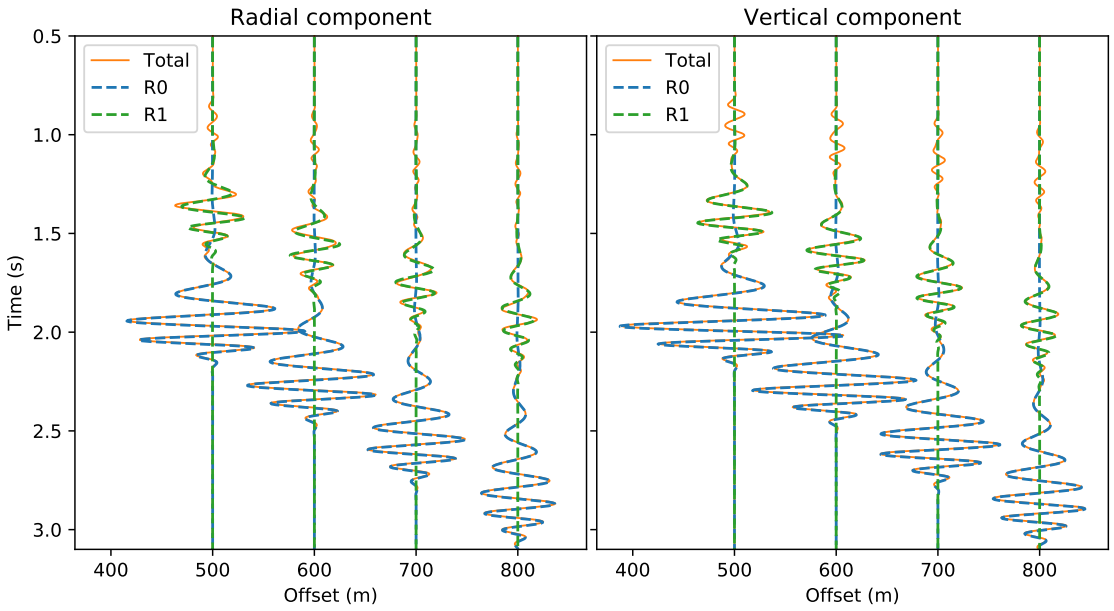

Figure 3.22 – Synthetic seismograms from the Lesage velocity model. Radial (*left*) and vertical (*righ*) components of ground velocity recorded along the surface of a flat model with Lesage velocity profile. The total signal (Total, solid orange) is overlaid with contributions from fundamental Rayleigh wave (R0, dashed blue) and 1st mode Rayleigh wave (R1, dashed green). Single modes were simulated using modal summation from *Computer Programs in Seismology* (Herrmann, 2013).

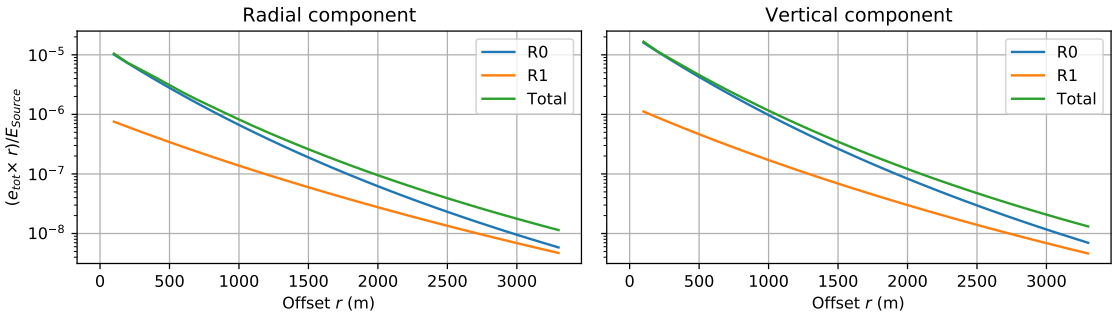

Figure 3.23 – Seismic energy decay of different wave field components. Energy decay along the surface on top of Lesage velocity model for fundamental Rayleigh wave R0, first higher mode R1 and the total wave field. Energy density e_{tot} is calculated for radial (*left*) and vertical (*right*) ground velocity. Multiplication by offset r compensates for geometrical spreading of surface waves. Values are calculated in respect to the energy of the source E_{Source}. The curve of the total wave field corresponds to the one shown in Figure 3.17.

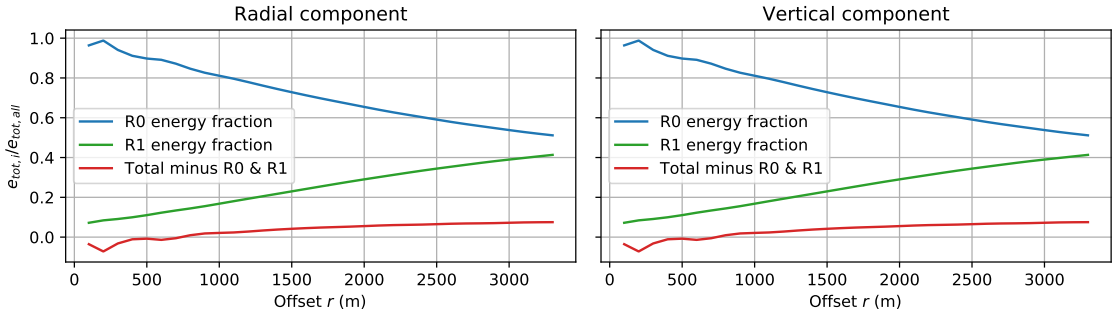

Figure 3.24 – Energy composition of the measured signal with distance. The relative energy density $e_{\text{tot,i}}/e_{\text{tot,all}}$ of different components in the seismic signal. $e_{\text{tot,all}}$ corresponds to the total energy density of the measured signal. $e_{\text{tot,i}}$ corresponds to to Rayleigh fundamental mode R0, 1st mode R1, and the total signal minus contributions from R0 and R1, respectively.

contributions from fundamental mode R0 weakens, the first mode becomes more important. This is due to different attenuation over distance: as the first mode is faster than the fundamental mode (see the corresponding velocity dispersion curves in Figure 1.6) attenuation factor α becomes smaller (see equation 3.4). Besides the contributions from fundamental and first mode, we remark increasing residual energy with distance. This energy originates from body waves or superposition of higher modes and is attenuated even less than the first mode Rayleigh wave.
As the main contribution within the studied offset range is mainly constituted from the first two Rayleigh modes, we follow the approach of the previous section for integrating their energy over time and space in order to retrieve the source energy. For this, the energy measured at the surface has to be integrated in depth as a function of the energy-depth distribution of each individual mode. The energy-depth functions are described by the squared eigenfunctions. Figure 3.25 displays radial and vertical depth-functions of fundamental and first mode. The depth axis is normalized by wavelength λ. The values of three different frequencies are plotted in order to evaluate the spectral variability.

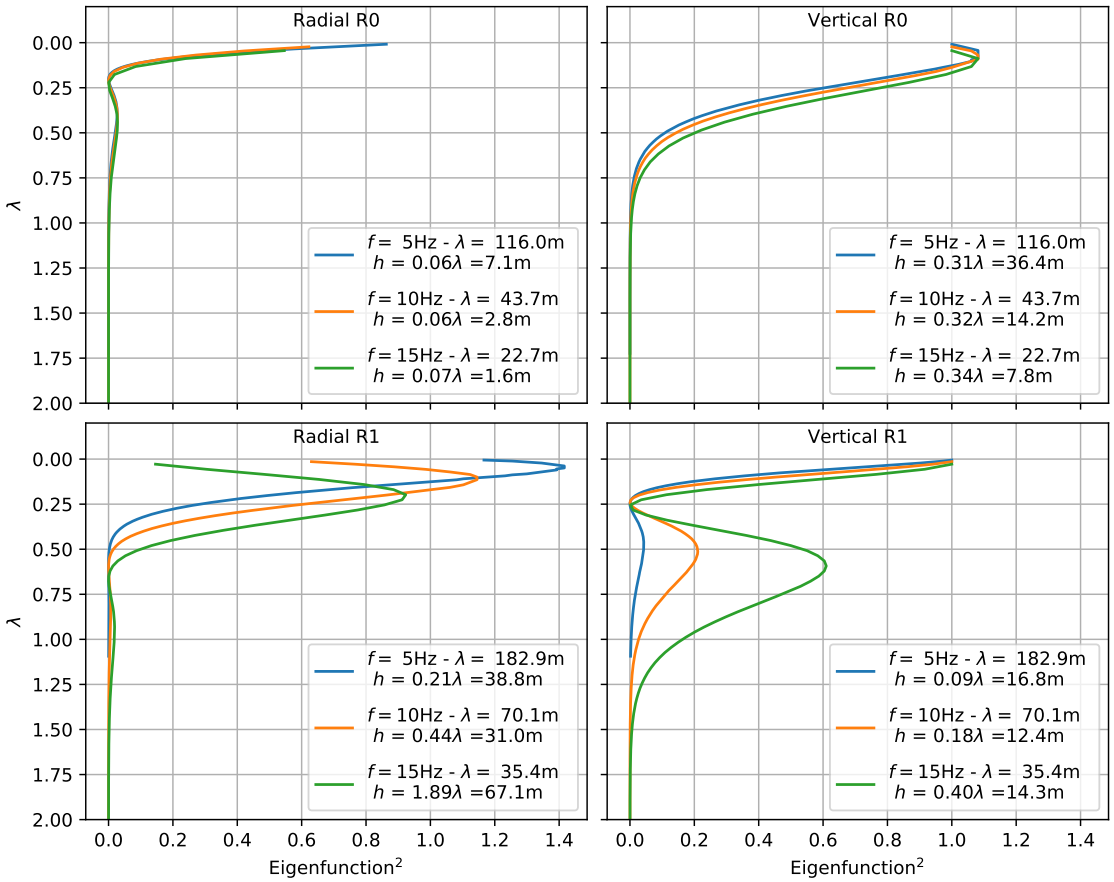

Figure 3.25 – Rayleigh wave eigenfunctions for the Lesage velocity model. Squared eigenfunctions for radial (*left*) and vertical (*right*) component of Rayleigh fundamental mode R0 (*top*) and first higher mode R1 (*bottom*). The functions are computed for the Lesage velocity profile (see 1.6) in respect to frequencies of 5 Hz, 10 Hz and 15 Hz. Annotations show the corresponding wavelength λ as well as penetration depth h. The depth axis is expressed in units of wavelength λ.

It can be observed, that the energy is similarly distributed in depth for all frequencies in case of the fundamental mode. This allows to define an effective depth h_{eff} which is

independent of the frequency, as done for the homogeneous medium above. Neglecting the slight variations, we define $h_{x,\text{eff}} = 0.06$ and $h_{z,\text{eff}} = 0.32$. These values can be multiplied by the wavelength to compute the true penetration depth of each frequency
Defining an effective depth is no longer possible for the first mode for which the energy is differently distributed in depth dependent on the frequency. More concretely, the higher the frequency, the more energy is in the subsurface in respect to the value at the surface. Consequently, effective depth h_{eff} varies drastically. On the other hand, the true penetration depths show less relative variation than in case of the fundamental mode. Hence, we decide to approximate a constant penetration depth of $h_x = 39\,\text{m}$ for the radial component and $h_z = 14\,\text{m}$ for the vertical component, which are the rounded medians of the shown frequencies. This way, we do not rely on a dispersive effective depth.
Besides the contribution of different wave types, we are confronted with dispersive surface waves due to the velocity gradient in depth. Consequently, equation 3.37 has to be adapted in terms of the dispersive velocity. For each mode i the radiated energy $E_{R,i}$ becomes:

$$E_{R,i} = 4\pi r\,\rho \int_0^\infty c_{g,i}\; h_{ji}\hat{v}_{ji}^2\; \mathrm{e}^{2\alpha_i r}\;\mathrm{d}f, \tag{3.38}$$

where $c_{g,i} = c_{g,i}(f)$ is the dispersive group velocity and summation over all components j is implicit. Attenuation factor α_i is given by

$$\alpha_i = \frac{f\pi}{Q_i c_{g,i}}. \tag{3.39}$$

Note that in case of propagating waves the *spatial* quality factor is usually determined and attenuation factor α_i is calculated using group velocity $c_{g,i}$. However, it is also possible to measure the *temporal* quality factor. Then, the phase velocity has to be used to determine the attenuation factor (see e.g. Aki and Richards, 2002). Note also, that energy partition factor p_R was omitted as it is only valid for surface loads at the surface of a homogeneous medium. For our numerical model, we know exactly the Rayleigh wave group velocities $c_{g,i}$ as well as the quality factors Q_i [1]. We can hence compute $E_{R,i}$ relative to the source energy E_{Source}. This is shown in Figure 3.26 for radial and vertical component of each mode as a function of offset.
The constant values in Figure 3.26 proof that we can exactly correct geometrical spreading and attenuation for the dispersive Rayleigh waves. Also, we can observe their relative contributions within the assumption regarding the constant penetration depth of first mode Rayleigh waves. Interesting to see is that the vertical component of the fundamental Rayleigh wave contains by far the most energy. This can be useful to know in order to conduct a first order estimation of the source energy.
In general, the different wave types cannot be separated (in particular when considering rockfall seismic signals due to the continuous source activity). Consequently, we have to find an equation which can estimate the source energy based on a signal which contains mixed wave types. For this, we will now test the impact of different assumptions. Namely,

1. In fact, quality factor Q is identical for all Rayleigh modes. Yet, it is dispersive as can be seen from equation 3.45 in appendix 3.4.1. However, this can generally be neglected. For $Q_S = 50$ and $Q_P = 80$ Rayleigh quality factor Q_R ranges between 58.3 and 54.8 at frequencies between 3 Hz and 20 Hz. This was computed numerically.

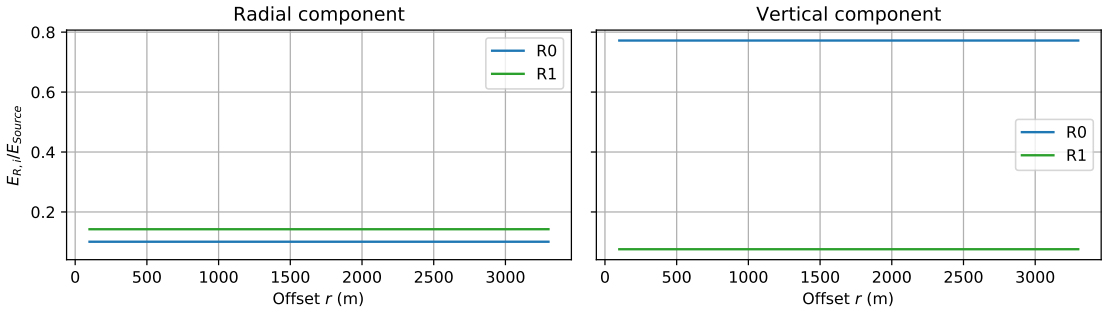

Figure 3.26 – Radiated energy of Rayleigh fundamental and first mode. Estimation of energy composition radiated by the source regarding radial and vertical component for fundamental mode (R0) and first mode (R1) Rayleigh wave. The value is normalized by the total source energy E_{Source}.

it is assumed that the measured signal contains

1. only fundamental Rayleigh waves R0,
2. only 1$^{\text{st}}$ mode Rayleigh waves R1,
3. contribution from both R0 and R1 in proportions changing with offset r as found in Figure 3.24.

Figure 3.27 shows the estimated normalized source energy E_R/E_{Source} under these assumptions as a function of offset.

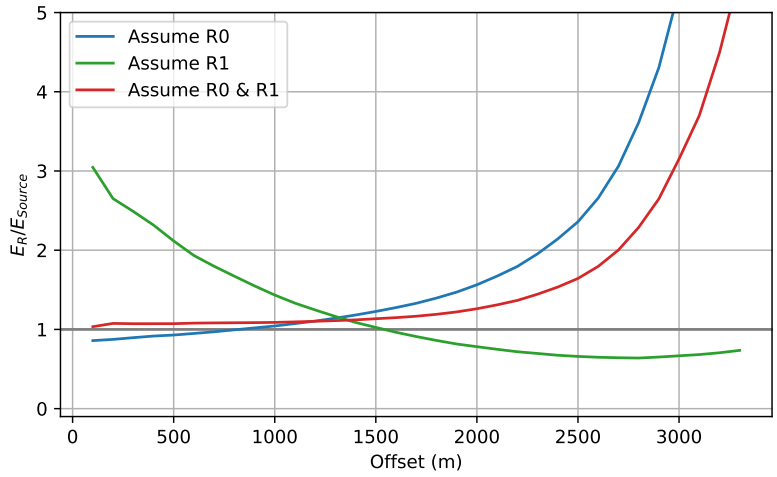

Figure 3.27 – Source energy estimation on heterogeneous medium. Estimation of radiated seismic energy E_R from the total seismic signal with mixed wave types assuming that the signal contains 1) only fundamental mode R0, 2) only fist mode R1, and 3) contributions from both R0 and R1. Values are normalized in respect to source energy E_{Source}.

Assuming only fundamental mode Rayleigh waves we can see that the source energy is underestimated at very short distances within 500 m. The estimation increases steadily with offset becomes overestimated at around 800 m. At offsets larger than 1500 m an exponential growth starts which eventually leads to an exploding value. This can be explained by the fact that the contribution of first mode Rayleigh waves as well as body waves increases with offset. As this contribution is not considered, the exponential decay due to attenuation is compensated assuming too big attenuation factors α (corresponding to the relatively too small group velocity of fundamental mode Rayleigh waves). This leads to the exponential growth of the estimation with offset.
Assuming only first mode Rayleigh waves, the source energy is strongly overestimated at short offsets. This mainly originates from overestimating the group velocity at which the energy is propagating. The overestimation of group velocity becomes successively balanced

by the underestimation of attenuation. Consequently, the energy estimation decreases with offset. However, regarding the positive gradient of the curve we can expect a similar exponential growth as for the first assumption for offsets larger than the shown range.
Finally, under the third assumption, the source energy is well estimated for offsets up to 2000 m. A slight overestimation can be remarked, which is probably explained by the contribution of body waves. This overestimation increases successively with offset as the contribution of body waves is increasing (see Figure 3.24). Eventually, it leads to an exponential growth of the estimated energy from offsets larger than 2000 m.
In conclusion, taking into account contribution from both Rayleigh fundamental and first mode results in the best source energy estimation with constant values up to source-receiver offsets of 2000 m. However, the contribution of residual energy leads to an overestimation of attenuation and consequently an exponential growth of the estimated energy.
In the literature, landslide seismic energy is typically estimated under the assumption of a dominant frequency (e.g. Vilajosana et al., 2008; Hibert et al., 2011, 2014b; Levy et al., 2015). This means, that the estimation is carried out neglecting the dispersive nature of surface waves, thus assuming constant propagation speed $c_{g,i}$ and constant penetration depth h_{ji}. The dispersion of quality factor Q is generally small (see discussion above) and can be neglected. In the following we test the consequences of the non-dispersive assumption by assuming different dominant frequencies. Figure 3.28 shows the estimated energy based on a dominant frequency of 7 Hz which corresponds to the true dominant frequency of the Ricker source.

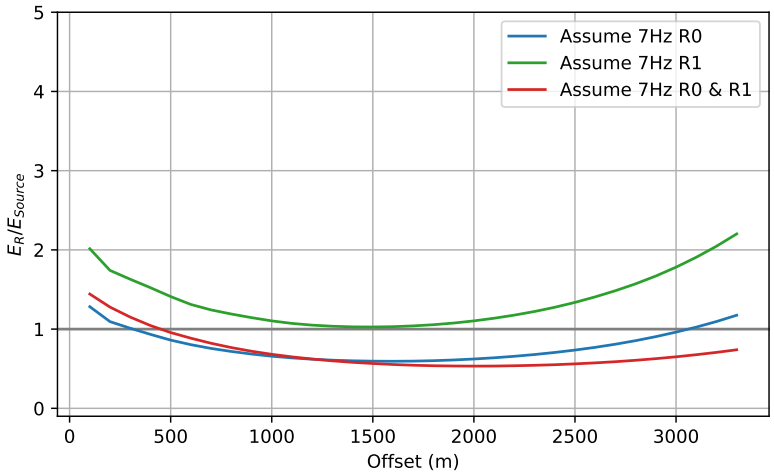

Figure 3.28 – Non-dispersive source energy estimation on heterogeneous medium. Estimation of normalized radiated seismic energy E_R/E_{Source} similar to Figure 3.27. Here the calculation is performed under the assumption of 7 Hz dominant frequency, i.e. group velocity $c_{g,i} = c_{g,i}(7\,\text{Hz})$, penetration depth $h_{ji} = h_{ji}(7\,\text{Hz})$, and quality factor $Q_i = Q_i(7\,\text{Hz})$.

We can see that all assumptions lead to curves of estimated energy of similar shapes. To understand the behavior of the functions with offset, we have to be aware that the velocity of waves with frequencies below the dominant frequency is underestimated while the velocity of waves with higher frequencies is overestimated. Consequently, at short offsets, where a lot of high frequency content is present, the estimated energy is overestimated. The underestimation of propagation speed for low frequencies leads to the observable decline of estimated energy. Eventually, the contribution of residual energy leads to a growth of energy at large offsets. Comparing the different assumptions, we can notice that by considering contribution from both R0 and R1 results in the curve of least curvature. This means that this assumption is the most stable to estimate the source energy as a function

of offset.
In the preceding test we were lucky enough to know exactly the dominant frequency of the source. We will now analyze the consequences when underestimating or overestimating the dominant frequency. Figure 3.29 shows the energy estimation assuming a dominant frequency of 4 Hz and 10 Hz, respectively.

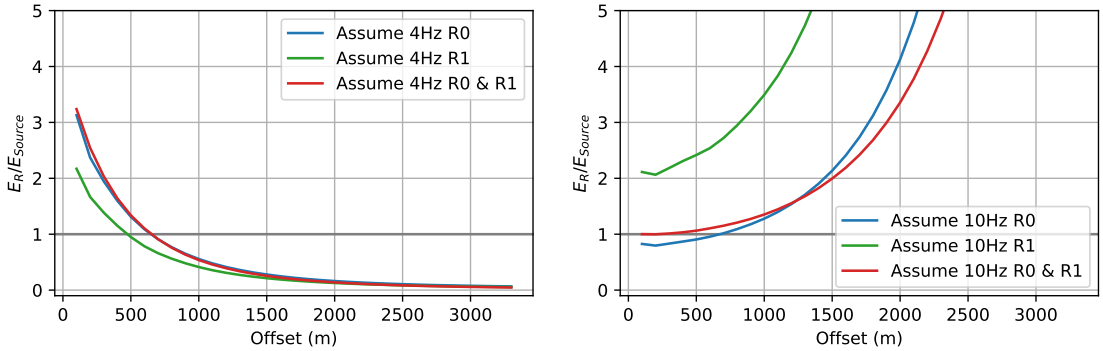

Figure 3.29 – Non-dispersive source energy estimation with wrongly estimated dominant frequency. Estimation of normalized radiated seismic energy E_R/E_{Source} similar to Figure 3.28 for underestimated 4 Hz (*left*) and overestimated 10 Hz (*right*) dominant frequency. The actual dominant frequency is 7 Hz.

The underestimation of the dominant frequency (4 Hz, left in Figure 3.29) leads to overestimation of the estimated energy at short distances up to 500 m due to the general overestimation of propagation speeds. Subsequently, the too large propagation speed leads to too small attenuation factors. Consequently, intrinsic attenuation is not compensated entirely, leading to a sharp decline of estimated source energy. Overestimating the dominant frequency (10 Hz, right in Figure 3.29) results to the opposite behavior. As the attenuation factor is overestimated, the estimated source energy grows exponentially. This behavior is observed for all assumptions.
It is evident that fixing a dominant frequency can be very risky due to the under- or overestimation of properties of the propagating wave field. To improve the estimation we now test the effect of fixing the propagation speed and the penetration depth, but keeping a frequency dependent attenuation factor, that is:

$$\alpha_i(f) = \frac{f\pi}{Q_i(f_{\text{dom}})\, c_{g,i}(f_{\text{dom}})}. \tag{3.40}$$

We can see that quality factor Q and group velocity $c_{g,i}$ are now fixed to a dominant frequency f_{dom}, but attenuation factor α still varies with frequency f. As said before, the dispersive character of quality factor Q can generally be neglected. Figure 3.30 shows the resulting source energy estimation as function of offset for underestimated frequency 4 Hz and overestimated frequency 10 Hz.
The frequency dependent attenuation factor as defined in equation 3.40 results in a more stable energy estimations in comparison to the attenuation factor fixed to a dominant frequency (see Figure 3.29). The general behavior of the curves is still similar, but the gradients of the decay (in case of underestimation of the dominant frequency) and the growth (in case of overestimation of the dominant frequency) of estimated energy are weaker than for the fixed attenuation factor. The curves suggest that at short offsets it is better to overestimate the dominant frequency (necessarily assuming the contribution

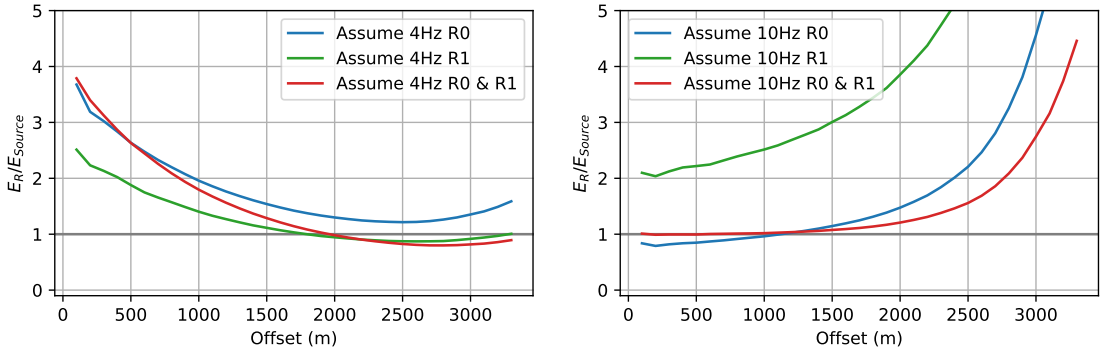

Figure 3.30 – Source energy estimation with wrongly estimated dominant frequency but spectral attenuation factor. Estimation of normalized radiated seismic energy E_R/E_{Source} similar to Figure 3.28 for underestimated 4 Hz (*left*) and overestimated 10 Hz (*right*) dominant frequency. Here, a frequency dependent attenuation factor as defined in equation 3.40 is taken into account. The actual dominant frequency is 7 Hz.

of fundamental Rayleigh waves as they dominate the signal at short offsets). In contrast, at larger offsets it is safer to underestimate the dominant frequency in order to avoid the correction with too large attenuation factors.

In conclusion, as we exactly know the medium parameters of the synthetic model, we are able to back-calculate reasonably well the source energy within receiver distances of 2000 m (see Figure 3.27). However, in practice the subsurface properties are in general poorly known. For this reason, assumptions on the involved propagations speeds and penetration depths have to be made. Assuming a single dominant frequency can lead to very wrong energy estimations as could be seen in Figure 3.29. A slightly more stable energy estimation can be achieved by keeping a frequency dependent attenuation factor as defined in equation 3.40. The frequency dependent attenuation factor can easily be taking into account by the integration in the frequency domain instead of integrating the measured ground velocity in the time domain.

3.4 Appendices

3.4.1 Velocity dispersion due to intrinsic attenuation

Intrinsic attenuation causes velocity dispersion which can be described as follows (Liu et al., 1976):

$$\frac{c_i}{c_{i,0}} = 1 + \frac{1}{\pi Q_{i,0}} \ln\left(\frac{f}{f_0}\right), \tag{3.41}$$

where c denotes the wave propagation velocity, Q the quality factor and f the frequency, while index $i = P, S$ is for P-waves and S-waves, respectively, and index 0 for a reference system in which the quality factor is defined. In the following, the effect of this velocity dispersion on the energy decay of Rayleigh waves in a homogeneous half-space is investigated.

Effect of attenuation on Rayleigh wave phase velocity

The velocity dispersion in equation 3.41 is valid for P-waves and S-waves. Slepyan (2010) shows that Rayleigh wave velocity c_R can be approximated with S-wave velocity c_S and 's ratios σ as

$$c_R \approx c_S \cdot (0.8740 + 0.2004\sigma - 0.07567\sigma^2) \tag{3.42}$$

For a typical Poisson's ratio of $0.0 \leq \sigma \leq 0.5$, the Rayleigh wave velocity ranges between $0.8740 c_S \leq c_R \leq 0.9723 c_S$. Due to the strong dependency on S-wave velocity, influence of P-wave velocity dispersion on the Rayleigh wave velocity is neglected in the following.
Reformulating equation 3.41 and following the approach of Liu et al. (1976), the relative velocity variation of S-waves due to attenuation is expressed as follows:

$$\frac{\delta c_S}{c_{S,0}} = \frac{c_S - c_{S,0}}{c_{S,0}} = \frac{1}{\pi Q_{S,0}} \ln\left(\frac{f}{f_0}\right). \tag{3.43}$$

The Rayleigh wave phase velocity is thus varying with

$$\delta c_R = \frac{\partial c_R}{\partial c_S} \delta c_S = \frac{\partial c_R}{\partial c_S} \frac{c_{S,0}}{\pi Q_{S,0}} \ln\left(\frac{f}{f_0}\right). \tag{3.44}$$

Anderson et al. (1965) relates quality factors of P-wave and S-wave with Rayleigh wave quality factor Q_R (here for a half-space without stratification):

$$Q_R^{-1} = \left(\frac{c_P}{c_R}\frac{\partial c_R}{\partial c_P}\right) Q_P^{-1} + \left(\frac{c_S}{c_R}\frac{\partial c_R}{\partial c_S}\right) Q_S^{-1}. \tag{3.45}$$

We have already seen the strong dependency of Rayleigh wave velocity on S-wave velocity which is why we approximate $\partial c_R / \partial c_P \approx 0$. With this approximation, equation 3.44 can be rewritten as

$$\frac{\delta c_R}{c_R} = \frac{1}{\pi Q_{R,0}} \ln\left(\frac{f}{f_0}\right). \tag{3.46}$$

Figure 3.31 shows the relative velocity variations in a frequency range from 0.1 Hz to 50 Hz caused by attenuation with quality factors $Q_{R,0} = 50$ and $Q_{R,0} = 50$ at a reference

frequency $f_0 = 1\,\text{Hz}$. We can observe a velocity correction of up to 2.5% for $Q_{R,0} = 50$.

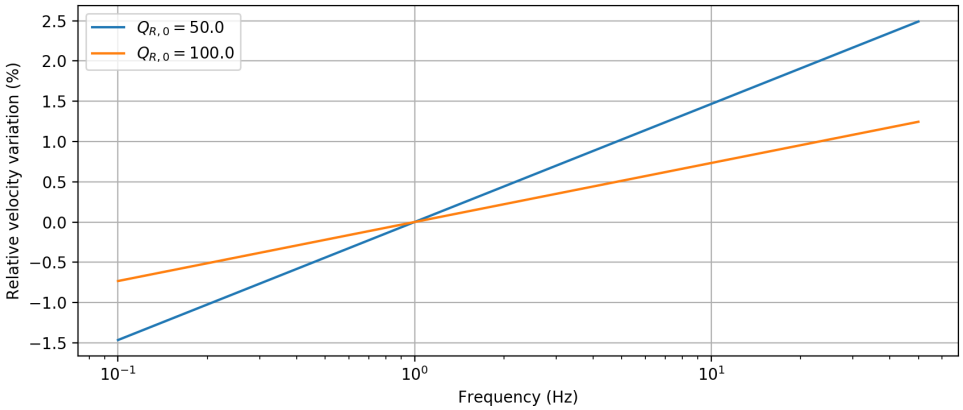

Figure 3.31 – Rayleigh wave dispersion due to attenuation. Rayleigh wave phase velocity variations due to attenuation with quality factors $Q_{R,0} = 50$ and $Q_{R,0} = 100$ at a reference frequency $f_0 = 1$ Hz.

3.4.2 Calculation of energy generated by a point force

In the SEM simulations we implement the seismic source by a point force. This means that we know the magnitude of the force, but the magnitude of the generated seismic energy is unknown as it depends on the medium properties.
In order to measure generated seismic energy, we record the ground velocity $\mathbf{v}$ at the source position x_S. Assuming that source force $\mathbf{F}$ is known, the source generated energy E_S can be computed by

$$E_S(x_S) = \int_{t_0}^{t_1} F_i(x_S, t) v_i(x_S, t) \mathrm{d}\, t, \tag{3.47}$$

where times t_0 and t_1 correspond to the time window in which the source is active and where we used the summation convention on repeated indices.
In order to validate equation 3.47, we conducted a test in which we measured the total energy passing through a surface surrounding the source. For this we design a cylinder of stations as illustrated in Figure 3.32.
Measuring particle velocity $\mathbf{v}$ and stress tensor σ at each position of the cylinder surface, we can infer the total energy $E_{R,\text{tot}}$ radiated by the source into the medium (Madariaga, 2015):

$$E_{R,\text{tot}} = \int_0^t \int_S \sigma_{ij}(x) v_i(x,t) n_j(x)\ \mathrm{d}S\mathrm{d}t, \tag{3.48}$$

where n_i is the outward normal to surface S and t is the time at which the total energy has propagated across the surface. Stress σ is measured by $\sigma_{ij} = \lambda \varepsilon_{ii} \delta_{ij} + 2\mu\varepsilon_{ij}$ with strain ε and Lame parameters λ and μ. Strain ε is related to the gradients of particle displacement $\mathbf{u}$ by $\varepsilon_{ij} = (\partial_j u_i + \partial_j u_i)/2$.
With the help of the simulation we find

$$E_S(x_s) = E_{R,\text{tot}}, \tag{3.49}$$

which means that the source energy calculated by equation 3.47 is indeed the totally generated energy propagating in the medium.

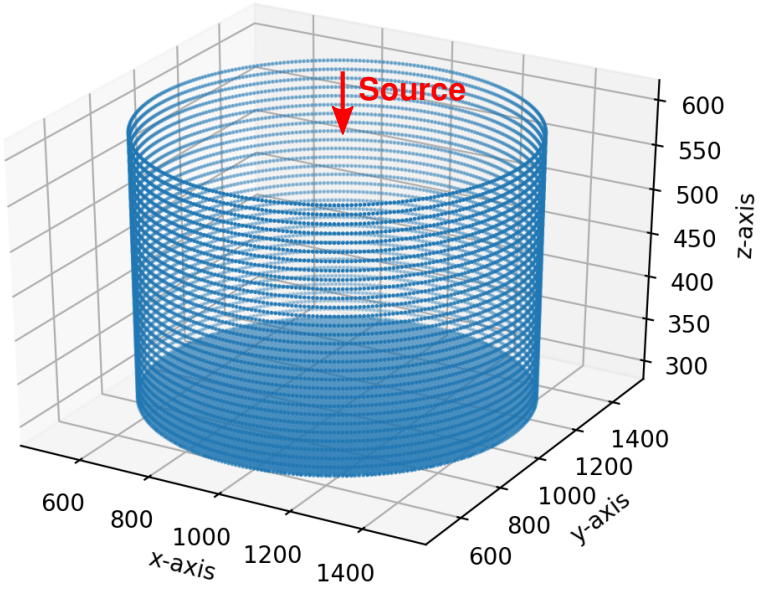

Figure 3.32 – Cylindrical station arrangement around source.
Blue dots represent the stations which are arranged on a cylindrical surface (including the bottom) surrounding the source. The source is located at the surface of the domain which corresponds to $z = 600$.

Chapter 4

Simulation of rockfall generated seismic signals and the influence of surface topography

In this chapter the seismic wave propagation at Dolomieu crater is explored and topography induced amplification is evaluated. After a purely numerical study, observed rockfall signals from Dolomieu crater are analyzed and compared with simulations. The findings build the basis for the rockfall localization method proposed in following Chapter 5. A second part (section 4.8) is attached to this chapter, which picks up the previously derived theory for the estimation of radiated energy and proposes to introduce a correction factor which accounts for the influence of topography. Improvements of the energy estimation are shown by preliminary results using an exemplary rockfall at Dolomieu crater.

4.1 Abstract

Rockfalls generate seismic waves which contain valuable information on their properties. However, as they predominately occur in mountainous regions, the generated seismic waves are prone to be affected by the strong surface topography. For this reason, the influence of topography on ground motion and in particular surface wave propagation is investigated using the spectral element method on a 3D domain with realistic surface topography of Dolomieu crater at Piton de la Fournaise volcano, La Réunion. Amplification patterns are presented in terms of Peak Ground Velocity (PGV) and total kinetic energy. Depending on the receiver position, topography can (de-)amplify PGV values by factors up to 10, while kinetic energy values can be affected by factors up to 20 relative to a reference model with flat surface. Amplification factors are however strongly depend on the underlying velocity model. Even though laterally smoothly varying velocity models are used without local heterogeneities, amplification patterns differ strongly due to the changes of velocity with depth. Further, the influence of topography resolution is studied. Considerable effects are found on wavelengths which are up to 5 times bigger than the resolution. Analyzing amplification as a function of crater geometry suggests that the variation of topography

curvature affects the seismic wave propagation more than variation of the crater depth.
Spectral ratios of recorded signals generated by rockfalls at Dolomieu crater are computed between different stations. It is demonstrated that these ratios taken within specific time windows are characteristic of the corresponding source position. Comparison with simulations suggests that ratios are dominated by the propagation along the topography rather than by the polarization of the acting source.
Finally, the seismic signature of single impacts are studied. Comparison with simulations help to associate signal pulses to impact sources. It is revealed that a single impact can provoke complex waveforms of multiple peaks, especially when considering topography. Impact forces derived from Hertz contact theory result in comparable magnitudes of real and simulated signals amplitudes. It is emphasized that topography increases variability of both waveforms and amplitudes in dependency of source position and its polarization.

4.2 Introduction

The interaction of the seismic wave field with complex surface geometries can locally modify the seismic ground motion. Anomalously strong shaking on hill tops, mountain ridges or flanks causing severe structural damages at buildings (Lee et al., 1994; Hartzell et al., 1994; Hough et al., 2010) or triggering earthquake-induced landslides (Meunier et al., 2008; Harp et al., 2014) have been related to seismic amplification due to this topographic effect. Data from field experiments support the assumption of amplified ground motion at the mountain top relative to its base (Davis and West, 1973; Pedersen et al., 1994; Spudich et al., 1996).
Numerous studies have tried to quantify numerically the topographic effect on seismic waves generated by deep sources in order to better understand and predict site specific ground motion. Geli et al. (1988) compiled previous results from experimental and theoretical studies with new results of more complex models (i.e. including subsurface layering and neighboring ridges), trying to explain the underestimation of amplification factors in previous numerical simulations. Besides confirming significant amplification at hill tops for wavelengths comparable to the mountain width, they express the need of more complex, three-dimensional models. Bouchon and Barker (1996), simulating the ground motion after the 1994 Northridge, California, earthquake on a homogeneous model with three-dimensional topography, point out that a small hill of less than 20-m high can amplify ground acceleration by 30% to 40% for frequencies between 2 Hz and 15 Hz. Lee et al. (2009a) model the seismic response of the mountainous region of Yangminshan, Taiwan, using the 3D spectral element method and a detailed representation of the topography. They find amplification in peak ground acceleration (PGA) as high as 100% relative to a flat surface. Additionally, they report an increase of up to 200% in cumulative kinetic energy as a result of increased duration of shaking due to complex reflection and scattering processes of the seismic waves at the topography.
Yet, due to complex patterns of amplification and deamplification it is difficult to quantify the effect of topography in a generic way. Maufroy et al. (2015) propose to use the topography curvature, smoothed in dependency of the studied wavelength, as proxy for amplification factors. They confirm correlation between the smoothed curvature and to-

pographic amplification using a database of 200 earthquake ground-motion simulations. Based on the NGA-West2 earthquake catalog (Ancheta et al., 2014), Rai et al. (2017) show statistical biases of site residuals in the ground motion prediction equation (GMPE) presented by Chiou and Youngs (2014) towards relative elevation and smoothed curvature and suggest topographic modification factors dependent on signal frequency and relative elevation. Besides these successful findings, some authors point out the complex coupling between topography and the underlying soil structure which must not be neglected when estimating topographic amplification (Assimaki and Jeong, 2013; Hailemikael et al., 2016; Wang et al., 2018; Jeong et al., 2019).

All the studies mentioned above investigate topographic effects on a seismic wave field of vertical incidence. Lee et al. (2009b) investigates the influence of the source depth on ground motion amplification and demonstrates that amplification in a basin can be reduced when a mountain range is located in between the basin and a shallow source. This suggests that surface topography can have a pronounced influence on the propagation of surface waves as they are subject to an accumulated effect of scattering, diffraction, reflection and conversion. It is crucial to enhance understanding of these mechanisms for the study of shallow seismic sources which have gained increasing attention with the emerging field of environmental seismology (Larose et al., 2015). Several authors investigate numerically the interaction of surface waves with 2D surface geometries such as corners, hills or canyons (Fuyuku and Matsumoto, 1980; Weaver, 1982; Snieder, 1986; Sánchez-Sesma and Campillo, 1993; Zhang et al., 2018b; Wang et al., 2018). Ma et al. (2007) demonstrate that a topographic feature 10 times smaller than the wavelength can still considerably reduce the amplitude of by-passing surface waves. Similar to Lee et al. (2009b), they simulate on a 3D model of San Gabriel Mountains, Los Angeles, California, the shielding effects of large-scale topography on fault-generated surface waves, finding amplification factors in peak ground velocity (PGV) of up to +50 % on the source-side of the mountain range and up to -50 % on the opposite site. Wang et al. (2015) model the influence of an uplifted and a depressed topography on the wave field generated by a vertical point source at the surface above a 2D homogeneous half space. Comparing amplitudes and frequency content between source side and far source side they find that the depressed topography causes stronger contrasts than the uplifted topography, especially for steeper slopes and at higher frequencies.

The present study is focused on seismic waves generated by rockfalls at Dolomieu crater on Piton de la Fournaise volcano, La Réunion. Seismic signals from rockfalls, or more generally from landslides, have been demonstrated to be of great usefulness in order to classify and locate events as well as constrain flow dynamics and rheology (e.g. Vilajosana et al., 2008; Deparis et al., 2008; Favreau et al., 2010; Hibert et al., 2011; Dammeier et al., 2011; Moretti et al., 2012; Bottelin et al., 2014). However, as landslides predominantly occur in areas of strong topographic relief, the measurements are prone to be strongly influenced by topography variations which can lead to erroneous landslide estimates. For example, in order to calculate landslide volumes, the generated seismic energy is estimated from seismic recordings (Hibert et al., 2011). At the same time, energy estimations can vary from station to station. We will show here that topography can partly explain relative signal amplitudes between seismic stations.

In the following we will introduce the study site and present an exemplary rockfall event

at Dolomieu crater by means of camera images and recorded seismic signals. Then, the numerical model for the SEM simulations will be defined which entails a discussion on the seismic velocity profile of Piton de la Fournaise. After setting up the Earth model, the simulated wave propagation is studied on different velocity models. Using a reference model with flat surface, topography induced amplification patterns regarding peak ground velocity (PGV) and total kinetic energy are computed. By this, the influence of the underlying velocity model is shown. Additionally, amplification patterns from horizontal seismic sources are discussed. As the resolution of topography on the numerical domains is limited, synthetic seismograms are compared on models with different topography resolutions. Also, similar to authors of previous studies who try to quantify the effect of topography in terms of its geometric parameters, as for example canyon width over canyon depth (Wang et al., 2015) or frequency-scaled curvature (Maufroy et al., 2015), the influence of crater depth and its curvature on ground motion is investigated.
Finally, real seismic signals generated by rockfalls at Dolomieu crater are analyzed. To begin, simulated and observed spectral ratios between seismic stations are compared. The ratios allow to investigate the spectral content of the signals independently of the rockfall source. The aim is to find out, whether the spectral ratios are characteristic to the source position, to its polarization or to path effects from the propagation along the topography. Subsequently, we investigate the seismic signature of a rockfall impact. For this, an event consisting of a single boulder is selected in order to be able to well separate between different impacts. The synthetic waveforms from a model with flat surface and from the model with topography are compared to characteristics of the real rockfall signals. In order to compare signal amplitudes, impact forces are estimated based on Hertz contact theory.

4.3 Study site

The study site of the present work is located on Piton de la Fournaise volcano, La Réunion (see Figure 4.1). Its summit is characterized by 340 m deep Dolomieu crater which collapsed in 2007 (e.g. Staudacher et al., 2009). Since then, due to instabilities of the crater walls, high rates of rockfall events are observed within the crater (Hibert et al., 2011, 2014b, 2017b; Durand et al., 2018; Derrien et al., 2019).
The high quantity of events together with a dense seismic network monitored by the *Observatoire Volcanologique du Piton de La Fournaise* (OVPF) provide excellent conditions for the study of rockfalls. Using recorded seismic signals, past studies investigate the link between rockfall activity and external forcings such as rain or seismicity, the spatio-temporal evolution of rockfall occurrences as well as their volumes (Hibert et al., 2014a, 2017b; Durand et al., 2018). Additional to the seismic stations, three cameras positioned on the crater rim are monitoring rockfall activity. This allows to correlate video images to rockfall seismic signals.
As an example, Figure 4.2 shows images and seismic signals of a rockfall on the southern crater wall on February 28, 2016. The presented event consists of a few boulders (clearly detectable on the video are three boulders) which are moving from the top of the crater wall towards its bottom within around 30 s. As we want to study in detail high frequency rockfall signals (> 1 Hz), events which contain a minimum number of involved boulders are

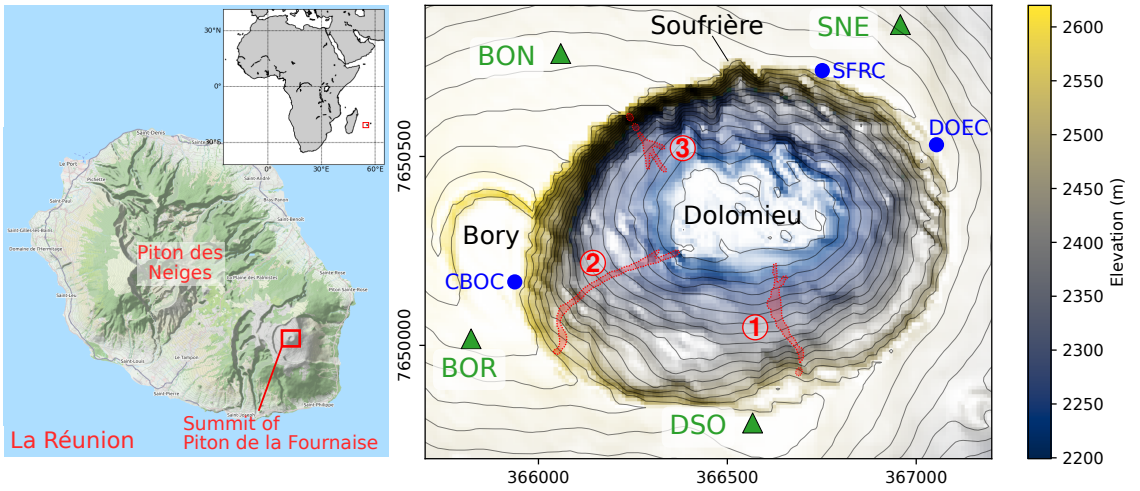

Figure 4.1 – Map of La Réunion and Dolomieu crater. *Left:* The island of La Réunion located in the Indian Ocean, built up by two volcanoes: dormant Piton des Neiges in the northwest and active Piton de la Fournaise in the southeast. *Right:* The summit of Piton de la Fournaise with 340 m deep Dolomieu crater and smaller craters Bory and Soufrière. Trajectories of three rockfalls which will be analyzed in the following are approximated by red shaded zones. Seismic stations BON, BOR, DSO and SNE are marked by green triangles. Cameras CBOC, DOEC and SFRC are marked by blue dots. Contour lines show elevation differences of 20 m.

of advantage as they imply a less complex seismic source which can be located with the help of camera images. In contrast, rockfalls of multiple blocks or granular flows constitute a spatially distributed source in which single impacts can hardly be identified.
The first movement for the shown rockfall can be detected in snapshot a). At that time, a large signal amplitude is recorded on station DSO, which is located very close to the source position. Subsequently, the rockfall travels through a small valley (see b)) and accelerates towards the position in c). The acceleration of the boulder results in strong impacts which can be detected on both the signal and the spectrogram after time c) at all stations. A time corresponding to snapshot d), the first boulder arrives at the crater bottom, whereas a second boulder is half-way down. Again strong amplitudes are measured around time d), probably corresponding to the second boulder. Around time e), the last movements of a third block is visible. Afterwards, some hints of motion of smaller blocks detected. Signal amplitudes are decaying correspondingly.
It can be observed that station DSO records very strong signals in the beginning, while signal amplitudes increase slowly at the other stations. This is certainly related to the changing source-receiver distance. Additionally, as shown hereafter, topography may influence the signal amplitudes depending on the source position in respect to the receiver position. From the spectrograms we can see that the main frequency content is between 3 Hz and 20 Hz. Later we will discuss on the frequency content of single impacts using Hertz contact theory. This suggests that the high frequency content is limited by the inverse of the impact time which is greatly dependent on the impact speed.

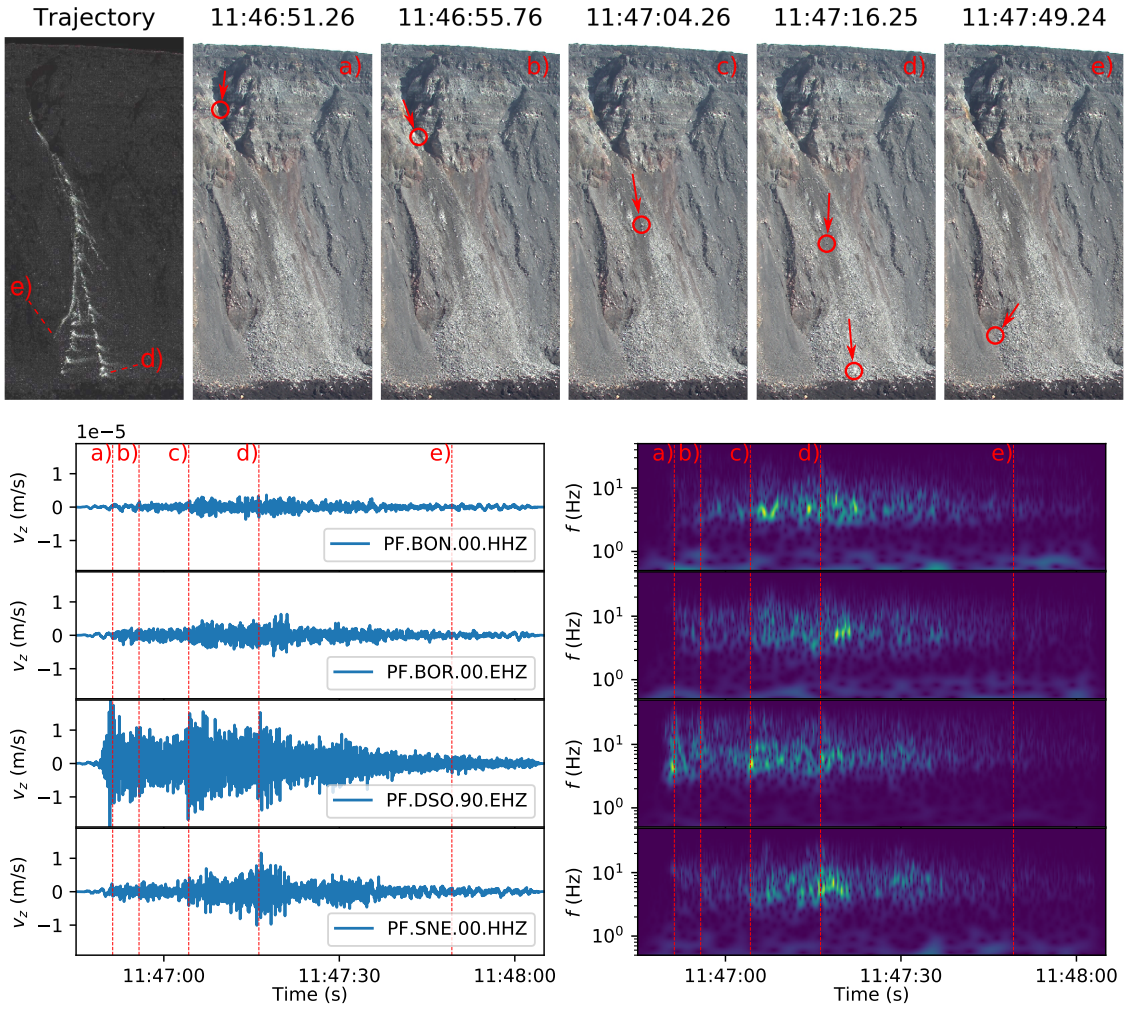

Figure 4.2 – Rockfall at the southern wall of Dolomieu crater on February 28, 2016. For location see rockfall **1** in Figure 4.1. *Top*: The left image shows the rockfall trajectory, reconstructed from differences between successive camera images during the whole rockfall duration. To the right, 5 snapshots are shown taken at specific times from camera SFRC. Circles mark a selection of rockfall positions, while the arrows indicate the direction of arrival. *Bottom*: Vertical ground velocity recorded at stations BON, BOR, DSO and SNE with corresponding spectrogram to the right (calculated using Stockwell transform). Vertical lines from a) to e) mark the times of camera snapshots above.

4.4 SEM simulations

In order to study the effect of topography on rockfall seismic signals recorded at different stations, seismic wave propagation is simulated based with the 3D Spectral Element Method (SEM, e.g. Festa and Vilotte, 2005; Chaljub et al., 2007). The seismic source is modeled using a Ricker wavelet with dominant frequency of 7 Hz, implemented as point force on the surface. This source covers the bandwidth between 2 Hz and 20 Hz which is predominantly observed for the rockfalls at Dolomieu crater.

4.4.1 Mesh of the Earth model

Figure 4.3 shows a cross-section through the spectral-element mesh. The dimensions of the domain measure $x = 2100\,\text{m}$, $y = 1800\,\text{m}$, and $z = 600\,\text{m}$. Absorbing boundaries

(PMLs) of 160 m thickness are added on the sides and on the bottom in order to simulate an open domain. The elements are successively deformed in vertical direction in order to accommodate the surface topography which is taken from a digital elevation model (DEM) of 10 m resolution. In the following we will first use a filtered topography with 30 m corner wavelength, implemented on a mesh with elements of 20 m side length and afterwards the unfiltered topography on a mesh with elements of 10 m side length which corresponds to the best available DEM. For the latter, in order to decrease computational costs, the element size is increased from 10 m to 30 m at 150 m below the surface as shown in Figure 4.3 (*Zone of refinement*). However, problems in the numerical method can arise when the mesh refinement is distorted by small-scale topography variations. For this reason a low-pass filtered topography is introduced as reference horizon (*Buffer layer*) at 100 m below the surface.

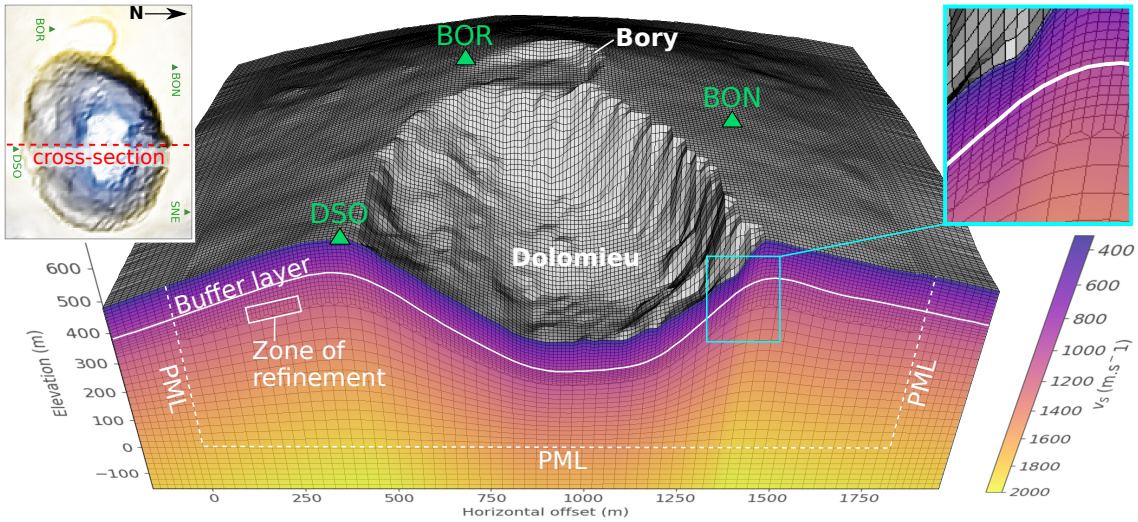

Figure 4.3 – SEM mesh with topography of Piton de la Fournaise. Cross-section through Dolomieu crater of model with topography resolution of 10 m. Perspective as seen from the East with Bory crater located in the background. The color map corresponds to the Lesage velocity model (see section 4.4.2). The buffer layer 100 m below the surface dampens small-scale topography variations. The zone of refinement at 150 m below the surface connects elements of 10 m and 30 m side length. Absorbing boundaries (PMLs) of 160 m thickness on the sides and on the bottom of the domain are implemented so that topography and velocity model are smoothly continued outwards.

4.4.2 Velocity model

Three different velocity models are implemented: (1) a homogeneous model, (2) a model with shallow low S-wave velocity layer, and (3) a model with smoothly increasing velocity as proposed by Lesage et al. (2018) for shallow volcano structures. The velocity-depth profiles are illustrated on the left hand side of Figure 4.4 and summarized in Table 4.1. The generic model by Lesage et al. (2018) is based upon measurements at multiple andesitic and basaltic volcanoes. Wave speed c for P- and S-wave is expressed as follows:

$$c_i(z) = c_{i0}[(z + a_i)^{\alpha_i} - a_i^{\alpha_i} + 1], \quad i = P, S, \tag{4.1}$$

where z is the depth below surface while α_i and a_i are fitting parameters as defined in Table 4.1.

The velocity profiles are compared to the S-wave velocity model inverted from ambient noise recordings at Piton de la Fournaise by Mordret et al. (2015). The shaded zone shown in Figure 4.4 corresponds to depth-profiles extracted from the inverted 3D model in the vicinity of Dolomieu crater. A good agreement is observed with the Lesage velocity profile. The discrepancy in the first 100 m can be associated to missing high frequency content in the model of Mordret et al. (2015), who inverted frequencies below 2.5 Hz.

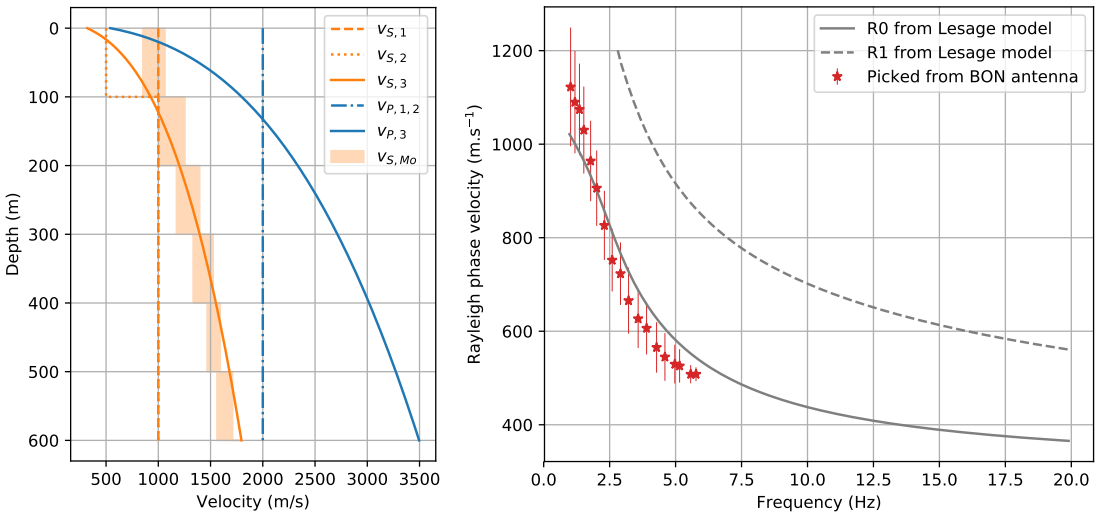

Figure 4.4 – Velocity profiles and dispersion curve measurement at Piton de la Fournaise *Left:* S- and P-wave velocity for (1) homogeneous model ($v_{S,1}$ and $v_{P,1}$), (2) model with shallow S-wave velocity layer ($v_{S,2}$ and $v_{P,2}$), and (3) Lesage velocity model ($v_{S,3}$ and $v_{P,3}$). The shaded zone ($v_{S,Mo}$) is extracted from the inverted 3D S-wave model of Mordret et al. (2015). *Right:* Theoretical dispersion curves of Lesage model for fundamental (R0) and first mode (R1) Rayleigh wave velocity together with picked dispersion curves from antenna around BON. The errors are estimated from the uncertainty during dispersion curve picking.

In order to further validate the Lesage model for our study site, we compare Rayleigh velocity dispersion curves from noise measurements at an antenna located around station BON with theoretical values from the Lesage model (right hand side of Figure 4.4). Picks from the antenna measurements are determined using the Modified Spatial Autocorrelation (MSPAC) Toolbox (Köhler et al., 2007; Wathelet et al., 2008) as implemented in the Geopsy software (www.geopsy.org). Theoretical dispersion curves are calculated from the Lesage model using modal summation from *Computer Programs in Seismology* (Herrmann, 2013). The measured values are in good agreement with the fundamental Rayleigh velocity dispersion curve. Due to minimum antenna aperture of 30 m, coherent dispersion curves could not be picked above 6 Hz.

Despite missing measurements above 6 Hz, the Lesage model is assumed to be the most reasonable model for the shallow high frequency velocity structure of Piton de la Fournaise volcano as it is based upon measurements at comparable volcanoes.

Implementation of the velocity model on the SEM mesh is realized so that it follows the topography elevation. This means, in respect to the velocity profiles shown in Figure 4.4, that 0 m depth is imposed for each point at the surface of the domain. This is reasonable as a main cause for velocity variation is the compaction of material with depth due to increasing overburden pressure. The resulting model is visualized in Figure 4.3 for the case

of the Lesage velocity profile.
Rock density ρ as well as quality factors Q_P and Q_S for intrinsic attenuation of P- and S-wave velocity, respectively, are chosen based on previous studies on Piton de la Fournaise and similar volcanoes (Battaglia and Aki, 2003; O'Brien and Bean, 2009; Hibert et al., 2011). All parameters are summarized in Table 4.1.

Table 4.1 – Model parameters for the SEM simulations. P- and S-wave velocity v_P and v_S, density ρ, and P- and S-wave quality factor Q_P and Q_S for (1) homogeneous model, (2) model with shallow S-wave velocity layer, and (3) Lesage velocity model.

Model	v_P	v_S	ρ (kg.m^{-3})	Q_P	Q_S
1) homogeneous	$2000\,\mathrm{m.s^{-1}}$	$1000\,\mathrm{m.s^{-1}}$	2000	80	50
2) low v_S layer	$2000\,\mathrm{m.s^{-1}}$	$\begin{cases} 500\,\mathrm{m.s^{-1}} \text{ (top } 100\,\mathrm{m}) \\ 1000\,\mathrm{m.s^{-1}} \text{ (below)} \end{cases}$	2000	80	50
3) Lesage	$\begin{cases} c_{P0} = 540\,\mathrm{m.s^{-1}} \\ \alpha_P = 0.315 \\ a_P = 10 \end{cases}$	$\begin{cases} c_{S0} = 320\,\mathrm{m.s^{-1}} \\ \alpha_S = 0.300 \\ a_S = 15 \end{cases}$	2000	80	50

4.4.3 Wave propagation from a vertical surface load

In the following the wave propagation along the topography is illustrated on different velocity models. A vertical point source is placed on the southern crater wall, corresponding approximately to the starting position of the rockfall shown in Figure 4.2. Simulations are carried out on the domain with 20 m elements and topography filtered at 30 m corner wavelength. A comparison to simulations on the high resolution topography is carried out later. Figure 4.5 shows synthetic seismograms recorded on the surface along an array crossing the source position, Dolomieu crater and station BON (see inset for location of the array). Snapshots of the propagating seismic wave field on a cross-section along the array are shown below. Note that all amplitudes correspond to vertical ground velocity. The simulations were realized without intrinsic attenuation in order to enhance visibility of the wave field over time. This caused reflections from the boundaries which we will ignore here. Attenuation is implemented in the simulations for the analyses in the following sections.
For the simulation with the homogeneous domain (left column of Fig. 4.5), we can identify in the first snapshot at time $t = 0.8\,\mathrm{s}$ the P-wave traveling downwards as being the fastest wave with propagation direction parallel to the the shown vertical ground velocity. At time $t = 1.6\,\mathrm{s}$ the original S-wave is visible on the bottom of the cross-section. The S-wave can be identified as the direction of propagation is perpendicular to the vertical ground velocity. Just above is a newly created S-wave (annotated as SR) which separated at the bottom of the crater from the Rayleigh wave due to the convex topography. Yet, part of the energy continues as Rayleigh wave along the topography towards the rim of the crater. Also visible is a diffracted surface wave (annotated as Rd). It split from a wave front traveling towards station BOR and took a curved path along the flank of the crater. At time $t = 2.0\,\mathrm{s}$ we can see this diffracted Rayleigh wave continuing outside the crater

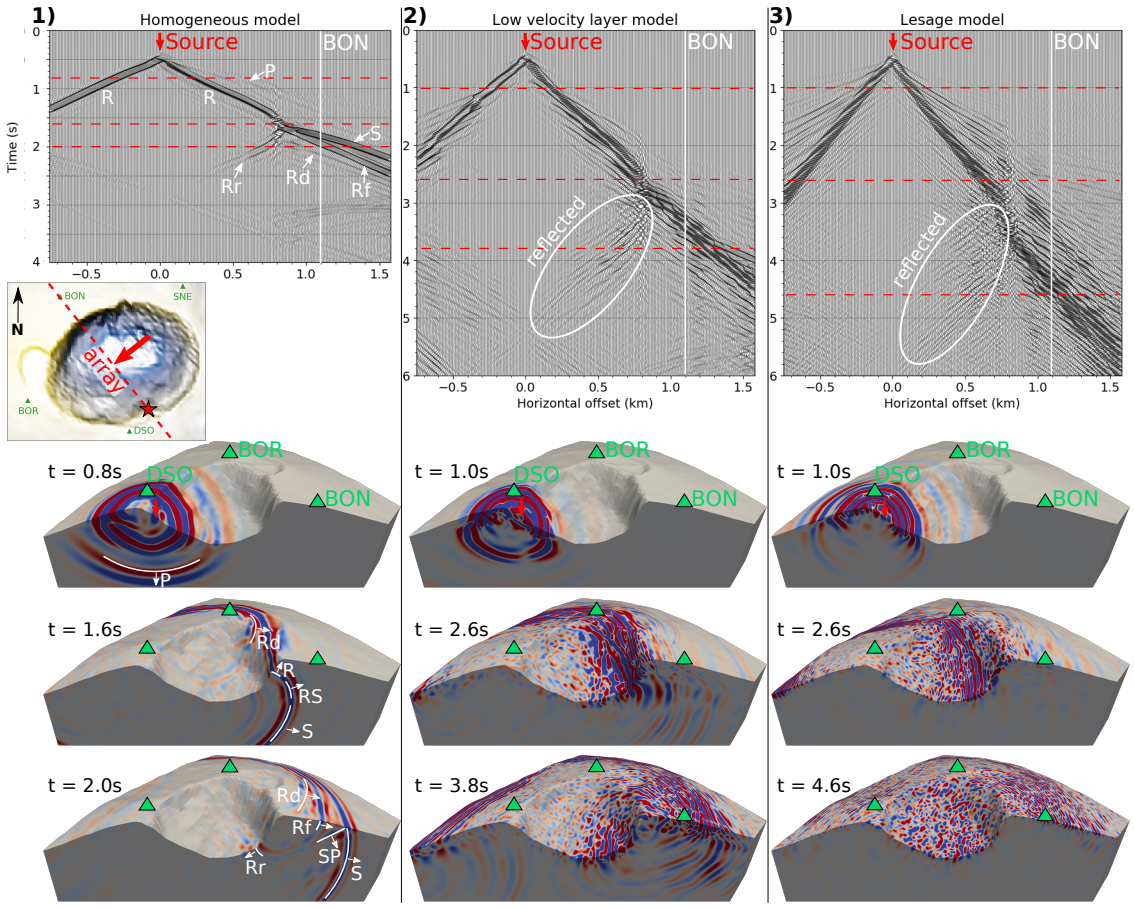

Figure 4.5 – Wave propagation from a vertical surface load on different velocity models. Synthetic seismograms (*top row*) recorded at an array crossing the source, Dolomieu crater and station BON (see inset) for (1) homogeneous model (*left*), (2) model with shallow S-wave velocity layer (*middle*), and (3) Lesage velocity model (*right*). Traces are normalized to themselves and show vertical ground velocity. Snapshots of the wave field on cross-sections along the same array are shown below, corresponding to the times marked by red dashed lines. Intrinsic attenuation was not applied in these models in order to enhance visibility of the propagation wave field. Reflections from the boundary on the left can be observed at later times. These vanish when introducing attenuation as has been done for the analyses in the sections hereafter.

and arriving at station BON at different azimuth than the Rayleigh wave which traveled diagonally across the crater and its rim (annotated as Rf). The energy of Rayleigh wave Rf was partly reflected at the crater rim so that a new Rayleigh wave Rr is traveling backwards through the crater. Up front (on the very right of the domain), a direct S-wave hits the surface and is partly reflected and converted to build a straight P-wave front traveling downwards at an oblique angle to the horizontal (annotated as SP).

Adding a low S-wave velocity layer (middle column in Fig. 4.5) drastically changes the wave field due to reflections within this layer and the dispersive character of Rayleigh waves. Looking at the synthetic seismograms we can observe in the first 2.5 s a wave train of dispersive character overlaid by multiples (compare to Fig. 3.16 in Chapter 3). Compared to the homogeneous model, it is of increased complexity and longer duration. At around $t = 2.6$ s the waves hit the crater rim opposite to the source and are partly reflected (marked by ellipse) just as in the homogeneous case. The snapshots at times $t = 2.6$ s and $t = 3.8$ s show in contrast to the homogeneous case a much more scattered wave field of

irregular amplitude patterns. Similar to Lee et al. (2009a) who find characteristic patterns dependent on the resolution of the imposed topography, the characteristic length of these patterns is likely to be related to the resolution of the topography and the flat element surfaces of 20 m side length.
In the case of Lesage velocity model (right column of Fig. 4.5) the majority of energy stays close to the surface of the domain due to the velocity gradient. Scattering of the wave field along the topography is even more elevated than in the case with low velocity layer and the duration of shaking is prolonged. From synthetic seismograms (top right of Fig. 4.5) we can still identify the outward propagation of energy as well as the reflection of part of the energy at the crater rim (marked by ellipse).
Figure 4.6 compares the seismograms of the three different velocity models recorded at station BON (their locations are indicated by a white lines in Fig. 4.5). It can be observed

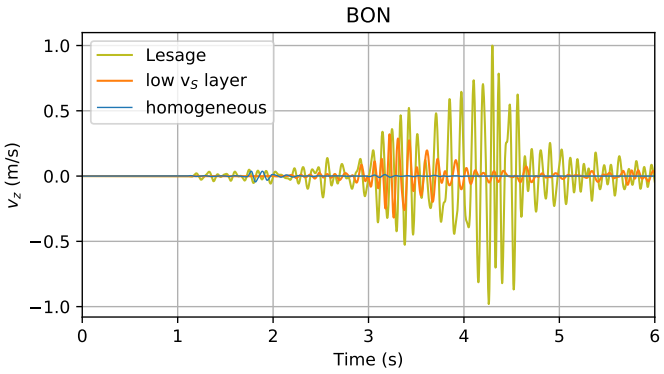

Figure 4.6 – Seismograms at stations BON simulated on different velocity models.
Comparison of seismograms simulated on different velocity models recorded at station BON (see Fig. 4.5 for location). Complexity and duration of waveforms as well as their amplitudes increase from homogeneous model over low v_S layer model towards Lesage model.

that the smallest amplitudes are obtained in the case of the homogeneous model as a big part of the energy is directed downwards into the subsurface. Amplitudes for the Lesage model are the biggest since more energy stays close to the surface due to the velocity gradient. The amplitudes for the model with low velocity layer are intermediate. Furthermore, the complexity of the wave forms as well as their duration increases when going from the homogeneous model over low v_S layer model towards the Lesage model. This is caused by increased scattering along the topography as already mentioned before as well as the appearance of multiples and first mode Rayleigh waves (see Fig. 3.16 in Chapter 3).

4.5 Influence of topography on simulated wave propagation

4.5.1 Amplification of peak ground velocity (PGV)

In order to quantify topographic ground motion amplification, simulations on a model with topography are compared to a reference model with flat surface. For this, the ratio between PGV values measured on both models at the same horizontal coordinates is calculated. Figure 4.7 shows the peak ground velocity ratio $\mathrm{PGV}_{\mathrm{z,t}}/\mathrm{PGV}_{\mathrm{z,f}}$ between model with topography and flat reference model for the three velocity models.
The homogeneous model shows a contrast between source side of the crater and the opposite side. On the source side an amplification of PGV is present while the far side is

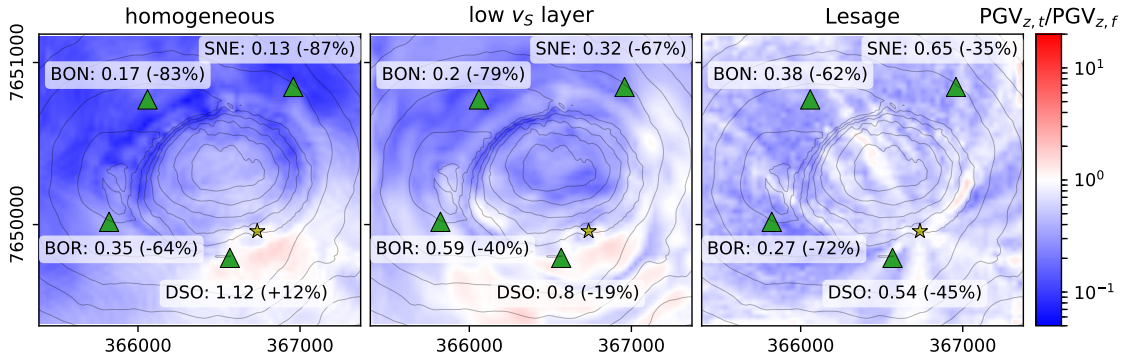

Figure 4.7 – Topographic amplification of vertical PGV. PGV amplification in respect to a flat reference model for the homogeneous model (*left*), the model with shallow low velocity layer (*middle*) and the Lesage velocity model (*right*). The yellow star denotes the source, green triangles the stations. Annotations give ratios measured at the station locations as well as percentage of topographic amplification. Neighboring contour lines differ 60 m in elevation.

characterized by a strong deamplification. The amplification on the source side (+12% at DSO) can be explained by the simultaneous arrival of surface and direct waves emitted from the source. Deamplification on the far-side of the source (−83% at BON and −87% at SNE)can be understood as shadow zone behind the crater as a major part of wave energy is diverted downwards into the subsurface due to the crater shape.

In case of the model with low velocity layer, general amplification on the source side and deamplification on the far-source side of the crater are still present but contrast are less pronounced (deamplification at station DSO goes down to −67%) and patterns become more complex (DSO is now deamplified by −19%). The introduction of a low velocity layer causes more energy to stay at the surface and thus reduces the shadow zone behind the crater. The uneven topography together with the underlying low velocity layer causes complicated reflections and wave conversions which lead to increased complexity of amplification patterns.

The contrast between source side and far-source side of the crater decreases further for the Lesage velocity model (−45% at DSO, −62% at BON and −35% at SNE). As could be seen on the wave propagation snapshots in Figure 4.5, the gradient causes energy to stay close to the surface. Whereas a lot of energy is lost downwards due to the crater topography in the homogeneous model as well as in the low velocity layer model, the velocity gradient in the Lesage model guides waves efficiently along the crater topography or back to the surface which causes a more homogeneous amplification pattern. Scattering away from the surface due to surface roughness as well as conversion from vertical to horizontal energy leads to an overall deamplification in vertical PGV. Still, due to focusing mechanisms of the 3D topography, ray-shaped zones starting off the source location can experience PGV amplification.

The conversion from vertical to horizontal energy is illustrated in appendix 4.9.1. The amplification patterns of horizontal PGV from a vertical source are shown in Figure 4.42 and 4.43 for north- and east-component of ground motion, respectively. Strong topographic amplification can be observed east-west from the source for the north-component and north-south from the source for the east-component. This is due to the fact that a vertical source does not generate energy on the transverse components. Topography can

cause energy on the transverse component due to wave conversion or diffraction resulting in the strong directionality of amplification.

4.5.2 Amplification of kinetic energy

Scattering and diffraction of the wave field along the topography increase the complexity and the duration of recorded waveforms. This is not taken into account when measuring PGV amplification. For this reason, we will measure amplification of kinetic energy over the whole signal duration. This is done by time integration of the squared ground velocity $\mathbf{v}^2(\mathbf{x}, t) = [v_x^2(\mathbf{x}, t) + v_y^2(\mathbf{x}, t) + v_z^2(\mathbf{x}, t)]^{0.5}$, where $\mathbf{x}$ denotes the horizontal coordinates of the receiver position. The resulting ratio $E_{\text{topo}}/E_{\text{flat}}$ of total kinetic energy between model with topography and flat reference model is shown in Figure 4.8 for the three different velocity models.

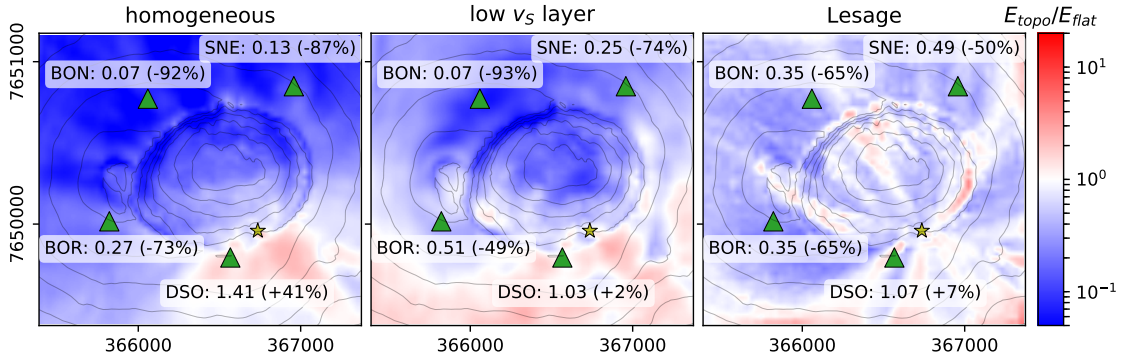

Figure 4.8 – Topographic amplification of total kinetic energy. Energy amplification in respect to a flat reference model for the homogeneous model (*left*), the model with shallow low velocity layer (*middle*) and the Lesage velocity model (*right*). The yellow star denotes the source, green triangles the stations. Annotations give ratios measured at the station locations as well as percentage of topographic amplification. Neighboring contour lines differ 60 m in elevation.

The amplification patterns of kinetic energy show more contrast than the PGV ratios. For the homogeneous model, amplification increases to +41% at DSO and decreases to −92% at BON. Again, this is due to the fact that topography does not only influence peak amplitude, but also complexity and duration of the signal. Similar to the homogeneous model, amplification patterns on the two heterogeneous models show increased contrasts. The ray-shaped zones of amplification on the Lesage model are more pronounced than for the PGV ratios. This means, that topography guides both vertical and horizontal energy along these paths. Remarkable as well is increased amplification at parts of the crater cliff ridge which is possibly due to the discussed reflection of Rayleigh waves at these positions. In order to verify that the amplification pattern differences between the velocity models do not solely arise from changes in wavelength, amplification patterns in different frequency bands are compared in appendix 4.9.2. Figure 4.44 and 4.45 show energy amplification in three different frequency bands for the homogeneous model and the Lesage model. While the amplified source side and deamplified far-source side remain for all frequency bands on the homogeneous model, we can see complex amplification patterns for all frequency bands on the Lesage model. If differences in amplification were only due to changes in wavelength, we would expect similar patterns for the intermediate frequency band on

homogeneous model (Rayleigh wavelength $\lambda \approx 1000\,\mathrm{m.s^{-1}} \div 10\,\mathrm{Hz} = 100\,\mathrm{m}$) and the low frequency band on the Lesage model (Rayleigh wave length $\lambda \approx 580\,\mathrm{m.s^{-1}} \div 5\,\mathrm{Hz} \approx 116\,\mathrm{m}$, see dispersion curves in Fig. 4.4).

4.5.3 Horizontal sources

Up to now only vertical surface loads were considered. However, the basal forces generated by rockfalls on the ground can also have horizontal components. Here we show amplification patterns for horizontal sources on the Lesage velocity model. Figure 4.9 illustrates vertical PGV amplification for a wave field generated by a horizontal surface force in east-direction (*left*) and in north-direction (*right*).

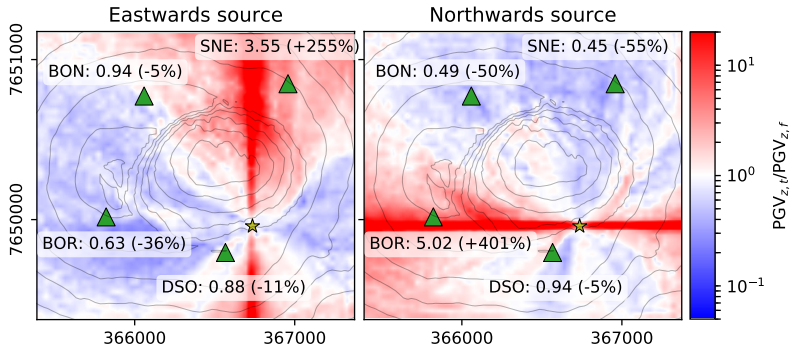

Figure 4.9 – PGV amplification for horizontal source. Vertical PGV amplification for eastwards- and northwards-directed source. The star denotes the source position and neighboring contour lines differ 60 m in elevation.

A strong directionality is visible in the PGV amplification pattern. This is due to the fact that in case of the flat reference model a horizontal source does not generate radial or vertical seismic energy perpendicular to its polarization. Topography however can give raise to radial or vertical energy in this direction by conversion from transverse energy or due to diffracted waves paths.
Amplification of total kinetic energy is shown in Figure 4.10. The directionality patterns

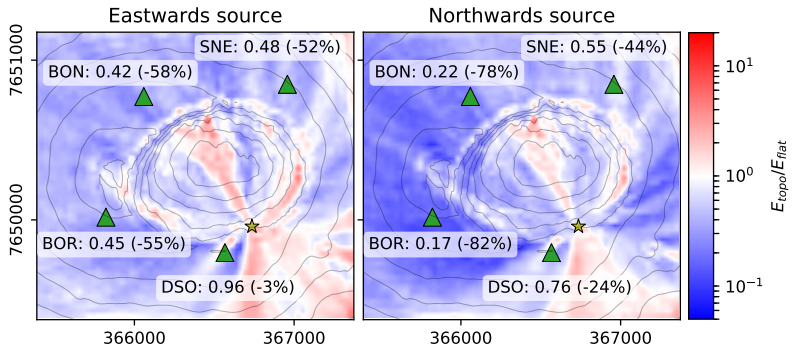

Figure 4.10 – Energy amplification for horizontal source. Energy amplification for eastwards- and northwards-directed source. The star denotes the source position and neighboring contour lines differ 60 m in elevation.

are no longer visible as the total kinetic energy takes into account all components of the measured ground velocity. It is remarkable that the amplification patterns are comparable between the two different horizontal source directions as well as the vertical source direction shown before in Figure 4.8. This suggests that topography guides seismic energy on trajectories along the surface in dependency of the source position and only weakly dependent on the source polarization.

4.5.4 Topography resolution

In the following we investigate the influence of topography resolution on the simulated wave propagation. Figure 4.11 compares synthetic seismograms obtained from a model with flat surface, from a model with 20 m topography resolution (low-pass filtered with 30 m corner wavelength), and from a model with 10 m topography resolution. Waveforms recorded at the crater surrounding stations BON, BOR, DSO and SNE are shown.

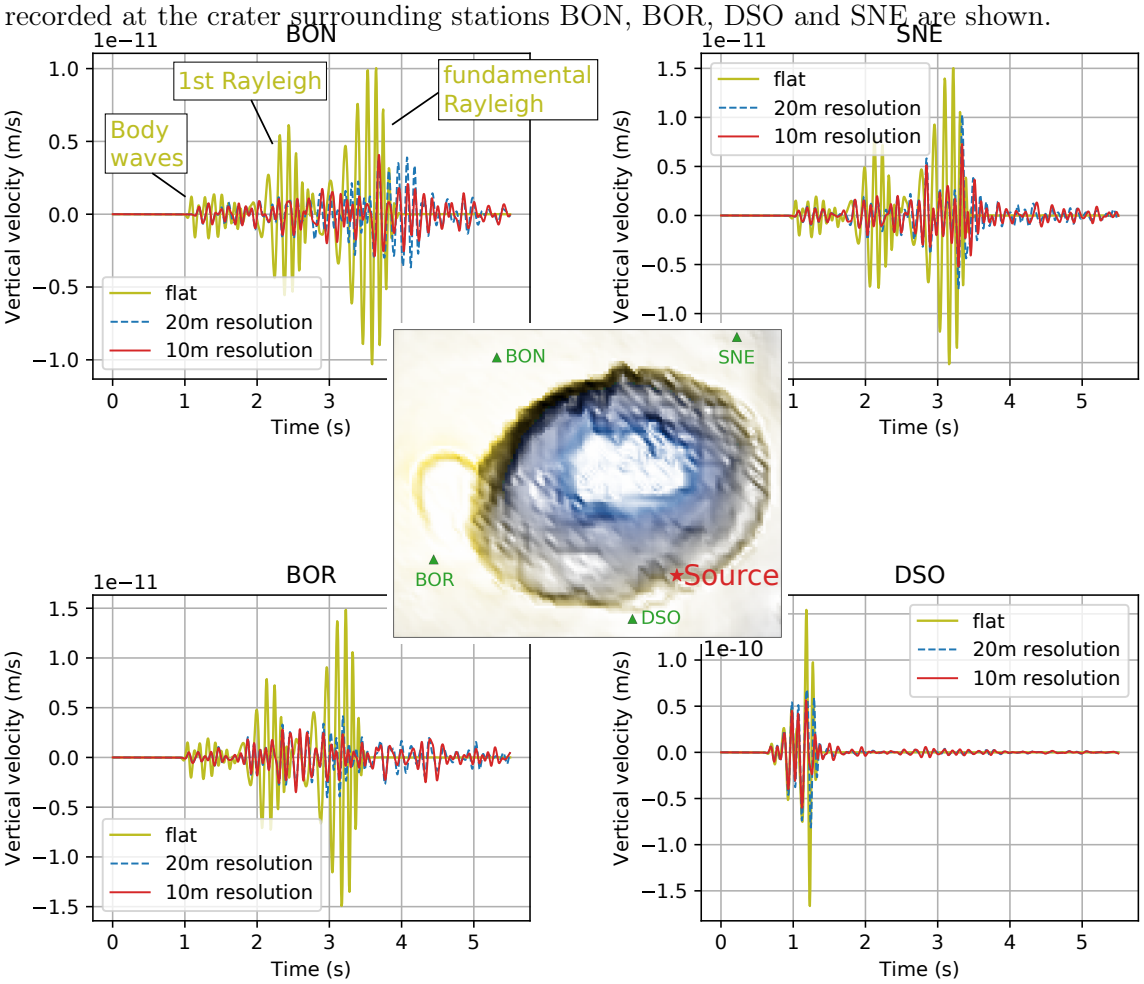

Figure 4.11 – Influence of topography resolution on synthetic waveforms. Comparison of synthetic seismograms on model with flat surface, model with 20 m topography resolution and model with 10 m topography resolution. Seismograms recorded at stations BON, BOR, DSO and SNE which are surrounding Dolomieu crater. The source is located on the southwestern crater wall.

First of all we can observe that the amplitude diminishes on the models with topography in respect to the simulations from the flat model. This was expected form the preceding analyses. Further, topography causes waveforms of longer duration and of more complex forms. For the flat model, wave packets corresponding to body waves, 1st mode Rayleigh waves and fundamental mode Rayleigh waves are well separated (see Figure 3.16 in Chapter 3, where wave types for the Lesage model are analyzed). They become less distinguishable when introducing topography. However, it is noticeable that the first part of the wave train is almost identical for both models with topography. At later times, amplitudes are smaller on the model with 10 m topography resolution. This suggests, that mainly fundamental Rayleigh waves are affected as well as 1st mode Rayleigh waves of higher frequencies which

arrive later due to their lower velocity compared to low frequencies of the 1st mode. Body waves may stay unaffected as they interact less with topography and the recording stations are located at relatively flat planes. Figure 4.12 shows the spectra of the signals recorded at station BON. Differences between the two models with topography become evident above

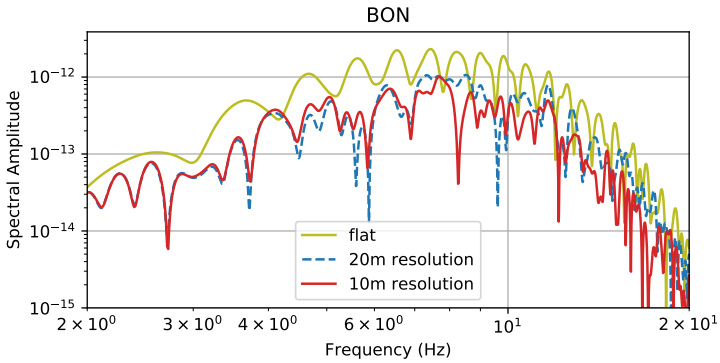

Figure 4.12 – Synthetic crater model. SEM mesh with synthetic crater topography and imposed surface roughness. The Lesage velocity model is implemented to follow the surface elevation.

around 5 Hz. This corresponds to a minimum wavelength of 116 m for the fundamental Rayleigh wave ($\lambda \approx 580\,\mathrm{m.s^{-1}} \div 5\,\mathrm{Hz} \approx 116\,\mathrm{m}$). Concluding that wavelength below 116 m are still sensitive to the change in topography resolution, it means that 1st mode Rayleigh waves of above 7 Hz are affected ($\lambda \approx 800\,\mathrm{m.s^{-1}} \div 7\,\mathrm{Hz} \approx 114\,\mathrm{m}$). This analysis suggests surface waves are sensitive to changes in topography resolution which are 5 times smaller than their wavelength.

The decrease of the amplitude for higher resolved topography can be attributed to increased scattering away from the surface. Interestingly, Lee et al. (2009a) finds the opposite when comparing waveforms on different topography resolution for a source deep beneath the surface. This implies that the source position plays a major role for the effect of topography. On the one hand, topography can increase ground shaking and thus trap energy close to the surface. On the other hand, in the case of waves traveling along the surface, the topography can increase scattering and thus prevent energy to propagate. Similar conclusions are drawn by Lee et al. (2009b) who investigate how topography effects are modulated by the source depth in regards to ground motion in a basin located behind a mountain range.

4.5.5 Crater depth and curvature

In order to investigate the effect of topography curvature and crater depth on seismic ground motion, we create a synthetic crater model. For this, we use the equation for crater topographies proposed by Soontiens et al. (2013), suppressing the crater rim. Figure 4.13 shows a cross section through one of the created synthetic crater models. The underlying medium corresponds to the Lesage velocity model.

A natural surface roughness is imposed in order to break the perfect symmetry of the crater shape which leads to symmetric interferences of the propagating wave field (illustrated in appendix 4.9.3 on the left hand side of Figure 4.46). The surface roughness is taken from a real DEM and band-pass filtered at corner wavelengths of 40 m and 100 m (illustrated on the right hand side of Figure 4.46). Figure 4.14 compares synthetic seismograms recorded along arrays on the models with flat surface, with rough surface and with crater topography. In comparison to the simulation on the flat surface, rough surface introduces scattering

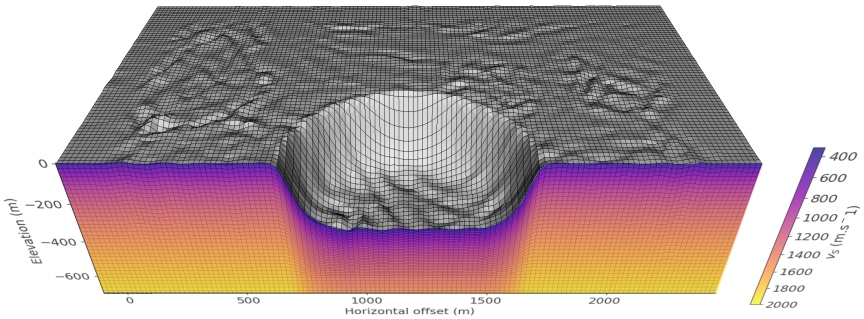

Figure 4.13 – Synthetic crater model. SEM mesh with synthetic crater topography and imposed surface roughness. The Lesage velocity model is implemented to follow the surface elevation.

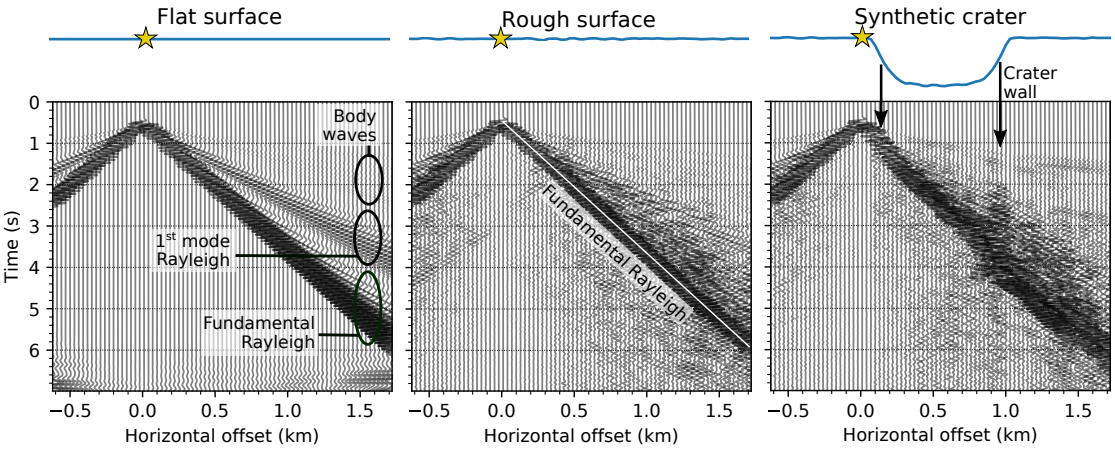

Figure 4.14 – Synthetic seismograms on arrays along different surface topographies. Blue lines illustrate profiles of the surface topographies for the models with flat surface (*left*), rough surface (*middle*), and synthetic crater shape (*right*). Seismograms of vertical ground velocity recorded at the corresponding horizontal positions are shown below, normalized by themselves. Wave types on the flat model are identified as in Figure 3.16 of Chapter 3. The yellow star marks the position of the vertical source. Note that the spurious reverberations in case of the flat surface model after the signal (> 6 s) are trimmed for the analyses hereafter.

of both Rayleigh modes. This leads to prolonged ground shaking. The two modes are no longer clearly separated, even though the main energy from the fundamental mode can be identified. Introducing the crater topography adds more complexity. The wave field becomes distorted particularly close the crater walls. This is similar as for the real crater topography before (see Fig. 4.5).

Before modifying crater depth and curvature in order to investigate their effect on topographic amplification, let us first have a look on amplification patterns due to the surface roughness alone. Figure 4.15 compares total kinetic energy ratio $E_{\text{topo}}/E_{\text{flat}}$ of model with rough surface and model with flat surface for three different frequency bands. All frequency bands are influenced by the surface roughness. We remember that the rough topography is band pass filtered at corner wavelengths 40 m and 100 m. Fundamental Rayleigh wavelengths on the Lesage model are slightly above this range for the average of the lowest frequency band ($\lambda \approx 580\,\text{m.s}^{-1} \div 5\,\text{Hz} = 116\,\text{m}$) and slightly below this range for the average of the highest frequency band ($\lambda \approx 390\,\text{m.s}^{-1} \div 15\,\text{Hz} = 26\,\text{m}$). We remark ray-shaped zones of amplification which are blurred in the lower frequency band and become sharper towards higher frequencies. The variation of topography seem to guide energy along this ray paths. In contrast, some areas of pronounced topography variation (visible by the densification of contour lines) seem to shield the propagation of energy and cause shadow zone behind them. This can for example be observed in north-east direction of the source.

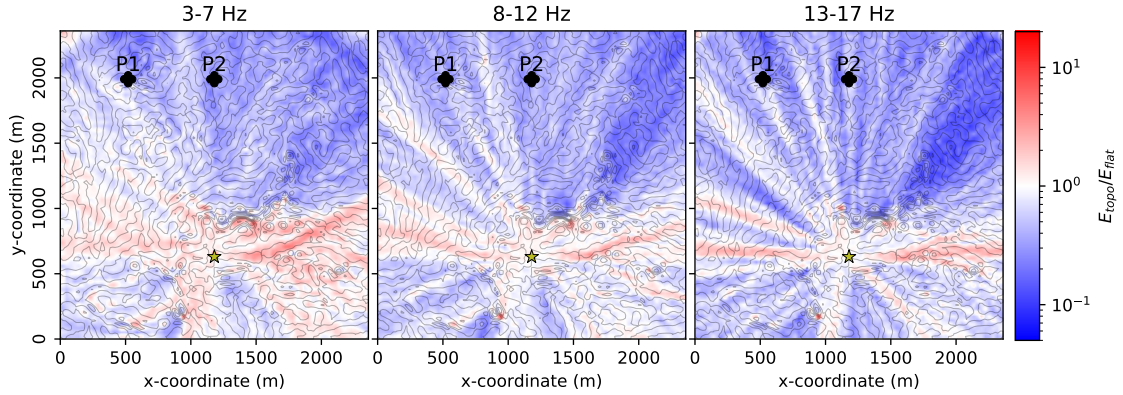

Figure 4.15 – Energy amplification on rough surface in different frequency bands. Energy amplification in respect to a flat reference model in frequency bands 3-7 Hz (*left*), 8-12 Hz (*middle*) and 13-17 Hz (*right*). Spectral ratios at positions P1 and P2 are evaluated in Figure 4.20 and 4.21, respectively. The yellow star denotes the source.

The kinetic energy ratios between model with synthetic crater topography and flat reference model are presented in Figure 4.16. We can recognize amplification patterns caused by

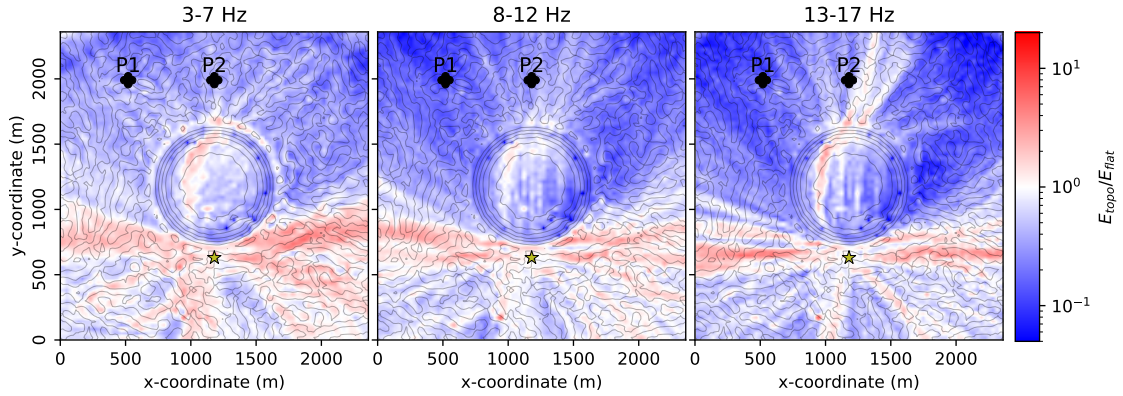

Figure 4.16 – Energy amplification on crater topography in different frequency bands. Energy amplification in respect to a flat reference model in frequency bands 3-7 Hz (*left*), 8-12 Hz (*middle*) and 13-17 Hz (*right*). Spectral ratios at positions P1 and P2 are evaluated in Figure 4.20 and 4.21, respectively. The yellow star denotes the source.

the surface roughness as seen before (compare with Fig. 4.15), superimposed with amplification caused by the crater topography. Globally, the wave field is deamplified behind the crater (as seen from the source position). Higher frequencies seem to be more affected by this than lower frequencies. Nonetheless, paths of amplifications are traversing the crater. The amplification opposite to the source might also be associated to waves which travel on both sides around the crater and interfere opposite to the source (this effect is very pronounced in the case without surface roughness as illustrated in Fig. 4.46 in appendix 4.9.3). This amplification across the crater is also visible in the simulations on the models with real topography of Dolomieu crater (compare to Fig. 4.8 and 4.10).

We will now investigate the sensitivity of amplification on different crater depths and curvatures. The crater parameters were chosen so that on the one hand crater depth varies from small to big with fixed curvature and on the other hand curvature varies from weak to strong with fixed crater depth. Natural surface roughness is imposed on all crater shapes in order to break the perfect symmetry. Figure 4.17 gives an overview of all synthetic crater topographies and compares them to a profile through Dolomieu crater.

To get a first impression on the influence of crater depth and crater curvature, amplification

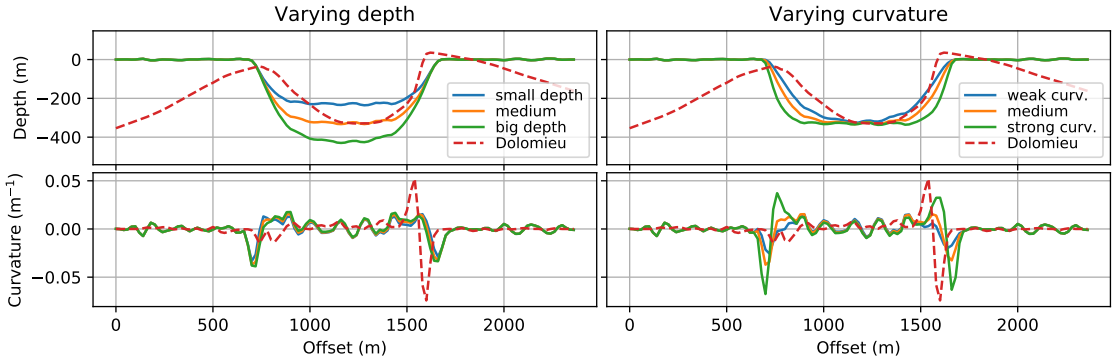

Figure 4.17 – Synthetic crater shapes. Profiles through the created synthetic crater topographies (*top*) and their corresponding curvatures (*bottom*). With fixed curvatures, crater depths vary from small to big (*left*) and with fixed crater depth, curvatures vary from weak to strong (*right*). Red dashed lines correspond to a profile trough Dolomieu crater and its corresponding curvature.

patters of the total kinetic energy are illustrated in Figures 4.18 and 4.19, respectively.

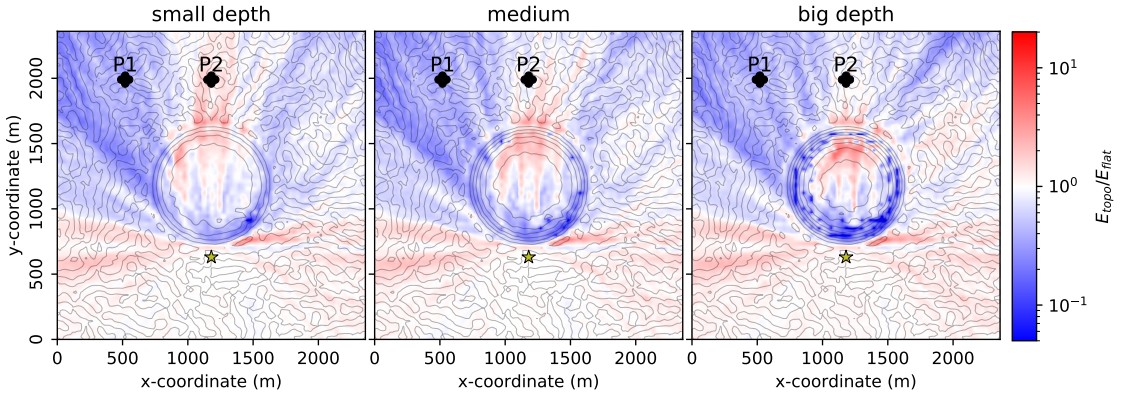

Figure 4.18 – Energy amplification on crater topography for different depths. Ratios of total energy between model with topography and reference model with flat surface for small, medium and big crater depth. Contour lines mark elevation differences of 50 m. Spectral ratios at positions P1 and P2 are evaluated in Figure 4.20 and 4.21, respectively. The yellow star denotes the source. Note that spurious blue dots inside the crater (especially at steep flanks in case of big depth) were caused by numerical measurement problems at these positions.

Comparing amplification patterns from varying crater depth and curvature, it seems that the curvature has a stronger influence on the ground motion. Going from small depth to big depth in Figure 4.18, the amplification pattern just varies slightly. The biggest change is observed behind the crater directly opposite to the source (at position P2). Amplification is decrasing at this point with increasing crater depth. In contrast, inside the crater an increase of amplification can be detected. This changes of amplification patterns might be related to interferences caused by the symmetric crater form. On the other hand, going from weak to strong curvature the shadow zone behind the crater is strongly increasing. This is not only true directly opposite to the source position but also in north-west and north-east direction.

It is expected that the influence of the crater geometry differs for different wavelength of the propagating seismic wave. In order to evaluate this, spectral ratios of the simulated seismograms are calculated in respect to a flat reference model at positions P1 and P2 (see Figure 4.15 and 4.16 for exact locations). The positions are located behind the crater on the other side of the source. Position P1 was chosen to not only have a measurement

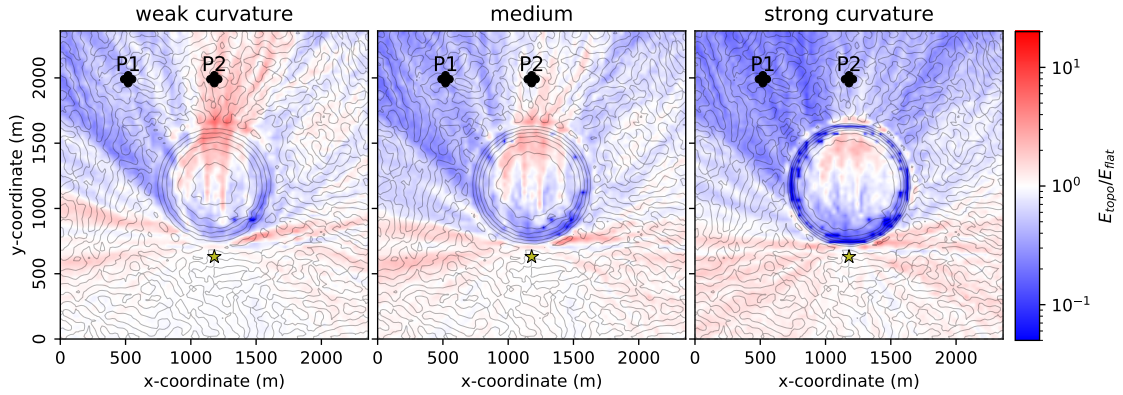

Figure 4.19 – Energy amplification on crater topography for different curvatures. Ratios of total energy between model with topography and reference model with flat surface for weak, medium and strong crater curvature. Contour lines mark elevation differences of 50 m. Spectral ratios at positions P1 and P2 are evaluated in Figure 4.20 and 4.21, respectively. The yellow star denotes the source. Note that spurious blue dots inside the crater (especially at steep flanks in case of strong curvature) were caused by numerical measurement problems at these positions.

point directly opposite to the source where we have seen increased amplification due to the round crater symmetry. In practice we measure the mean spectral ratio of 5 measurement positions located in a square with 30 m spacing to the central point. This way we can also evaluate the spatial variation of amplification.
The obtained spectral ratios from all crater shapes are shown in Figure 4.20 and 4.21 for position P1 and P2, respectively. The ratio between rough surface and flat surface is additionally plotted for comparison.

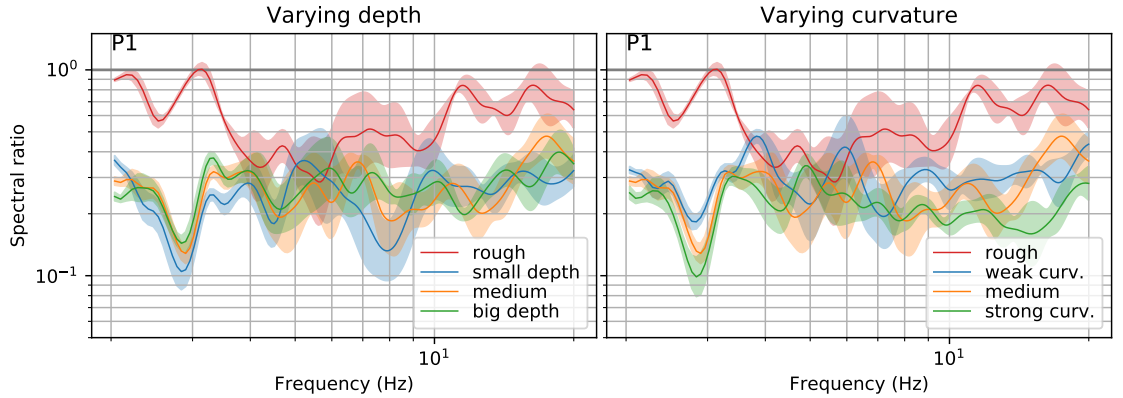

Figure 4.20 – Spectral ratios at position P1 for different surface topographies. Spectral ratios of synthetic seismograms at position P1 for the model with rough surface and models with varying crater depth (*left*) and varying crater curvature (*right*) in respect to a flat reference model. The solid curve corresponds to the mean of 5 ratios measured at positions on a square with 30 m spacing from the central point. The shaded area represents their standard deviation.

At both positions P1 and P2, the spectral ratio from the rough surface is minimal for intermediate frequencies. A possible explanation for this is that the intermediate frequency range corresponds to fundamental Rayleigh wavelengths which are comparable to the wavelengths of the roughness (between 40 m and 100 m as already discussed before). Shorter and longer wavelengths may interact less with the topography variations, thus are less scattered and continue to propagate more easily. However, these interpretations have to be used very carefully as amplification patterns vary strongly spatially.

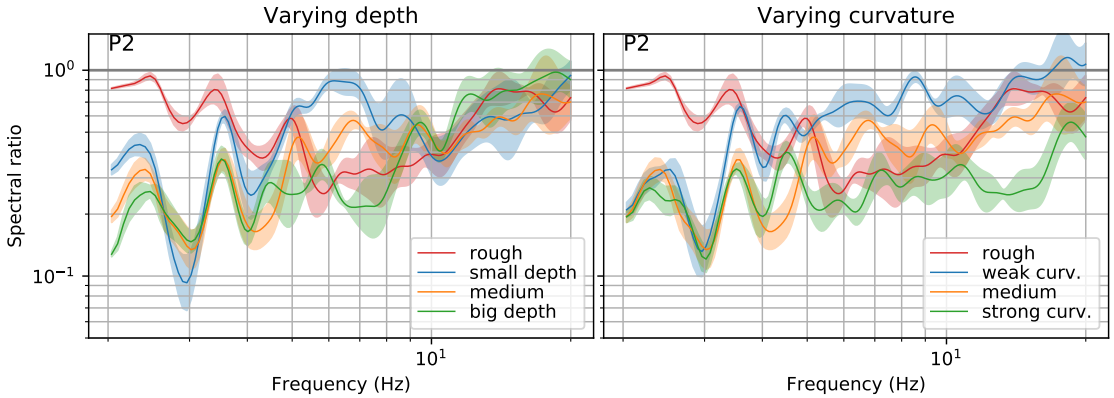

Figure 4.21 – Spectral ratios at position P2 for different surface topographies. Spectral ratios of synthetic seismograms at position P2 for the model with rough surface and models with varying crater depth (*left*) and varying crater curvature (*right*) in respect to a flat reference model. The solid curve corresponds to the mean of 5 ratios measured at positions on a square with 30 m spacing from the central point. The shaded area represents their standard deviation.

All different crater shapes cause deamplification at position P1 across the whole frequency range (see Fig. 4.20). Variation of the crater depth (*left*) does not show major effects. It is interesting to note however that the smaller crater depth partially cause higher deamplification. On the other hand, when varying the crater curvature (*right*) influences in the high frequencies range above 10 Hz appear. The crater with strongest curvature causes more deamplification in this frequency range.
A different picture is presented when analyzing position P2 (see Fig. 4.21). The spectral ratios from the crater models are no longer flat across the whole frequency range but increase towards higher frequencies. This has to be associated to the observed amplification behind the crater opposite to the source. Varying the crater depth does not strongly influence the results except for frequencies from 5 Hz to 8 Hz where the small crater depth causes far less deamplification. In turn, varying the curvature have stronger effects. Spectral ratios for the three different curvatures differ clearly above 5 Hz. As a result, the strongest curvature causes the strongest deamplification while the weakest curvature even causes slight amplification for very high frequencies.
All in all, variation of curvature seem to have stronger effects on ground motion amplification than variation of crater depth. Nonetheless, all crater models influence the whole frequency range which was studied.

4.6 Seismic signals from rockfalls at Dolomieu crater

We will now study observed seismic signals generated by rockfalls at Dolomieu crater. As the influence of the topography changes with the source position, we analyze the signals at specific times corresponding to specific rockfall positions. First we will investigate spectral ratios of time windowed rockfall signals between different measurement positions. We investigate as to whether if simulations can reproduce the observed spectral ratios when taking into account topography. Subsequently we will focus on a single block impact, identifying its seismic signature and comparing signal amplitudes by estimating the generated impact force using Hertz contact theory.

4.6.1 Observed Spectral ratios between stations

Three rockfalls at the southern crater wall (rockfall location **1** in Fig. 4.1) with similar trajectories are chosen for analysis. Trajectories of the rockfalls were identified from camera recordings. Snapshots of the three events are shown in Figure 4.22 together with an image of the whole trajectory reconstructed from differences of successive snapshots. Below, the corresponding seismic signals recorded at the 4 stations surrounding the crater are presented.

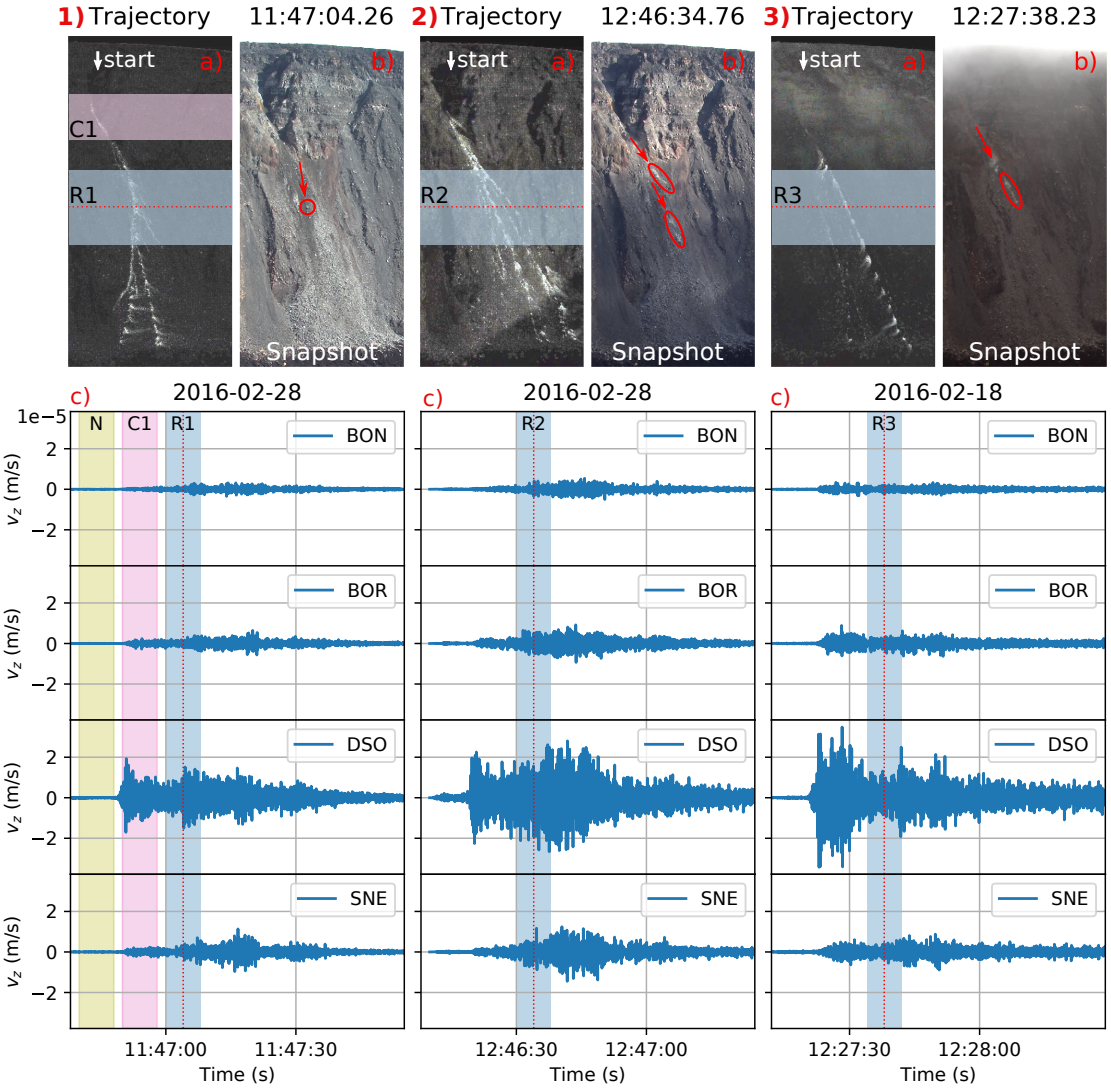

Figure 4.22 – Three similar rockfalls on the southern wall of Dolomieu crater. The events correspond to rockfall location **1** in Figure 4.1, occurring on 1) February 28, 2016 at around 11:47 (*left*), 2) February 28, 2016 at around 12:46 (*middle*), and 3) February 18, 2016 at around 12:27 (*right*). Panel a) shows the total trajectory of each event (seen from camera SFRC). The approximate starting positions are located at top of the small valley, indicated by white arrows. Panel b) shows snapshots (seen from camera SFRC) at a chosen time for which all three rockfalls are at comparable positions. Panel c) presents the rockfall seismic signals, on which the red dotted lines mark the time of the snapshots. Time windows R1, R2, and R3 (blue shaded zones) are defined ± 4 s around these times. The corresponding location of these time windows are also indicated as blue shaded zones on the trajectories. Same holds for reference time window C1 (magenta shaded zone), which corresponds to the beginning of event 1). Noise time window N is taken from recordings before event 1).

Station DSO shows the strongest amplitudes, especially in the beginning of the rockfall.

This is due to the fact that the three rockfalls are starting very close to the location of this station. BON contains the smallest amplitudes, being the furthest station and on the opposite side of the crater. The dynamics of the three events is not entirely identical. Event 1) consists of a single boulder bouncing down towards the bottom of the crater while some more blocks are following with a time lag of around 15 s. In contrast, event 2) has two blocks moving down closely following each other with a time lag of only 4 s as can be seen on snapshot 2b). Event 3) consists of a main boulder (corresponding to trajectory 3a on the right) with a smaller block following much later with a lag of about 50 s.
Despite these differences in the rockfall dynamics, we compare spectral ratios between stations for the time when the main blocks are passing the same position, corresponding to windows R1, R2 and R3 around the time of the shown snapshots. The spectral ratios are computed from the measurements at stations BOR, DSO (only vertical component) and SNE with respect to station BON. In order to avoid spurious fluctuations, the spectra are smoothed using the smoothing function proposed by Konno and Ohmachi (1998) before calculating the ratios. The obtained curves are shown as dark blue lines (TW-R1, -R2, -R3) in Figure 4.23 for the vertical component and in Figures 4.24 and 4.25 for north- and east-component, respectively.

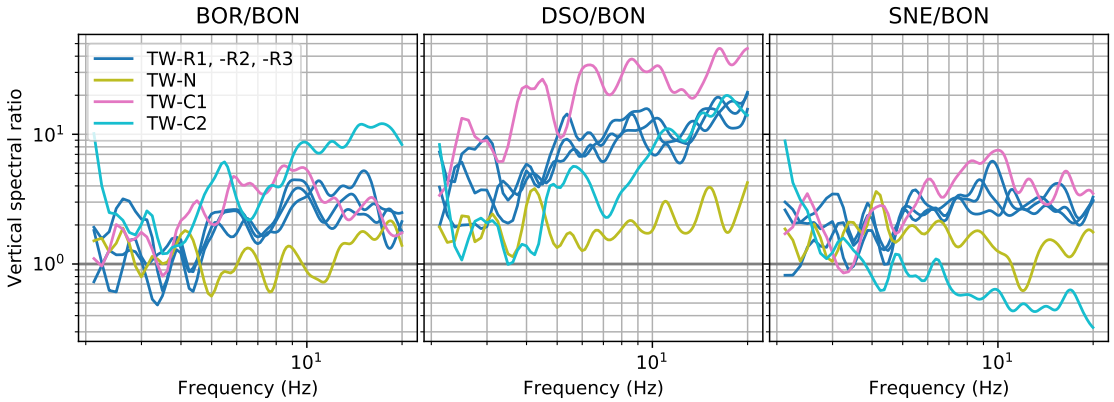

Figure 4.23 – Spectral ratios from rockfall seismic signals of vertical component. Spectral ratios on the vertical component for BOR, DSO and SNE in respect to BON. Time windows TW-R1, -R2, and -R3 correspond to rockfalls 1), 2), and 3) as defined in Figure 4.22. Time windows TW-N and TW-C1 correspond to noise recordings and beginning of rockfall 1), respectively. Time window TW-C2 is taken from a rockfall on the southwestern crater wall (location **2** in Fig. 4.1).

It is visible that the spectral ratios behave similarly for each of the events and for each component. Only low frequency values on the east-component (Fig. 4.25) deviate stronger from each other. In order to verify that the spectral values are indeed characteristic to the rockfall signals at the chosen positions, the curves are compared to ratios from noise recordings (TW-N), ratios from beginning of event 1) (TW-C1), and ratios from rockfall occurring at a different position in the crater (TW-C2, rockfall position **2** in Figure 4.1). The ratios from noise recordings and from the rockfall at different location show strong deviations from curves R1, R2 and R3. Curve C1 from the beginning of event 1) is quite similar on some station components (e.g. for north-component of ratio BOR/BON in Fig. 4.24) but deviates strongly on other components (e.g. vertical component of ratio DSO/BON in Fig. 4.23).
The findings suggest that the spectral ratios are characteristic for the position of the rockfall seismic source. The source-receiver distance is one factor which leads to this

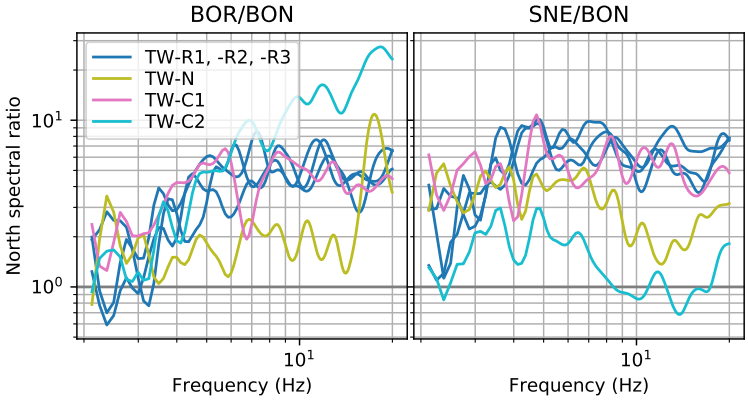

Figure 4.24 – Spectral ratios from rockfall seismic signals of north component.
Spectral ratios on the north component for BOR and SNE in respect to BON. Time windows from rockfall signals are defined as in Figure 4.23.

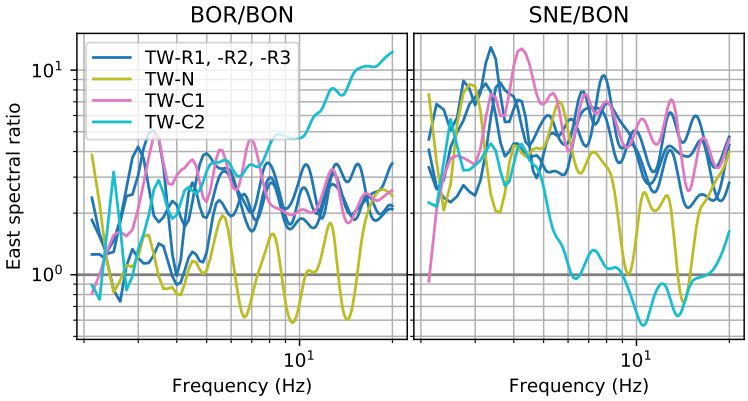

Figure 4.25 – Spectral ratios from rockfall seismic signals of east component.
Spectral ratios on the east component for BOR and SNE in respect to BON. Time windows from rockfall signals are defined as in Figure 4.23.

result. Hereafter we will investigate as to whether the source-receiver distance alone can explain the spectral ratios or if they are better reproduced when topography is accounted for the simulations. Further, different radiation patterns are produced when changing the direction of the source. For this reason we additionally study the influence of the source direction on the spectral ratios.

4.6.2 Comparison of observed and simulated spectral ratios

The seismic source of a rockfall can be very complex as multiple impacts of different magnitude can occur simultaneously at different positions. Hence, it is very difficult to correctly simulate the rockfall seismic signal, especially at high frequencies. For this reason, spectral ratios between stations are very convenient in order to compare real and synthetic signals. By this, the signature of the source is removed from the signal and solely propagation path effects are left. However, different source polarizations cause different radiation patterns. This is illustrated on the left hand side of Figure 4.26 on a model with flat surface. If the radiation pattern is not radial symmetric, which in only the case for vertical ground motion from a vertical source, the spectral ratios are affected depending on the azimuthal position of the respective receivers.
The direction of a rockfall seismic source depends on the rockfall dynamics and on the underlying slope. Generated forces in case of an impact are schematically illustrated on the right hand side of Figure 4.26. Depending on the slope angle, the direction of movement and the friction between the moving mass and the ground, the resulting force is composed

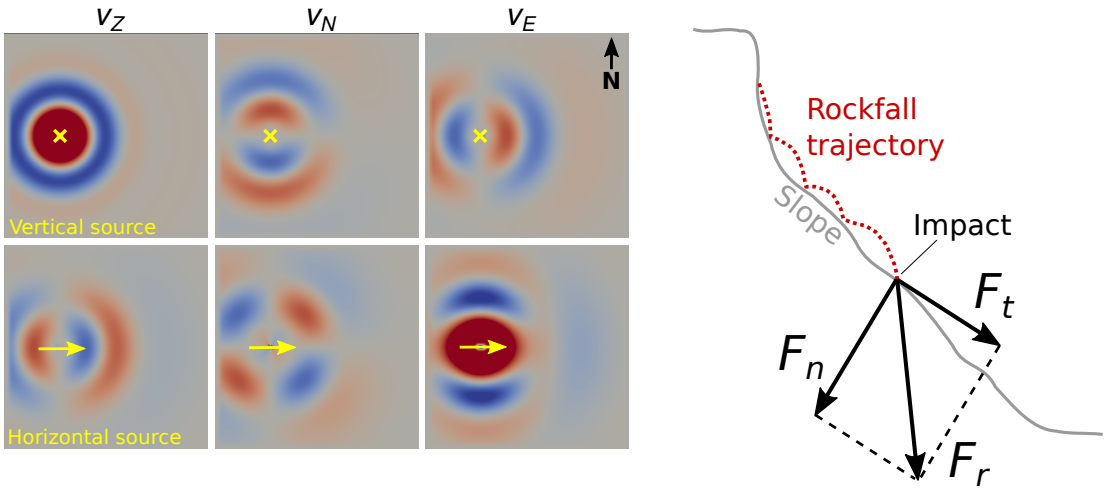

Figure 4.26 – Seismic radiation patterns and forces from rockfall impact. *Left:* Seismic radiation patterns from a vertical source (*top*) and from a horizontal force (*bottom*) for ground velocity in vertical-, north-, and east-direction. *Right:* Forces generated by a rockfall impact. The red dotted line illustrates the trajectory of a bouncing boulder. The impact generates force F_n normal to the slope. Depending on the boulder velocity tangential to the slope and of the friction coefficient μ, a tangential force $F_t = \mu F_n$ is generated (assuming Coulomb friction). Normal and tangential force add up to resulting force F_r.

of a force normal and a force tangential to the slope. Neglecting mass movements perpendicular to the slope of steepest descent, the direction of the horizontal component of the resulting force is determined by the orientation of the slope. In order to analyze the influence of the source direction on the spectral ratios, we compare a vertical force to a normal force and a tangential force. Note that the vertical force direction is in between the normal and the tangential force direction and might perhaps be similar to the direction of the resulting force.

To calculate the spectral ratios, 7 source positions are picked from a grid of 10 m spacing. The chosen source positions can be seen in Figure 4.27. As the rockfalls are moving during the 8 s time windows, it is more reasonable to assume a distributed source. Furthermore, choosing several sources allows to evaluate the sensitivity of the curves on the source positions. The positions correspond to the area in which rockfalls 1), 2), and 3) are present during time windows R1, R2, and R3, respectively (see Fig. 4.22).

Figure 4.28 compares spectral ratios from the vertical component of the rockfall signal as seen before with the ones from simulated seismograms on models with flat surface and with the Dolomieu topography. Synthetic seismograms are obtained assuming either a vertical force, a force normal to the slope or a force tangential to the slope in direction of the steepest descent. The source on the flat model is varied accordingly (i.e. with the same angles to vertical, north and east). The shown spectral ratios are the mean value from all picked source positions. The shaded zone indicates their standard deviation.

Some behaviors of the curves can be attributed to the relative source-receiver distances and are reproduced from both models. This can most clearly be seen from ratios DSO/BON which are of high value as the source is much closer to station DSO. The values increase towards higher frequencies. This is related to the attenuating properties of the medium which causes the amplitudes of higher frequencies to decrease faster with traveled distance than lower frequencies.

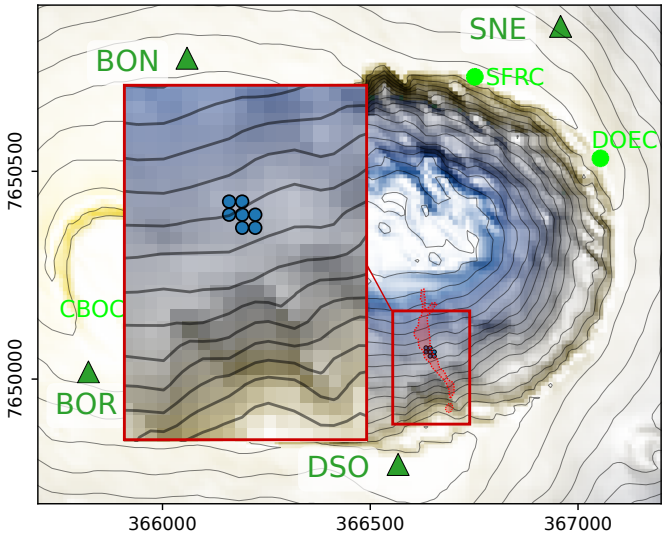

Figure 4.27 – Picked source positions for simulated spectral ratios. A total of 7 source positions are picked (blue dots) for the evaluation of spectral ratios from synthetic seismograms. The source positions are in the area which corresponds to the locations of rockfalls 1), 2), and 3) during time windows R1, R2, and R3 (see Fig. 4.22).

Influences from radiation patterns can be detected on the flat model, especially for ratio BOR/BON. Ratios from the tangential force are much smaller than from the other sources. As the slope is dipping northwards, the direction of the tangential force is in north-direction. Station BOR is located east of the source position which is transverse to the source direction. For this reason, a smaller signal amplitude is measured at station BOR in comparison with station BON (ratio < 1), even though BOR is slightly closer to the source. These effects from the radiation patterns cannot be identified for the model with topography. This indicates that effects from the propagation along the topography dominate over effects from the source polarization. We will come back to this point again later in the discussion.

Apart from that, larger fluctuations around the mean are detectable for the simulations on the model with topography. We remember that the fluctuations are caused by the different source positions. For both models, changes of the source position affect the source-receiver distance as well as the direction of the source which is defined by the local gradient of the topography (and also applied to the simulations on the flat model). Thus, the larger fluctuations on the topography must arise from variations of the propagation path.

All in all, ratios from the simulations seem to be smaller than the real values except for ratio BOR/BON on the model with topography. In particular the SNE/BON seems to be strongly amplified. Similar observations are drawn from the ratios of the the horizontal components. These are shown in Figure 4.47 and 4.48 of appendix 4.9.4 for north- and east-component, respectively. The deviation between observations and simulations might be caused by local structures in the subsurface which are not accounted for in the simulations. In the following we estimate local site effects at the stations using signals from volcano-tectonic events. Afterwards we will remove these site effects from the signals in order to allow a better comparison with the simulations.

Estimation of site effects caused by local subsurface structures

Site effects are estimated from seismic signals of 36 volcano-tectonic (VT) events which are located around 2 km below Dolomieu crater (see 1.8 in Chapter 1). As spectral ratios of

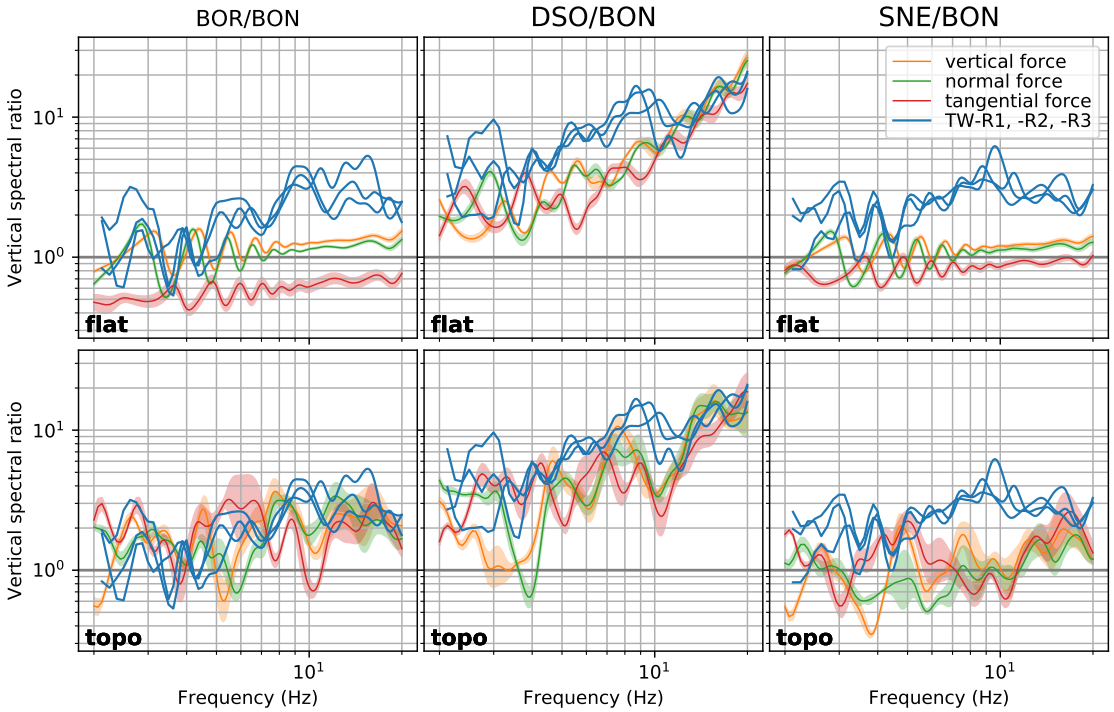

Figure 4.28 – Observed and simulated spectral ratios of vertical component. Vertical spectral ratios for BOR, DSO and SNE in respect to BON. Blue lines (TW-R1, -R2, -R3) correspond to observed rockfall signals as shown before in Fig. 4.23. Spectral ratios from synthetic seismograms are shown for a vertical force, a force normal to the slope and a force tangential to the slope on the model with flat surface (**flat**) and with topography (**topo**).

rockfall signals are analyzed in respect to station BON, we choose this station as reference for the site effect estimation. Also, based on H/V ratios of noise recordings and observed spectra of VT signals, BON has been qualified in Chapter 1 as an adequate reference station. The spectral ratios are computed from FFT spectra after applying the smoothing function proposed by Konno and Ohmachi (1998) in order to avoid spurious fluctuations. Figure 4.29 shows the mean spectral amplification calculated from all events together with its standard deviation. Spectral amplification on north- and east-component are presented in Figure 4.30.

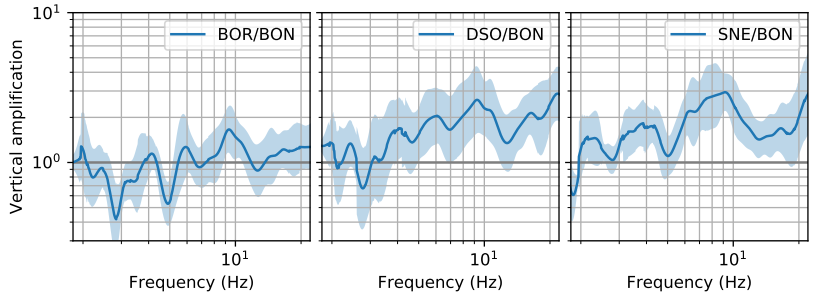

Figure 4.29 – Site effects on vertical component. Spectral amplification in respect to reference BON for vertical ground velocity. Blue shaded zone indicates standard deviation of the amplification distribution from all VTs.

No evidence of amplification is found for station BOR, except on its north-component which is amplified by a factor of 2 for frequencies above 5 Hz. Single-component station DSO seems to be amplified on its vertical component with a peak around 9 Hz. Strongest amplification is experienced by station SNE with factors up to 7 on its horizontal components.

Based on the disussion in section 1.3.2 of Chapter 1, where site effects from a vertically

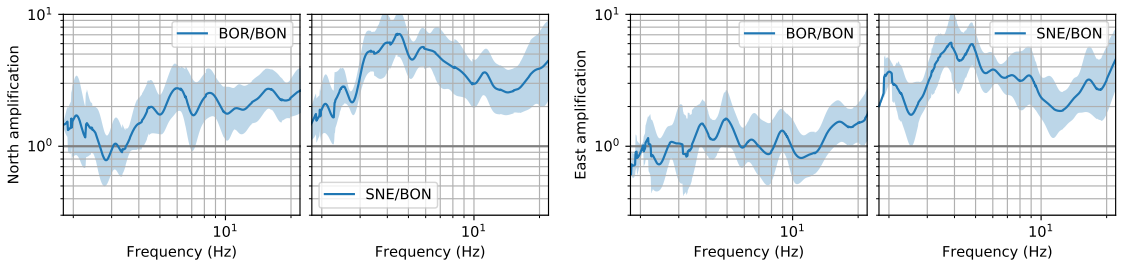

Figure 4.30 – Site effects on horizontal components. Spectral amplification factor in respect to reference BON for ground velocity in north-direction (*left*) and east-direction (*right*). Blue shaded zone indicates standard deviation of the amplification distribution from all VTs.

incident plane wave were evaluated, we can assume that topography does not have a major effect on the estimated geological site effects from VT signals. In other words this means, that the here presented amplification curves are caused by local subsurface structure alone. As the simulations for the rockfall signals does not consider local subsurface structures, we want to use the just revealed site effect information in order to enhance the comparison to the real rockfall signals. However, it is not evident that the site effects estimated from the VT events are similar to site effects on the rockfall signals which mainly involve surface waves due to the source position. For a proper correction of amplified rockfall signals, site effects have to be simulated for a surface source on a model including local heterogeneities in the ground. However, this goes beyond the scope of the present work. In the following we will assume that site effects are comparable for both deep sources and rockfall sources and correct the observed rockfall seismic signals accordingly.

Comparison of spectral ratios after site effect deconvolution

To improve comparability between observations and simulations, site effects which are not considered in the numerical model are removed from the recorded rockfall signals. This is realized by deconvolution of the signals with the site effects estimated in the previous section. Spectral ratios computed from the site corrected signals are compared to the simulated ratios in Figures 4.31, 4.32, and 4.33 for vertical-, north-, and east-component, respectively.

After removal of site amplification from the recorded seismic signals, spectral ratios between stations are better reproduced by the simulations.

The previously underestimated vertical spectral ratios DSO/BON and SNE/BON (see Fig. 4.28) show now a good agreement between observations and simulations. The same is true for the north-component of ratio BOR/BON (see Fig. 4.47 before and Fig. 4.32 after deconvolution). Most evident are the improvements of the horizontal spectral ratios SNE/BON (compare Fig. 4.47 and 4.32 for north-component Fig. 4.48 and 4.33 for east-component).

Comparing results from simulations on the model with flat surface and the model with topography, spectral ratios of the latter show in general a better agreement with the ratios from real events. Not only do the simulations on the topography allow more variability of the ratios (observable by the wider shaded zone of uncertainty around the mean due to changes in the source position), but also ratios are less affected by the source direction. This is clearly illustrated on ratio BOR/BON for the north-component (Fig. 4.32). As

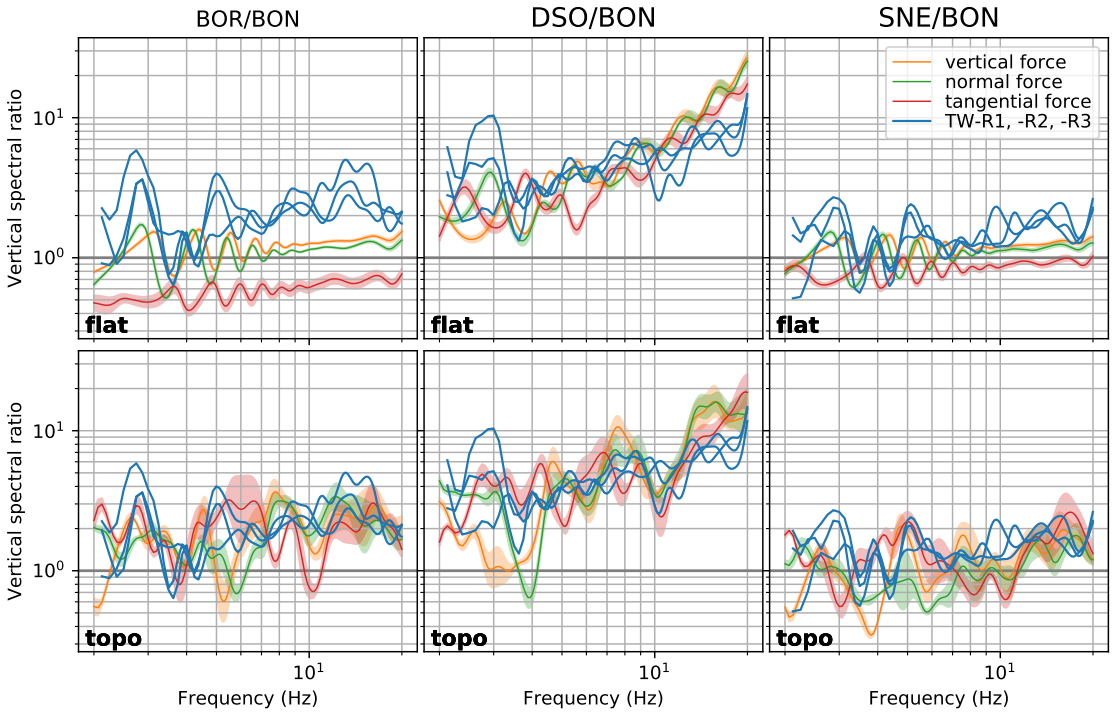

Figure 4.31 – Observed and simulated spectral ratios of vertical component after site effect deconvolution. Vertical spectral ratios for BOR, DSO and SNE in respect to BON. Blue lines (TW-R1, -R2, -R3) correspond to observed rockfall signals as shown before in Fig. 4.23. Spectral ratios from synthetic seismograms are shown for a vertical force, a force normal to the slope and a force tangential to the slope on the model with flat surface (**flat**) and with topography (**topo**).

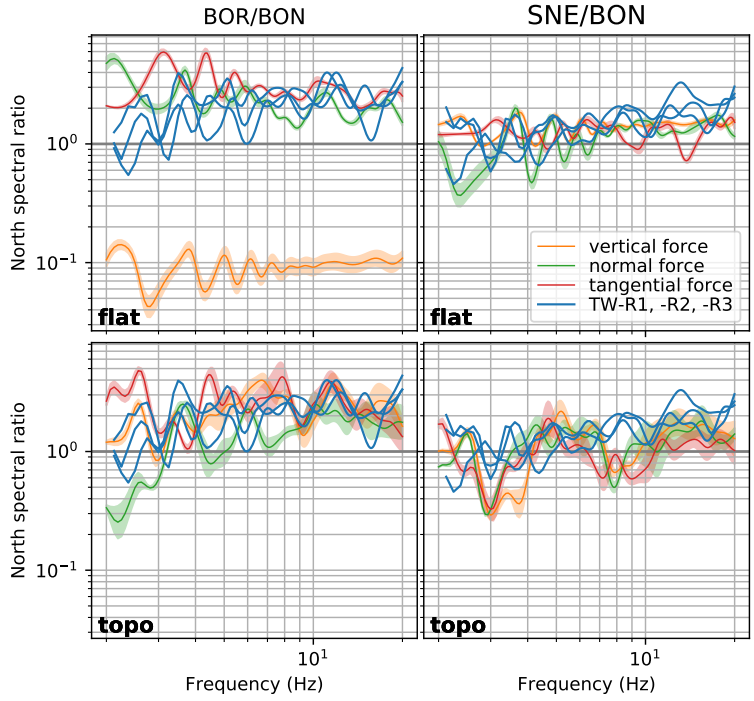

Figure 4.32 – Observed and simulated spectral ratios of north-component after site effect deconvolution. Spectral ratios for BOR and SNE in respect to BON. Blue lines (TW-R1, -R2, -R3) correspond to observed rockfall signals as shown before in Fig. 4.24. Spectral ratios from synthetic seismograms are shown for a vertical force, a force normal to the slope and a force tangential to the slope on the model with flat surface (**flat**) and with topography (**topo**).

station BOR is located almost perfectly east of the source position (see Fig. 4.27), almost no signal from a vertical source is recorded on the north-component which is transverse to the the direction of propagation from source to receiver. For this reason, the spectral ratio BOR/BON is so small in case of the vertical force. However, after introducing topography,

the spectral ratio BOR/BON behave similarly for all source directions. This means, that the spectral ratios are in this case not dominated by the source characteristics but by the propagation along the topography.

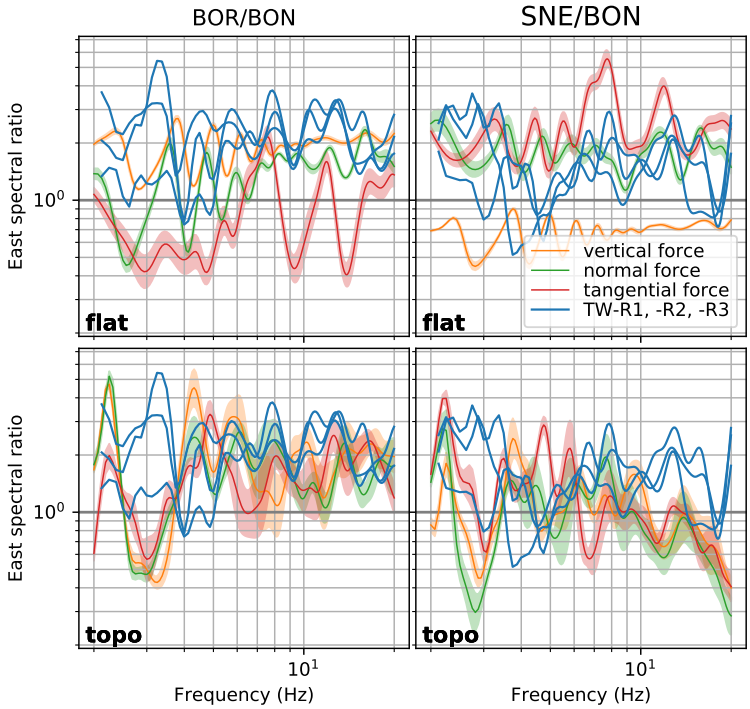

Figure 4.33 – Observed and simulated spectral ratios of east-component after site effect deconvolution. Vertical spectral ratios for BOR and SNE in respect to BON. Blue lines (TW-R1, -R2, -R3) correspond to observed rockfall signals as shown before in Fig. 4.25. Spectral ratios from synthetic seismograms are shown for a vertical force, a force normal to the slope and a force tangential to the slope on the model with flat surface (**flat**) and with topography (**topo**).

This can be observed similarly for the east-component shown in Figure 4.33. While curves from different source direction differ from each other in case of the flat model, they are more similar for simulations on the model with topography.
Trying to identify topographic effects in the spectral ratios, we could argue that the minimum in ratio DSO/BON (Fig. 4.31) at around 10 Hz can be explained by topography. However, the spatial (i.e. picked source positions) and temporal (i.e. the chosen time windows) uncertainty of the rockfall source make it difficult to pinpoint exactly topographic effects in the spectral ratios. Nevertheless, we are confident that the station ratios are influenced by topography. In Chapter 5 we will use the influence of the topography for rockfall localization. The method is based on the principle to search for the source position which best describes the observed inter-station ratios of observed signals.
In the final part of the present chapter we will focus on a single rockfall impact and try to identify the characteristic of its seismic signal as well as compare signal amplitudes with simulations based upon the Hertz contact theory.

4.6.3 Seismic signature of a rockfall impact

In the following we will have a detailed look at the seismic signal generated by single impacts of a rockfall at Dolomieu crater. We will try to understand their characteristics by comparison with synthetics simulated on models with and without topography. The comparison between observed and simulated signal has to be carried out very carefully due to the lack of precise source and subsurface information. It is important to emphasize that we do not want to reproduce the recorded signal but rather understand some of its features

as for example arrival times, waveform complexity and amplitudes.
For the analysis, a single boulder rockfall is preferably chosen with well separated impacts which can be tracked on video. The most adequate event was found on January 22, 2017, which took place on the northern crater wall. Figure 4.34 shows a camera snapshot of the rockfall at time of impact N2, location of the impacts and the rockfall seismic signal recorded on the vertical component at the closest station BON. Two boulder impacts, N1

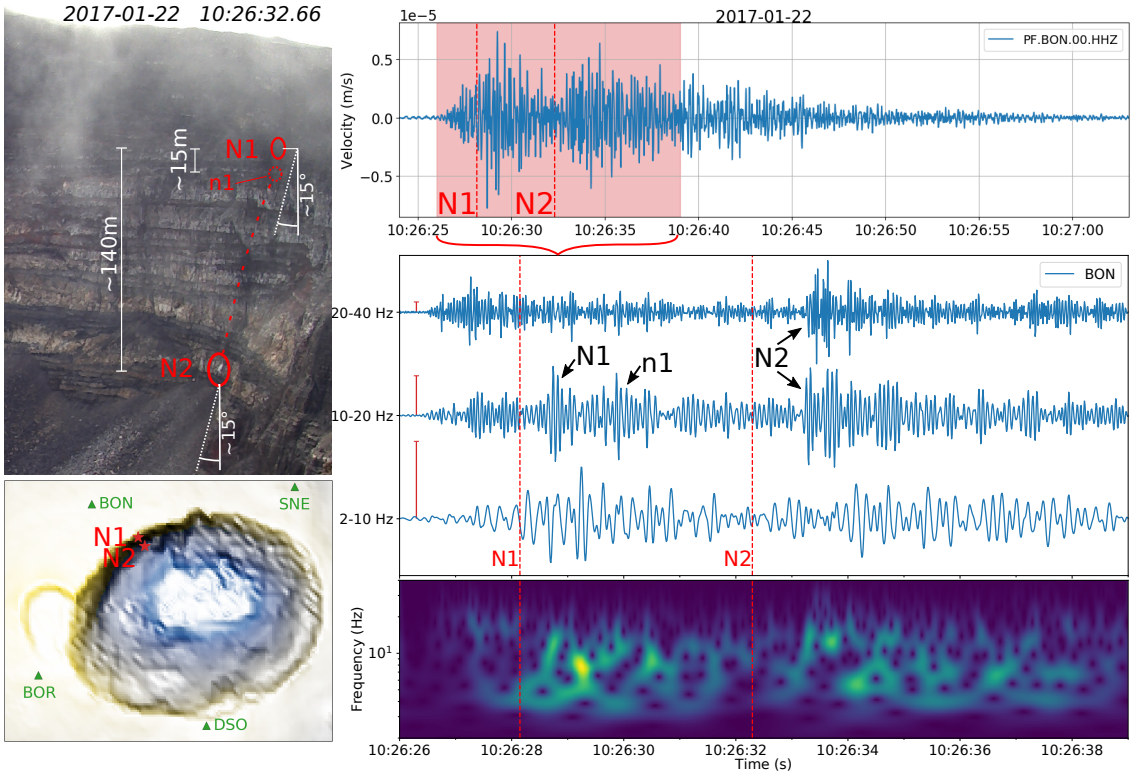

Figure 4.34 – Single boulder rockfall on January 22, 2017. *Top left:* Camera snapshot taken shortly after impact N2. Estimated vertical distance between impacts N1 and N2 and estimated slope angle to the vertical at impact positions. *Bottom left:* Location of impacts N1 and N2 in Dolomieu crater. *Top right:* Vertical ground velocity recorded at closest station BON in frequency band 2-40 Hz. Red shaded area illustrates the time window of graph below. Dashed lines mark impact times N1 and N2 estimated from video. *Middle right:* Comparison of frequency bands 2-10 Hz, 10-20 Hz, and 20-40 Hz. Signals are normalized to their maximum. Red bar to the left indicates relative amplitudes. *Bottom right:* Time-frequency representation of rockfall signal (calculated using the Stockwell transform).

and N2, separated around 4 s from each other, are analyzed hereafter. A minor impact n1 can be detected 1 s after impact N1. We will use it afterwards to estimate the vertical velocity of the boulder.
Note that the impact time is estimated according to the appearance of small dust clouds which are caused by the impacts. Thus, the precision of the impact time is affected by the time delay between true impact and visibility of the dust cloud. The precision is further limited by the sampling time of 0.5 s between successive snapshots.
The broadband seismic signal of the rockfall (top right of Figure 4.34) is characterized by two main lobes. These two main lobes are separated by a gap of low seismic energy at around 10:26:32. During this gap, no impact is detectable on the video. Thus, the boulder is in free fall before hitting the ground at impact location N2. Afterwards, the rockfall

splits into several blocks which continue to move downwards on the debris cone of former rockfalls. At these later times it is very difficult to identify single impacts.
In order to be able to better distinguish single impacts, the seismic signal is filtered in different frequency bands. The graph on the middle right of Figure 4.34 compares the signal band-pass filtered in ranges of 2-10 Hz, 10-20 Hz, and 20-40 Hz. Note that the signals are normalized. Their relative amplitudes can be inferred from the red bars plotted in the beginning of the signal as well as from the spectrogram below.
The signal filtered in the low frequency band (2-10 Hz) exhibits a smooth amplitude envelope. The two main lobes discussed before can be observed whereas no single pulses can be identified. It contains the strongest amplitudes and thus dominates the broadband signal. Short signal pulses emerge in the high frequency bands. It is evident that seismic sources were already active before impact N1. Unfortunately, these could not be detected on the video. Impacts are possibly hidden behind the clouds on the top of the crater wall. A clear seismic pulse in the frequency range 10-20 Hz can be associated to impact N1. It arrives around 0.5 s after the time determined from the video. A second pulse around one second later can be associated to impact n1. It is slightly smaller and seems to be wider. The highest frequency band does not show clear corresponding signals to these two impacts. This is different for impact N2. Both high frequency bands show abrupt signal onsets around 1 s after detection time of impact N2 on the video. The following signal can not be described as a single pulse but contains several peaks. This raises the question as to whether the source is made of several impacts or if these peaks result from the seismic wave propagation. Using synthetic seismograms generated by a point source, we will see hereafter that a single impact can indeed cause such complex waveforms. This in turn means that we cannot simply associate an individual impact to each seismic pulse detected in the signal.
Another interesting observation concerns the impact generated frequencies. As we could see, impact N1 is hardly detectable in the highest frequency range (20-40 Hz), whereas impact N2 produces clear signals in both high frequency bands (10-20 Hz and 20-40 Hz). Arguing with the changing source-receiver distance, we would expect the contrary as N1 is slightly closer to station BON than N2. If we assume that the properties of the boulder and of the underlying ground are identical for both impacts, the change in frequency content must be related to the impact velocity. According to Hertz contact theory, which we will introduce hereafter, higher impact velocities are associated with shorter collision times, according to Hertz contact theory. The inverse of the collision time constitute the upper limit of the force spectrum. Hence, as the boulder is accelerating between impact N1 and impact N2, the higher velocity at impact N2 should cause a shorter collision time and has therefore a higher cut-off frequency.

Hertz contact theory

In order to predict relative amplitudes of signals generated by impacts N1 and N2, the respective impact forces of the boulder on the ground are estimated. Farin et al. (2015) use the theory of Hertz (1882) to describe the force of an elastic sphere impacting a solid elastic surface. After successfully applying the theory on seismic signals generated during laboratory experiments they analyze real-size rockfall experiments carried out by Dewez

et al. (2010). Here we estimate the impact forces in similar fashion, assuming a spherical boulder of radius R and mass m. As derived in section 2.2.2 in Chapter 2, the maximum impact force F_0 exerted by the sphere perpendicularly to the plane can be described as

$$F_0 = \frac{4}{3} E R^{1/2} \, \delta_{\max}^{3/2}, \tag{4.2}$$

where $\delta_{\max}$ is the maximum indentation depth

$$\delta_{\max} = \left(\frac{15 m v_n^2}{16 E R^{1/2}} \right)^{2/5}, \tag{4.3}$$

with impact speed v_n normal to the slope. E is the effective Young's modulus $1/E^* = (1-\nu_s^2)/E_s + (1-\nu_p^2)/E_p$, where ν_s, ν_p, E_s, and E_p are Poisson's ratio and Young's modulus of sphere and impacted plane, respectively.

First of all, the impact speed v_n normal to the slope is estimated. For both impacts N1 and N2 we assume a sub-vertical fall of the boulder before collision. In other words, the boulder has a vertical speed of v_c at the time of collision. Slope angles at the impact positions are inferred from the DEM to be around $\alpha = 15\,°$. The normal impact speed can then be calculated as $v_n = v_c \, \sin\alpha$. To estimate v_c for N1 and N2, height differences between the impacts are determined from the DEM using the impact positions estimated from the video. As labeled in Figure 4.34, we find a height difference of around $H_1 = 15\,\mathrm{m}$ between N1 and n1, and a height difference of around $H_2 = 140\,\mathrm{m}$ between N1 and N2. Impacts N1 and n1 are detected 1 s apart from each other. Assuming an approximately constant velocity during this short time window, the vertical speed for impact N1 is $v_{c,1} = 15\,\mathrm{m/s}$. For impact N2, acceleration during the long free fall cannot be neglected. The speed is thus derived by $v_{c,2} = v_{c,1} + (2g(H_2 - H_1))^{0.5}$, where $g = 10\,\mathrm{m.s^{-2}}$ is the gravitational acceleration. Hence, a vertical speed $v_{c,2} = 65\,\mathrm{m/s}$ is found for impact N2. The so inferred normal impact speeds are summarized in Table 4.2.

As only the dust clouds of the impacts and not the boulder itself is traceable on the video, the boulder radius is roughly estimated to be $R = 0.3\,\mathrm{m}$. This results in a boulder mass of $m = 225\,\mathrm{kg}$, given a mass density $\rho = 2000\,\mathrm{kg.m^{-3}}$ similar to the one used in the simulations. Due to lack of more precise information, a typical effective Young's modulus of $E = 10\,\mathrm{MPa}$ is applied (Farin et al., 2015).

The maximum impact force F_0 can now be calculated using equation 4.2. As presented in Table 4.2, we find 83 kN and 485 kN for impact N1 and N2, respectively. These values will be used hereafter to calibrate the seismic source in the numerical simulations.

Concerning the frequency content of the impacts, we have a look at the contact duration of the impacts. Following Johnson (1987), the temporal evolution of the Hertzian impact force F_H can be approximated by

$$F_H(t) \approx F_0 \sin(\pi t / T_c)^{3/2}, \quad 0 \le t \le T_c. \tag{4.4}$$

The force-time function and its frequency spectrum are shown in Figure 4.35 as a function of impact duration T_c.

We can observe an exponential decay of the spectral amplitude above corner frequency $f_c = 1/T_c$. Johnson (1987) showed, that the impact duration can be approximated by

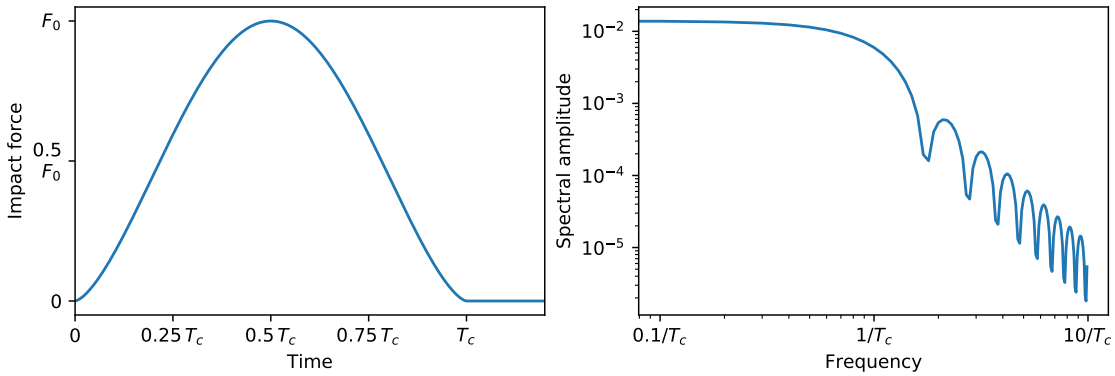

Figure 4.35 – Hertzian impact force and corresponding frequency spectrum. *Left:* Hertzian force-time function F_H normalized by maximum impact force F_0 in dependency of impact duration T_c, which represents the time during which the two bodies are in contact. *Right:* Frequency spectrum of the force-time function. The inverse impact time $1/T_c$ is related to the corner frequency f_c after which the spectral amplitude decays exponentially.

means of maximum indentation depth $\delta_{\max}$ and impact normal speed v_n as

$$T_c \approx 2.94 \frac{\delta_{\max}}{v_n}. \tag{4.5}$$

Applied to N1 and N2, the impact durations are estimated to be 0.038 s and 0.029 s, respectively. It then follows, using the relation $f_c = 1/T_c$, that the high frequency content of the impacts are limited by corner frequency 26 Hz and 35 Hz, respectively. Table 4.2 gives an overview over all impact parameters.

Table 4.2 – Impact parameters. For impact N1 and N2: vertical impact speed v_c, angle α between slope and vertical, impact speed v_n normal to the slope, maximum indentation depth $\delta_{\max}$, contact time T_c, and corner frequency f_c.

	v_c	α	v_n	$\delta_{\max}$	F_0	T_c	f_c
N1	$15\,\mathrm{m.s^{-1}}$	15 °	$4\,\mathrm{m.s^{-1}}$	0.05 m	84 kN	0.038 s	26 Hz
N2	$65\,\mathrm{m.s^{-1}}$	15 °	$17\,\mathrm{m.s^{-1}}$	0.16 m	485 kN	0.029 s	35 Hz

As a result, Hertz contact theory predicts a higher frequency content for N2 due to its higher impact velocity. This corresponds to the observed waveforms in Figure 4.34. Impact N1 can hardly be detected in the high frequency band (20-40 Hz), whereas impact N2 shows a clear pulse despite the slightly bigger source-receiver distance. Our estimations are in good agreement with these observations, predicting frequencies up to 26 Hz for N1 and up to 35 Hz for N2. Even though the absolute values contain a high uncertainty due to the rough estimations of boulder and ground parameters, their relative values are mainly determined on the respective impact speeds which we can constrain reasonably well thanks to the videos. For this reason it is very possible that the observed differences in high frequency content are related to the changing impact speed.

Comparison of observed and synthetic waveforms

Above, we tried to associate pulses in the observed seismic signal to impacts detected on the video. This was done in a crude way by analyzing the signal after the time of im-

pact. We will now use numerical simulations to get insights into travel times and expected waveforms. As mentioned before, the intention is not to reproduce observed waveforms, but rather to understand which signal characteristics can be associated to a single impact. The source-time function is represented by a Ricker wavelet. As it is very compact in time with a single main lobe, its signature can be neglected on the synthetic waveforms which hence mainly represent the response from the propagation path. Observed and synthetic signals are compared in the frequency band of 10-20 Hz. This is because in this frequency band we could identify short signal pulses which we associated to the rockfall impacts. At the same time, 20 Hz constitutes the upper frequency limit of our simulations.

We use the maximum impact forces estimated above to calibrate the simulations from sources N1 and N2. First of all, observed and synthetic seismograms are normalized in order to allow an easier comparison of the waveforms. Figure 4.36 show vertical ground velocity recorded at stations BON, BOR, DSO, and SNE and simulations from impacts N1 and N2 on models with flat surface and with Dolomieu topography. Source positions of the two impacts are estimated from the video (see the positions on the map in Fig. 4.34). As the exact source direction of the real impacts are unknown, the variability of synthetic waveforms is shown in dependency of the force direction. Signals generated by a vertical force F_z, a force F_n normal to the slope and a force F_t tangential to the slope are demonstrated.

Analyzing the synthetic seismograms, we can observe in general that N1 produces smaller amplitudes in respect to N2. This is due to the estimated impact forces of 84 kN and 485 kN, respectively (see Table 4.2). Going more into detail, seismograms from the model with flat surface show the same relative amplitudes between N1 and N2 for all different source directions. This is different for the model with topography, where the relative amplitudes between N1 and N2 can vary. For example, on the closest station BON, the signal from a force F_n normal to the slope results in a smaller amplitude relative to N2 than for forces F_z and F_t vertical and tangential to the slope. This suggest, that topography allows more variability of the signal amplitude when changing the source direction than a flat surface. Further, still for station BON, the amplitudes of impact N1 are bigger on the model with topography than for the model on the flat surface. This corresponds better to the real observations, where the maximum amplitude of impact N1 is almost as big as maximum amplitude of impact N2. Similarly we can observe on station DSO that the signal of impact N1 is very small in respect to the signal of N2 in the case of topography. While the amplitudes on the flat surface model are strongly dependent on the source-receiver distance, amplitudes on the model with topography can be modified due to the propagation path. This could be seen already before by analyzing amplification patterns of topography in respect to the flat reference.

Besides the variability of amplitudes due to topography, we can have a look on the simulated waveforms. On the model with flat surface, three wave packets following each impact can be detected, which are well separated from each other on the more distant stations BOR, DSO, and SNE. These three wave packets correspond to body wave, 1^{st} mode Rayleigh wave, and fundamental mode Rayleigh wave (see e.g. Figure 4.14). The arrival time of the 1^{st} mode Rayleigh wave is in good agreement with the first major pulse after each impact. This suggests that the Lesage velocity model represents the shallow subsurface velocity around Dolomieu crater reasonably well. However, on the flat model

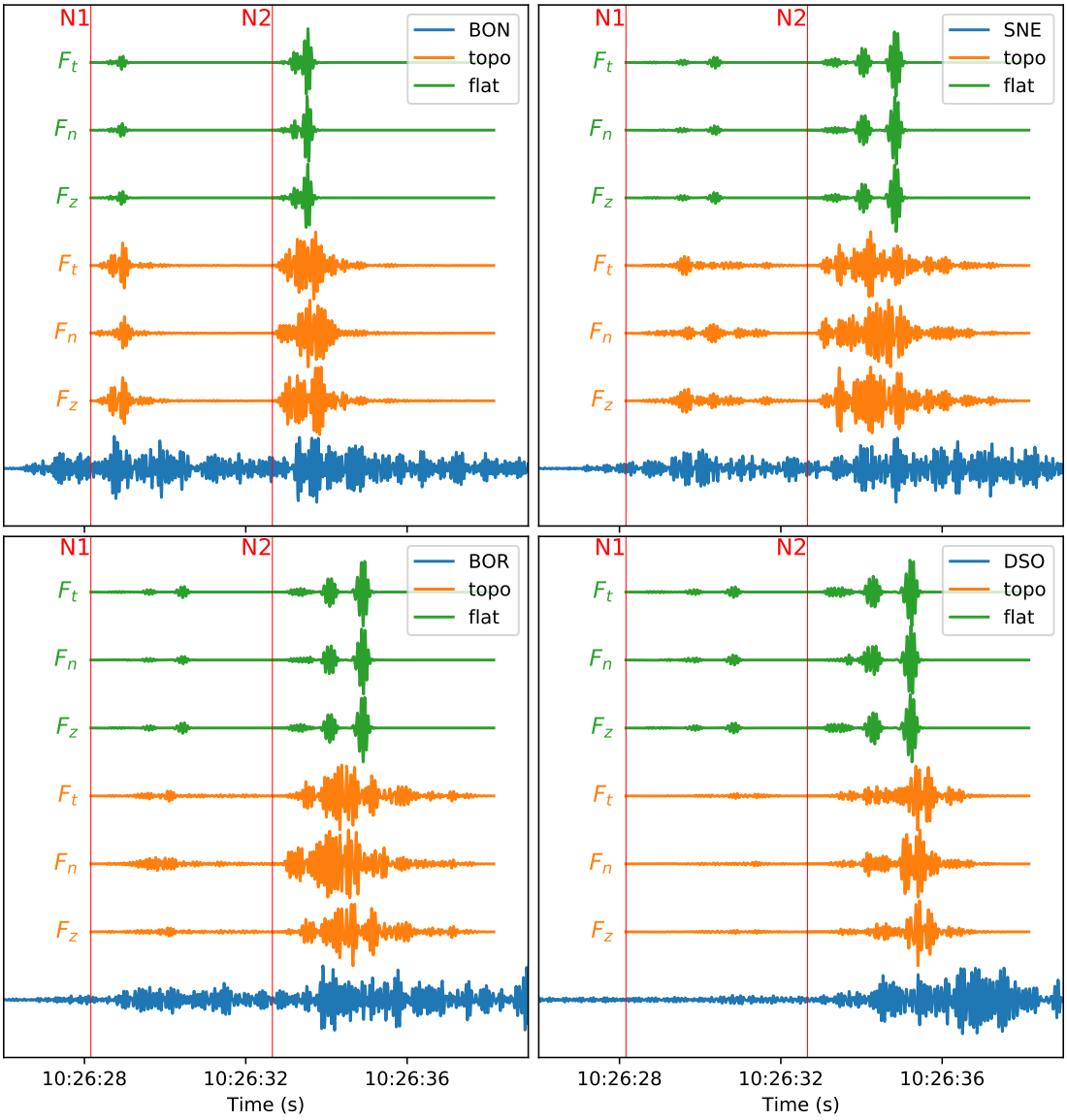

Figure 4.36 – Comparison of rockfall signal with synthetic waveforms from different force directions. Blue lines correspond to vertical ground velocity recorded at different stations for the same time window as shown in Figure 4.34. Red vertical lines indicate impact times N1 and N2 from the video. Synthetic waveforms of impacts N1 and N2 are shown for the model with flat surface (green) and with Dolomieu topography (orange). Source positions are illustrated in Figure 4.34. The variability of waveforms is demonstrated in dependency of a vertical force F_z, a force F_n normal and a force F_t tangential to the slope. All traces are normalized by their maximum.

the amplitude of the 1st mode Rayleigh wave is consistently smaller than the amplitude of the fundamental mode. A corresponding amplitude variation cannot be identified on the real signals. In contrast, simulations on the model with topography generate waveforms of more complexity. This increased complexity corresponds better to the observed signals, even if the waveforms do not fit perfectly. The variation of the force direction modifies the waveforms stronger than in the flat case. Also, waveforms vary strongly from station to station. This is not observed in the flat case, in which the waveforms are very similar on stations at comparable source-receiver distances (i.e. BOR, DSO, and SNE).

The analysis shows that topography allows for more variability of both amplitudes and waveforms. Appendix 4.9.5 additionally demonstrates the increased variability of signals

in dependency of a slightly changing source position. Furthermore, a polarization analysis is carried out. From this, a similar conclusion is drawn regarding the variability of polarization caused by topography.
Besides variability of the waveforms, it has been observed that a single impact can produce complex waveforms, in particular when topography variations are involved. Consequently, it is generally not possible to deduce from a rockfall seismic signal, if the source consists of a single impact of multiple impacts.
Finally, observed and synthetic seismograms are compared without normalization. This way, the absolute signal amplitudes calibrated by the Hertz impact force are evaluated. The total value of the acting force as well as its direction is determined by summing the force normal and the force tangential to the slope. Tangential force F_t is inferred from the maximum normal impact force $F_n = F_0$ assuming Coulomb friction $F_t = \mu F_0$, where μ is the material specific friction coefficient. We define $\mu = 0.7$, which is a typical value used for rockfall at Dolomieu crater (e.g. Hibert et al., 2014b). The resulting signal amplitudes for model with flat surface and model with topography are compared in Figure 4.37 with the observed rockfall signals.
First of all, despite the rough parameter estimations concerning the falling boulder and the impacted ground, comparable amplitude magnitudes in respect to the observed signal are achieved using the Hertz contact theory. Synthetic seismograms from the flat model generally overestimate the observed amplitudes. From simulations on topography, signals of impact N1 are always underestimated, while signals from N2 are overestimated on BON and DSO and underestimated on BOR and SNE. This can partly be also related to local site effects which are not considered in the simulation. For example, the underestimation at SNE could be related to the strong amplification at this station found by the above presented site effect estimation (compare with Fig. 4.29).
Noteworthy are the relative amplitude changes between the stations. While in the case of the flat model, amplitudes are decreasing with distance from the source, the model with topography breaks this relation. For example, on the flat model the maximum amplitude decreases drastically from station BON to station DSO. In contrast for the model with topography, the signal amplitude of impact N2 is almost half as the one of station BON. This topography induced amplitude change was shown before by means of ratios between model with and without topography.

4.7 Conclusion

We investigated the effect of topography on the propagation of wave fields generated by surface point loads. The dependency of topography induced amplification on the underlying velocity model is demonstrated. A velocity-depth profile with strong gradient, as proposed by Lesage et al. (2018) for the shallow velocity structure of volcanoes, leads to increased scattering at the surface topography and prolonged ground shaking as more seismic energy stays close to the surface. This results in spatial amplification patterns which can contain zones of high amplification. The sensitivity study on crater geometry indicates that modifications of the crater curvature affects the wave field stronger than modification

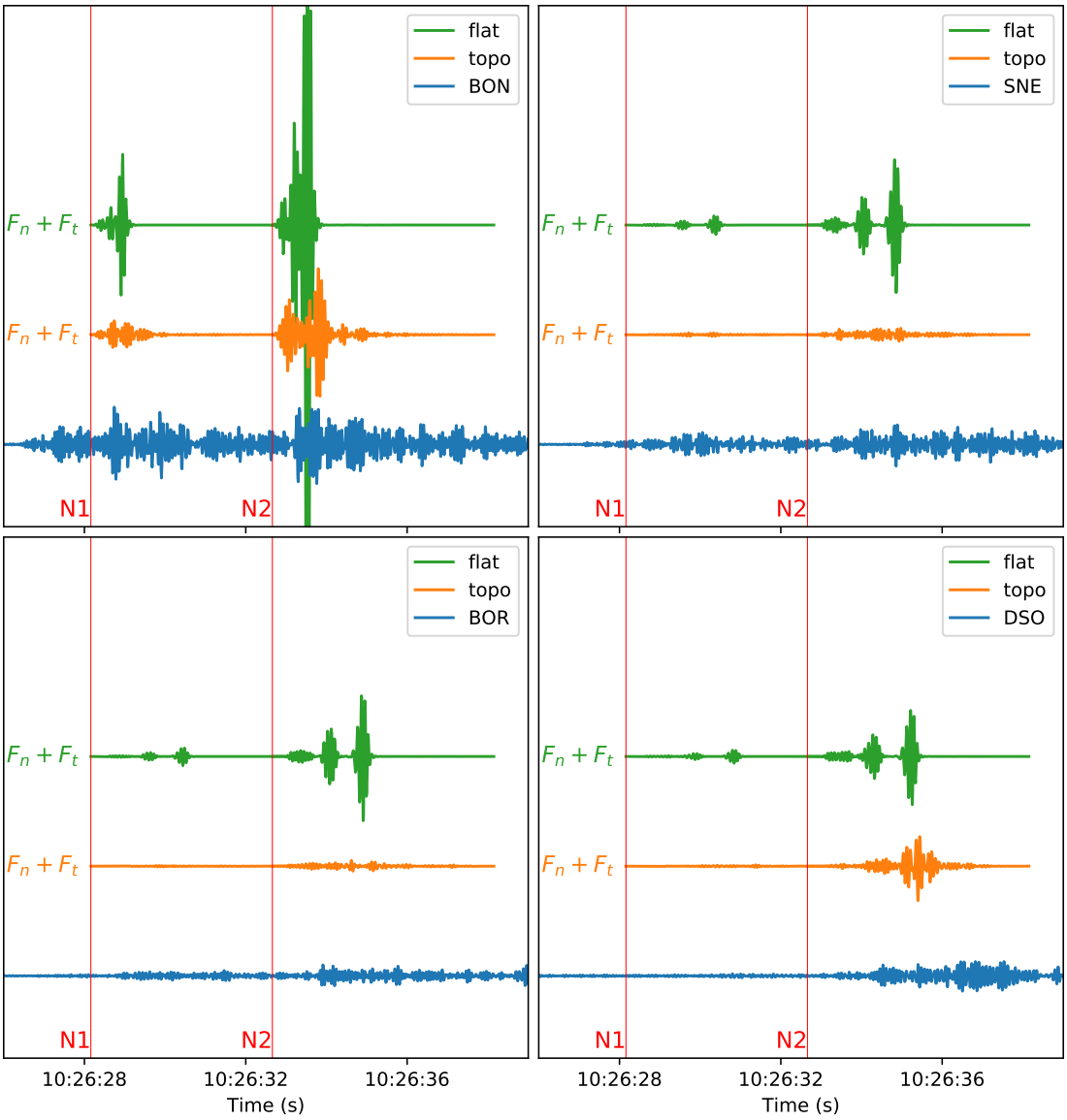

Figure 4.37 – Amplitude comparison between observed and synthetic seismograms. Blue lines correspond to vertical ground velocity recorded at different stations for the same time window as shown in Figure 4.34. Red vertical lines indicate impact times N1 and N2 from the video. Synthetic waveforms of impacts N1 and N2 are shown for the model with flat surface (green) and with Dolomieu topography (orange). The seismic source is constructed by summing force F_n and F_t normal and tangential to the slope. F_n corresponds to the maximum impact force F_0 as shown in Table 4.2. Source positions are illustrated in Figure 4.34.

of the crater depth.

Simulation were compared with measurement from rockfalls at Dolomieu crater. By analyzing signals generated at specific rockfall locations, it is demonstrated that spectral ratios between stations are characteristic to the source positions. Comparison with simulations further suggests that the spectral ratios are dominated by the propagation along the topography rather than the polarization of the seismic source. After validating this finding for different rockfall locations, it will be used in Chapter 5 for the localization of events. Assuming that the observation holds for all rockfall locations, the proposed method can be applied without dependency on the implied source direction. In this context it is

important to point out that the influence of the topography on surface waves has to be considered as a propagation effect rather than a local site effect at the recording station. In other words, a surface wave arriving at a recording stations is affected by its total path along the topography. This is similar to body waves which are affected by their total path though the subsurface. Just as body waves are used to infer subsurface properties, the information imprinted on surface waves might be used to infer properties of their origin. In contrast to subsurface properties, surface topography can be measured quite easily and accurately. This allows to accurately simulate the response of topography with numerical models. Nonetheless, the coupling of topographic effects and local site effects from heterogeneities in the subsurface should additionally be considered. In the present study we accounted for local site amplification by estimating amplification factors from VT events. However, it is not granted that surface waves experience the same amplification as a vertical incident wave field. Thus, to better estimate influence of the subsurface, the surface wave propagation has to be modeled including subsurface heterogeneities. Unfortunately, this is not in the scope of the present work.

Finally, analysis of seismic signature of single impacts demonstrate the potential information hidden in rockfall seismic signals. Synthetic waveforms show that a single impact can produce a complex waveform with multiple pulses. While seismograms from the flat model show similar waveforms at all stations, surface topography modulates waveforms as a function of source direction and source position. Also, the relative amplitudes between different stations can strongly be influenced by the topography. Calculations based on the Hertz contact theory suggest that the observed differences in frequency content of the two presented impacts can be explained by differences in impact speeds. For identical boulder and ground parameters, a higher impact speed results in a higher frequency content. Furthermore, amplitudes calibrated by the maximum impact force predicted from the Hertz theory results in magnitudes comparable to the real signals.

The combination of Hertz contact theory and wave propagation simulations is an important step for the interpretation of rockfall seismic signals based on the underlying physical processes. The Hertz impact theory is frequently used to predict the impact force of rockfalls, for example for the design of structural protections (e.g Volkwein et al., 2011). Also, laboratory experiments show the validity of Hertz theory concerning the waves generated by the collision of a ball on a massive plate (e.g. McLaskey and Glaser, 2010). However, only few studies apply the theory to seismic signals from real-scale rockfalls, as done by Farin et al. (2015); Bachelet et al. (2018). A limiting factor is the complex rockfall source which often consists of multiple simultaneous impacts. For this reason, application to artificially triggered rockfalls which ensures separated impacts of a single boulder would help validate the Hertz theory in the field and to enhance understanding of real impact processes.

4.8 Landslide generated seismic energy: Improved estimation through consideration of topography *(Work in progress)*

The seismic energy radiated by a landslide can give important insights on landslide properties. For example, it has been shown that the radiated energy can be related to the landslide volume (e.g. Hibert et al., 2011, 2014b). In Chapter 3 we derived an equation in order to estimate the totally radiated energy by means of the measurement of a single seismometer located at the surface. We discussed the influence of different subsurface velocity models. However, the equations are based on the propagation of seismic waves along flat surfaces. The formalism becomes invalid when surface topography is introduced. This is illustrated in Figure 4.38.
In order to take surface topography into account when estimating the source radiated energy, we propose to introduce a topography correction factor. The idea is presented in the following. Implementation and results are preliminary.

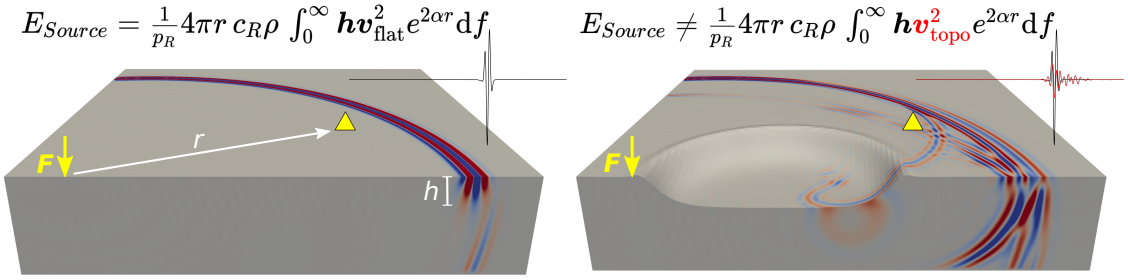

Figure 4.38 – Illustration of topography influence on estimation of source radiated energy. The illustration shows the seismic wave propagation from a vertical point force on a homogeneous model with flat surface (*left*) and surface topography (*right*). The seismic station (yellow triangle) is placed at distance r from the source. The total energy E_{Source} radiated by the source can be calculated from the recorded ground velocity $\mathbf{v}$ as defined in equation 3.37. The equation becomes invalid when surface topography modifies ground velocity $\mathbf{v}_{\text{topo}}$ (red signal).

4.8.1 Topography correction factor

In order to account for topography when estimating the total energy radiated by the source, a correction factor is introduced. This correction factor is dependent on the source position. The idea is to relate the measurements from the domain with topography to corresponding values which would be measured in the case of a flat surface. As a result, the equation derived in Chapter 3 for the energy estimation on flat surfaces can be used.
The correction factor is determined from seismic wave simulations on a model with realistic 3D topography and on a flat reference model. Here, we assume a frequency independent correction factor C_{topo}, which we define as

$$C_{\text{topo}} = \frac{E_{\text{flat}}}{E_{\text{topo}}}, \tag{4.6}$$

where E_{flat} and E_{topo} is the energy calculated from the synthetic seismograms from a model with flat surface and with topography, respectively. Remember that we quantified

the influence of topography similarly in Chapter 4. Carrying out reciprocal simulations [1] for each seismometer, we can determine the correction factor at each potential rockfall position. The correction factor $C_{z,\text{topo}}$ calculated from vertical ground velocity is visualized in Figure 4.39.

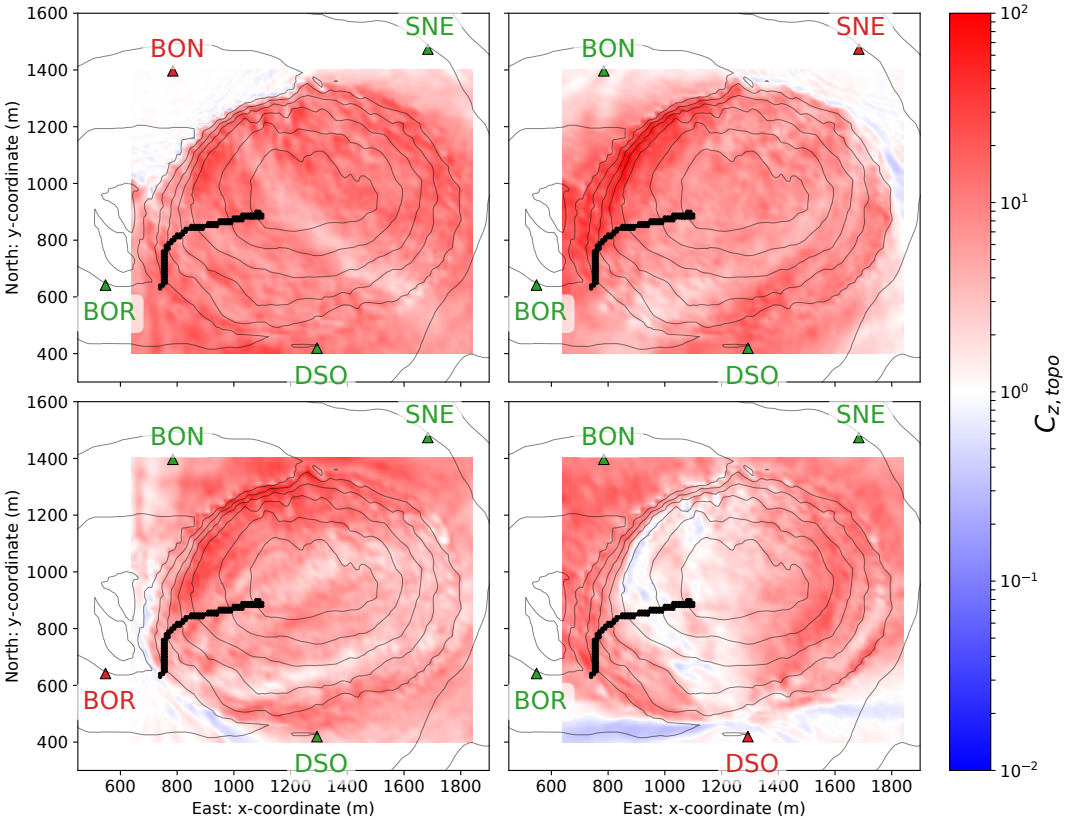

Figure 4.39 – Topography correction factors for each seismometer as a function of source position. The correction factors $C_{z,\text{topo}}$ of vertical components are calculated for stations BON, BOR, DSO, and SNE (counterclockwise). The general value > 1 corresponds to the findings in Chapter 4 where we could see deamplification of surface waves due to scattering along the topography (see section 4.5). Black dots mark the trajectory of the rockfall analyzed hereafter.

Correction factor C_{topo} is then introduced in the calculation of the source energy. For a heterogeneous model, assuming fundamental Rayleigh waves only, equation 3.38 becomes:

$$E_R = C_{\text{topo}}\ 4\pi r\,\rho \int_0^\infty c_g\ h_j \hat{v}_j^2\ \mathrm{e}^{2\alpha r}\ \mathrm{d}f, \tag{4.7}$$

with source-receiver distance r, mass density ρ, Rayleigh group velocity c_g, and attenuation factor α. Penetration depth h_j and ground velocity $\hat{v}_j(f)$ are associated to components $j = \{E, N, Z\}$. Note, that a frequency dependent correction factor can easily be considered by moving C_{topo} under the integral.

4.8.2 Test example of rockfall at Dolomieu crater

By introducing the topography correction factor, we hope to achieve a more coherent energy estimation from different stations. As the rockfall is moving, the energy is calculated in a

1. Reciprocal simulations are introduced in section 5.4.2 of Chapter 5.

sliding time window with correction factors corresponding to the current rockfall position. A first test is conducted by applying the topography corrected energy estimation to a rockfall on December 13, 2016 which occurred on the southwestern crater wall (the rockfall corresponds to event 3 presented in section 2.3 of Chapter 2). The observed seismic signals are displayed in Figure 4.40.

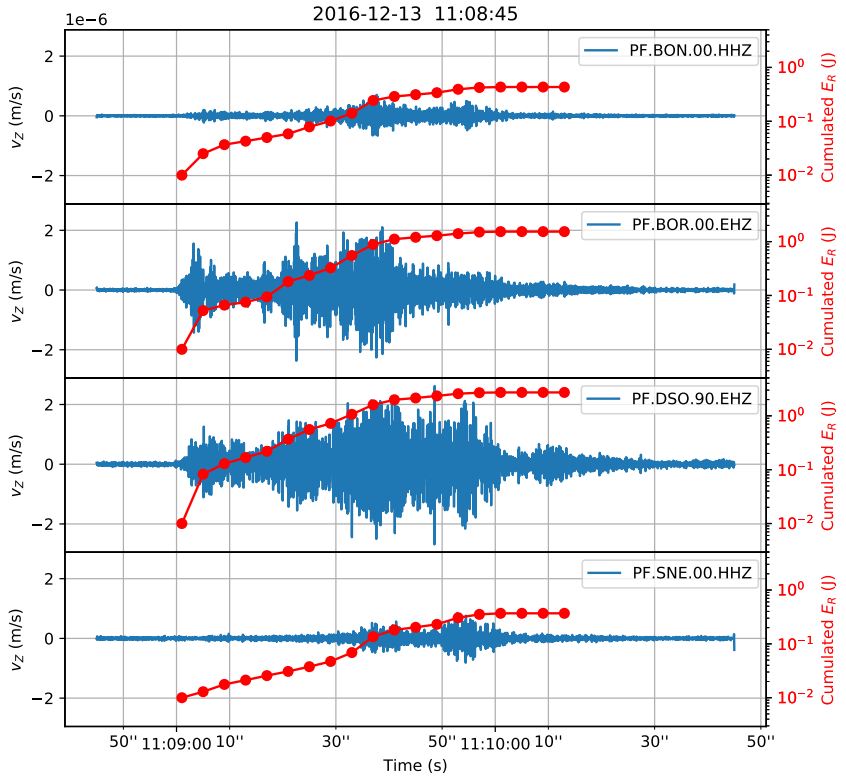

Figure 4.40 – Seismic signals and cumulated radiated energy of rockfall on December 13, 2016.
Vertical ground velocity recorded at stations BON, BOR, DSO, and SNE. Overlaid is the cumulated radiated energy estimated in a sliding time window of 4 s length without overlaps. Note that the energy is calculated only from vertical components and without topography correction factor. Site effects are removed from the signals.

For demonstration, only the vertical components are used in the energy estimation. The subsurface is assumed to be well described by the Lesage velocity model (see section 1.3.1) with Rayleigh attenuation factor of $Q_R \approx Q_S = 50$. As derived in section 3.3.3, an effective penetration depth of $h_{z,\text{eff}} = 0.32$ is used. The cumulated radiated energy, calculated in time windows of 4 s without correction factor, is overlaid on the seismic signals in Figure 4.40.
In order to consider the influence of topography, an area of the current rockfall position is determined and correction factors are averaged over this area. Subsequently, the energy calculated in each time window is corrected following equation 4.7. Figure 4.41 compares the cumulative radiated energy estimated without and with topography correction factor.

It can be observed that the topography corrected energy estimation yields higher values of radiated energy. The mean value of the two estimations differ by a factor of 6. This means that energy lost due to scattering during propagation of surface waves along the topography is restored. It is also shown that the relative difference between energy estimations of different stations is reduced. While the maximum deviation from the mean is 116 % before correction, it is 54 % after accounting for topography.
The results are preliminary in a sense that only vertical components are considered and only one event is analyzed. Still, they suggest that the energy estimation is substantially

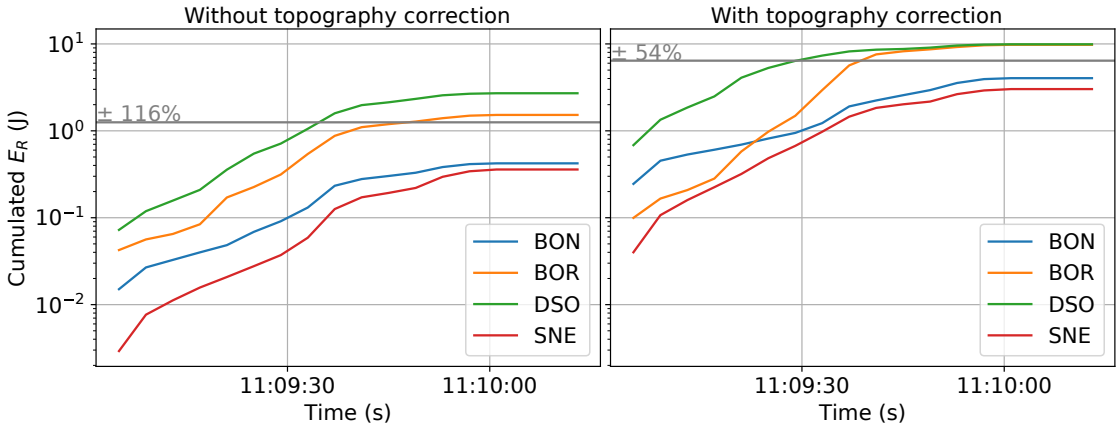

Figure 4.41 – Cumulative radiated energy calculated without and with topography correction factor. Radiated energy estimated without (*left*) and with (*right*) topography correction. Only vertical components are considered and the vertical correction factor $C_{z,\text{topo}}$ is used. The mean estimated energy is marked by the gray line. Percentages give the maximum deviations from the mean. Site effects are removed from the signals prior to energy calculation.

influenced by the topography. Thus, topography correction factors should be considered to correctly estimate the source energy. This is important for example to assess rockfall volumes.

4.8.3 Perspectives

The topography corrected energy estimation was demonstrated using solely vertical components. It goes without saying that it is crucial to consider all components in order to achieve a correct energy estimation. For this, it has to be carefully evaluated how the horizontal components on the topography can be related to a signal measured on a flat surface. Source related radiation pattern can complicate this relation additionally. If only single-component seismometers are available, assumptions have to be made to account for the energy on the other components.

Another issue is the frequency dependency of correction factors. The best solution would be to directly deconvolve the signals with the spectral transfer function between simulations on the flat model and on the model with topography. However, regarding the uncertainty of the source position as well as the superposition of multiple sources, it has to be tested if results are systematically better.

This brings us to the moving seismic source. It is very laborious to determine for each time window the exact source position. To avoid this, it has to be investigated if longer time windows and correction factors averaged over larger areas achieve comparable energy estimations. An elegant solution would be to combine the energy estimation with the localization method proposed in the previous chapter. This way, correction factors are defined based on the probability of the source locations.

Synthetic rockfall signals can help to develop all the previous points. In contrast to real rockfalls, the totally radiated energy of synthetic examples is known. This way, the topography specific correction can be tested under different conditions, as for example the superposition of multiple sources at different locations and also the influence of heterogeneities in the subsurface.

4.9 Appendices

4.9.1 Amplification of horizontal peak ground velocity (PGV)

Figure 4.42 and 4.43 show amplification patterns of horizontal PGV from a vertical source for north- and east-component, respectively. The strong topographic amplification east-west from the source for the north-component and north-south from the source for the east-component is caused as no transverse energy is present in case of the flat reference model. In contrast, energy is measured on these components when waves are propagating along topography as a result of diffraction or of conversion between horizontal and vertical energy.

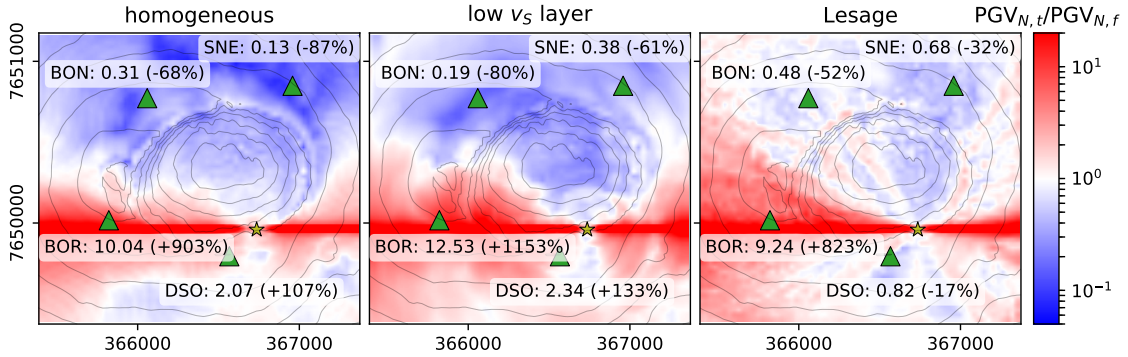

Figure 4.42 – Topographic amplification of north-component PGV. Ratio $PGV_{N,t}/PGV_{N,f}$ between model with topography and flat reference model from vertical source for the homogeneous model (*left*), the model with shallow low velocity layer (*middle*) and the Lesage velocity model (*right*). The yellow star denotes the source, green triangles the stations. Annotations give ratios measured at the station locations as well as percentage of topographic amplification. Neighboring contour lines differ 60 m in elevation.

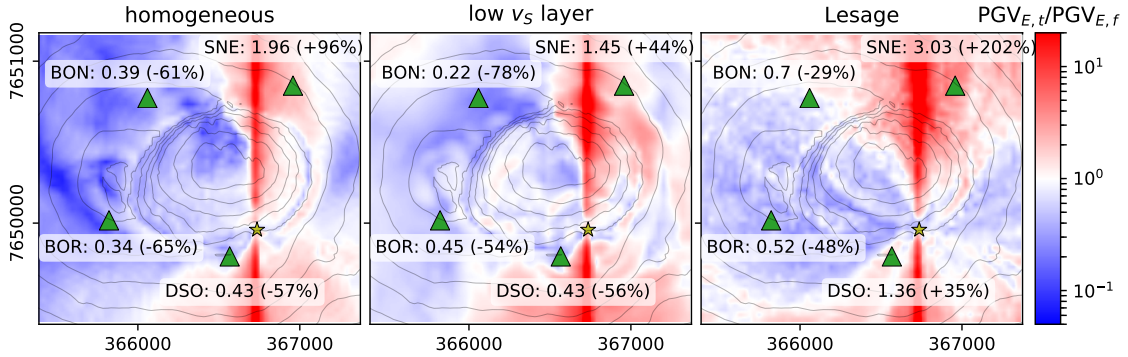

Figure 4.43 – Topographic amplification of east-component PGV. Ratio $PGV_{E,t}/PGV_{E,f}$ between model with topography and flat reference model from vertical source for the homogeneous model (*left*), the model with shallow low velocity layer (*middle*) and the Lesage velocity model (*right*). The yellow star denotes the source, green triangles the stations. Annotations give ratios measured at the station locations as well as percentage of topographic amplification. Neighboring contour lines differ 60 m in elevation.

4.9.2 Energy amplification in different frequency bands

Figure 4.44 and 4.45 show energy amplification in three different frequency bands for homogeneous model and Lesage model, respectively. Rayleigh wavelengths on the two models are

comparable in frequency band 3-7 Hz for the homogeneous model ($\lambda \approx 1000\,\mathrm{m.s^{-1}} \div 10\,\mathrm{Hz} = 100\,\mathrm{m}$) and in frequency band 8-12 Hz for the Lesage model ($\lambda \approx 580\,\mathrm{m.s^{-1}} \div 5\,\mathrm{Hz} \approx 116\,\mathrm{m}$, see dispersion curves in Fig. 4.4). However, we can observe that the amplification patterns differ from each other in these two frequency bands. This suggests that the respective amplification patterns are not only characteristic of a certain wavelength. The wave propagation essentially depends on the velocity model which hence results in different amplification patterns.

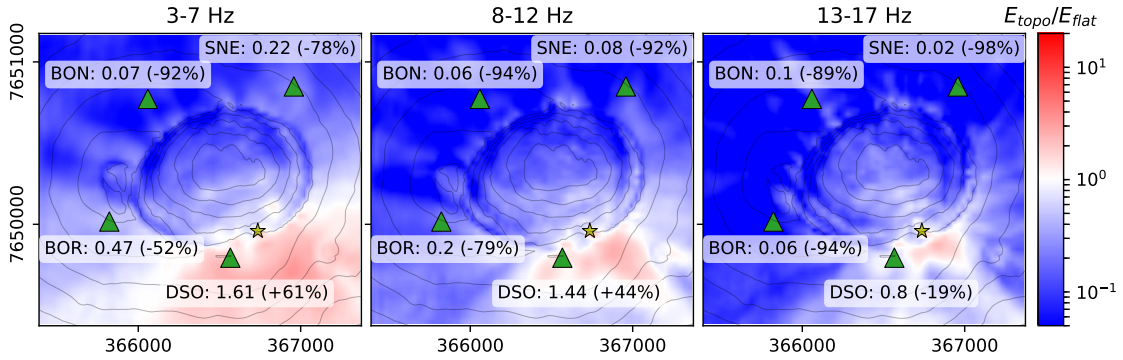

Figure 4.44 – Amplification of total kinetic energy in different frequency bands for homogeneous model. Energy amplification in respect to a flat reference model in frequency bands 3-7 Hz (*left*), 8-12 Hz (*middle*) and 13-17 Hz (*right*). The yellow star denotes the source, green triangles the stations. Annotations give ratios measured at the station locations as well as percentage of topographic amplification. Neighboring contour lines differ 60 m in elevation.

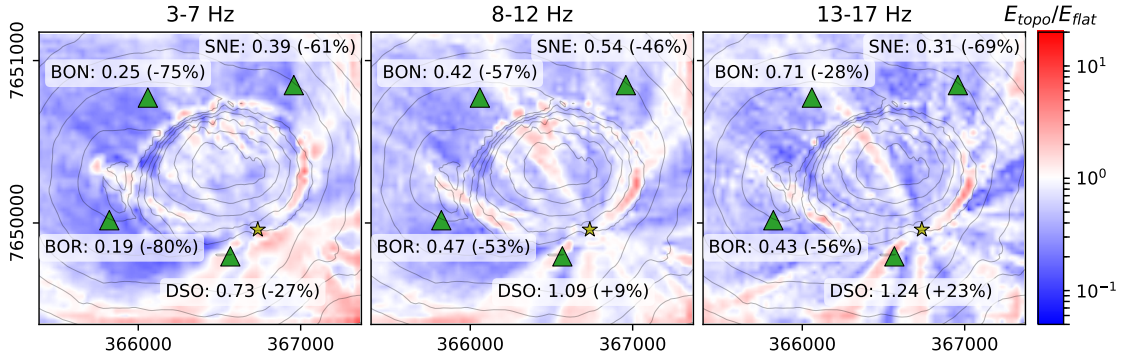

Figure 4.45 – Amplification of total kinetic energy in different frequency bands for Lesage model. Energy amplification in respect to a flat reference model in frequency bands 3-7 Hz (*left*), 8-12 Hz (*middle*) and 13-17 Hz (*right*). The yellow star denotes the source, green triangles the stations. Annotations give ratios measured at the station locations as well as percentage of topographic amplification. Neighboring contour lines differ 60 m in elevation.

4.9.3 Synthetic crater and surface roughness

Left hand side of Figure 4.46 demonstrates the symmetric interference patter caused by a perfectly symmetric synthetic crater. Seismic waves are guided on symmetric paths around the crater and interfere constructively on the opposite side of the source where strong amplification is visible. In order to break this symmetry and get a more realistic crater model, the surface roughness illustrated on the right hand side of Figure 4.46 is imposed onto the model. It is extracted from a real DEM and band-pass filtered between corner wavelengths of 40 m and 100 m.

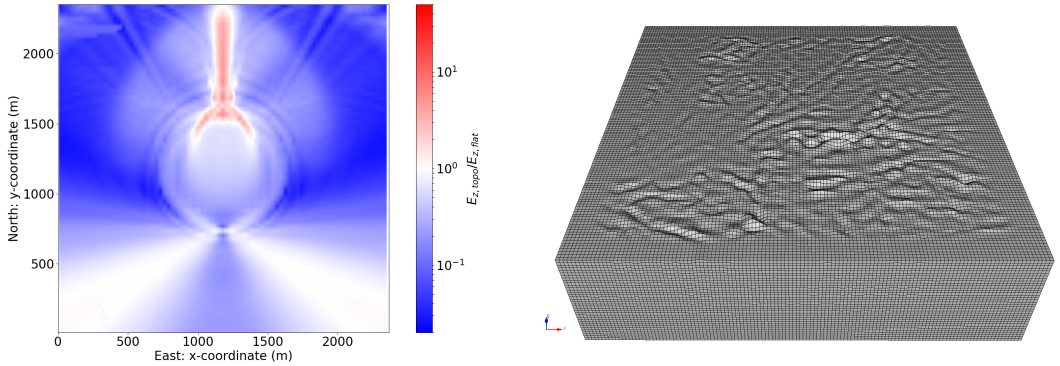

Figure 4.46 – Energy amplification on symmetric crater and domain with imposed surface roughness. *Left:* Amplification pattern of vertical energy caused by perfect symmetric crater shape. *Right:* Model domain with surface roughness of wavelengths between 40 m and 100 m. This roughness is imposed on synthetic crater topography in order to prevent symmetric interference patterns as illustrated on the left.

4.9.4 Observed and simulated spectral ratios for horizontal components

In section 4.6.2 we could see that the vertical spectral ratios from the real rockfall signals are generally higher than the simulated values. This can also be observed on the horizontal ratios. Spectral ratios from the north-component are shown in Figure 4.47. While ratios BOR/BON are slightly underestimated from the simulations, ratios SNE/BON show deviations of almost a factor 10. Ratios on the east-component are better reproduced as can be seen in Figure 4.48. However, similarly to the north-component, simulated ratios deviate more from the observed values in case of ratio SNE/BON.

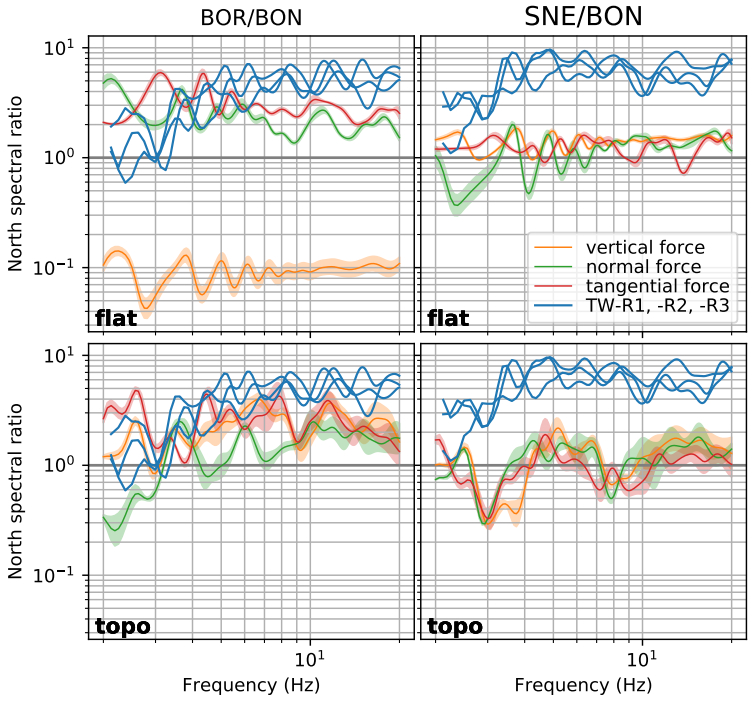

Figure 4.47 – Observed and simulated spectral ratios of north-component. Spectral ratios for BOR and SNE in respect to BON. Blue lines (TW-R1, -R2, -R3) correspond to observed rockfall signals as shown before in Fig. 4.24. Spectral ratios from synthetic seismograms are shown for a vertical force, a force normal to the slope and a force tangential to the slope on the model with flat surface (**flat**) and with topography (**topo**).

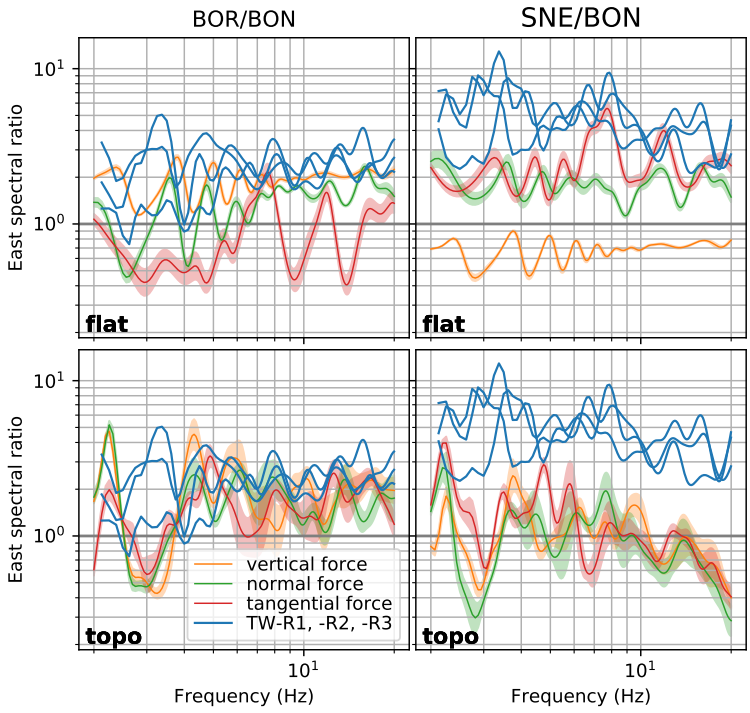

Figure 4.48 – Observed and simulated spectral ratios of east-component. Spectral ratios for BOR and SNE in respect to BON. Blue lines (TW-R1, -R2, -R3) correspond to observed rockfall signals as shown before in Fig. 4.24. Spectral ratios from synthetic seismograms are shown for a vertical force, a force normal to the slope and a force tangential to the slope on the model with flat surface (**flat**) and with topography (**topo**).

4.9.5 Variability of synthetic seismograms with source position

For the simulation of rockfall impacts, the impact position has to be estimated. The uncertainty of the estimation from the videos is expected to be in the order of at least 10 m. In the following, the variability of the waveforms with the source position is shown. Afterwards, a polarization analysis is carried out which also shows the variability of the signals, especially in case of surface topography.

Variability of waveforms

To evaluate the variability of waveforms on the source position, the synthetic seismograms from 5 different source-pairs are compared. Each source-pair corresponds to impacts N1 and N2. Besides the original source positions used in the analyses for N1 and N2 above, four additional positions are picked from a grid of 10 m spacing. Figure 4.49 illustrates the selected positions, whereas the red dots in the center correspond to the original position for N1 and N2.

The synthetic waveforms from each station pair are plotted in Figure 4.50 for both the flat model and the model with topography. In the case of the model with flat surface, a change of the waveforms can hardly be noticed when changing the source position. In contrast to that, the simulated waveforms on the topography show strong variations. The strong variability of waveforms indicates that a perfect fit with the observed signals is almost impossible due to uncertainties on source position and subsurface information. Simultaneously, it can be assumed that topography is one of the factors which causes of the different waveforms observed for the real signals at different stations.

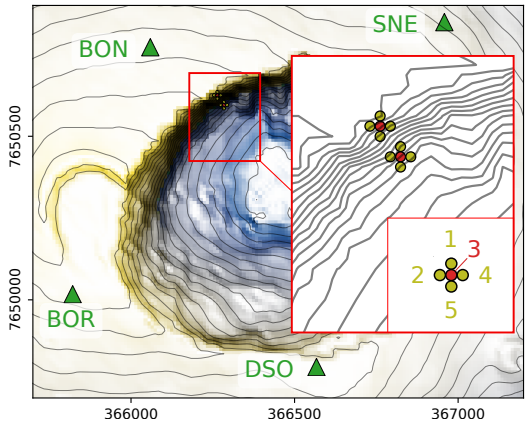

Figure 4.49 – Variation of source position for impacts N1 and N2. Four additional positions on a grid of 10 m spacing are picked around the original source position of impacts N1 and N2. The original position is marked by a red dot and annotated by number 3. The numbering of the synthetic waveforms shown in 4.50 corresponds to the definitions here.

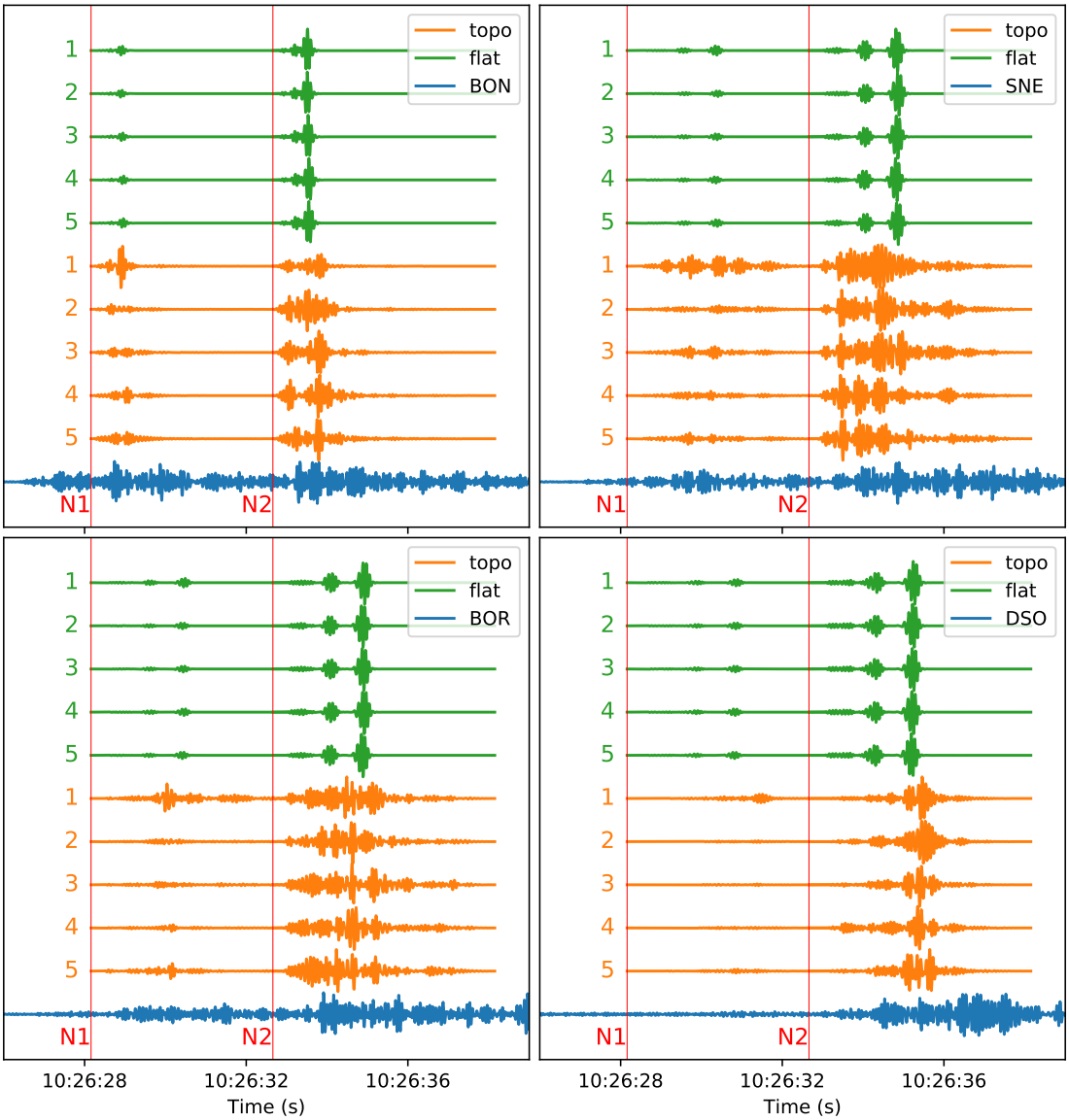

Figure 4.50 – Comparison of rockfall signal with synthetic waveforms for different source positions. Blue lines correspond to real seismograms at different stations. Red vertical lines indicate impact times N1 and N2 from the video. Synthetic waveforms of impacts N1 and N2 are shown for the model with flat surface (green) and with Dolomieu topography (orange). The variability of waveforms is demonstrated in dependency of source positions, which are illustrated in Figure 4.49. The source is composed of normal and tangential force (see Fig. 4.26). All traces are normalized by their maximum.

Variability of polarization

Polarization analyses can be used for the localization of landslides (e.g. Vilajosana et al., 2008; Bottelin et al., 2014). However, the polarization of surface waves can be strongly affected by topography. Ripperger et al. (2003) and Métaxian et al. (2009) demonstrate the complexity of particle motions for surface waves traveling along the topography of volcanoes. In the following, we will carry out a polarization analysis of the signal generated by impact N2. Observations and simulations are compared as above in a frequency band of 10-20 Hz. Two source positions are compared, located 10 m apart from each other. Figures 4.51 and 4.52 present the polarization analysis at station BON for source positions 2 and 3, respectively (the source positions are defined in Figure 4.49). The figures show synthetics from the flat model, from the model with topography as well as the real signals in terms of vertical (Z), radial (R), and transverse (T) component. Radial and transverse component are defined in respect to the source-receiver direction. Note that the synthetic signals correspond to a source composed by forces normal and tangential to the slope as illustrated in Figure 4.26. The same source direction is applied on the flat model. The polarization analysis is carried out for three time windows.

Regarding signals on the flat model for source position 2 (Fig. 4.51), we can infer from previous interpretations of the wave propagation on the Lesage model that TW1 contains the body wave, TW2 the 1st mode and TW3 the fundamental mode Rayleigh wave. Additionally, a signal on the transverse component indicates that the non-vertical source is also generating a Love wave. The polarization diagrams correspond to this interpretation. In TW1 a very small signal of mainly radial polarization is visible. TW2 contains a mixture of radial and transverse signal resulting from Rayleigh and Love wave. TW3 is circularly polarized in the radial-vertical plane, indicating a Rayleigh wave.

In contrast to the flat model, signals from the model with topography as well as real signals show different polarizations and stronger amplitudes in the first TW1. Polarizations correspond well to each other, also for TW2. In TW3, the particle motion becomes more complex. This complexity is not reproduced by the flat model.

Modifying the source from position 2 to 3 (from Fig. 4.51 to 4.52) completely switches polarization so that the polarization in the horizontal plane on the model with topography does not correspondent anymore to the real case. We can observe that also on the flat model the polarization changes. This means, that the change of polarization is partly caused by a change in source direction. The explanation for this is that the orientation of the slope is different at the new source position. Thus, the azimuth of the source changes. The question arises if the source polarization at more distant receivers is rather dominated by the propagation along topography than on the source polarization. Carrying out analyses in different time windows at station BOR and SNE, no clear answer for this question was found. Figures 4.53 and 4.54 present the polarization analysis at station SNE from source locations 2 and 3, respectively. We can observe that the particle motion changes with source position on the model with topography which indicate that the polarization is not completely dominated by the travel path. Nevertheless, the increased complexity of particle motion on topography corresponds better to the observed particle motion.

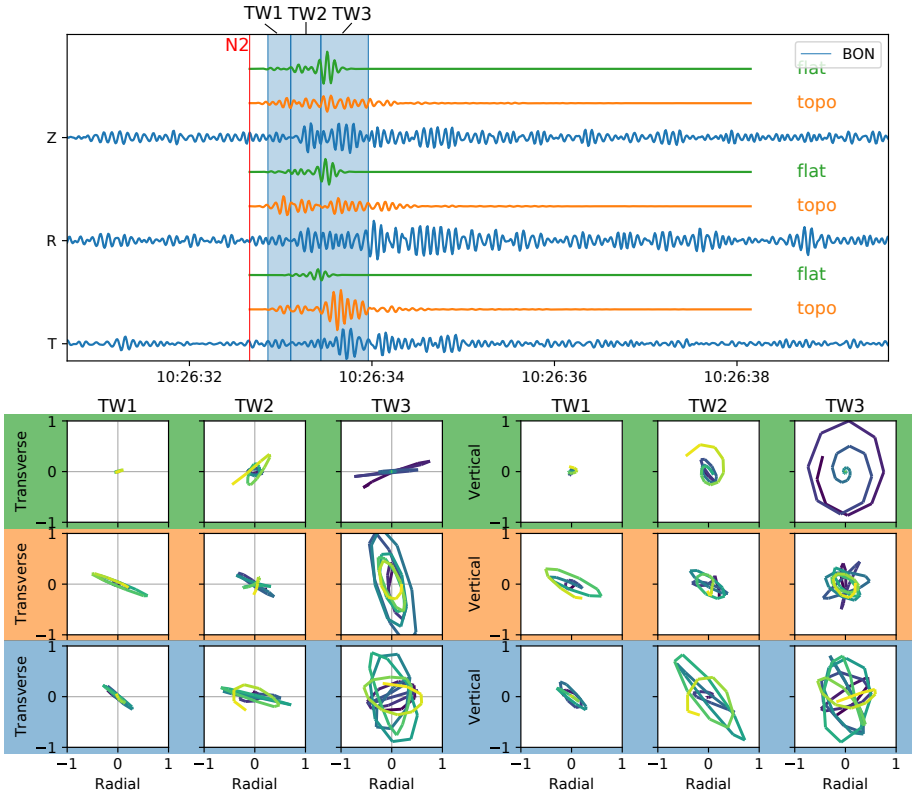

Figure 4.51 – Polarization analysis at station BON from source 2. *Top:* Vertical (Z), radial (R), and transverse (T) signal for flat model, model with topography and real recordings. *Bottom:* Particle motion in the transverse-radial plane (left) and the vertical-radial plane (right) for flat model(top), model with topography (middle) and real observations. Source position 2 is defined in Figure 4.50.

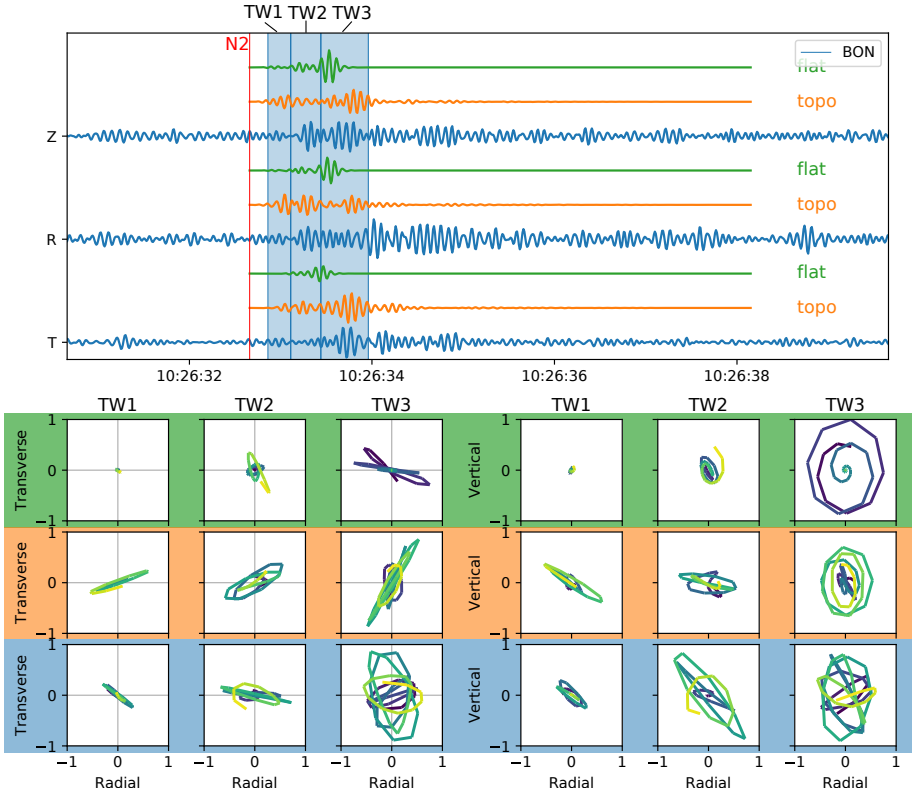

Figure 4.52 – Polarization analysis at station BON from source 3. As in Figure 4.51 for source position 3, which is defined in Figure 4.50.

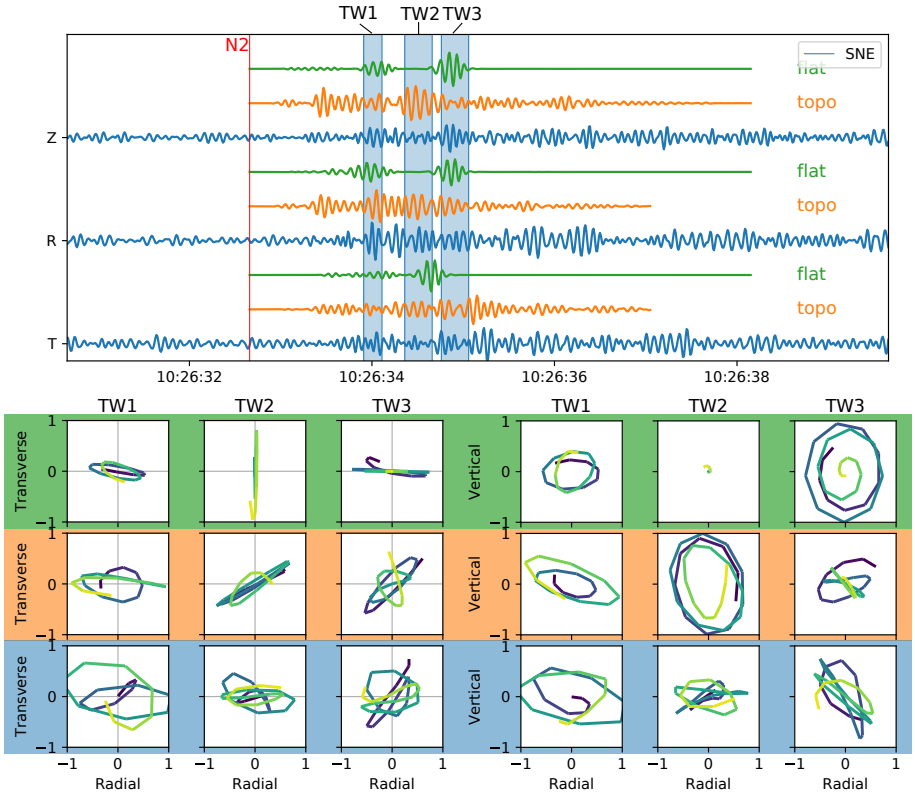

Figure 4.53 – Polarization analysis at station SNE from source 3. *Top:* Vertical (Z), radial (R), and transverse (T) signal for flat model, model with topography and real recordings. *Bottom:* Particle motion in the transverse-radial plane (left) and the vertical-radial plane (right) for flat model(top), model with topography (middle) and real observations. Source position 3 is defined in Figure 4.50.

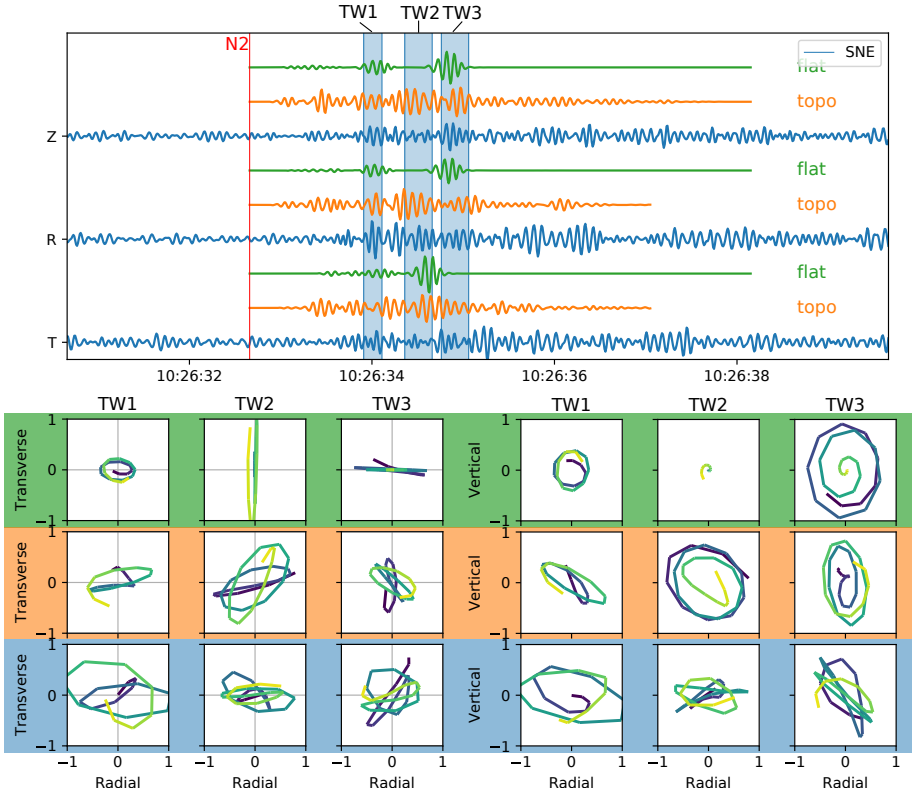

Figure 4.54 – Polarization analysis at station SNE from source 3. As in Figure 4.53 for source position 3, which is defined in Figure 4.50.

Chapter 5

Rockfall localization based on inter-station energy ratios

5.1 Abstract

Landslide generated seismic signals have been shown to be of great utility in order to detect and monitor landslide activity. Furthermore, landslide locations were successfully estimated using methods which rely on either arrival times, amplitudes or polarization of the seismic signal. However, strong surface topography can significantly influence seismic wave propagation and thus flaw the estimates if not taken into account correctly.
On the upside, the imprint of topography on the seismic signal can be characteristic of the source position. We show that this additional information can be used to get a more detailed landslide location estimation. In order to do so, the seismic impulse response is modeled on a domain with 3D topography using the spectral element method. Subsequently, in order to locate events, station energy ratios of the synthetic seismograms are compared with energy ratios of landslide signals in a sliding time window.
We test the method on rockfalls which occurred at Dolomieu crater of Piton de la Fournaise, La Réunion. We propose that the method can be applied for monitoring landslide activity in a specific area with multiple seismic stations after calculating once the impulse response for the corresponding topography.

5.2 Introduction

Besides investigating the structure and dynamics of the Earth's interior, seismology is increasingly used to study and monitor processes on the Earth's surface. This study is commonly referred to as environmental seismology (Larose et al., 2015). Surface processes can include natural phenomena such as storms (e.g. Ebeling and Stein, 2011), glaciers (e.g. Tsai et al., 2008; Podolskiy and Walter, 2016; Sergeant et al., 2016), rivers (e.g. Gimbert

et al., 2014), debris flow (e.g. Burtin et al., 2009) and landslides (e.g. Hibert et al., 2011; Allstadt, 2013; Bottelin et al., 2014; Vouillamoz et al., 2018). Furthermore, seismic signals can be used to monitor urban structures (e.g. Mordret et al., 2017) as well as human activity such as traffic (e.g. Riahi and Gerstoft, 2015; Fuchs and Bokelmann, 2018).
In the context of landslides, seismic signals can be used to identify hazard. Growing networks of seismic stations offer the opportunity to continuously monitor large regions of interest. Events can be detected, classified, characterized and located. This helps create catalogs of landslide events which serve to understand their occurrences. Thanks to this, triggering mechanism could be studied by correlating landslide catalogs with meteorological data (Burtin et al., 2009; Helmstetter and Garambois, 2010; Durand et al., 2018) or with data of volcanic seismicity (Hibert et al., 2017b; Durand et al., 2018). Besides monitoring hazard, rockfall localization can also give insight into volcano summit deformation (Durand et al., 2018).
Several methods for landslide localization by means of seismic signals have been proposed. We can divide the methods into two groups of approaches. The first group infers the source position geometrically by pointing towards it from several stations and determining the intersection. For this, the azimuth of incoming phases has to be determined. This can either be done by polarization analysis with three-component seismometers (Vilajosana et al., 2008) or with array methods to estimate the apparent slowness vector (Almendros et al., 2002). The second group back-projects properties of the signal onto the source position, trying to find the best correlation between multiple stations. The back-projection relies either on the decay of amplitudes with distance (Battaglia and Aki, 2003), or on travel time differences between stations. Travel time differences can be inferred from cross-correlation of signal envelopes (Burtin et al., 2009; Lacroix and Helmstetter, 2011; Yamada et al., 2012) or from picking of first arrival times (Hibert et al., 2014b; Fuchs et al., 2018).
As landslides predominantly occur in mountainous regions, generated seismic waves are prone to interact with the strong surface topography variations. The influence of topography on seismic wave propagation has long been subject of study (Geli et al., 1988). Topography can affect the wave path, wave polarization (Ripperger et al., 2003; Métaxian et al., 2009) and seismic amplitudes (Lee et al., 2009a). If not taken into account correctly, these topographic effects compromise localization methods and decrease their precision.
Assuming elongated wave paths along the topography, back-projection methods can take topography into account adjusting source-receiver distances and thus travel times. This is done for example by Hibert et al. (2014b) to locate rockfalls at Dolomieu crater, La Réunion. However, elongation of wave paths does not consider diffraction or scattering along the topography. In fact, the influence of topography can be described as a propagation effect as waves which travel along the surface are subject to an accumulation of effects.
In the following we try to predict the characteristic imprint of topography on the seismic signal as a function of the source location. For this, we use the Spectral Element Method (SEM) on a numerical domain with 3D topography. Simulations are compared with observed signals generated by rockfalls at Dolomieu crater on Piton de la Fournaise, La Réunion, by means of spectral ratios. Subsequently, a method is proposed for the localization of rockfall seismic sources. The method is based on energy ratios between station pairs with the assumption that the ratios are characteristic of the position of the seismic source. A higher resolution of the localization is expected when considering topography.

5.3 Data from rockfalls at Dolomieu crater

The study site is located on Piton de la Fournaise volcano, La Réunion, shown in Figure 5.1b). Rockfalls occur frequently at the instable flanks of Dolomieu crater, which was formed during the caldera collapse in 2007 (Michon et al., 2007). The volcano is monitored by the *Observatoire Volcanologique du Piton de la Fournaise* (OVPF). Instrumentation includes a dense network of seismic stations and three cameras on top of Piton de la Fournaise, looking into Dolomieu crater. This allows to correlate seismic signals generated with camera images which is of great benefit to study rockfalls and the generated seismic waves.

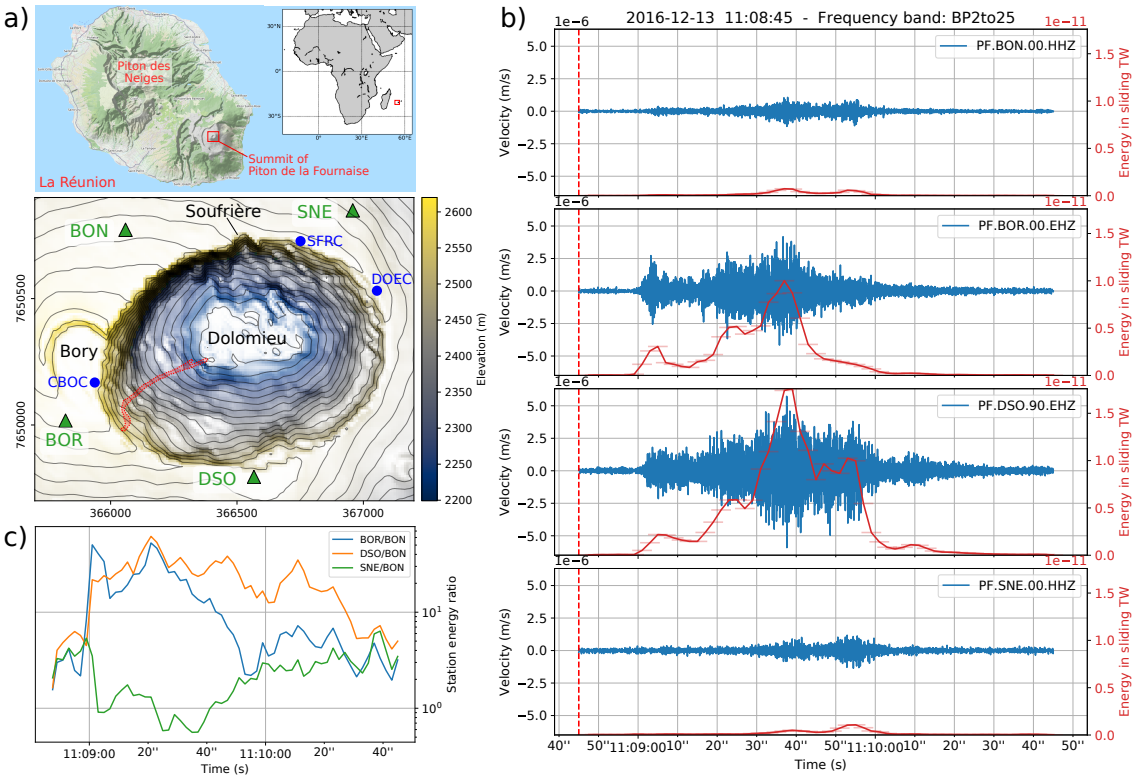

Figure 5.1 – Rockfall seismic signals at Dolomieu volcano crater. a) Dolomieu crater is located on the summit of Piton de la Fournaise volcano, which is on the island of La Réunion in the Indian Ocean, east of Madagascar. Smaller craters Bory and Soufrière are located east and north of Dolomieu crater, respectively. Seismic stations are marked by green triangles and cameras by blue dots. The red zone marks a rockfall trajectory estimated from the video. **b)** Seismic signals generated by the rockfall indicated in a). Signals are recorded at the four seismic stations surrounding Dolomieu crater. The red lines show the evolution of recorded seismic energy, which is calculated in windows of 4 s length which are sliding with time steps of 2 s. **c)** Ratios of seismic energy between station pairs. The beginning of the rockfall is marked by an abrupt change of the ratios.

Figure 5.1 shows the recorded ground velocity caused by a rockfall on the southwestern crater wall. It can be observed that the signal at the closest station BOR is starting most abruptly, whereas signals at further stations BON and SNE show slowly emerging amplitudes. The different temporal evolution of the recorded signals can nicely be seen by the evolution of recorded seismic energy which is overlaid in Figure 5.1b). To measure the temporal evolution of seismic energy at each station, we integrate squared ground velocity

over a sliding time window of 4 s width. [1]
Station energy ratios are shown in Figure 5.1c), where station BON is chosen as reference station. Note that BON is also chosen as reference site for the site amplification functions as it is found to be the least amplified station. The beginning of the rockfall is marked by an abrupt increase of the ratios BOR/BON and DSO/BON, whereas ratio SNE/BON is dropping. Subsequently, the ratios are evolving differently as the rockfall is moving towards the bottom of the crater.
As the seismic source is identical for all stations, the temporal evolution of energy ratios is caused by the path of wave propagation. First of all, the moving source position changes source-receiver distances and hence modifies signal amplitudes due to geometrical spreading and intrinsic attenuation. However, additional propagation effects can be introduced by soil heterogeneities and topography between source and corresponding receiver. In the following we will model the influence of topography whereas soil heterogeneities are considered with the help of empirical site amplification factors.

5.4 Methodology

The proposed methodology for the estimation of rockfall localization is based on the assumption that energy ratios between stations are characteristic for a given source position. This assumption was validated in Chapter 4 by analyzing spectral ratios for three rockfalls occurring on the southern crater wall. In the following we will show another example for rockfalls located on the southwestern crater side. Using this assumption, we try to infer the rockfall source position by comparing observed energy ratios with simulations. Note here that the method is not using the spectral ratios but rather the energy ratio averaged within frequency bands of 4 Hz. This makes the method robust against spurious variations of the spectral values. In order to explore all potential rockfall sources, reciprocal simulations will be carried out where the synthetic source is placed on the location of the seismometers. Then, a grid search is performed in order to find the source positions which best fit the observed energy ratios. This method will first be tested on a synthetic example, discussing the limits of the approach, and finally applied to real events.

5.4.1 Observed spectral ratios

Similar to the analysis carried out in section 4.6.1 of Chapter 4, we compare spectral station ratios for different rockfalls. The spectral ratios are computed in a time window for which all rockfalls are in the same area. If the spectral ratios are found to be similar, it can be assumed that they are characteristic of the source position. They are then compared with synthetic spectral ratios from a model with flat surface and a model with Dolomieu topography. Note that in order to enhance comparability between real and observed spectral ratios, site effects due to the local subsurface structure are removed from the real

1. Note that in order to calculate the actual kinetic energy, the squared ground velocity has to be multiplied by the material density times a factor of one half (see equation 3.20). However, as we are interested in station energy ratios, we neglect this multiplication assuming similar material densities at all four stations.

signals. As discussed in Chapter 4, we assume that amplification factors estimated from volcano-tectonic (VT) seismic signals are similar for rockfall signals. The site amplification functions are shown in Figures 4.29 and 4.30 for vertical and horizontal ground motion, respectively.
The trajectories of the chosen rockfalls are mapped on the left hand side of Figure 5.2. Their locations are approximated based on camera images.

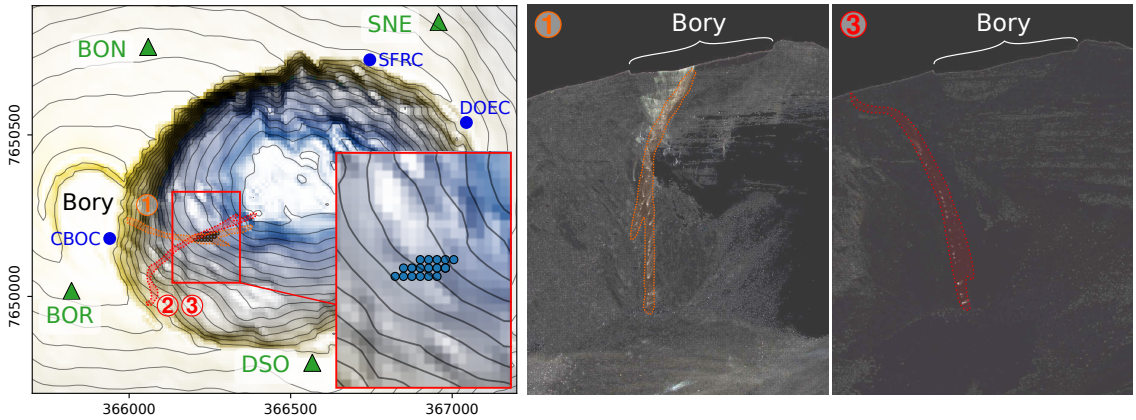

Figure 5.2 – Rockfalls at the southwestern crater wall. *Left:* Estimated trajectories of three events: rockfall **1** starts right below crater Bory, whereas rockfalls **2** and **3** start further south with similar trajectories. All trajectories meet within the red rectangle where synthetic sources are placed for the comparison of spectral ratios. The inset shows a zoom of the synthetic source positions, marked by blue dots. *Right:* Trajectories of rockfall **1** and **3** reconstructed from differences of successive images taken from camera DOEC. The profile of crater Bory can be recognized and serve for orientation.

Rockfall **1** starts right beneath crater Bory which is located on the western side of Dolomieu crater. Rockfalls **2** and **3** start further south until crossing the trajectory of rockfall **1** half way down on their way to the crater bottom. The generated seismic signals will be compared at a time which corresponds to this crossing position. Trajectories of rockfall **1** and **3** are visualized on the right hand side of Figure 5.2 in images which are reconstructed from differences between successive snapshot taken from camera DOEC. This allows to see the whole trajectory in a single image.
The seismic signals generated by rockfalls **1-3** are shown in Figure 5.3, together with images taken from camera CBOC. At the time of the shown images, all rockfalls are located in the same area. The time is marked on the seismic signals by the vertical dotted red lines R1, R2, and R3.
The camera images reveal that each of the rockfalls involves at least two boulders moving downslope simultaneously. Their locations are marked by red ellipses. The associated arrows indicate their direction of movement. We can see that while the boulders of rockfall **1** originate from below the camera position, boulders of rockfall **2** and **3** come from the right hand border of the image. This corresponds to the mapped trajectories in Figure 5.2. The waveforms of the signals differ accordingly to the different trajectories. Looking at the signal on closest station BOR, amplitudes are strongest right in the beginning in case of rockfall **1**. In contrast, signals of rockfalls **2** and **3** show different shapes, in which the strongest amplitudes are recorded later in the signal. As station BOR is at similar distance from the starting positions of the two different trajectories (see Figure 5.2), the different waveforms cannot be explained by source-receiver distance alone. It is possibly the source

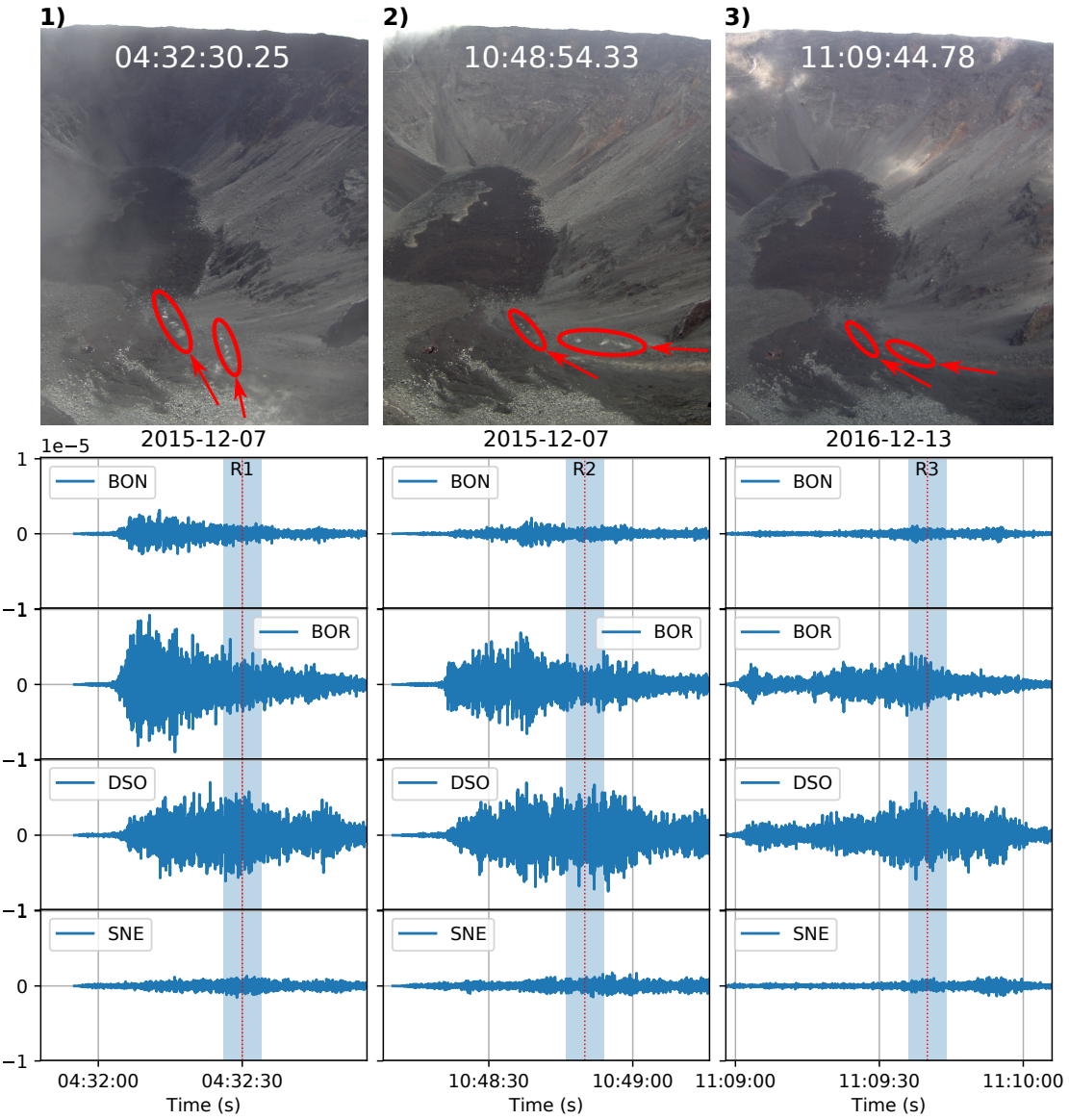

Figure 5.3 – Camera snapshots and seismic signals of the three rockfalls on the southwestern crater side. *Top:* Camera images taken from camera CBOC of rockfalls **1**, **2** and **3** at the time for which all rockfalls are in comparable positions (compare with Figure 5.2). Trajectory and directions of the boulders are indicated by red circles and arrows. *Bottom:* Seismic signals corresponding to rockfalls **1**, **2** and **3**. The vertical dotted lines R1, R2 and R3 mark the time of the camera snapshot shown above. Blue shaded zones display the time windows of ± 4 s around R1, R2, and R3 in which spectral station ratios of the signals are computed.

mechanism which dominates the waveforms. Rockfall **1** starts at the very steep flank right below Bory crater. It is thus immediately accelerated very strongly resulting in strong impacts. On the other hand, rockfalls **2** and **3** start on less steep flanks. It can hence be assumed that their velocities are smaller in the beginning resulting in smaller amplitudes at station BOR compared to the signals of rockfall **1**.

Later on, the trajectories of the three rockfalls cross (see map in Figure 5.2 and snapshots in Figure 5.3). At this point the spectral station ratios are compared in order to find out if they are similar according to the similar source location. The spectral ratios are computed from the signals in a window of ± 4 s around the time of the shown snapshots. Ratios computed from vertical ground velocity are shown by the blue lines in Figure 5.4

(note that site amplification is already removed here). It can be observed that the spectral ratios from the three events are indeed very similar across the whole frequency range for all station pairs, i.e. BOR/BON, DSO/BON and SNE/BON.

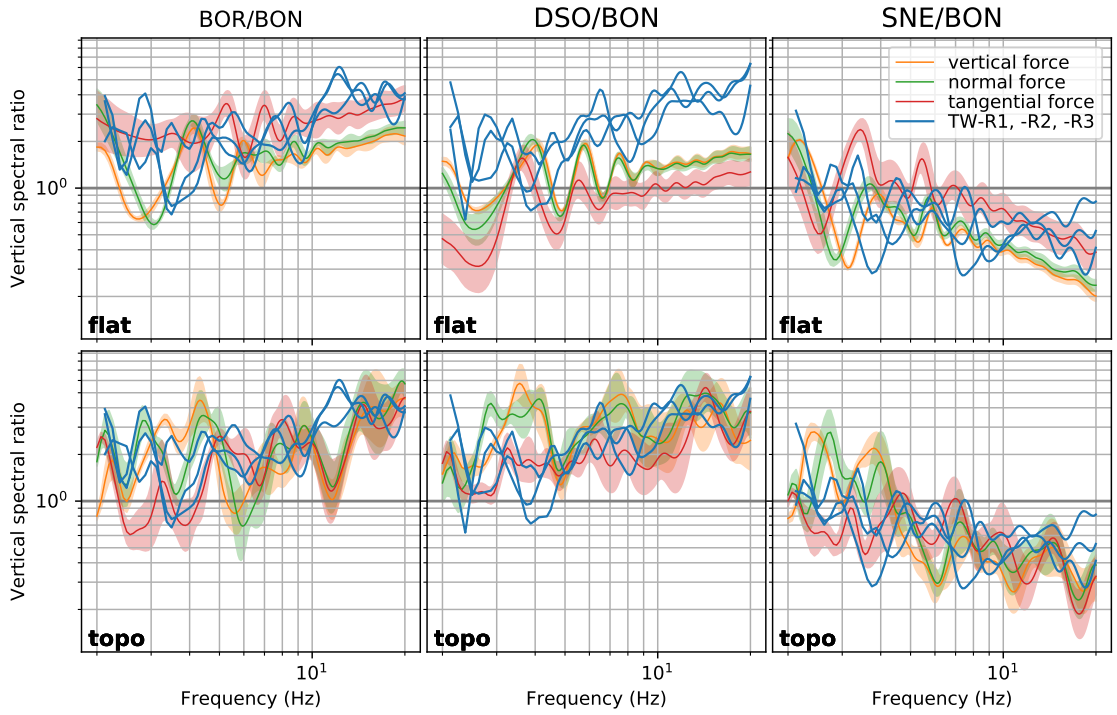

Figure 5.4 – Observed and simulated spectral ratios of vertical component. Vertical spectral ratios for BOR, DSO and SNE in respect to BON. Blue lines (TW-R1, -R2, -R3) correspond to observed rockfall signals as shown before in Fig. 5.3. Spectral ratios from synthetic seismograms are shown for a vertical force, a force normal to the slope and a force tangential to the slope on the model with flat surface (**flat**) and with topography (**topo**). Prior to calculating the ratio, site effects are removed and FFTs are smoothed using the function proposed by Konno and Ohmachi (1998).

The spectral ratios are compared to simulations from a model with flat surface (top of Figure 5.4) and a model with Dolomieu topography (bottom of Figure 5.4). The dependency of the ratios on the source direction is investigated. Three input force configurations are tested, namely a vertical force, a force normal to the slope and a force tangential to the slope in direction of the strongest slope gradient. Furthermore, the variability of the ratios in regards to the source location is assessed by calculating the mean spectral ratio from 17 source positions on a grid of 10 m spacing. The different source positions are illustrated by blue dots in Figure 5.2.

The biggest difference between simulations on flat surface and topography can be observed on ratio DSO/BON. While the flat surface model predicts ratios close to unity, the model with topography contains amplified factors (values > 1), especially for frequencies above 7 Hz (corresponding to fundamental Rayleigh wavelengths below 70 m on the Lesage velocity model). This means that the topography causes stronger amplitudes at station DSO with respect to station BON which are both at comparable distances from the source of more than 500 m (corresponding to at least seven wavelengths). This agrees very well with the observed spectral ratios which cannot be explained by the flat model.

Other than this we can see that changing the source direction does not essentially influence the spectral ratios from the model with topography, except for frequencies below 5 Hz. The

similarity at higher frequencies suggest that the ratios are dominated by the propagation along the topography rather than by the source mechanism. Based on this finding, we can estimate the source position independently of the source direction. This will be used in the proposed method for localization estimation in the following, in which we will assume a vertical input force. In contrast, on the model with flat surface, more influence can is observed when changing the source direction. The ratios of the tangential force differ systematically from the ratios of vertical and normal force. This is caused by the different radiation patters from changing source direction, as illustrated in Figure 4.26 in Chapter 4.

The strong influence of the source direction on the flat surface model becomes more evident on the horizontal components. Figures 5.5 and 5.6 show the spectral ratios calculated from signals recorded on the north- and east-component, respectively.

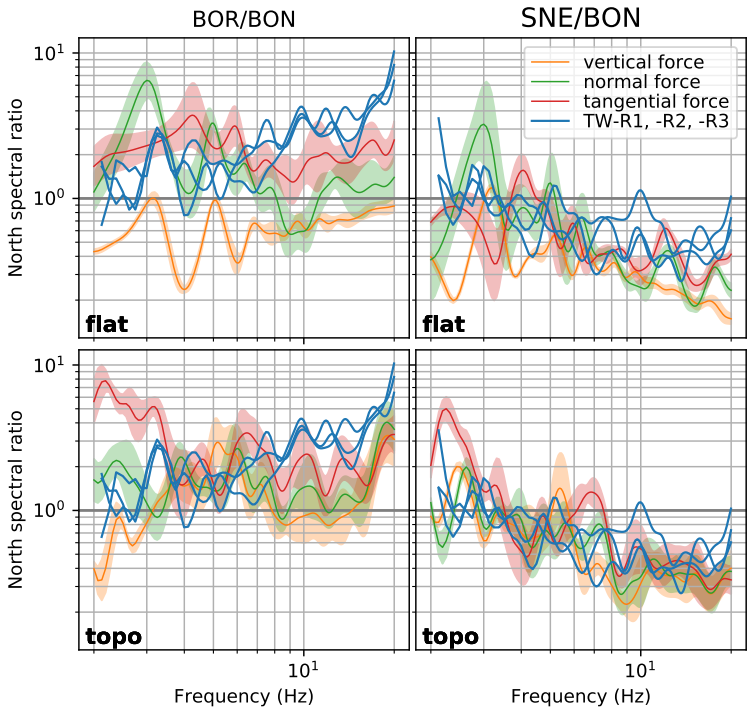

Figure 5.5 – Observed and simulated spectral ratios of north component.
North-component spectral ratios for BOR and SNE in respect to BON. Blue lines (TW-R1, -R2, -R3) correspond to observed rockfall signals as shown before in Fig. 5.3. Spectral ratios from synthetic seismograms are shown for a vertical force, a force normal to the slope and a force tangential to the slope on the model with flat surface (**flat**) and with topography (**topo**).

Again we can observe that the spectral ratios from the real signals are very similar between the three rockfall events (plotted by blue lines R1, R2, and R3). Comparing with simulations from the model with flat surface, it is obvious that changing the source direction has a strong effect on the spectral ratios. This can be in particular seen on the east-component in Figure 5.6. As just mentioned above, the differences are caused by the radiation patterns from different source directions. In contrast, ratios from the simulation on the model with topography are less influenced by the source direction, especially at frequencies above 5 Hz. The ratios agree reasonably well with the observed ratios from the rockfall signals. The strongest deviation is visible towards high frequencies on ratio SNE/BON for the east-component (see bottom right in Figure 5.6). In comparison with the observed spectral ratios, the simulated amplitudes measured at station SNE are strongly underestimated with respect to station BON. On the one hand, this could be caused by the simplified Earth model of the simulations, which does not take into account lateral

soil heterogeneities. On the other hand, we could see from the videos that the rockfall source is made of at least two boulders at slightly different positions. The recorded signal is hence a superposition of the generated seismic waves. This is not considered for the simulated spectral ratios which are computed from single forces. Furthermore, it is very difficult to pick exact source positions based on the video. Therefore, rather than picking source positions manually, we will establish an algorithm with which we can search for the positions which best explain all observed station ratios. The algorithm is based on a single force assumption which is a strong limitation of the method. We will see that the source location estimation works best in the beginning of the rockfall, as the source is very confined. Later on, when the rockfall source becomes spatially distributed, the uncertainty of the estimation is increasing. However, the general movement towards the crater bottom can still be inferred.

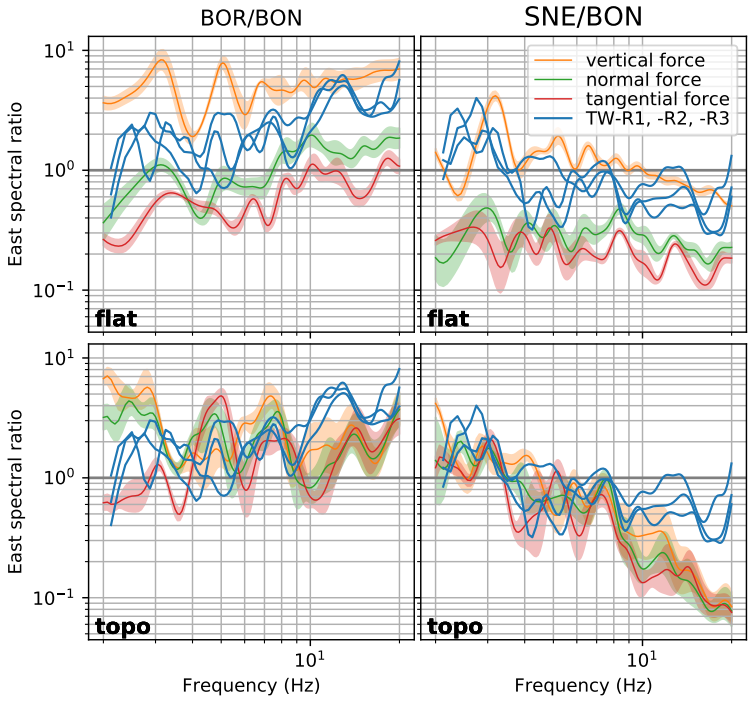

Figure 5.6 – Observed and simulated spectral ratios of east-component.
East-component spectral ratios for BOR and SNE with respect to BON. Blue lines (TW-R1, -R2, -R3) correspond to observed rockfall signals as shown before in Fig. 5.3. Spectral ratios from synthetic seismograms are shown for a vertical force, a force normal to the slope and a force tangential to the slope on the model with flat surface (**flat**) and with topography (**topo**).

5.4.2 Reciprocal SEM simulations

In order to explore a multitude of potential rockfall source positions without carrying out a simulation for each of them, simulations are carried out reciprocally. This means that the synthetic source is placed at the location of the seismometer and the wave field is recorded at the actual source location. Potential rockfall source positions are confined to a rectangular area at Dolomieu crater, illustrated in Figure 5.7. The area is sampled by a grid of measurement points with 10 m spacing.
After defining the points of measurement, simulations for each seismometer are carried out. For this, a point source is placed at the position of the seismometer while the input force direction is aligned with the component of the seismometer. In total, 10 simulations are carried out: 3×3 simulations for three-component seismometers BON, BOR, and SNE,

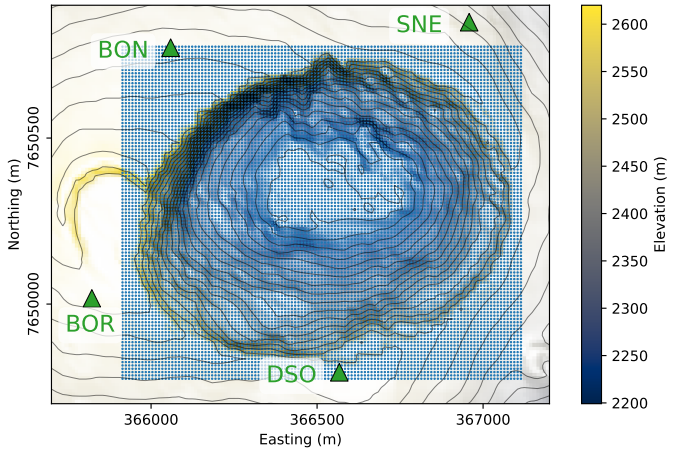

Figure 5.7 – Grid of stations for reciprocal simulations. The sampled area is of dimensions 1200 m × 1000 m (east×north). Sample spacing is 10 m, resulting in 121 × 101 = 12221 grid points.

and 1 simulation for single-component seismometer DSO. This is done for both the model with Dolomieu crater topography and a model with flat surface for comparison.
The wave propagation is simulated on a domain with Lesage velocity profile as presented in Figure 4.3 of Chapter 4. A Ricker wavelet of 7 Hz dominant frequency is used as force-time function.

Simulated station energy ratios

For the localization of rockfall sources, we will compare observed and simulated station energy ratios. Here, we demonstrate the influence of topography on these energy ratios.
As an example, we simulate the vertical ground velocity generated by a vertical source. For each station pair, the total kinetic energy ratio is computed at each grid position. The total kinetic energy is the squared ground velocity (here on the vertical component), integrated over the total duration of the signal. Note that for the demonstration here, we use the unfiltered signal. For the localization of rockfalls afterwards, we will consider the frequency dependency of the ratios by band-pass filtering the signal in frequency bands of 4 Hz.
First of all, let's have a look on the energy ratios from the model with flat surface. The spatial distributions of ratios BOR/BON, DSO/BON, and SNE/BON are visualized in Figure 5.8.

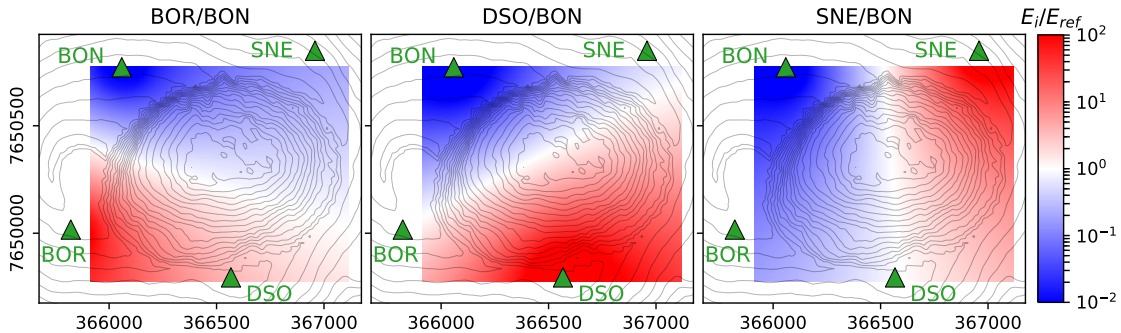

Figure 5.8 – Station energy ratios from simulations on model with flat surface. At each grid position (see Fig. 5.7) the ratio is computed between seismic energy E_i at station BOR (*left*), DSO (*middle*), and SNE (*right*) and seismic energy E_{ref} at reference station BON.

We can observe bipolar pattern of the energy ratios with negative values towards reference station BON and positive values towards the respective station in the numerator. Unity of the ratios can be followed by a white line which represents the equidistant positions between the station-pairs. In conclusion, the values are purely determined by the source-receiver distances.
This is different for the energy ratios on the model with surface topography, displayed in Figure 5.9. In general, the bipolar spatial distribution of ratios still persists as the source-receiver distance still dominate the decay of seismic amplitudes. However, the patterns become distorted due to the influence of the topography on the wave field.

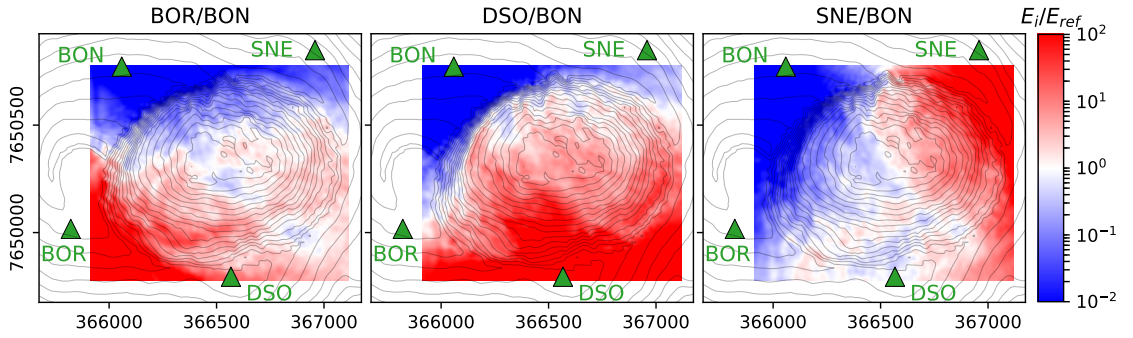

Figure 5.9 – Station energy ratios from simulations on model with flat surface. At each grid position (see Fig. 5.7) the ratio is computed between seismic energy E_i at station BOR (*left*), DSO (*middle*), and SNE (*right*) and seismic energy E_{ref} at reference station BON. In comparison with energy ratios on the flat surface model shown in Figure 5.8, topography distorts the values.

Using the predicted spatial distribution of energy ratios from the simulation, we try to better reproduce observed energy ratios and enhance the capability to locate the source position. Here, we demonstrated the influence of topography on the unfiltered energy ratios. For locating rockfall, we will band pass filter the signals in order not to blur informations from different frequencies. The energy ratios filtered in three different frequency bands can be seen in appendix 5.7.1 from the model with topography.

5.4.3 Optimization method for source localization

After introducing the database of synthetic energy ratios in the previous section, we will now propose an equation which allows to compare observed and synthetic energy ratios in order to find the most probable source position. To do this, a probability value is associated to each point of the grid presented in Figure 5.7.
The probability at each grid point is defined by the inverse of the error between synthetic energy ratio $E_i^{\text{simu}}/E_{\text{ref}}^{\text{simu}}$ and observed energy ratio $E_{i,\text{tw}}^{\text{obs}}/E_{\text{ref,tw}}^{\text{obs}}$, where 'ref' is the station of reference and i is one of the remaining stations. As the rockfall source is moving, the observed energy ratio is evaluated in time window 'tw'. The error e_{tw} for each time window is defined as follows:

$$e_{\text{tw}} = \frac{1}{N_{\text{Sta}}} \sum_{i=1}^{N_{\text{Sta}}} \left| \log_{10} \left(\frac{E_i^{\text{simu}}}{E_{\text{ref}}^{\text{simu}}} \div \frac{E_{i,\text{tw}}^{\text{obs}}}{E_{\text{ref,tw}}^{\text{obs}}} \right) \right|, \tag{5.1}$$

where N_{Sta} is the number of station pairs used for the calculation. Zero error is achieved if simulated and observed energy ratios are equal. Using the logarithm in equation 5.1 ensures that the relative values between simulations and observations are equally spaced around zero. This, combined with the absolute, results in an error estimation which is independent on the station of reference.
In the following, the proposed method is tested on synthetic and real examples. The probability of the source location is calculated by the inverse of error e_{tw} and scaled to a probability density function (PDF) with relative values between 0 and 1.

5.5 Application

In the previous section we proposed a formalism to evaluate the relative probability of potential source locations on a predefined grid of positions. We will now test this method initially on a synthetic example and subsequently on real rockfall signals. Finally, the probabilities of all time windows are combined in the attempt to reconstruct the full rockfall trajectory.

5.5.1 Synthetic example

For the synthetic example, three vertical single force sources are defined at different positions well separated in time. Synthetic seismograms are simulated on the model with topography.
The location is estimated using simulations from the model with topography and the model with flat surface. This way we can make sure that the energy ratios are influenced by the topography and not solely dominated by source-receiver distances, in which case the source could be localized using the flat model. The energy ratios are calculated from the signals filtered in a frequency band of 13-17 Hz. We will later compare the results with estimations using signals filtered in frequency bands 3-7 Hz and 8-12 Hz. The highest frequency band is found to have the best spatial resolution due to the shorter wavelengths (15 Hz correspond to a fundamental Rayleigh wavelength of around 26 m on the Lesage velocity model). Also note that the time windows are chosen long enough so that the whole signal of a single source is measured at each station. For the real rockfall, the time window will be shortened in order to better separate successive source positions.
First of all, we calculate the source location probability using only the vertical components. Having 4 stations available, error e_{tw} is calculated from $N_{\mathrm{Sta}} = 3$ station pairs. The resulting probability maps are shown in Figure 5.10 for the three source locations (P1, P2, and P3), comparing the estimations using the model with topography (**Topo**) with the flat model (**Flat**). The source location is positioned in the center of the red circle.
Using the simulations from the model with topography, the true source position is found in all cases P1, P2, and P3 (observable by the dark purple dot in the center of the red circles). This is not surprising as the station energy ratios are calculated from exactly the same synthetic seismograms. However, what is more interesting is that the results are ambiguous, meaning that several positions of high probability are found. On the other hand, using the simulations from the flat model, the true source position is not found. Areas of

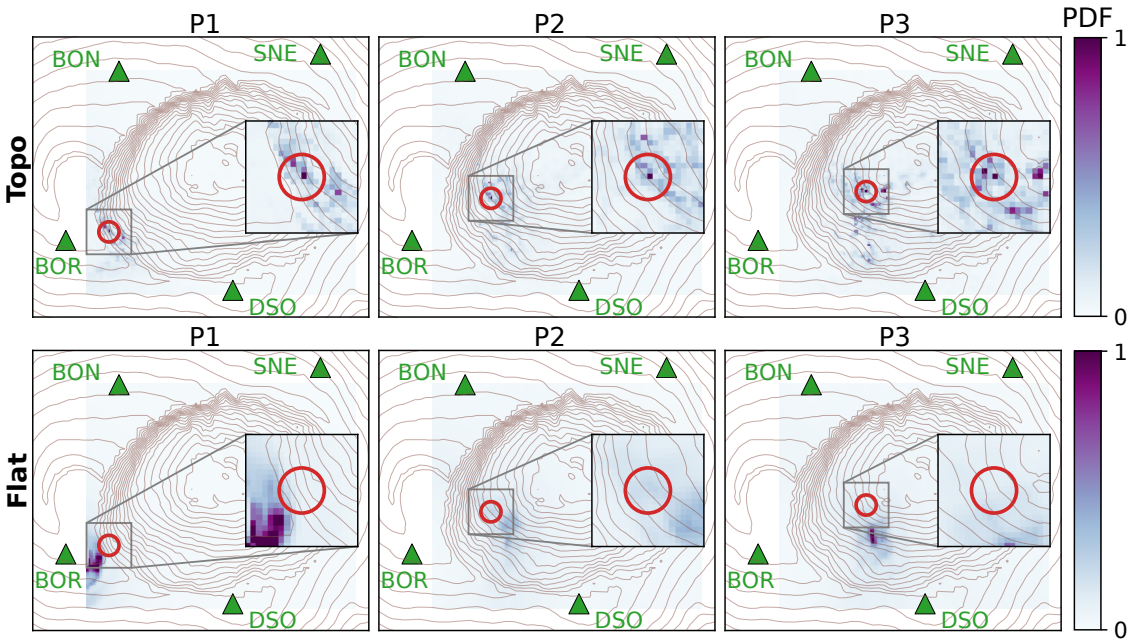

Figure 5.10 – Localization of single vertical forces using vertical energy ratios. Synthetic test for localization of three single vertical sources at different positions P1, P2, and P3. The source location is positioned in the center of the red circle. Localization is carried out in frequency band 13-17 Hz using synthetic seismograms of vertical component from a model with topography (*top*) and a model with flat surface (*bottom*).

high probability are located outside the red circles which have a diameter of around 90 m. This means that the station energy ratios are influenced by the topography and not only determined by the source-receiver distance.

In order to reduce ambiguity of the results, the horizontal components are included in the calculation. This way, we have $N_{\text{Sta}} = 7$ station pairs: 3 station pairs of vertical component and 2 stations pairs for each north- and east-component as DSO only has a vertical component. The resulting probability maps are shown in Figure 5.11, again for all source positions (P1, P2, and P3), and using simulations from the model with topography (**Topo**) and from the flat model (**Flat**).

Introducing the horizontal components reduces the ambiguity of the source position. Using the model with topography, a single point of high probability is found at the true source positions in the center of the red circles. In contrast, using the flat model, hardly any source location of higher probability can be found when introducing the horizontal components. This is due to the fact that a vertical source on a flat model does not generate energy on the transverse components. This is related to the behavior already seen on the spectral ratios for the horizontal components (see Figures 5.5 and 5.6). For certain source directions, the predictions of the flat model were in strong disagreement with the observed ratios, whereas a better agreement was found for the model with topography.

Finally we compare the source localization using different frequency bands. The probability maps for frequency bands of 3-7 Hz, 7-12 Hz, and 13-17 Hz are shown in Figure 5.12. The localization is carried out with the simulations from the model with topography. Results are compared using only vertical components (**Z**) and all three components (**ENZ**).

We can observe that the ambiguity of the localization reduces towards higher frequencies. The low frequency band 3-7 Hz show very blurred probability maps. This is related to

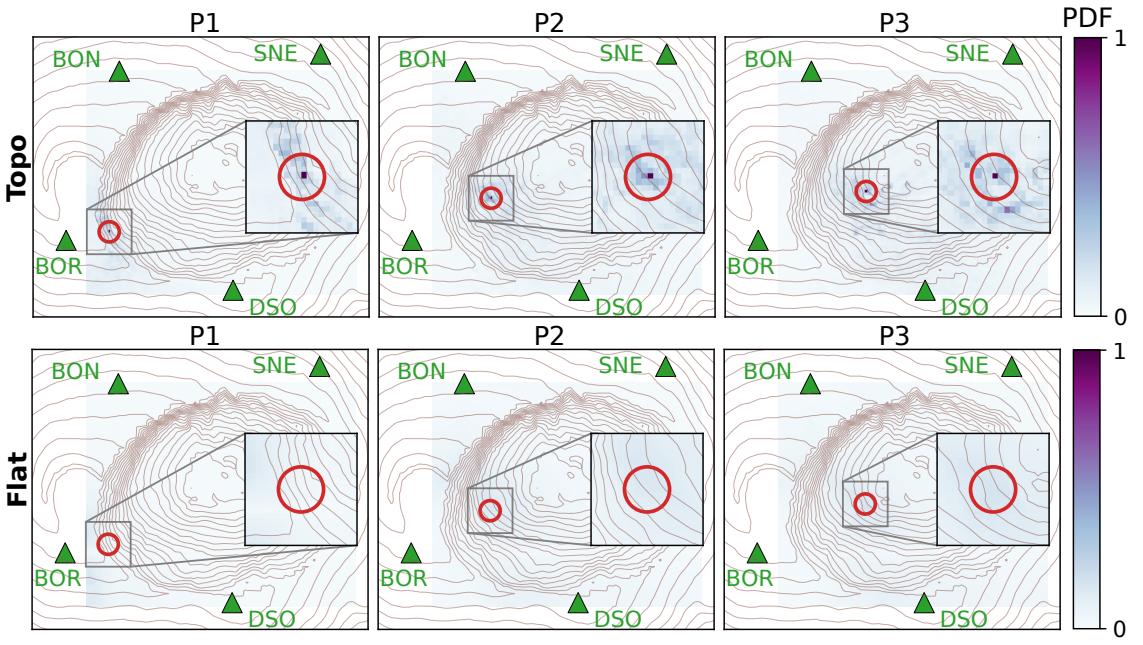

Figure 5.11 – Localization of single vertical forces using vertical and horizontal energy ratios. Synthetic test for localization of three single vertical sources at different positions P1, P2, and P3. The source location is positioned in the center of the red circle. Localization is carried out in frequency band 13-17 Hz using synthetic seismograms of vertical and horizontal components from a model with topography (*top*) and a model with flat surface (*bottom*).

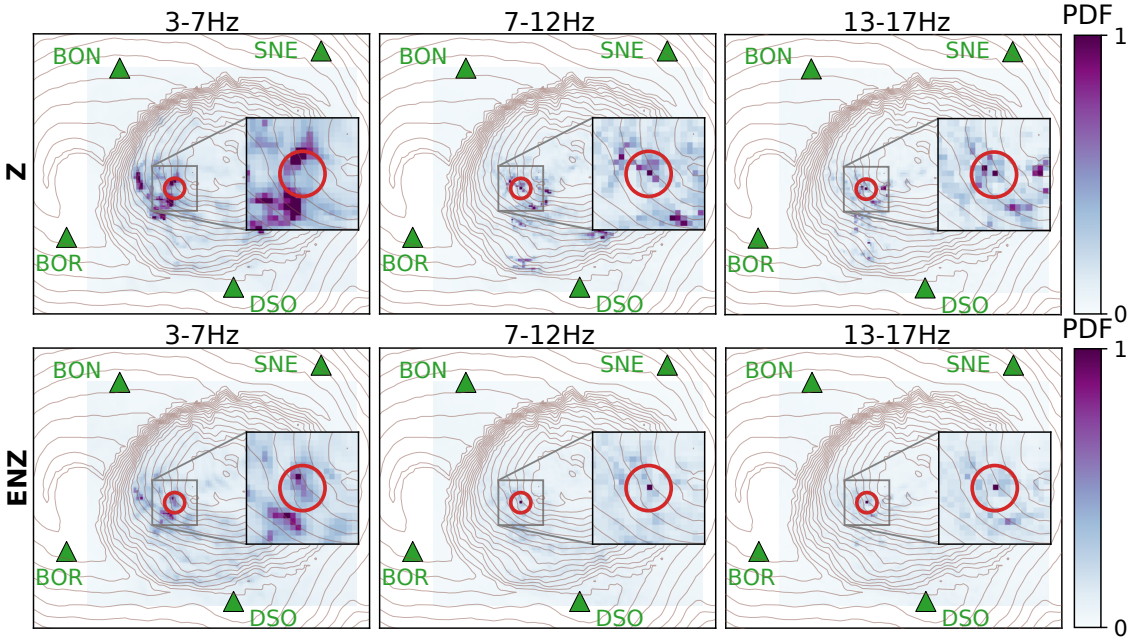

Figure 5.12 – Localization of single vertical forces energy ratios in different frequency bands. Synthetic test for localization of three single vertical sources at different positions P1, P2, and P3 after filtering the signals in frequency bands 3-7 Hz (*left*), 8-12 Hz (*middle*), and 13-17 Hz (*right*). The source location is positioned in the center of the red circle. Localization is carried out using synthetic seismograms from only vertical components (**Z**, *top*) as well as vertical and horizontal components (**ENZ**, *bottom*) from a model with topography.

the longer wavelengths (5 Hz corresponds to a fundamental Rayleigh wavelength of 116 m on the Lesage model) and thus reduced spatial resolution. The medium frequency band 8-12 Hz shows similar estimation as from the highest frequency band. A really good result

is found when considering all three components. Yet, using only vertical components leads to slightly more ambiguity.
To summarize, station energy ratios are influenced by topography and can help to localize single seismic sources with the method defined by equation 5.1. Ambiguity of the localization can be reduced by considering both vertical and horizontal components. The spatial resolution of the localization is enhanced by the use of higher frequencies which correspond to shorter wavelengths.
The synthetic test showed the general capability of the method. However, it presents a very special case in which the seismic sources are very well separated in time. In reality, the seismic source of a rockfall can be much more complicated consisting of multiple blocks or granular material imposing forces on the ground simultaneously at different positions. In the following we will apply the method on a first example rockfall which consists only of a few boulders and can be nicely observed on video.

5.5.2 Rockfalls at Dolomieu crater

Rockfall localization at given time steps

The localization method is tested on a rockfall on December 13, 2016, corresponding to event **3** in Figure 5.2. The analysis is carried out at 6 different times a) to f) as defined on the seismogram in Figure 5.13. Above the seismogram, the whole trajectory is visualized as well as snapshots of times b) to e).
Time a) is right before the start of the rockfall. Time b) is after the detachment, when movements can be detected on the video. At time c), the rockfall appears from behind a small valley at the top of the crater wall. A total of three boulders are detectable time d) on their way down towards the crater bottom. At time e), the third boulder arrives at the bottom. No movement is detectable anymore on the video at time f). Yet, it can be assumed that smaller granular material is still active on the flank, causing small amplitude seismic signals.
The localization method is performed in the high frequency band of 13-17 Hz. The energy is calculated from the signals within a window of ± 2 s around the defined times. The window length should be chosen as small as possible in order to sample the moving source. However, as we use the same time windows for the recordings at all stations, the whole signal generated by a given source has to arrive at each of the stations within the time window. For this reason a window length of 4 s was defined which seems an appropriate compromise (see e.g. Figure 4.36 for arrival time and duration of signals from a single source).
As concluded from the synthetic test in the previous section, the localization performs best when considering all components and simulations from the model with topography. To begin with, the real rockfall event is analyzed accordingly. The resulting source location probabilities are shown in Figure 5.14 for the 6 successive time windows.
We can observe probable source locations at the southeastern crater side at time a). As the rockfall has not started at that time, the source locations must be related to ambient seismic noise. Then, after the start of the rockfall, the source probability moves westwards in direction of the rockfall. However, the detachment position is wrongly localized outside

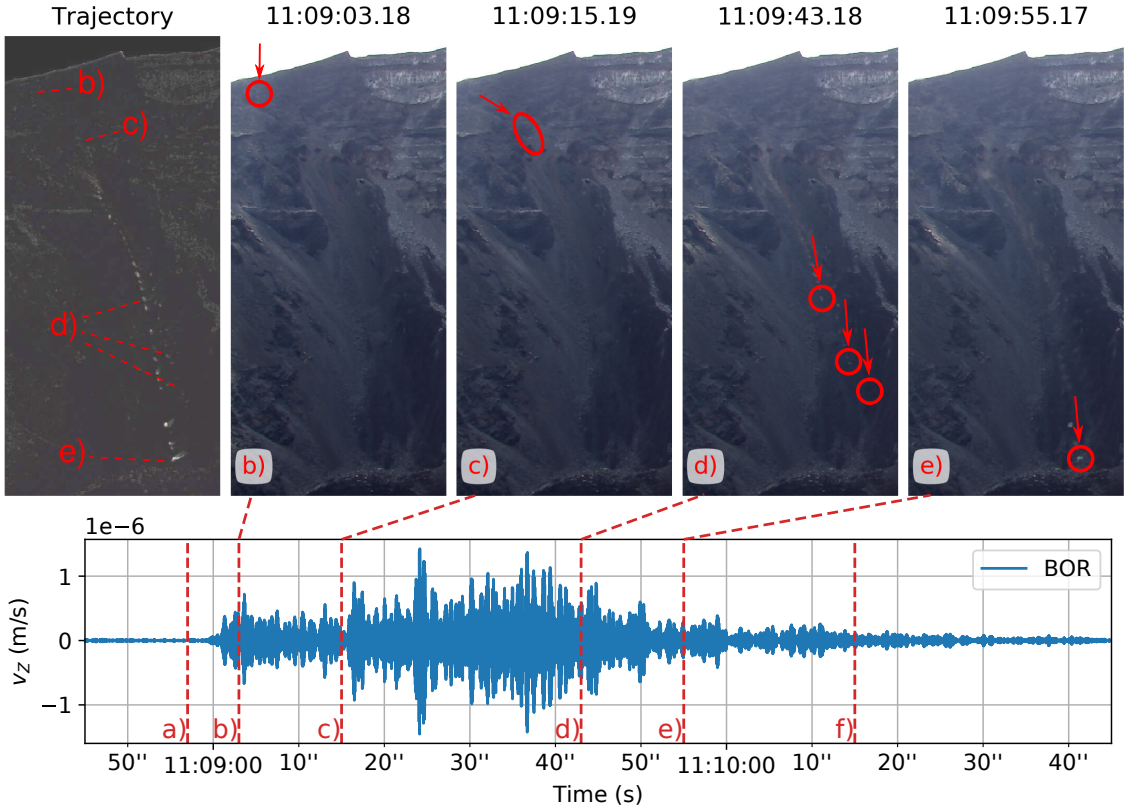

Figure 5.13 – Camera images and seismic signal of rockfall on December 13, 2016. *Top:* Images taken from camera DOEC. Image on the left shows the whole rockfall trajectory. Towards the right, snapshots at times b) to e) are displayed. Rockfall positions are indicated by red circles, the direction of movement with red arrows. *Bottom:* Vertical ground velocity v_Z recorded at closest station BOR. Time steps a) to f) are marked by red vertical dashed lines. Localization is performed in time windows of ± 2 s around these time steps. The signal is bandpass filtered at 13-17 Hz.

the crater. The area of probable sources does not move significantly for time step c). At time d), a movement in northeast direction is visible which continues till time e) which corresponds to the time at which the third boulder has arrived at the bottom of the crater. Time f) finds similar source positions as the previous two time steps.

All in all, we can observe that the area of probable source locations move during the course of the rockfall. However, the locations do not correspond well with the true rockfall trajectory. The offset might be caused by local site amplification at the stations which are not considered in the simulations. For this reason, we perform the same analysis with signals from which the site effects are removed. For this the site effects estimated from VT seismic signals are used as presented in Figures 4.29 and 4.30 for vertical and horizontal ground motion, respectively. The resulting localization probability maps are displayed in Figure 5.15.

Is is visible that the localization is in better agreement with the actual rockfall position. Right after the start of the rockfall, the source probability focused close to the position of detachment. It then moves northwest at time c), before moving northeast towards the crater bottom during times d) and e). At time e), after the last visible boulder arrived at the crater bottom at time, a zone of probable source positions rest in the bottom part of the trajectory. This can possibly be explained by movement of granular material which

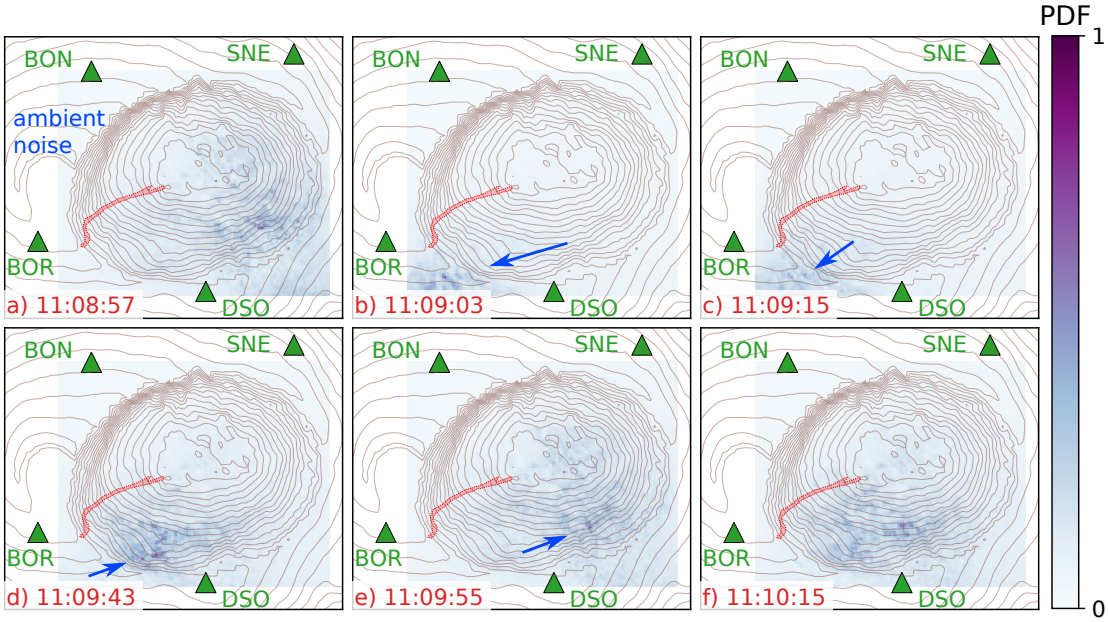

Figure 5.14 – Localization with seismic signals from which site effects are not removed. Localization of seismic source at time steps a) to f) as defined in Figure 5.13. The color-scale represents the source location probability. Blue arrows indicate the movement of the area of most probable source locations. Red shaded zone marks actual rockfall trajectory, estimated from video. Signals are filtered in frequency band of 13-17 Hz. Both vertical and horizontal components are employed. Simulations are carried out on model with topography.

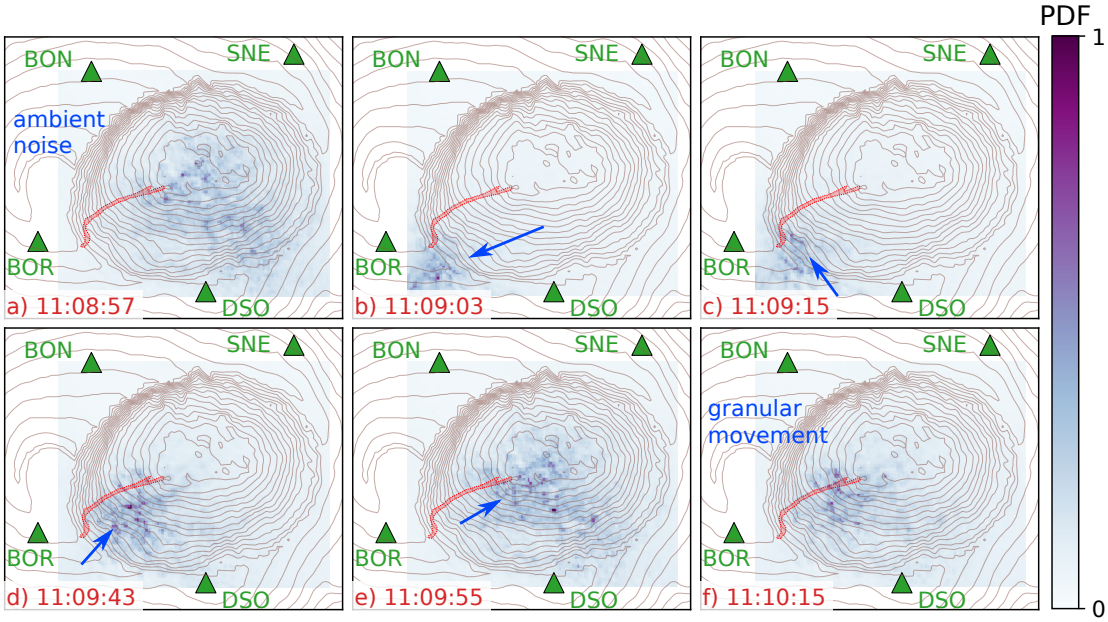

Figure 5.15 – Localization with site effect corrected seismic signals. Localization of seismic source at time steps a) to f) as defined in Figure 5.13. Site effects estimated from VT signals are removed from vertical and horizontal ground velocity (see Fig. 4.29 and 4.30 for site amplification functions). The color-scale represents the source location probability. Blue arrows indicate the movement of the area of most probable source locations. Red shaded zone marks actual rockfall trajectory, estimated from video. Signals are filtered in frequency band of 13-17 Hz. Simulations are carried out on model with topography.

can not be detected on the video.

The results are now compared with estimations using simulations from the model with flat surface in order to evaluate the benefit of taken into account the topography. For the

localization with the flat mode, only the vertical components are considered because the horizontal components are not well predicted from the vertical source (see discussion on the synthetic example in section 5.5.1). This leads to $N_{\mathrm{Sta}} = 4$ station pairs. The resulting probability maps are shown in Figure 5.16.

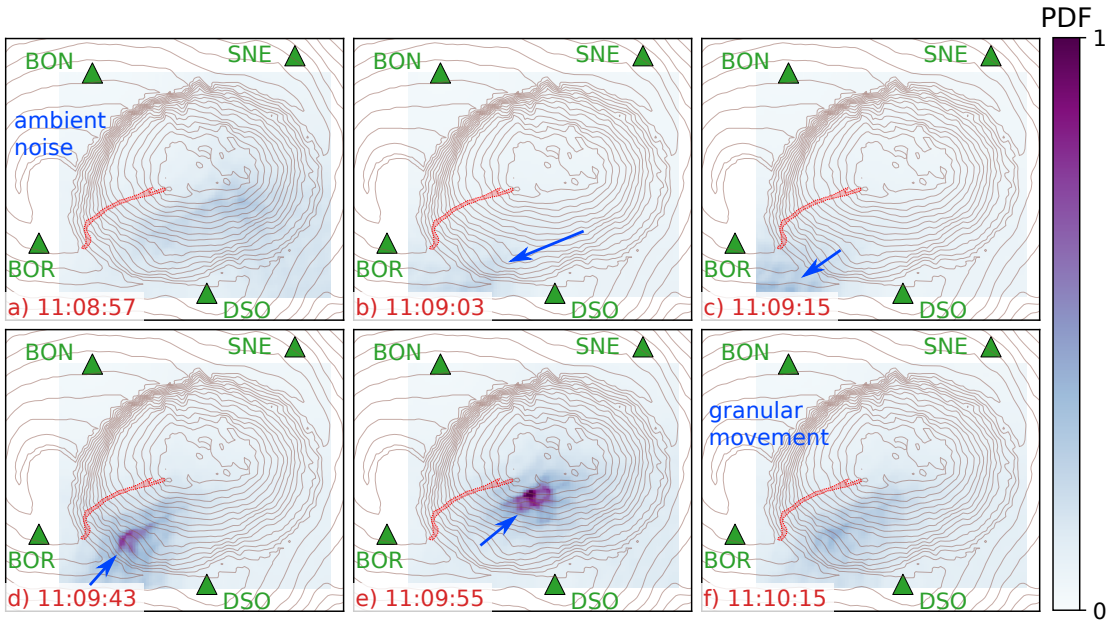

Figure 5.16 – Localization with site effect corrected seismic signals using simulations from flat model. Localization of seismic source at time steps a) to f) as defined in Figure 5.13. Site effects estimated from VT signals are removed from vertical and horizontal ground velocity. Simulations from the model with flat surface are used for the localization (in contrast to the results shown in Figure 5.15). The color-scale represents the source location probability. Blue arrows indicate the movement of the area of most probable source locations. Red shaded zone marks actual rockfall trajectory, estimated from video. Signals are filtered in frequency band of 13-17 Hz.

In general, a similar behavior of the moving source location probability can be observed as from the simulations with topography. However, comparing time b) at the beginning of the rockfall, the probability from the flat model does not focus close to the position of detachment. Instead, a very blurry zone of low probability is visible. This is similar for time c). In fact, it is possible that the probability focuses outside the sampled rectangular area. Then, for times d) and e) a focused area of high probability is observable moving towards the crater bottom. It is located south of the actual rockfall trajectory. At time f), again an unfocused zone of low probability is visible.

In general we could see that analyzing the station energy ratios in moving time windows allows to monitor rockfall activity. The beginning of the rockfall can clearly be detected as the location probability map is abruptly changing towards the position of the detachment. At this time, when the seismic source is still very confined in space, taking into account the topography seems to improve the focus of the method. Later, when the source becomes more distributed in space, the localization is becoming more scattered. In the following we will evaluate the localization of the whole rockfall by applying a sliding window analysis. The reconstructed temporal evolution will be visualized and compared between analyses using simulations from models with and without topography.

Spatio-temporal rockfall evolution

In order to reconstruct the full rockfall trajectory, the localization method of equation 5.1 is performed using a sliding time window. Subsequently, results from all time windows are combined at each potential source position by selecting the maximum probability over time. In other words, for each grid point, the minimum error e between observed and simulated energy ratios is defined by

$$e = \min_{\mathrm{tw}} e_{\mathrm{tw}}, \tag{5.2}$$

where e_{tw} it the error in each time window 'tw' as defined in equation 5.1. The maximum probability is the inverse of error e. The spatio-temporal evolution of the rockfall is then visualized by plotting at each grid point both maximum probability and corresponding time.

Figure 5.17 compares the localization from models without and with Dolomieu topography (*flat* and *topo*, respectively). Time is represented by color whereas intensity gives the probability of the source location. Only vertical components are used for both cases, i.e. $N_{\mathrm{Sta}} = 4$ station pairs. Signals were filtered in frequency band 13-17 Hz and site effects are removed. The time step of two successive time windows is set to 2 s. The window length of 4 s is kept from before.

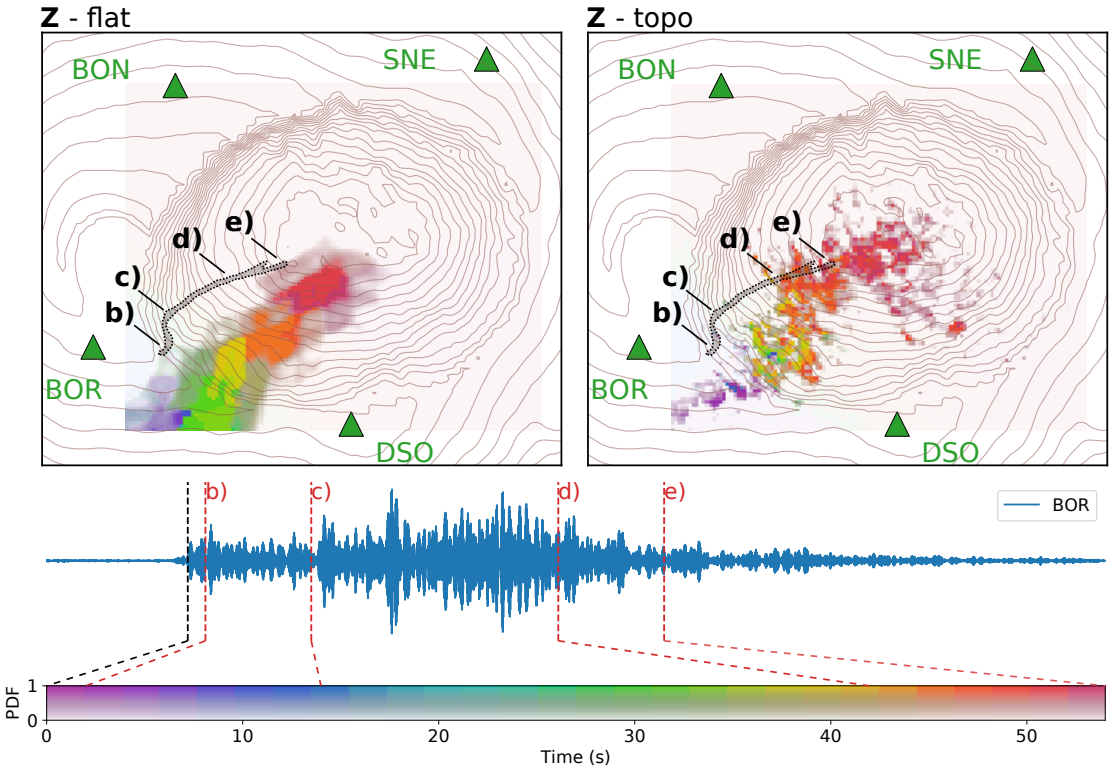

Figure 5.17 – Estimation of spatio-temporal rockfall evolution from vertical components. Comparison of localization using the flat model (*left*) and the model with topography (*right*). Color represents time, intensity represents probability of source location. Only vertical components are used for the localization. Seismic signals are filtered in frequency band of 13-17 Hz. The signal recorded at the closest station BOR is plotted below so that time steps b) to e) can be associated to colors (compare with Figure 5.13).

The localization using the flat model results in a probability distribution which is smooth

in space but discontinuous in time (i.e. patches of colors change abruptly to a different color). Looking at Figure 5.16, which shows the source location probability at certain time steps, we can observe for example at time e) a localized area of high probability. A similar patch at time e) can be recognized in Figure 5.17 in red color. The focalized areas of high probability at certain at certain time steps leads to the discontinuous patches.
In contrast, the localization with simulations from the model with topography result in a more continuous time evolution in which the colors change more smoothly. On the other hand, the patterns are more scattered.
Analyzing the rockfall evolution in more detail, the model with topography seems to better locate the detachment position in the beginning of the rockfall corresponding to time b) and purple color. Probable positions are located close to the crater rim, even though south of the actual position. Ambiguous positions are also found outside the crater. Position c) is not very well mapped from neither of the two models. However, probable source positions might also be overlaid by higher probabilities at later times. This is a limitation of the method which assumes a continuous forward movement of the source position. We will discuss about possible solutions for this later. Position d), corresponding to orange color, is mapped too far south by the flat model. The model with topography finds positions of high probability which are closer to the actual trajectory. Finally, at time e), corresponding to the red color, the source positions found by the model with topography are spatially strongly scattered. This can have different reasons. Firstly, source positions in this area might be more ambiguous which is accordingly to the test on the synthetic example for source position P3 (see Figure 5.10). Secondly, as the big boulders have arrived at the bottom on the crater by time e), the seismic signals might not be dominated by a single source anymore but rather consists of a superposition of spurious seismic sources from granular material. Hence, as the method is based on the assumption of a single source, the localization is flawed.
In general, the estimated locations from both models are south of the actual rockfall trajectory. This might be caused by soil heterogeneities which are not perfectly accounted for by the site effects. Nevertheless, the site effects estimated from the VT events significantly improve the localizations. This is illustrated in Figure 5.18, where we compare localizations of raw signals and signals from which the site amplifications are removed. The localization is carried out using the model with topography and including the horizontal components. This way, we can evaluate if including the horizontal components can improve the localization above.
The differences between raw and treated signals are evident. Taking into account the site effects moves the positions of high probability towards the actual rockfall trajectory.
Comparing the results with the results from the vertical components in Figure 5.17 shows, that the localization is improved when additionally considering the horizontal components. This is in particular true for position c) which corresponds to the blue color. While hardly any probable source position was found using the vertical components only, the horizontal components allow to map sources in good agreement with the true position. However, the positions are still ambiguous which is visible by the spatially distributed source positions.

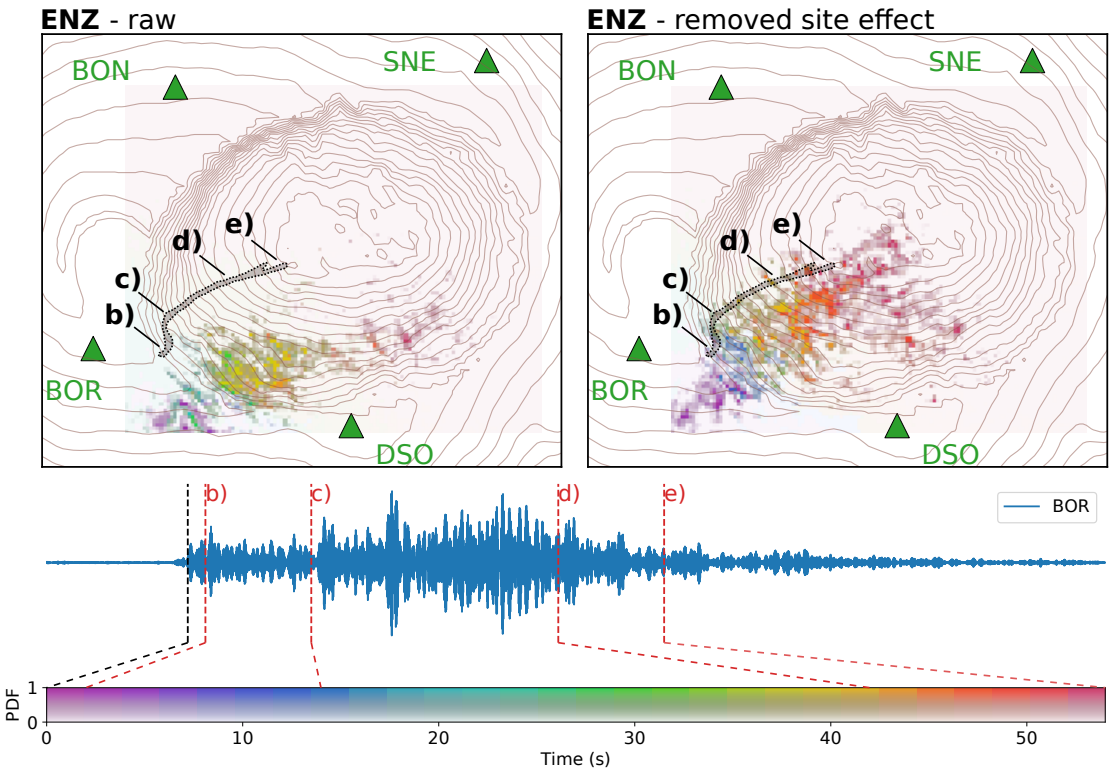

Figure 5.18 – Estimation of spatio-temporal rockfall evolution from vertical and horizontal components. Comparison of localization using raw signals (*left*) and signals from which site effects are removed (*right*). Color represents time, intensity represents probability of source location. Vertical and horizontal components are used for the localization. Seismic signals are filtered in frequency band of 13-17 Hz. The signal recorded at the closest station BOR is plotted below so that time steps b) to e) can be associated to colors (compare with Figure 5.13).

5.5.3 Localization of further rockfalls

After testing in detail the localization method on the rockfall of December 13, 2016, we now apply the method to different events. First of all, the two other rockfalls for which we analyzed spectral ratios in section 5.4.1 are localized. This is interesting as all of them are located in the southwestern part of Dolomieu crater, however, the detachment position of rockfall **1** is located further north. This way we can test if the method can resolve the different trajectories. Subsequently, we have a look on rockfalls examples on the northern crater wall. Here, a rockfall consisting of single boulder impacts is compared to a rockfall of fine granular material.

Rockfall in the southwestern part of Dolomieu crater

Here we localize the rockfalls from December 12, 2015, at 4:32 and at 10:48 corresponding to events **1** and **2** in Figure 5.2. The localization method is applied using vertical and horizontal components and energy ratios are compared with the simulation from the model with topography. The resulting probability maps are shown in Figure 5.19 for both events.

Rockfall **1** (left hand side of Figure 5.19) is very well located in the beginning of the event.

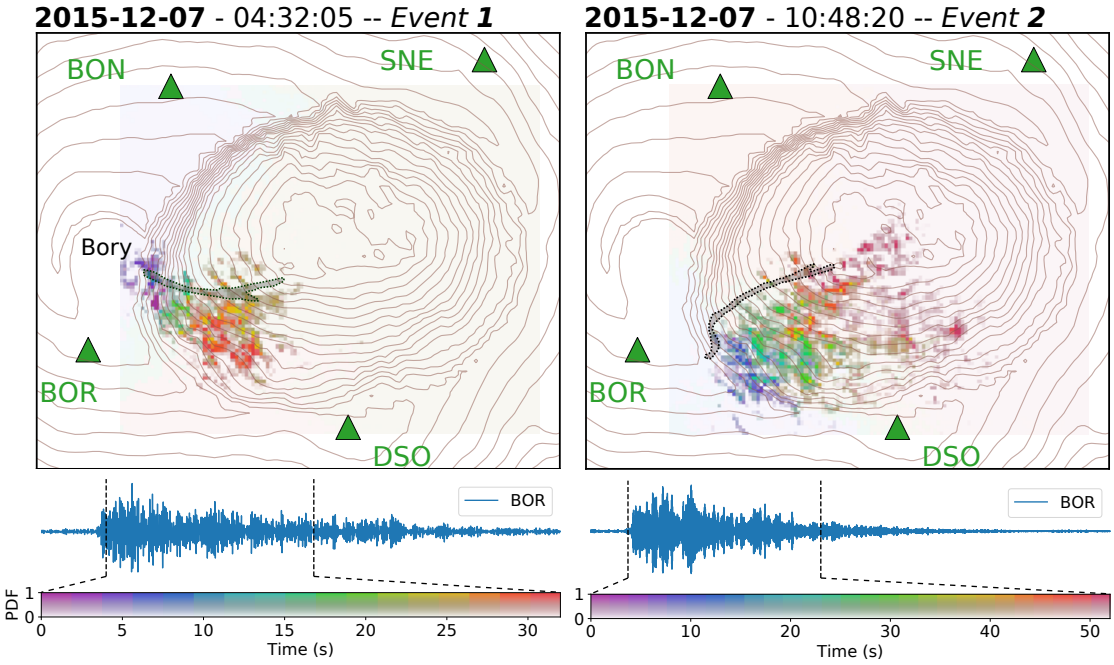

Figure 5.19 – Localization of rockfalls on the southwestern crater wall. Localization of rockfalls from December 12, 2015, at 4:32 (*left*) and at 10:48 (*right*) corresponding to events **1** and **2** in Figure 5.2. The corresponding seismic signals (vertical ground velocity) recorded at the closest station BOR is plotted below. Vertical and horizontal components are used for the localization, filtered in frequency band of 13-17 Hz.

It can be observed that the detachment phase which corresponds to the purple color is correctly positioned below crater Bory. Subsequently, the localization follows the actual trajectory in the right direction towards the east. However, with increasing time, the area of probable source locations becomes larger. The end of the rockfall the most probable source locations are mapped too far south on the wall of the crater instead on the crater bottom. This is possibly related to a wrong assumption of a single force.
Nevertheless, it is nicely visible that trajectory of rockfall **1** can be distinguished from rockfall **2**. For the latter, which is very similar to the previously analyzed rockfall **3**, the position of detachment is located further south compared to rockfall **1**. This suggests that the method is able to resolve different positions of detachment. Later in time, due to the increased spatial distribution of sources, the source location probabilities become more scattered.

Rockfalls on the northern Dolomieu crater wall

We now shift from rockfalls located in the southwest to rockfalls located at the northern wall of Dolomieu crater. Two events are chosen, namely a rockfall on January 22, 2017, which consists of single boulder impacts, and a rockfall on June 14, 2016, which consists of fine granular material flowing down the steep crater wall. The rockfall on January 22, 2017 is described in detail in 2.3 of Chapter 2. Again, vertical and horizontal components are used for the localization as well as the simulations from the model with topography. The resulting probability maps are presented in Figure 5.20.
The proposed method is able to correctly locate the two events on the northwestern crater

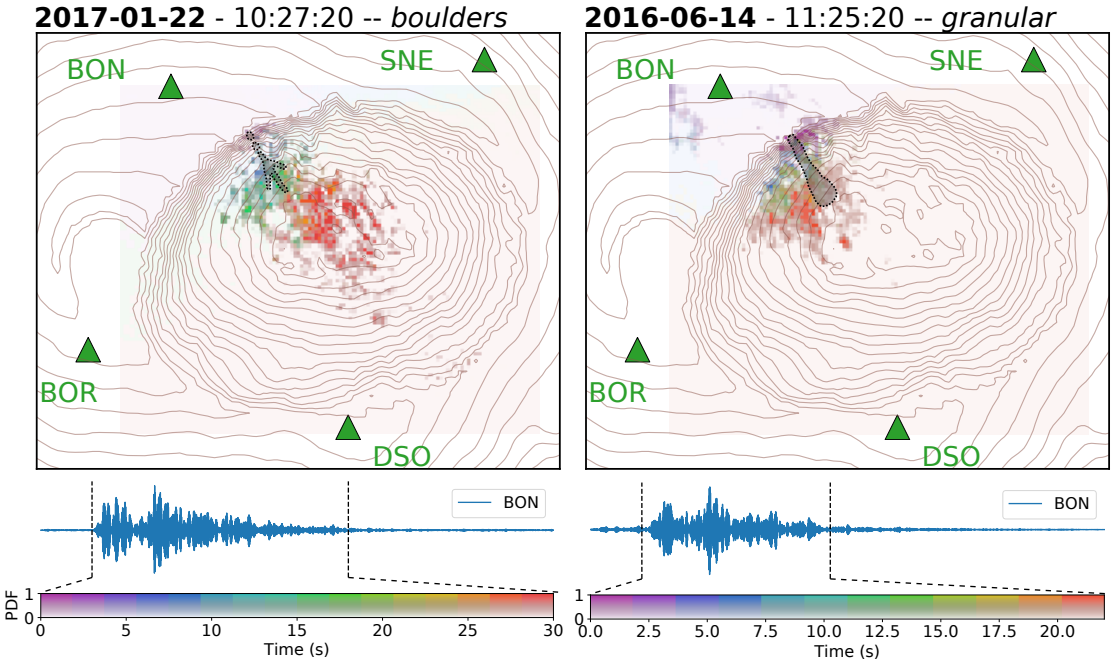

Figure 5.20 – Localization of rockfalls on the northern crater wall. Localization of rockfall from January 22, 2017 (*left*), which is a constituted of single boulders, and from June 6, 2014 (*right*), which consists of fine granular material. The corresponding seismic signals (vertical ground velocity) recorded at the closest station BON are plotted below. Vertical and horizontal components are used for the localization, filtered in frequency band of 13-17 Hz.

wall. As before, the position of detachment is better resolved than the subsequent part of the trajectory, for which the probable source locations are spatially scattered. It is remarkable that source locations could also reasonably well be extracted from the seismic signal generated by the granular flow, which is shown on the right hand side of Figure 5.20. This is not intuitive as the localization method is based on a single force assumption. The fact that a moving source position could still be mapped suggests that the recorded signals are dominated by a confined area of maximum source energy. It has to be investigated in more detail, if the maximum seismic energy which dominates the signal is generated right at the forefront of the spreading mass.

5.6 Conclusion

We proposed a method for the localization of rockfalls which is based on energy ratios between stations. The method is able to locate rockfalls which occurred within Dolomieu crater and follow their spatial evolution over time. Considering topography enhances the resolution of the localization, especially during detachment when the seismic source in very confined in space. As the detachment is mostly located at top of the crater walls, it is plausible to think that resolution is also improved on steeper slopes as their imprint on the seismic signal might be very characteristic. To further investigate this, the method has to be applied to other mountainous regions. As the topography can be retrieved easily and accurately for example by airborne photogrammetry (e.g. Derrien et al., 2019), it should definitely be considered for the localization of surface sources.
After the detachment phase, the localization becomes spatially scattered. This is possibly

linked to the fact that the rockfall seismic source becomes more complex with multiple impacts at different positions within short time windows. Indeed, the superposition of multiple sources is not considered in the method and can bias the localization. With regards to this limitation, the method performs remarkable well. Even for the granular flow a moving source location could be identified. Localization might be improved by correlating successive time windows. This way, former source positions could be identified and removed from the new signal. Testing on synthetic rockfall signals can help in the process to optimize the method. The synthetic tests carried out in this work only considered single sources which were well separated in time.

In its current implementation, we suppose that the signal of a seismic sources arrives fully within the defined time window at all stations. This is possible due to the relative positions of the seismometers with respect to the rockfalls sources at Dolomieu crater. This might be a limitation for other source-receiver configurations. However, if the region of interest is defined and the seismic velocities known, a time shift for the windows at different stations can easily be introduced. For practical purposes the method also has to be tested on different numbers of seismometers in order to evaluate its performance if for example only 2 station pairs are involved.

Future refinements also include the combination of different frequency bands. Here we predominantly analyzed the frequency band of 13-17 Hz which was concluded to have the best spatial resolution with respect to lower frequency bands. A joint analysis of several, possibly also narrower, frequency bands could improve localization.

A huge benefit of the method is its simplicity of implementation. Once the impulse response of the domain in regards to different seismic stations is simulated, localization is estimated quickly without the need for complicated analyses such as precise arrival time picking. Its potential use for continuous monitoring in real time is natural due to the sliding window approach.

5.7 Appendices

5.7.1 Band-pass filtered station energy ratios from simulations on model with topography

Figures 5.21, 5.22, and 5.23 show simulated energy ratios between station pairs similar as Figure 5.9 in section 5.4.2. Here, synthetic seismograms are filtered in frequency bands of 3-7 Hz, 8-12 Hz, and 13-17 Hz, respectively. It can be observed how the spatial variation of energy ratios is blurred in the low frequency band and becomes sharper and of stronger contrasts towards the high frequency band.

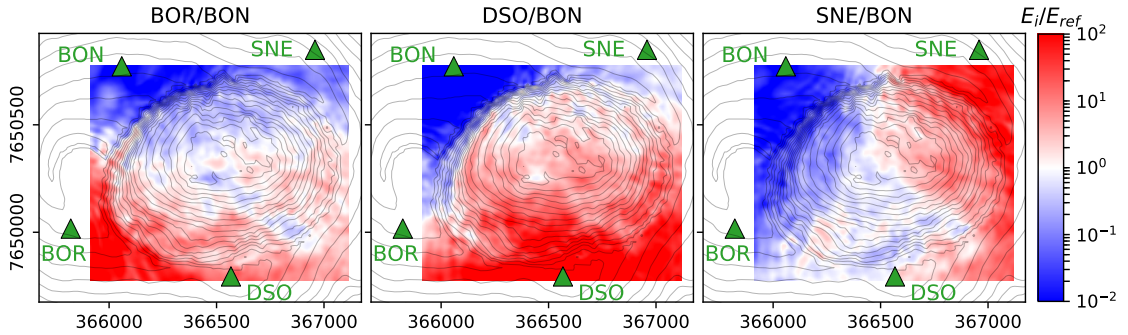

Figure 5.21 – Station energy ratios from synthetic seismograms filtered at 3-7 Hz. Synthetic seismograms are simulated on model with topography and filtered in a frequency band of 3-7 Hz. At each grid position (see Fig. 5.7) the ratio is computed between seismic energy E_i at station BOR (*left*), DSO (*middle*), and SNE (*right*) and seismic energy E_{ref} at reference station BON.

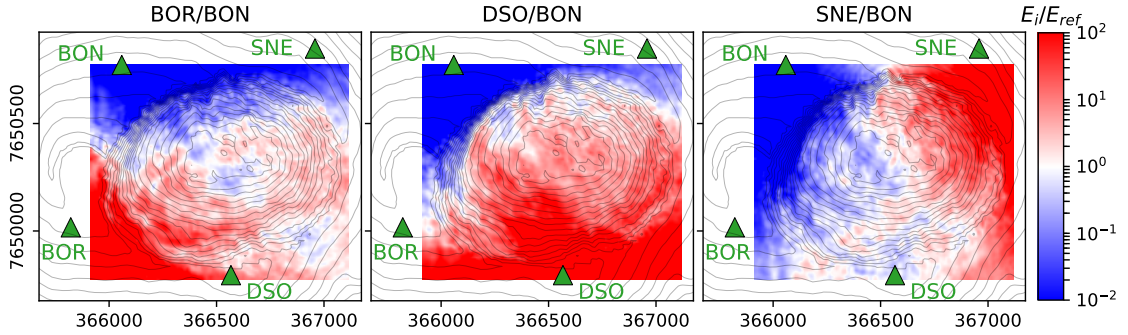

Figure 5.22 – Station energy ratios from synthetic seismograms filtered at 8-12 Hz. Similar as in Figure 5.21. Synthetic seismograms are simulated on model with topography and filtered in a frequency band of 8-12 Hz.

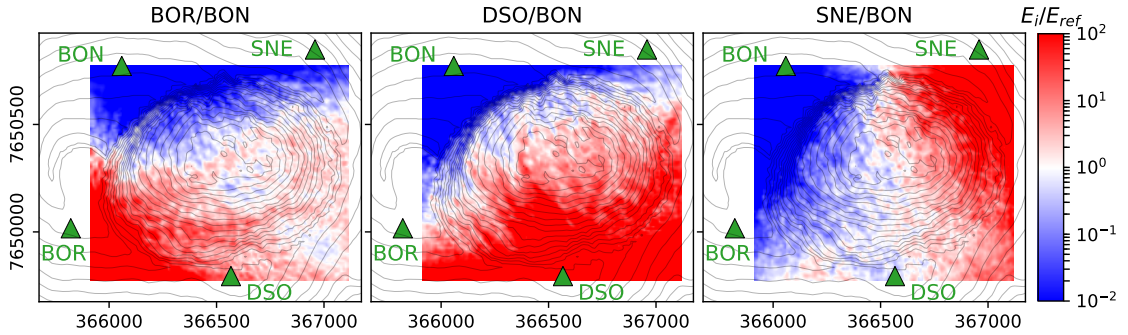

Figure 5.23 – Station energy ratios from synthetic seismograms filtered at 13-17 Hz. Similar as in Figure 5.21. Synthetic seismograms are simulated on model with topography and filtered in a frequency band of 13-17 Hz.

Conclusions

In this thesis we explore the potential information hidden in the high frequency seismic signals generated by rockfalls. To do this, the wave propagation is numerically simulated and compared with rockfalls signals recorded at Dolomieu crater on Piton de la Fournaise volcano, La Réunion. In the following we review the findings and give directions for related future work.

Discussion & Findings

Rockfall seismic signals can be used to retrieve information on event properties and dynamics. For this, the seismic signal has to be linked to the rockfall seismic source. However, high frequency seismic waves are strongly affected by soil heterogeneities and surface topography during their propagation so that it can be difficult to interpret the recorded seismic signals. We address this issue by numerically simulating the seismic wave field using the Spectral Element Method (SEM).

For this purpose, a model domain is designed and meshed which represent the study site of Dolomieu crater on Piton de la Fournaise volcano, La Réunion. This includes both the surface topography and the seismic velocity profile of the subsurface. For the surface topography, a Digital Elevation Model (DEM) of 10 m resolution is used. The subsurface velocity is implemented according to the generic velocity model proposed by Lesage et al. (2018) for the shallow subsurface structure of volcanoes. The validity of this velocity profile is verified by comparing theoretical and observed Rayleigh wave dispersion curves. The latter are determined by means of ambient noise measurements at seismic antennas. Additionally, spectral site amplification factors are analyzed in order to account for local soil heterogeneities. This is realized by computing site-to-reference spectral ratios using seismic signals generated by volcano-tectonic (VT) events. It is found that all components of station SNE are strongly amplified in respect to stations BON and BOR. Single-component station DSO also shows amplification on its vertical component. In order to test possible influences from topography on the observed spectral ratios, spectral ratios are simulated on a model with laterally smooth velocity profile and real topography. The results from a plane wave of vertical incidence suggest that the observed spectral amplification factors are not biased by topography.

The seismic wave propagation generated by vertical surface loads is simulated on flat domains and compared between three different velocity profiles, namely a homogeneous model, a model with a shallow low S-wave velocity layer and the Lesage velocity model. It

is observed that in contrast to the homogeneous model, a major part of the seismic energy propagates close to the surface in case of the heterogeneous models. This is due to reflections at the layer boundary and the velocity gradient, respectively. The decay of energy measured at the surface is studied as a function of source-receiver offset. While the energy decay on the homogeneous model can be related to the propagation of surface waves, it is influenced by body waves in the case of the heterogeneous models. Finding a relation of energy decay as a function of distance can help to estimate the totally generated source energy. This is of interest as the seismic energy generated by rockfalls can for example be related to their volumes.
For the homogeneous model, the fact that mainly fundamental mode Rayleigh waves are measured by a seismic station located at the surface makes it possible to analytically derive an equation which back-calculates the total energy radiated by the source. For this, wave partitioning factors as well as frequency dependent penetration depths are determined depend on the underlying medium properties.
The superposition of different wave types measured at the surface in case of heterogeneous media complicates the estimation of the source energy. For the Lesage velocity profile, fundamental as well as 1^{st} mode Rayleigh waves are identified. Additionally, body waves are measured at the surface. As the different waves types attenuate differently with distance, their relative contribution to the measured signal changes with distance. It is for this reason that the energy calculation has to be carried out carefully. We find that in the first 1500 m fundamental Rayleigh waves dominate the signal. Consequently, a good source energy estimation can be achieved by only considering fundamental Rayleigh waves. Estimation can be improved up to 2000 m by assuming both fundamental and 1^{st} mode Rayleigh waves. For this, their relative contribution as a function of offset has to be considered. Using the surface wave assumption at larger offsets leads to on overestimation of source energy which is growing exponentially with distance. This is due to the increasing contribution of body waves which are generally associated to lower attenuation factors due to higher propagation speeds and quality factors. When neglecting the dispersive nature of surface waves, a strong over- or underestimation of the source energy can already be obtained at short offsets. For this reason, it is advisable to keep a frequency dependent attenuation factor even if the group velocity is determined for a dominant frequency. Furthermore, at short distances (up to 1500 m) it is less severe to overestimate the dominant frequency, since the too high velocities of lower frequencies lead to a strong overestimation of seismic energy. In contrast, at offsets between 1500 m and 3000 m it is safer to underestimate the dominant frequency. Otherwise, the too high attenuation factors of higher frequencies result to exponentially growing overestimation of the source energy.

The derived equations for the estimation of source energy are generally only valid for flat surfaces. Topography can modify the seismic amplitudes and thus falsify the energy estimations. To avoid this, a topography correction factor is proposed to be introduced in the equations. This correction relates the actual measurements on the topography to reference measurements on a flat surface. It is determined by the ratios of simulated seismograms from a model with flat surface and with topography. This way, it is expected that the source energy estimations from different seismometers are more coherent which was verified in a first example.

Based on the same principle, namely the ratio of simulations from models with flat surface and with topography, the influence of topography on the wave field from a surface source is investigated in detail. Surface waves are exposed to constant interactions with topography as they propagate along the surface. The resulting scattering and diffraction is dependent on the underlying medium. For example, energy scattered along the topography on the homogeneous medium can be radiated down into the subsurface leading to a strong deamplification by factors up to 20 of the energy measured at the surface in respect to a flat surface. In contrast, as more energy is kept close to the surface on the Lesage model due to the velocity gradient, the scattering from the topography results in prolonged ground shaking. For this reason, deamplification is more moderate with factors up to 10.
It is found that seismic wavelengths are affected by a wide range topography characteristic lengths. On the one hand, it is shown that amplitudes of seismic wavelengths which are five times larger than the topography variations are modified. On the other hand, waves are influenced by crater diameters which are 30 times bigger than the seismic wavelength. In order to investigate the principal cause of this influence, a synthetic crater study is carried out. The objective of this study is to separately evaluate the influence of crater depth and topography curvature. The results suggest that curvature has a stronger influence on the wave field.
In general, the topographic amplification has to be evaluated carefully due to its strong spatial variability. Simulation of the wave propagation on 2D profiles might result in an oversimplified picture. Furthermore, it is important to be aware that the influence of topography is dependent on the source position. For surface waves from shallow sources, the influence of topography can be considered as a propagation effect rather than a site effect since they are affected along the whole propagation path. The comparison with simulations from a plane wave of vertical incidence demonstrate that the topography induced amplification is substantially different for deep sources.

Finally, simulations are compared with real seismic signals generated by rockfalls at Dolomieu crater. First of all, spectral ratios between station-pairs are analyzed. This way, the source signature is removed and simulations can be compared to observations without the need for a precise source description. Yet, radiation patterns related to the directionality of the source can influence the ratios. Analyzing multiple rockfalls at similar locations indicate that the spectral ratios are characteristic to the source position. Further, simulated spectral ratios from a flat model show strong dependency on the source direction. In contrast, the spectral ratios of different source directions are very similar in case of a model with topography. The comparison with the observed spectral ratios demonstrate a good agreement in case of the model with topography, whereas the spectral ratios can deviate strongly in case of the flat model dependent on the source direction which can be explained by a strong influence of the related radiation patterns. This suggest, that the spectral ratios are not only characteristic to the source position but also dominated by the wave propagation along the topography rather than the source direction. Note that prior to compare simulations and observations, the site amplification factors estimated from VT events had to be removed.

The characteristic of inter-station ratios with respect to the source position and the propagation along topography can be used for the localization of seismic sources. With the

assumption that the ratios are independent on the source direction, simulations from a vertical source are compared to observations in order to find the source position which can best explain the observed ratios. Rather than comparing the whole spectral ratios, the ratio of energy averaged over a frequency band of 4 Hz is used. A synthetic test of the method reveals that the least ambiguous localization is achieved by considering energy station ratios from both vertical and horizontal components. When using simulations from a flat model, localization shifts away from the true source position and consideration is degraded when horizontal components are considered due to the wrongly predicted radiation patterns.
Applying the method to real rockfall signals at Dolomieu crater shows, that simulations form the model with topography can estimate the position of detachment reasonably well. The localization becomes more scattered at later times. This is probably due to the superposition of spatially distributed sources which are not considered in the method.
The sliding window approach of the proposed localization method leads to an extremely simple implementation without the need of complicated analyses such as the picking of arrival times which involves large uncertainties in the case of dispersive surface waves. The impulse response of an area of interest only has to be simulated once for each seismometer. Once this is done, the method can potentially be used to monitor rockfall activity in real time thanks to the sliding window approach.

When directly comparing simulated and observed seismic signals (i.e. not via station ratios), the seismic source has to be described in terms of temporal and spatial variation as well as amplitude. In order to gain insight into the distributed force field imposed by granular flows on the ground, simulations are conducted using the thin-layer model SHALTOP. The generated forces are related to the acceleration and deceleration of the flow as well as the gravitational force from the mass. Simulations on the real topography of Dolomieu crater show that surface roughness as well as friction coefficient influence the frequency content of the exerted forces. This is because both of the determine the flow speed and the acceleration and deceleration of the mass. However, the model is not able to reproduce the high frequency content above 1 Hz of the rockfall seismic signals recorded at Dolomieu crater. This is because impacts of single particles are not considered with this model.
In order to estimate the forces generated by impacts of single boulders, the Hertz contact theory is introduced. Maximum impact force F_0 and the corresponding impact time T_c and upper corner frequency f_c are defined and their dependency on the impact parameters is discussed. The dependencies are again summarized in table C1.

Table C1 – Dependency of impact force, duration and corner frequency on impact parameters. Behavior of impact force F_0, impact duration T_c and upper corner frequency f_c as function of sphere mass m, sphere radius R, effective Young's modulus E, impact speed v_n and inelasticity P. Dependencies are derived from equations 2.5 and 2.10 except for the dependency on inelasticity P which is deduced from Farin et al. (2015). ↗: increasing value; ↘: decreasing value.

	m ↗	R ↗	E ↗	v_n ↗	P ↗
F_0	↗	↗	↗	↗	↘
T_c	↗	↘	↘	↘	↗
f_c	↘	↗	↗	↗	↘

Analyzing single impact seismic signals at Dolomieu crater, the predictions from the Hertz model is used to interpret signal characteristics and amplitude. For this, a rockfall example of two well separated impacts is selected. The first impact shortly after the detachment and contains less high frequency content (>20 Hz) than the second impact which followed after a free fall of around 4 s. As the boulder accelerates during the free fall the impact speed of the second impact is higher. The respective impact speeds v_n are estimated based on video material. This way, assuming similar ground parameters at the two impact positions, the upper corner frequency f_c could be determined. As a result, the missing high frequency content in the first impact is explained by the smaller impact speed which can be directly inferred from Table C1.
With the estimated impact speeds at hand, the maximum impact forces F_0 are calculated. These are used to calibrate the input force of the seismic wave frequencies. As a result, the synthetic seismograms are of similar magnitude as the observed seismograms.
Finally, the simulated and observed waveforms are compared. The simulations from the model with topography and Lesage velocity profile is able to reproduce the complexity of observed waveforms. It is emphasized that reproduction is not only limited by the estimation of the source-time function, but also by the variability of the waveforms with source direction as well as source position. The comparison of simulations and observations is proceeded by a polarization analysis with the attempt to separate successive wave phases. Again, the topography is able to better reproduce the observed polarization but an exact fitting is limited by the variability of the polarization with source position and source direction.

Limitations & Perspectives

The seismic wave propagation is simulated on a domain with realistic topography and a subsurface model which adequately represents the average shallow subsurface structure of volcanoes. This velocity profile was validated by dispersion curve estimation from antenna measurements. However, the measurements only allowed dispersion curve determination up to 6 Hz. A smaller antenna should be deployed to validate the model at higher frequencies. Furthermore, the velocity model is implemented in a way so that it follows the surface topography, thus assuming lateral continuity of the model. This assumption could be verified by measuring dispersion curved at multiple positions. Also, ambient noise cross-correlations could help to identify lateral soil heterogeneities.
Local soil heterogeneities at the position of the stations are accounted for by estimating spectral site amplification factors using signals generated by VT events. The good agreement between simulated and observed inter-station spectral ratios after deconvolution of the observed signals with the estimated site effects suggests that the functions correctly estimate the site amplification. This can also be concluded by the improved rockfall localization after site effect removal. However, it is not evident that rockfall generated surface wave experience the same amplification as the upwards traveling seismic waves from deep VT sources. In fact, horizontal and vertical amplification factors could be interchanged due to the different direction of propagation. In order to evaluate the amplification on rockfall generated surface waves, the wave propagation has to be simulated on a model

with local heterogeneities.
No evidence for a scattering related seismic coda is found on the rockfall signals. Yet, scattering could still slightly modify amplitudes and prolong ground shaking. To evaluate the effect, the seismic wave propagation can be simulated on a model with a stochastic variability of the velocity described by a fractal distribution as for example done by O'Brien and Bean (2009).

The estimation of the seismic energy is derived for the homogeneous model and the Lesage velocity. The validity of the equations have to be tested on other velocity profiles. Then, the theory has to be validated against field measurements. In case of the latter, empirical attenuation factors can be estimated and compared with theoretical values.
The method of the energy estimation in case of topography using a correction factor has to be further developed. This includes the consideration of horizontal components and how they can be related to the flat reference model. A further complication is represented by the source directionality and the related radiation patterns. In fact, if the signals are dominated by the propagation along the topography as could be seen by the comparison of observed and simulated spectral ratios, the energy estimation might be more robust on a topography than on a flat surface in the case of an unknown source direction.
All these issues can be addressed with the help of synthetic rockfall signals for which the exact source energy is known. To begin with, single point forces can be used to test the energy estimation on topography. Subsequently, the effect of an distributed source can be investigated. For this, rockfall seismic sources can be numerically modeled. However, insight in the limitations of the energy estimation method can also be evaluated by superposing point sources. An example for a synthetic rockfall signals is shown in Figure C1 for which point sources have been selected at different positions. For each position, a start time and an amplitude is defined. Here, all the point forces are described by a 7 Hz Ricker wavelet. In a first test, such a signal is totally sufficient to evaluate the performance of the energy estimation. Later on, more complicated synthetic rockfall signals can be designed.

The synthetic rockfall signal can also be used for developing the localization method. A synthetic test of single point forces has already been performed. However, a strong limitation of the method is the assumption that a dominant single source is measured within a given time window. This is because the observed energy ratios are compared to simulated energy ratios at a single position. Using synthetic rockfall signal, the limitations of the method can be evaluated. Furthermore it can be tested, how energy ratios from different frequency bands can best be combined to achieve optimal localization. For practical purposes it is also of interest how the method performs with different numbers of station pairs as well as for different source-receiver constellation. Furthermore, the performance of the method regarding different topographies has to be tested. An exciting hypothesis is that resolution is enhanced for steeper slopes as their imprint on the signals might be more characteristic.

We showed that the influence of topography is very prominent in case of shallow sources and the generated surface waves. The present thesis is focused on the Dolomieu crater topography on Piton de la Fournase volcano. The effect of topography should also be evaluated for different surface geometries. This is especially important when seismic signals from surface sources are analyzed. A first idea of the topography effect can be obtained by

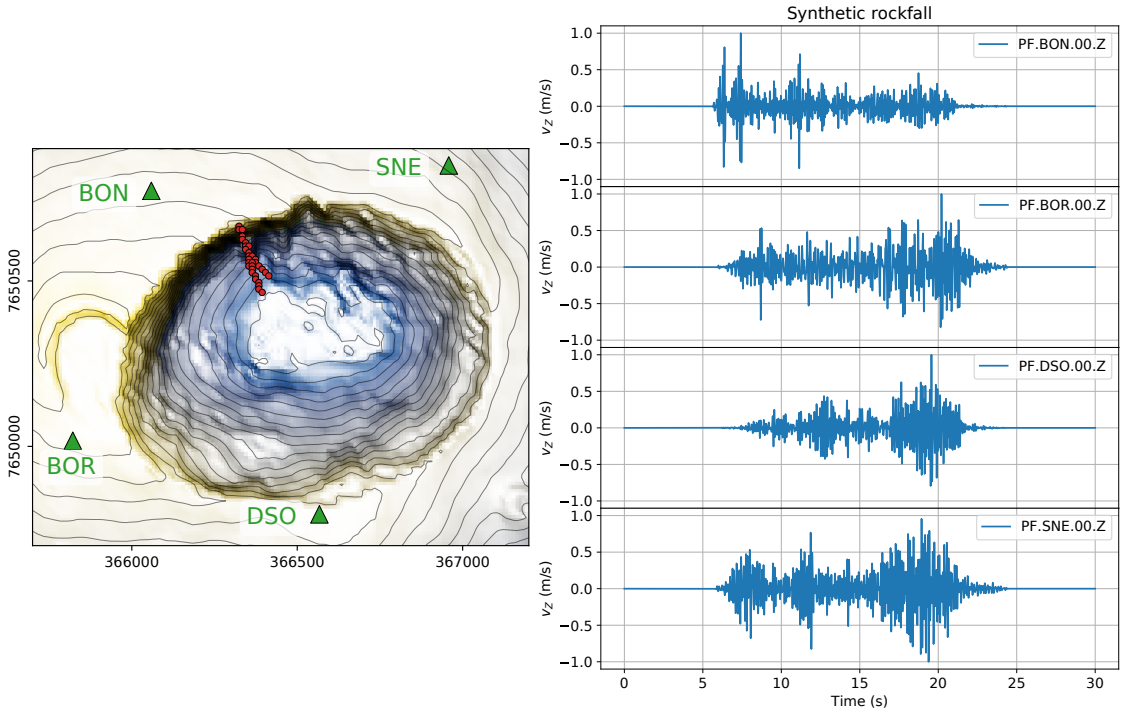

Figure C1 – Synthetic rockfall example. To create a synthetic rockfall signal with moving source, the positions of single point sources are selected. These are mark by the red dots on the map on the right hand side. Subsequently, a time shift and an amplitude is defined for each source. The resulting superposition of the single source synthetic seismograms is shown on the right hand side. The synthetic signals are shown for vertical ground velocity at stations BON, BOR, DSO, and SNE.

computing the energy ratio between simulation from a model with flat surface and with surface topography. An example of a different study site is shown in Figure C2, where the topography induced energy amplification is calculated on the topography of Stromboli volcano. Mainly deamplification is of the energy is observable in respect to a flat reference model. However, note that a homogeneous velocity model is used. As could be seen from the simulations on Dolomieu crater, a heterogeneous velocity model can strongly influence the amplification pattern.

Finally, the seismic wave propagation generated by a distributed rockfall source can be simulated. For this, the temporally varying and spatially distributed force field generated by rockfalls has to be modeled. As a continuum model such as SHALTOP hardly generates high frequency forces above 1 Hz, a discrete model can be used. Alternatively, the basal force field of the continuum model might be used as envelope within which stochastic high frequency impulses are defined. Once the distributed force field is modeled, it can be used to define the input source in the wave propagation model. As discussed in Chapter 3, the implementation in SEM of the surface source on the topography is easily realized by defining non-zero boundary conditions.

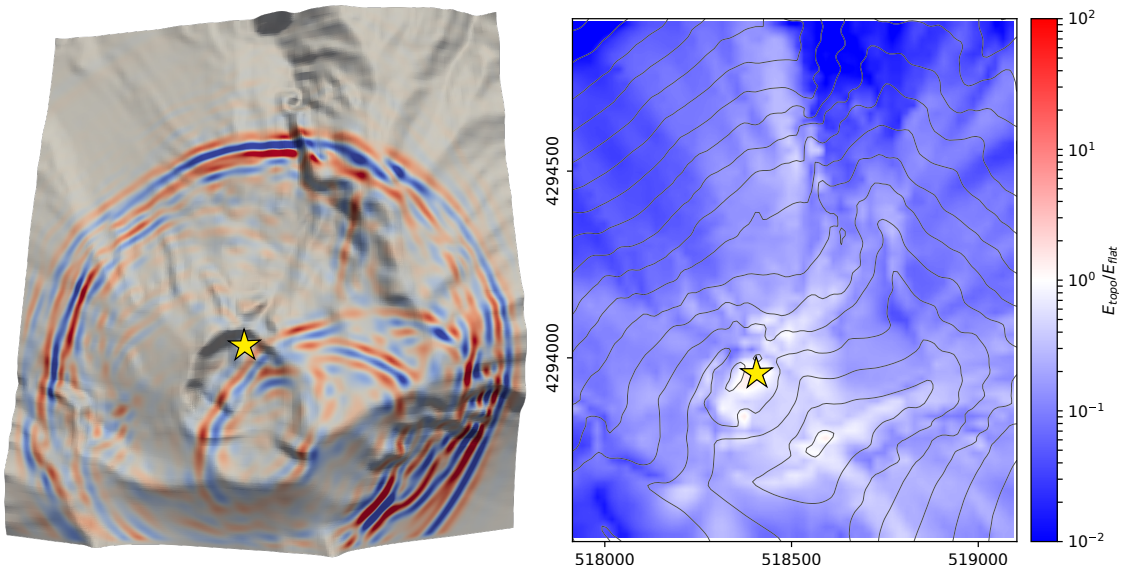

Figure C2 – Topography effect on Stromboli volcano. *Left:* Snapshot of seismic wave propagation on a domain with surface topography of Stromboli volcano. The vertical point source is described by a 6 Hz Ricker wavelet. The model is defined by $v_S = 500\,\mathrm{m.s}^{-1}$ and $v_P = 900\,\mathrm{m.s}^{-1}$ for S-wave and P-wave velocity, respectively, approximately according to measured velocity profiles. *Right:* Map of the topography induced amplification evaluated based on the energy ratio between model with topography and flat surface model.

References

Aki, K. (1957). Space and time spectra of stationary stochastic waves, with special reference to microtremors. *Bulletin of the Earthquake Research Institute*, 35:415–456.

Aki, K. and Richards, P. G. (2002). *Quantitative seismology*. University Science Books, Sausalito, CA.

Allstadt, K. (2013). Extracting source characteristics and dynamics of the August 2010 Mount Meager landslide from broadband seismograms. *Journal of Geophysical Research: Earth Surface*, 118(3):1472–1490.

Almendros, J., Chouet, B., Dawson, P., and Huber, C. (2002). Mapping the sources of the seismic wave field at Kilauea volcano. *Bulletin of the Seismological Society of America*, 92(6):2333–2351.

Ancheta, T. D., Darragh, R. B., Stewart, J. P., Seyhan, E., Silva, W. J., Chiou, B. S., Wooddell, K. E., Graves, R. W., Kottke, A. R., Boore, D. M., Kishida, T., and Donahue, J. L. (2014). NGA-West2 database. *Earthquake Spectra*, 30(3):989–1005.

Anderson, D. L., Ben-Menahem, A., and Archambeau, C. B. (1965). Attenuation of seismic energy in the upper mantle. *Journal of Geophysical Research*, 70(6):1441–1448.

Assimaki, D. and Jeong, S. (2013). Ground-motion observations at hotel Montana during the M 7.0 2010 Haiti earthquake: Topography or soil amplification? *Bulletin of the Seismological Society of America*, 103(5):2577–2590.

ASTRA (2008). Einwirkungen infolge Steinschlags auf Schutzgalerien (Richtlinie 12 006). V2.03:22.

Bachelet, V., Mangeney, A., De Rosny, J., Toussaint, R., and Farin, M. (2018). Elastic wave generated by granular impact on rough and erodible surfaces. *Journal of Applied Physics*, 123(4).

Bader, M., Gygax, J., Huwiler, S., Meyer, A., Héron, C., and Greppin, C. (2017). Quand la montagne s'effondre. *www.labs.letemps.ch/interactive/2017/longread-permafrost (Date accessed: 2019-10-06)*.

Battaglia, J. and Aki, K. (2003). Location of seismic events and eruptive fissures on the Piton de la Fournaise volcano using seismic amplitudes. *Journal of Geophysical Research*, 108(B8):2364.

Berrocal, J., Espinosa, A. F., and Galdos, J. (1978). Seismological and geological aspects of the Mantaro landslide in Peru. *Nature*, 275(5680):533–536.

Borcherdt, R. D. (1970). Effects of Local Geology on Ground Motion Near San Francisco Rbay. *Bulletin of the Seismological Society of America*.

Bottelin, P., Jongmans, D., Daudon, D., Mathy, A., Helmstetter, A., Bonilla-Sierra, V., Cadet, H., Amitrano, D., Richefeu, V., Lorier, L., Baillet, L., Villard, P., and Donzé, F. (2014). Seismic and mechanical studies of the artificially triggered rockfall at Mount Néron (French Alps, December 2011). *Natural Hazards and Earth System Sciences*, 14(12):3175–3193.

Bouchon, M. and Barker, J. S. (1996). Seismic response of a hill: The example of Tarzana, California. *Bulletin of the Seismological Society of America*.

Bouchut, F., Mangeney-Castelnau, A., Perthame, B., and Vilotte, J. P. (2003). A new model of Saint-Venant and Savage-Hutter type for gravity driven shallow water flows. *C. R. Acad. Sci. 1-Math*, 336:531–536.

Bouchut, F. and Westdickenberg, M. (2004). Gravity driven shallow water models for arbitrary topography. *Commun. Math. Sci.*, 2(3):359–389.

Brenguier, F., Kowalski, P., Ackerley, N., Nakata, N., Boué, P., Larose, E., Rambaud, S., Pequegnat, C., Lecocq, T., Roux, P., Ferrazzini, V., Villeneuve, N., Shapiro, N. M., and Chaput, J. (2016). Toward 4D Noise-Based Seismic Probing of Volcanoes : Perspectives from a Large- N Experiment on Piton de la Fournaise Volcano. *Seismological Research Letters*, 87(January/February):15–23.

Brenguier, F., Shapiro, N. M., Campillo, M., Nercessian, A., and Ferrazzini, V. (2007). 3-D surface wave tomography of the Piton de la Fournaise volcano using seismic noise correlations. *Geophysical Research Letters*, 34(2):2–6.

Brodsky, E. E., Gordeev, E., and Kanamori, H. (2003). Landslide basal friction as measured by seismic waves. *Geophysical Research Letters*, 30(24):2236.

Burtin, A., Bollinger, L., Cattin, R., Vergne, J., and Nábělek, J. L. (2009). Spatiotemporal sequence of Himalayan debris flow from analysis of high-frequency seismic noise. *Journal of Geophysical Research*, 114(F4):F04009.

Burtin, A., Hovius, N., and Turowski, J. M. (2016). Seismic monitoring of torrential and fluvial processes. *Earth Surface Dynamics*, 4(2):285–307.

Chaljub, E., Komatitsch, D., Vilotte, J. P., Capdeville, Y., Valette, B., and Festa, G. (2007). Spectral-element analysis in seismology. *Advances in Geophysics*, 48(06):365–419.

Chávez-García, F. J., Manakou, M. V., Hollender, F., and Raptakis, D. G. (2018). Site effects using methods based on lateral homogeneity and laterally heterogeneous media: An impossible marriage? *Bulletin of Earthquake Engineering*, 16(7):2729–2756.

Chiou, B. S. J. and Youngs, R. R. (2014). Update of the Chiou and Youngs NGA model for the average horizontal component of peak ground motion and response spectra. *Earthquake Spectra*, 30(3):1117–1153.

Chouet, B., De Luca, G., Milana, G., Dawson, P., Martini, M., and Scarpa, R. (1998). Shallow velocity structure of Stromboli Volcano, Italy, derived from small-aperture array measurements of Strombolian tremor. *Bulletin of the Seismological Society of America*.

Courant, R., Friedrichs, K., and Lewy, H. (1928). Über die partiellen Differenzengleichungen der mathematischen Physik. *Mathematische Annalen*, 100(1):32–74.

Dahlen, F. (1993). Single-force representation of shallow landslide sources. *Bulletin of the Seismological Society of America*, 83(1):130.

Dammeier, F., Moore, J. R., Haslinger, F., and Loew, S. (2011). Characterization of alpine rockslides using statistical analysis of seismic signals. *Journal of Geophysical Research*, 116(F4):F04024.

Davis, L. L. and West, L. R. (1973). Observed effects of topography on ground motion. *Bulletin of the Seismological Society of America*.

De Gori, P., Chiarabba, C., and Patanè, D. (2005). Qp structure of Mount Etna: Constraints for the physics of the plumbing system. *Journal of Geophysical Research*, 110(B5):B05303.

De Martin, F., Matsushima, S., and Kawase, H. (2013). Impact of geometric effects on near-surface Green's functions. *Bulletin of the Seismological Society of America*, 103(6):3289–3304.

Delannay, R., Valance, A., Mangeney, A., Roche, O., and Richard, P. (2017). Granular and particle-laden flows: From laboratory experiments to field observations. *Journal of Physics D: Applied Physics*, 50(5).

Deniel, C., Kieffer, G., and Lecointre, J. (1992). New 230Th-238U and 14C age determinations from Piton des Neiges volcano, Reunion - A revised chronology for the Differentiated Series. *Journal of Volcanology and Geothermal Research*, 51(3):253–267.

Deparis, J., Jongmans, D., Cotton, F., Baillet, L., Thouvenot, F., Hantz, D., Thouvenot, F., and Hantz, D. (2008). Analysis of Rock-Fall and Rock-Fall Avalanche Seismograms in the French Alps. *Bulletin of the Seismological Society of America*, 98(4):1781–1796.

Derrien, A., Villeneuve, N., Peltier, A., and Michon, L. (2019). Multi-temporal airborne structure-from-motion on caldera rim: Hazard, visitor exposure and origins of instabilities at Piton de la Fournaise. *Progress in Physical Geography*, 43(2):193–214.

Dewez, T. J., Nachbaur, A., Mathon, C., Sedan, O., Kobayashi, H., Rivière, C., Berger, F., Des Garets, E., and Nowak, E. (2010). OFAI: 3D block tracking experiment on a weathered volcanic rock slope of Tahiti, French Polynesia. *Conf. Procedings, Rock Slope Stability 2010, 24-25 Nov. 2010, Paris, France*.

Dorren, L. K., Maier, B., Putters, U. S., and Seijmonsbergen, A. C. (2004). Combining field and modelling techniques to assess rockfall dynamics on a protection forest hillslope in the European Alps. *Geomorphology*, 57(3-4):151–167.

Duputel, Z., Lengliné, O., and Ferrazzini, V. (2019). Constraining Spatiotemporal Characteristics of Magma Migration at Piton De La Fournaise Volcano From Pre-eruptive Seismicity. *Geophysical Research Letters*, 46(1):119–127.

Durand, V., Mangeney, A., Haas, F., Jia, X., Bonilla, F., Peltier, A., Hibert, C., Ferrazzini, V., Kowalski, P., Lauret, F., Brunet, C., Satriano, C., Wegner, K., Delorme, A., and Villeneuve, N. (2018). On the Link Between External Forcings and Slope Instabilities in the Piton de la Fournaise Summit Crater, Reunion Island. *Journal of Geophysical Research: Earth Surface*, 123(10):2422–2442.

Ebeling, C. W. and Stein, S. (2011). Seismological identification and characterization of a large hurricane. *Bulletin of the Seismological Society of America*, 101(1):399–403.

Eissler, H. K. and Kanamori, H. (1987). A single-force model for the 1975 Kalapana, Hawaii, Earthquake. *Journal of Geophysical Research*, 92(B6):4827.

Ekström, G. and Stark, C. P. (2013). Simple Scaling of Catastrophic Landslide Dynamics. *Science*, 339(6126):1416–1419.

EM-DAT. The Emergency Events Database. *Université catholique de Louvain (UCL) - CRED, D. Guha-Sapir - www.emdat.be, Brussels, Belgium.*

Farin, M., Mangeney, A., Toussaint, R., Rosny, J. D., Shapiro, N., Dewez, T., Hibert, C., Mathon, C., Sedan, O., and Berger, F. (2015). Characterization of rockfalls from seismic signal: Insights from laboratory experiments. *Journal of Geophysical Research B: Solid Earth*, 120(10):7102–7137.

Favreau, P., Mangeney, A., Lucas, A., Crosta, G., and Bouchut, F. (2010). Numerical modeling of landquakes. *Geophysical Research Letters*, 37(15):1–5.

Ferrazzini, V., Aki, K., and Chouet, B. (1991). Characteristics of seismic waves composing Hawaiian volcanic tremor and gas-piston events observed by a near-source array. *Journal of Geophysical Research.*

Festa, G. and Vilotte, J.-P. (2005). The Newmark scheme as velocity-stress time-staggering: an efficient PML implementation for spectral element simulations of elastodynamics. *Geophysical Journal International*, 161(3):789–812.

Fuchs, F. and Bokelmann, G. (2018). Equidistant spectral lines in train vibrations. *Seismological Research Letters*, 89(1):56–66.

Fuchs, F., Lenhardt, W., and Bokelmann, G. (2018). Seismic detection of rockslides at regional scale: examples from the Eastern Alps and feasibility of kurtosis-based event location. *Earth Surface Dynamics*, 6(4):955–970.

Fuyuku, M. and Matsumoto, Y. (1980). Finite difference analysis of Rayleigh wave scattering at a trench. *Bulletin of the Seismological Society of America.*

Gariano, S. L. and Guzzetti, F. (2016). Landslides in a changing climate. *Earth-Science Reviews*, 162:227–252.

Geli, L., Bard, P. Y., and Jullien, B. (1988). The Effect of Topography on Earthquake Ground Motion: A Review and new Results. *Bulletin of the Seismological Society of America*.

Gélis, C. and Bonilla, L. F. (2014). Influence of a sedimentary basin infilling description on the 2-D P-SV wave propagation using linear and non-linear constitutive models. *Geophysical Journal International*, 198(3):1684–1700.

Gimbert, F., Tsai, V. C., and Lamb, M. P. (2014). A physical model for seismic noise generation by turbulent flow in rivers. *Journal of Geophysical Research: Earth Surface*, 119(10):2209–2238.

Gualtieri, L. and Ekström, G. (2017). Seismic reconstruction of the 2012 Palisades rockfall using the analytical solution to Lamb's problem. *Bulletin of the Seismological Society of America*, 107(1):63–71.

Hailemikael, S., Lenti, L., Martino, S., Paciello, A., Rossi, D., and Mugnozza, G. S. (2016). Ground-motion amplification at the Colle di Roio ridge, central Italy: a combined effect of stratigraphy and topography. *Geophysical Journal International*, 206(1):1–18.

Handwerger, A. L., Huang, M. H., Fielding, E. J., Booth, A. M., and Bürgmann, R. (2019). A shift from drought to extreme rainfall drives a stable landslide to catastrophic failure. *Scientific Reports*, 9(1):1–12.

Harp, E. L., Hartzell, S. H., Jibson, R. W., Ramirez-Guzman, L., and Schmitt, R. G. (2014). Relation of landslides triggered by the Kiholo Bay Earthquake to modeled ground motion. *Bulletin of the Seismological Society of America*, 104(5):2529–2540.

Hartzell, S. H., Carver, D. L., and King, K. W. (1994). Initial investigation of site and topographic effects at Robinwood Ridge, California. *Bulletin of the Seismological Society of America*, 84(5):1336–1349.

Helmstetter, A. and Garambois, S. (2010). Seismic monitoring of Séchilienne rockslide (French Alps): Analysis of seismic signals and their correlation with rainfalls. *Journal of Geophysical Research*, 115(F3):F03016.

Herrmann, R. B. (2013). Computer Programs in Seismology: An Evolving Tool for Instruction and Research. *Seismological Research Letters*, 84(6):1081–1088.

Hertz, H. (1882). Über die Berührung fester elastischer Körper. *Journal für die reine und angewandte Mathematik*, 92:156–171.

Hibert, C., Ekström, G., and Stark, C. P. (2014a). Dynamics of the Bingham Canyon Mine landslides from seismic signal analysis. *Geophysical Research Letters*, 41(13):4535–4541.

Hibert, C., Malet, J.-P., Bourrier, F., Provost, F., Berger, F., Bornemann, P., Tardif, P., and Mermin, E. (2017a). Single-block rockfall dynamics inferred from seismic signal analysis. *Earth Surface Dynamics*, 5(2):283–292.

Hibert, C., Mangeney, A., Grandjean, G., Baillard, C., Rivet, D., Shapiro, N. M., Satriano, C., Maggi, A., Boissier, P., Ferrazzini, V., and Crawford, W. (2014b). Automated identification, location, and volume estimation of rockfalls at Piton de la Fournaise volcano. *Journal of Geophysical Research: Earth Surface*, 119(5):1082–1105.

Hibert, C., Mangeney, A., Grandjean, G., Peltier, A., DiMuro, A., Shapiro, N. M., Ferrazzini, V., Boissier, P., Durand, V., and Kowalski, P. (2017b). Spatio-temporal evolution of rockfall activity from 2007 to 2011 at the Piton de la Fournaise volcano inferred from seismic data. *Journal of Volcanology and Geothermal Research*, 333-334:36–52.

Hibert, C., Mangeney, A., Grandjean, G., and Shapiro, N. M. (2011). Slope instabilities in Dolomieu crater, Réunion Island: From seismic signals to rockfall characteristics. *Journal of Geophysical Research: Earth Surface*, 116(4):1–18.

Hibert, C., Provost, F., Malet, J. P., Maggi, A., Stumpf, A., and Ferrazzini, V. (2017c). Automatic identification of rockfalls and volcano-tectonic earthquakes at the Piton de la Fournaise volcano using a Random Forest algorithm. *Journal of Volcanology and Geothermal Research*, 340:130–142.

Hough, S. E., Altidor, J. R., Anglade, D., Given, D., Janvier, M. G., Maharrey, J. Z., Meremonte, M., Mildor, B. S. L., Prepetit, C., and Yong, A. (2010). Localized damage caused by topographic amplification during the 2010 M7.0 Haiti earthquake. *Nature Geoscience*, 3(11):778–782.

Hruby, D. (2019). 'Things are getting unstable': global heating and the rise of rockfalls in Swiss Alps. *www.theguardian.com/world/2019/oct/02/things-are-getting-unstable-global-heating-and-the-rise-of-rockfalls-in-swiss-alps (Date accessed: 2019-10-06)*.

Huggel, C., Allen, S., Deline, P., Fischer, L., Noetzli, J., and Ravanel, L. (2012). Ice thawing, mountains falling-are alpine rock slope failures increasing. *Geology Today*, 28(3):98–104.

Hughes, T. (1987). *The Finite Element Method: Linear Static and Dynamic Finite Element Analysis*. Prentice-Hall.

Hungr, O., Evans, S. G., Bovis, M. J., and Hutchinson, J. N. (2001). A review of the classification of landslides of the flow type. *Environmental and Engineering Geoscience*.

Igel, H. (2017). *Computational seismology: a practical introduction*. Oxford University Press.

Jeong, S., Asimaki, D., Dafni, J., and Wartman, J. (2019). How topography-dependent are topographic effects? Complementary numerical modeling of centrifuge experiments. *Soil Dynamics and Earthquake Engineering*, 116:654–667.

Johnson, K. L. K. L. (1987). *Contact mechanics*. Cambridge University Press.

Jones, D. K. C. (1992). Landslide hazard assessment in the context of development. In McCall, G. J. H., Laming, D. J. C., and Scott, S. C., editors, *Geohazards: Natural and man-made*, pages 117–141. Springer Netherlands, Dordrecht.

Kanamori, H. and Given, J. W. (1982). Analysis of long-period seismic waves excited by the May 18, 1980, eruption of Mount St. Helens-A terrestrial monopole? *Journal of Geophysical Research: Solid Earth*, 87(B7):5422–5432.

Kanamori, H., Given, J. W., and Lay, T. (1984). Analysis of seismic body waves excited by the Mount St. Helens eruption of May 18, 1980. *Journal of Geophysical Research: Solid Earth*, 89(B3):1856–1866.

Kawakatsu, H. (1989). Centroid single force inversion of seismic waves generated by landslides. *Journal of Geophysical Research*, 94(B9):12363.

Köhler, A., Ohrnberger, M., Scherbaum, F., Wathelet, M., and Cornou, C. (2007). Assessing the reliability of the modified three-component spatial autocorrelation technique. *Geophysical Journal International*, 168(2):779–796.

Komatitsch, D., Tsuboi, S., and Tromp, J. (2005). The Spectral-Element Method in Seismology. *Geophysical Monograph-American Geophysical Union*, 157:205–227.

Konno, K. and Ohmachi, T. (1998). Ground-motion characteristics estimated from spectral ratio between horizontal and vertical components of microtremor. *Bulletin of the Seismological Society of America*, 88(1):228–241.

Kuo, C. Y., Tai, Y. C., Bouchut, F., Mangeney, A., Pelanti, M., Chen, R. F., and Chang, K. J. (2009). Simulation of Tsaoling landslide, Taiwan, based on Saint Venant equations over general topography. *Engineering Geology*, 104(3-4):181–189.

La Rocca, M., Galluzzo, D., Saccorotti, G., Tinti, S., Cimini, G. B., and Del Pezzo, E. (2004). Seismic signals asssociated with landslides and with a tsunami at Stromboli volcano, Italy. *Bulletin of the Seismological Society of America*, 94(5):1850–1867.

Labiouse, V. and Heidenreich, B. (2009). Half-scale experimental study of rockfall impacts on sandy slopes. *Natural Hazards and Earth System Science*, 9(6):1981–1993.

Lacroix, P. and Helmstetter, A. (2011). Location of seismic signals associated with microearthquakes and rockfalls on the Séchilienne landslide, French Alps. *Bulletin of the Seismological Society of America*, 101(1):341–353.

Larose, E., Carrière, S., Voisin, C., Bottelin, P., Baillet, L., Guéguen, P., Walter, F., Jongmans, D., Guillier, B., Garambois, S., Gimbert, F., and Massey, C. (2015). Environmental seismology: What can we learn on earth surface processes with ambient noise? *Journal of Applied Geophysics*, 116:62–74.

Lee, S. J., Chan, Y. C., Komatitsch, D., Huang, B. S., and Tromp, J. (2009a). Effects of realistic surface topography on seismic ground motion in the Yangminshan region of Taiwan based upon the spectral-element method and LiDAR DTM. *Bulletin of the Seismological Society of America*, 99(2 A):681–693.

Lee, S. J., Komatitsch, D., Huang, B. S., and Tromp, J. (2009b). Effects of topography on seismic-wave propagation: An example from Northern Taiwan. *Bulletin of the Seismological Society of America*, 99(1):314–325.

Lee, W. H. K., White, R. A., Harlow, D. H., Rogers, J. A., Spudich, P., and Dodge, D. A. (1994). Digital seismograms of selected aftershocks of the Northridge earthquake recorded by a dense seismic array on February 11, 1994 at Cedar Hill Nursery in Tarzana, California. *US Geol. Surv. Open-File Rept. 94*, 234.

Leprettre, B., Martin, N., Glangeaud, F., and Navarre, J.-P. (1998). Three-component signal recognition using time, time-frequency, and polarization information-application to seismic detection of avalanches. *IEEE Transactions on Signal Processing*, 46(1):83–102.

Lesage, P., Heap, M. J., and Kushnir, A. (2018). A generic model for the shallow velocity structure of volcanoes. *Journal of Volcanology and Geothermal Research*, 356:114—-126.

Levy, C., Mangeney, A., Bonilla, F., Hibert, C., Calder, E. S., and Smith, P. J. (2015). Friction weakening in granular flows deduced from seismic records at the Soufrière Hills Volcano, Montserrat. *Journal of Geophysical Research B: Solid Earth*, 120(11):7536–7557.

Lin, C. H., Kumagai, H., Ando, M., and Shin, T. C. (2010). Detection of landslides and submarine slumps using broadband seismic networks. *Geophysical Research Letters*, 37(22).

Liu, H., Anderson, D. L., and Kanamori, H. (1976). Velocity dispersion due to anelasticity; implications for seismology and mantle composition. *Geophysical Journal of the Royal Astronomical Society*, 47(1):41–58.

Lucas, A., Mangeney, A., and Ampuero, J. P. (2014). Frictional velocity-weakening in landslides on Earth and on other planetary bodies. *Nature Communications*, 5(1):3417.

Ma, S., Archuleta, R. J., and Page, M. T. (2007). Effects of large-scale surface topography on ground motions, as demonstrated by a study of the San Gabriel Mountains, Los Angeles, California. *Bulletin of the Seismological Society of America*, 97(6):2066–2079.

Madariaga, R. (2015). *Seismic Source Theory*, volume 4. Elsevier B.V.

Maggi, A., Ferrazzini, V., Hibert, C., Beauducel, F., Boissier, P., and Amemoutou, A. (2017). Implementation of a Multistation Approach for Automated Event Classification at Piton de la Fournaise Volcano. *Seismological Research Letters*, 88(3):878–891.

Manconi, A., Picozzi, M., Coviello, V., De Santis, F., and Elia, L. (2016). Real-time detection, location, and characterization of rockslides using broadband regional seismic networks. *Geophysical Research Letters*, 43(13):6960–6967.

Mangeney, A., Bouchut, F., Thomas, N., Vilotte, J. P., and Bristeau, M. O. (2007). Numerical modeling of self-channeling granular flows and of their levee-channel deposits. *Journal of Geophysical Research: Earth Surface*, 112(2):1–21.

Mangeney-Castelnau, A., Bouchut, F., Vilotte, J. P., Lajeunesse, E., Aubertin, A., and Pirulli, M. (2005). On the use of Saint Venant equations to simulate the spreading of a granular mass. *Journal of Geophysical Research: Solid Earth*, 110(B9).

Maradudin, A. A. (1987). Surface acoustic waves on real surfaces. *Physics of Phonons*, pages 82–147.

Margerin, L., Campillo, M., Van Tiggelen, B. A., and Hennino, R. (2009). Energy partition of seismic coda waves in layered media: theory and application to Pinyon Flats Observatory. *Geophysical Journal International*, 177(2):571–585.

Maufroy, E., Cruz-Atienza, V. M., Cotton, F., and Gaffet, S. (2015). Frequency-scaled curvature as a proxy for topographic site-effect amplification and ground-motion variability. *Bulletin of the Seismological Society of America*, 105(1):354–367.

McLaskey, G. C. and Glaser, S. D. (2010). Hertzian impact: Experimental study of the force pulse and resulting stress waves. *The Journal of the Acoustical Society of America*, 128(3):1087.

Merle, O., Mairine, P., Michon, L., Bachèlery, P., and Smietana, M. (2010). Calderas, landslides and paleo-canyons on Piton de la Fournaise volcano (La Réunion Island, Indian Ocean). *Journal of Volcanology and Geothermal Research*, 189(1-2):131–142.

Métaxian, J.-P., Lesage, P., and Dorel, J. (1997). Permanent tremor of Masaya Volcano, Nicaragua: Wave field analysis and source location. *Journal of Geophysical Research: Solid Earth*, 102(B10):22529—-22545.

Métaxian, J. P., O'Brien, G. S., Bean, C. J., Valette, B., and Mora, M. (2009). Locating volcano-seismic signals in the presence of rough topography: wave simulations on Arenal volcano, Costa Rica. *Geophysical Journal International*, 179(3):1547–1557.

Meunier, P., Hovius, N., and Haines, J. A. (2008). Topographic site effects and the location of earthquake induced landslides. *Earth and Planetary Science Letters*, 275(3-4):221–232.

Michon, L., Di Muro, A., Villeneuve, N., Saint-Marc, C., Fadda, P., and Manta, F. (2013). Explosive activity of the summit cone of Piton de la Fournaise volcano (La Réunion island): A historical and geological review. *Journal of Volcanology and Geothermal Research*, 264:117–133.

Michon, L., Staudacher, T., Ferrazzini, V., Bachèlery, P., and Marti, J. (2007). April 2007 collapse of Piton de la Fournaise: A new example of caldera formation. *Geophysical Research Letters*, 34(21):L21301.

Michon, L., Villeneuve, N., Catry, T., and Merle, O. (2009). How summit calderas collapse on basaltic volcanoes: New insights from the April 2007 caldera collapse of Piton de la Fournaise volcano. *Journal of Volcanology and Geothermal Research*, 184(1-2):138–151.

Mora, M. M., Lesage, P., Valette, B., Alvarado, G. E., Leandro, C., Métaxian, J. P., and Dorel, J. (2006). Shallow velocity structure and seismic site effects at Arenal volcano, Costa Rica. *Journal of Volcanology and Geothermal Research*, 152(1-2):121—-139.

Mordret, A., Rivet, D., Landès, M., and Shapiro, N. M. (2015). Three-dimensional shear velocity anisotropic model of Piton de la Fournaise Volcano (La Réunion Island) from ambient seismic noise. *Journal of Geophysical Research B: Solid Earth*, 120(1):406–427.

Mordret, A., Sun, H., Prieto, G. A., Toksöz, M. N., and Büyüköztürk, O. (2017). Continuous Monitoring of High-Rise Buildings Using Seismic Interferometry. *Bulletin of the Seismological Society of America*, 107(6):2759–2773.

Moretti, L., Allstadt, K., Mangeney, A., Capdeville, Y., Stutzmann, E., and Bouchut, F. (2015). Numerical modeling of the Mount Meager landslide constrained by its force history derived from seismic data. *Journal of Geophysical Research B: Solid Earth*, 120(4):2579–2599.

Moretti, L., Mangeney, A., Capdeville, Y., Stutzmann, E., Huggel, C., Schneider, D., and Bouchut, F. (2012). Numerical modeling of the Mount Steller landslide flow history and of the generated long period seismic waves. *Geophysical Research Letters*, 39(16):1–7.

Nakata, N., Boué, P., Brenguier, F., Roux, P., Ferrazzini, V., and Campillo, M. (2016). Body and surface wave reconstruction from seismic noise correlations between arrays at Piton de la Fournaise volcano. *Geophysical Research Letters*, 43(3):1047—-1054.

Nercessian, A., Him, A., Tipine, J.-C., and Sapin, M. (1996). Internal structure of Piton de la Foumaise volcano from seismic wave propagation and earthquake distribution. *Journal of Volcanology and Geothermal Research*, 70(996):123–143.

Newmark, N. M. (1959). A method of computation for structural dynamics. 85(3):67–94.

O'Brien, G. S. and Bean, C. J. (2009). Volcano topography, structure and intrinsic attenuation: Their relative influences on a simulated 3D visco-elastic wavefield. *Journal of Volcanology and Geothermal Research*, 183(1-2):122–136.

Pedersen, H., Lebrun, B., Hatzfeld, D., Campillo, M., Bard, P.-Y. Y., Le Brun, B., Hatzfeld, D., Campillo, M., and Bard, P.-Y. Y. (1994). Ground-motion amplitude across ridges. *Bulletin of the Seismological Society of America*, 84(6):1786–1800.

Peltier, A., Massin, F., Bachèlery, P., and Finizola, A. (2012). Internal structure and building of basaltic shield volcanoes: The example of the Piton de La Fournaise terminal cone (La Réunion). *Bulletin of Volcanology*, 74(8):1881–1897.

Perrier, L., Métaxian, J.-P., Battaglia, J., and Garaebiti, E. (2012). Estimation of the near-surface velocity structure of the Yasur-Yenkahe volcanic complex, Vanuatu. *Journal of Volcanology and Geothermal Research*, 227-228:50–60.

Petley, D. (2019). The ten most important landslides events of 2018. *www.blogs.agu.org/landslideblog/2019/01/04/important-landslide-events-of-2018 (Date accessed: 2019-10-06)*.

Podolskiy, E. A. and Walter, F. (2016). Cryoseismology. *Reviews of Geophysics*, 54(4):708–758.

Prôno, E., Battaglia, J., Monteiller, V., Got, J. L., and Ferrazzini, V. (2009). P-wave velocity structure of Piton de la Fournaise volcano deduced from seismic data recorded between 1996 and 1999. *Journal of Volcanology and Geothermal Research*, 184(1-2):49–62.

Provost, F., Hibert, C., and Malet, J.-P. (2017). Automatic classification of endogenous landslide seismicity using the Random Forest supervised classifier. *Geophysical Research Letters*, 44(1):113–120.

Provost, F., Malet, J. P., Hibert, C., Helmstetter, A., Radiguet, M., Amitrano, D., Langet, N., Larose, E., Abancó, C., Hürlimann, M., Lebourg, T., Levy, C., Le Roy, G., Ulrich, P., Vidal, M., and Vial, B. (2018). Towards a standard typology of endogenous landslide seismic sources. *Earth Surface Dynamics*, 6(4):1059–1088.

Rai, M., Rodriguez-Marek, A., and Chiou, B. S. (2017). Empirical Terrain-Based Topographic Modification Factors for Use in Ground Motion Prediction. *Earthquake Spectra*, 33(1):157—-177.

Riahi, N. and Gerstoft, P. (2015). The seismic traffic footprint: Tracking trains, aircraft, and cars seismically. *Geophysical Research Letters*, 42(8):2674–2681.

Ripperger, J., Igel, H., and Wasserman, J. (2003). Seismic wave simulation in the presence of real volcano topography. *Journal of Volcanology and Geothermal Research*, 128(1-3):31–44.

Roche, O., Attali, M., Mangeney, A., and Lucas, A. (2011). On the run-out distance of geophysical gravitational flows: Insight from fluidized granular collapse experiments. *Earth and Planetary Science Letters*, 311(3-4):375–385.

Roult, G., Peltier, A., Taisne, B., Staudacher, T., Ferrazzini, V., and Di Muro, A. (2012). A new comprehensive classification of the Piton de la Fournaise activity spanning the 1985-2010 period. Search and analysis of short-term precursors from a broad-band seismological station. *Journal of Volcanology and Geothermal Research*, 241-242:78–104.

Saccorotti, G., Chouet, B., and Dawson, P. (2003). Shallow-velocity models at the Kilauea Volcano, Hawaii, determined from array analyses of tremor wavefields. *Geophysical Journal International*, 152(3):633—-648.

Sánchez-Sesma, F. J. and Campillo, M. (1993). Topographic effects for incident P, SV and Rayleigh waves. *Tectonophysics*, 218(1-3):113–125.

Sánchez-Sesma, F. J., Weaver, R. L., Kawase, H., Matsushima, S., Luzón, F., and Campillo, M. (2011). Energy partitions among elastic waves for dynamic surface loads in a semi-infinite solid. *Bulletin of the Seismological Society of America*, 101(4):1704–1709.

Savage, S. B. and Hutter, K. (1989). The motion of a finite mass of granular material down a rough incline. *Journal of Fluid Mechanics*, 199:177–215.

Sergeant, A., Mangeney, A., Stutzmann, E., Montagner, J. P., Walter, F., Moretti, L., and Castelnau, O. (2016). Complex force history of a calving-generated glacial earthquake derived from broadband seismic inversion. *Geophysical Research Letters*, 43(3):1055–1065.

Slepyan, L. I. (2010). Dynamic crack growth under Rayleigh wave. *Journal of the Mechanics and Physics of Solids*, 58(5):636–655.

Snieder, R. (1986). The influence of topography on the propagation and scattering of surface waves. *Physics of the Earth and Planetary Interiors*, 44(3):226–241.

Soontiens, N., Stastna, M., Waite, M. L., Soontiens, N., Stastna, M., and Waite, M. L. (2013). Numerical Simulations of Waves over Large Crater Topography in the Atmosphere. *Journal of the Atmospheric Sciences*, 70(4):1216–1232.

Souriau, A., Chaljub, E., Cornou, C., Margerin, L., Calvet, M., Maury, J., Wathelet, M., Grimaud, F., Ponsolles, C., Pequegnat, C., Langlais, M., and Guéguen, P. (2011). Multimethod characterization of the French-Pyrenean valley of bagnères-de-bigorre for seismic-hazard evaluation: Observations and models. *Bulletin of the Seismological Society of America*, 101(4):1912–1937.

Spudich, P., Hellweg, M., and Lee, W. H. (1996). Directional topographic site response at Tarzana observed in aftershocks of the 1994 Northridge, California, earthquake: Implications for mainshock motions. *Bulletin of the Seismological Society of America*, 86(1 SUPPL. B):193–208.

Staudacher, T., Ferrazzini, V., Peltier, A., Kowalski, P., Boissier, P., Catherine, P., Lauret, F., and Massin, F. (2009). The April 2007 eruption and the Dolomieu crater collapse, two major events at Piton de la Fournaise (La Réunion Island, Indian Ocean). *Journal of Volcanology and Geothermal Research*, 184(1-2):126–137.

Suriñach, E., Vilajosana, I., Khazaradze, G., Biescas, B., Furdada, G., and Vilaplana, J. M. (2005). Seismic detection and characterization of landslides and other mass movements. *Natural Hazards and Earth System Science*, 5(6):791–798.

Tsai, V. C., Rice, J. R., and Fahnestock, M. (2008). Possible mechanisms for glacial earthquakes. *Journal of Geophysical Research*, 113(F3):F03014.

Varnes, D. J. (1978). Slope movement types and processes. *National Academy of Sciences Transportation Research Board Special Report*, 176:11–33.

Vilajosana, I., Suriñach, E., Abellán, A., Khazaradze, G., Garcia, D., and Llosa, J. (2008). Rockfall induced seismic signals: Case study in Montserrat, Catalonia. *Natural Hazards and Earth System Science*, 8(4):805–812.

Volkwein, A., Schellenberg, K., Labiouse, V., Agliardi, F., Berger, F., Bourrier, F., Dorren, L., Gerber, W., and Jaboyedoff, M. (2011). Rockfall characterisation and structural protection - a review. *Natural Hazards and Earth System Sciences*, 11:2617–2651.

Vouillamoz, N., Rothmund, S., and Joswig, M. (2018). Characterizing the complexity of microseismic signals at slow-moving clay-rich debris slides: the Super-Sauze (southeastern France) and Pechgraben (Upper Austria) case studies. *Earth Surface Dynamics*, 6(2):525–550.

Wang, B., Da, Y., and Qian, Z. (2018). Forward and Inverse Studies on Scattering of Rayleigh Wave at Surface Flaws. *Applied Sciences*, 8(3):427.

Wang, L., Xu, Y., Xia, J., and Luo, Y. (2015). Effect of near-surface topography on high-frequency Rayleigh-wave propagation. *Journal of Applied Geophysics*, 116:93–103.

Wang, Y. (2015). Frequencies of the Ricker wavelet. *GEOPHYSICS*, 80(2):A31–A37.

Wathelet, M., Jongmans, D., Ohrnberger, M., and Bonnefoy-Claudet, S. (2008). Array performances for ambient vibrations on a shallow structure and consequences over V s inversion. *Journal of Seismology*, 12(1):1–19.

Weaver, R. L. (1982). On diffuse waves in solid media. *The Journal of the Acoustical Society of America*, 71(6):1608–1609.

Weaver, R. L. (1985). Diffuse elastic waves at a free surface. *The Journal of the Acoustical Society of America*, 78(1):131–136.

Weichert, D., Horner, R. B., and Evans, S. G. (1994). Seismic signatures of landslides: the 1990 Brenda Mine collapse and the 1965 Hope rockslides. *Bulletin - Seismological Society of America*, 84(5):1523–1532.

Yamada, M., Kumagai, H., Matsushi, Y., and Matsuzawa, T. (2013). Dynamic landslide processes revealed by broadband seismic records. *Geophysical Research Letters*, 40(12):2998–3002.

Yamada, M., Mangeney, A., Matsushi, Y., and Moretti, L. (2016). Estimation of dynamic friction of the Akatani landslide from seismic waveform inversion and numerical simulation. *Geophysical Journal International*, 206(3):1479—-1486.

Yamada, M., Matsushi, Y., Chigira, M., and Mori, J. (2012). Seismic recordings of landslides caused by Typhoon Talas (2011), Japan. *Geophysical Research Letters*, 39(13).

Zhang, S.-l., Yang, X.-g., and Zhou, J.-w. (2018a). A theoretical model for the estimation of maximum impact force from a rockfall based on contact theory. *Journal of Mountain Science*, 15(2):430–443.

Zhang, Z., Fleurisson, J. A., and Pellet, F. (2018b). The effects of slope topography on acceleration amplification and interaction between slope topography and seismic input motion. *Soil Dynamics and Earthquake Engineering*, 113(May):420–431.

Zhao, J., Moretti, L., Mangeney, A., Stutzmann, E., Kanamori, H., Capdeville, Y., Calder, E. S., Hibert, C., Smith, P. J., Cole, P., and LeFriant, A. (2015). Model space exploration for determining landslide source history from long-period seismic data. *Pure and Applied Geophysics*, 172(2):389–413.

Zimmer, V. L. and Sitar, N. (2015). Detection and location of rock falls using seismic and infrasound sensors. *Engineering Geology*, 193:49–60.

Chapter A

Annexes

A.1 The discrete Parseval's theorem

The Fourier transform of a continuous function $x(t)$ is written as

$$\hat{x}(\omega) = \int_{-\infty}^{\infty} x(t) \mathrm{e}^{-i\omega t} \, \mathrm{d}t. \tag{A.1}$$

For a finite sequence of N sampling points separated by time step Δt, the integral becomes a summation over N:

$$\hat{x}(\omega) = \sum_{k=0}^{N-1} x[k] \mathrm{e}^{-i\omega k \Delta t} \, \Delta t. \tag{A.2}$$

The sequence can be regarded as periodic with the fundamental frequency ω_0 determined by the total duration T of the sequence: $\omega_0 = 2\pi/T = 2\pi/N\Delta t$. With N sample points, the periodic cycle can be subdivided into N frequencies:

$$\omega = 0, 1 \cdot \frac{2\pi}{N\Delta t}, 2 \cdot \frac{2\pi}{N\Delta t}, ..., n \cdot \frac{2\pi}{N\Delta t}, ..., (N-1) \cdot \frac{2\pi}{N\Delta t}. \tag{A.3}$$

Note that $\omega = 0$ corresponds to the average of the data. Evaluating equation A.2 at these frequencies only gives the discrete Fourier transform (DFT):

$$\hat{x}[n] = \sum_{k=0}^{N-1} x[k] \mathrm{e}^{-in\frac{2\pi}{N}k} \, \Delta t, \text{ with } n = 0, (N-1). \tag{A.4}$$

With the discrete Fourier transform by hand, we can now show Parseval's theorem for a discrete sequence. For this, we

$$|\hat{x}[n]|^2 = \sum_{k=0}^{N-1} x[k] \sum_{k'=0}^{N-1} x^*[k'] \mathrm{e}^{-in\frac{2\pi}{N}(k-k')} \, \Delta t^2 \tag{A.5}$$

$$= \sum_{k=0}^{N-1} x[k] \sum_{k'=0}^{N-1} x^*[k'] \mathrm{e}^{-in\frac{2\pi}{N}(k-k')} \, \Delta t \frac{1}{N\Delta f}, \tag{A.6}$$

where the relation $\Delta t = 1/N\Delta f$ was used which can be deduced form the frequency series in equation A.3. Rearranging the terms and summing over all frequencies leads to

$$\sum_{n=0}^{N-1} |\hat{x}[n]|^2 \, \Delta f = \frac{1}{N} \sum_{k=0}^{N-1} x[k] \sum_{k'=0}^{N-1} x^*[k'] \sum_{n=0}^{N-1} \mathrm{e}^{-in\frac{2\pi}{N}(k-k')} \, \Delta t. \tag{A.7}$$

Making use of the formula for a finite geometric series $\sum_{n=0}^{N-1} ar^n = \frac{a(1-r^N)}{1-r}$, the inner sum on the right hand side can be rewritten as

$$\sum_{n=0}^{N-1} \mathrm{e}^{-in\frac{2\pi}{N}(k-k')} = \frac{1 - \mathrm{e}^{-i2\pi(k-k')}}{1 - \mathrm{e}^{-i2\pi N(k-k')/N}} = N\delta_{kk'}, \tag{A.8}$$

where $\delta_{kk'}$ denotes the Kronecker delta which is 1 if $k = k'$ and 0 elsewhere. It follows directly

$$\sum_{n=0}^{N-1} |\hat{x}[n]|^2 \, \Delta f = \sum_{k=0}^{N-1} |x[k]|^2 \Delta t. \tag{A.9}$$